Integrated Experimental and Computational Approaches for the Prediction of Drug-Drug Interactions

Thesis submitted in accordance with the requirements of the University of Liverpool for the degree of Doctor in Philosophy

by Hannah Mae Kinvig

April 2021

This thesis is the results of my own work. The material contained within the thesis has not been presented, either wholly or in part, for any other degree or qualification.

Hannah Mae Kinvig

This research was carried out in the

Department of Pharmacology and Therapeutics

Institute of Systems, Molecular and Integrative Biology

University of Liverpool, UK

Table of Contents

Acknowledgements

I would like to begin by thanking University Hospital Basel for funding my PhD studentship at the University of Liverpool. I would also like to thank my primary supervisor Dr Marco Siccardi and my secondary supervisors Prof Catia Marzolini and Prof Andrew Owen. Marco has been both a mentor and a friend throughout my PhD, providing guidance, knowledge and encouragement in all aspects of my studies. He has taught me how to be a good scientist and team member and I am forever grateful for the supportive, collaborative and enjoyable environment he has created within our team at the university. I am thankful for Catia's support, her extensive knowledge of drug-drug interactions has been invaluable during my PhD, as well as our monthly scientific discussions with Dr Felix Stader. A special thank you to Andrew for supporting my decision to pursue a PhD to further my scientific career. I would also like to thank all those past and present in "H Block", you have taught me so much and I will cherish the friendships I have made along this journey. From hilarious storytelling during lunch under the stairs, snowshoeing in Seattle before CROI, to socially distanced games nights playing Among Us on Zoom, this has been one of the most enjoyable experiences of my life.

I would like to thank my Mum, Dad and Brother for their continued love and support over the past few years. For all the lifts to the train station, cups of tea and listening to me talk about troubleshooting the LC-MS/MS. You believe in me without hesitation and I wouldn't be where I am today without you. I would also like to thank Nan and Alan for being a special part of my life. And to Alfie the Cavachon, thank you for greeting me every day when I got back from university as if I had been gone for a lifetime. Lastly, I would like to thank my fiancée Kat. You are my inspiration and your love, support and advice has helped me more than words can say. Thank you for being my person and I cannot wait for our life together in Boston with our cats Henry and Beanz.

Abbreviations

3TC	Lamivudine
AA	Automatic Integration
AAFE	Absolute Average-Fold Error
ABC	Adenosine Triphosphate-Binding Cassette
ABS	Absorption
$Abundance_E$	Enzyme Abundance
ACN	Acetonitrile
ACN_L	LC-MS/MS Grade Acetonitrile
ADME	Absorption, Distribution, Metabolism And Excretion
AIDS	Acquired Immune Deficiency Syndrome
AIR	Arterial Infusion Rate
AR	Arterial Blood
arb	Arbitrary Unit
ART	Antiretroviral Therapy
ARV	Antiretroviral
ATP	Adenosine Triphosphate
ATV/r	Ritonavir Boosted Atazanavir
AUC	Area Under The Curve
AZT	Zidovudine
BCA	Bicinchoninic Acid
BCG	Bacillus Calmette-Guérin
BCRP	Breast Cancer Resistance Protein
BID	Twice Daily

BMI	Body Mass Index
BSA	Body Surface Area
BSEP	Bile-Salt Export Pump
C	Plasma Concentration
CAB	Cabotegravir
CAR	Constitutive Androstane Receptor
C_{avg}	Average Plasma Concentration
C_B	Concentration In The Blood
CCR5	C-C Chemokine Receptor Type 5
CD4	Cluster Of Differentiation 4
CHRM	Cryopreserved Hepatocyte Recovery Medium
C_{Inh}	Concentration Of Inhibitor
CL	Clearance
CL/F	Apparent Oral Clearance
$CL_{Biliary}$	Biliary Clearance
CL_{gut}	Gut Clearance
$CL_{int,CYP}$	Cytochrome P450 Enzyme Intrinsic Clearance
$CL_{int,CYP3A4}$	CYP3A4 Intrinsic Clearance
$CL_{int,E}$	Enzyme Intrinsic Clearance
$CL_{int,liver}$	Total Metabolic Intrinsic Clearance
$CL_{int,liverE}$	Enzyme Intrinsic Clearance Scaled To Whole Liver
$CL_{int,T}$	Hepatic Transporter Intrinsic Clearance
$CL_{int,T,a}$	Active Hepatic Transporter Intrinsic Clearance
$CL_{int,T,p}$	Passive Hepatic Transporter Intrinsic Clearance
$CL_{int,UGT}$	UDP-Glucuronosyltransferase Enzyme Intrinsic Clearance

C_{Liver}	Liver Concentration
CL_{sys}	Systemic Clearance
C_{max}	Maximum Plasma Concentration
C_{min}	Minimum Plasma Concentration
COBI	Cobicistat
COL	Colon
C_{PV}	Portal Vein Concentration
C_{SI}	Small Intestine Concentration
C_{sol}	Soluble Concentration
CV	Coefficient Of Variation
CXCR4	C-X-C Chemokine Receptor Type 4
CYP	Cytochrome P450
CYP2C9	Cytochrome P450 2C9
CYP3A4	Cytochrome P450 3A4
D	Dose
$D^*_{vo:w}$	Olive Oil:Buffer Partition Coefficient Of Nonionised And Ionised Species at pH 7.4
DAAs	Direct Acting Antivirals
DDI	Drug-Drug Interaction
DDI_R	Drug-Drug Interaction Ratio
dH_2O	Deionised H_2O
DIS	Dissolved
DMSO	Dimethyl Sulfoxide
DNA	Deoxyribonucleic Acid

$drug_{DDI}$	Substrate Drug Parameter Value In The Presence Of The Perpetrator Drug
$drug_{sub}$	Substrate Drug Parameter Value
DRV	Darunavir
DRV/r	Ritonavir Boosted Darunavir
DTG	Dolutegravir
E	Experimentally Determined
E:P	Erythrocyte:Plasma Ratio
E_{CYP3A4}	CYP3A4 Estimated Value
EFV	Efavirenz
ELISA	Enzyme-Linked Immunosorbent Assays
ENZYME	Induction Value Of Enzyme
$ENZYME_0$	Baseline Value Of Enzyme
$ENZYME^I$	Fold Change Value Of Enzyme
ESI	Electrospray Ionisation
EXP	Exponential
F	Bioavailability
F_a	Fraction Of Drug Absorbed Across The Gi Tract
FA_L	LC-MS/MS Grade Formic Acid
FDA	U.S Food And Drug Administration
F_g	Fraction Of Drug Escaping Metabolism In The GI Tract
F_h	Fraction Of Drug Escaping First-Pass Metabolism In The Liver
FTC	Emtricitabine
FTR	Fostemsavir
f_u	Fraction Of Unbound Drug In Plasma

$f_{u,b}$	Fraction Unbound In Blood
$f_{u,g}$	Fraction Unbound In The Gut
$f_{u,t}$	Fraction Unbound In Tissue
$f_{u,Liver}$	Fraction Unbound In The Liver
GI	Gastrointestinal
gp120	Glycoprotein 120
gp41	Glycoprotein 41
GU	Gut
GZR	Grazoprevir
H	High Range
H_2O_L	LC-MS/MS Grade Water
HAV	Hepatitis A
HBD	Hydrogen Bond Donor
HBV	Hepatitis B
HCV	Hepatitis C
HEK293	Human Embryonic Kidney 293
HIV	Human Immunodeficiency Virus
HNF4α	Hepatocyte Nuclear Factor 4A
HRP	Horseradish Peroxidase
IC_{50}	Half Maximal Inhibitory Concentration
IM	Intramuscular
IPA	Isopropanol Alcohol
IS	Internal Standard
ITC	International Transporter Consortium
IV	Intravenous

IVIVE	In Vitro-In Vivo Extrapolation
K_a	Absorption Rate Constant
K_c	Colon Transit Rate Constant
$K_{cyp,deg}$	CYP Enzyme Degradation Rate Constant
$K_{cyp,rna}$	CYP RNA Degradation Rate Constant
K_D	Dissociation Rate Constant
$k_{enzyme,deg}$	Rate Constants For Enzyme Degradation
$k_{enzyme,syn}$	Rate Constants For Enzyme Synthesis
KHB	Krebs-Henseleit Buffer
K_i	Inhibition Constant
$K_{i,NF}$	Constant For Negative Feedback Inhibition
$K_{inact,pxr}$	PXR Inactivation Rate Constant
K_m	Michaelis Constant
K_r	Renal Elimination Rate Constant
$k_{rna,deg}$	Rate Constants Form mRNA Degradation
K_s	Transit Rates For Stomach
K_t	Small Intestine Transit Rate Constant
$K_{ugt,deg}$	UGT Enzyme Degradation Rate Constant
$K_{ugt,rna}$	UGT RNA Degradation Rate Constant
L	Low Range
LC-MS/MS	Liquid Chromatography With Tandem Mass Spectrometry
LLOQ	Lower Limit Of Quantification
Log $P_{O:W}$	Partition Coefficient Between Octanol And Water
LPV	Lopinavir
LPV/r	Ritonavir Boosted Lopinavir

LU	Lungs
M	Mid-Range
m/z	Mass-To-Charge
MA	Manual Integration
MATE1	Multidrug And Toxin Extrusion Protein 1
MDCK	Madin-Darby Canine Kidney
MDT	Multi-Drug Therapy
MDZ	Midazolam
MEC	Minimum Effective Concentration
MPPGL	Microsomal Protein Per Gram Of Liver
mRNA	Messenger RNA
MRP	Multidrug Resistance-Associated Protein
MRP2	Multidrug Resistance-Associated Protein 2
MRP3	Multidrug Resistance-Associated Protein 3
MRP4	Multidrug Resistance-Associated Protein 4
MRP6	Multidrug Resistance-Associated Protein 6
MS	Mass Spectrometer
MTC	Minimum Toxic Concentration
NC	Not Calculated
NIF	Nifedipine
NNRTI	Non-Nucleoside Reverse Transcriptase Inhibitor
NRTI	Nucleoside Reverse Transcriptase Inhibitor
NTCP	Sodium/Taurocholate Co-Transporting Peptide
NVP	Nevirapine
OALWH	Older Adults Living With HIV

OAT	Organic Anion Transporter
OAT2	Organic Anion Transporter 2
OAT7	Organic Anion Transporter 7
OATP	Organic Anion Transporting Polypeptides
OATP1B1	Organic Anion Transporting Polypeptides 1B1
OATP1B3	Organic Anion Transporting Polypeptides 1B3
OATP2B1	Organic Anion Transporting Polypeptides 2B1
OCT	Organic Cation Transporter
OCT 1	Organic Cation Transporter 1
OSTα	Organic Solute Transporter Alpha
OSTβ	Organic Solute Transporter Beta
PA-IC_{90}	Protein Adjusted 90% Inhibitory Constant
P_{app}	Apparent Permeability
PB	Paucibacillary
PBPK	Physiologically-Based Pharmacokinetic Modelling
PBS	Phosphate Buffered Saline
PCR	Polymerase Chain Reaction
PEP	Post-Exposure Prophylaxis
P-gp	P-Glycoprotein
PHH	Primary Human Hepatocyte
PI	Protease Inhibitor
PI/r	Ritonavir Boosted Protease Inhibitor
PIT	Pitavastatin
pK_a	Logarithmic Value Of The Dissociation Constant
pK_a1	Logarithmic Value Of The Dissociation Constant For Acid

pK_a2	Logarithmic Value Of The Dissociation Constant For Base
PLWH	People Living With HIV
$P_{o:w}$	Partition Coefficient Between Octanol And Water
PPHH	Plated Primary Human Hepatocyte
PRA	Pravastatin
PrEP	Pre-Exposure Prophylaxis
PSA	Polar Surface Area
$P_{t:p}$	Adipose And Non-Adipose Tissue:Plasma Partition Coefficient
$P_{vo:w}$	N-Octanol:Buffer Partition Coefficient Of Nonionised Species at pH 7.4
PWID	People Who Inject Drugs
PXR	Pregnane X Receptor
PXR_{act}	Normalised Amount Of Activated PXR
QC	Quality Control
QD	Once Daily
Q_{gut}	Blood Flow To The Gut
QMT	Once Monthly
R	Blood-To-Plasma Ratio
RAL	Raltegravir
RIF	Rifampicin
RNA	Ribonucleic Acid
RNA_0	Baseline Value Of mRNA
RNA^I	Fold Change Value Of mRNA
ROS	Rosuvastatin
RPV	Rilpivirine

RT	Retention Time
RTV	Ritonavir
S	Substrate Concentration
SC	Subcutaneous
SCHH	Sandwich-Cultured Human Hepatocyte
SD	Standard Deviation
SDR	Single Dose Rifampicin
SE	Standard Error
SI	Small Intestine
SLC	Solute Carrier
SNPs	Single Nucleotide Polymorphisms
SPHH	Suspension Primary Human Hepatocyte
SRM	Selective Reaction Monitoring
ST	Stomach
T	Other Non-Eliminating Organs And Tissues
TAF	Tenofovir Alafenamide
TB	Tuberculosis
TDF	Tenofovir Disoproxil Fumarate
TFV	Tenofovir
TFV-DP	Tenofovir Diphosphate
TIA	Total Intestinal Absorption
T_{max}	Time Of Maximum Concentration
UGT	Uridine 5'-Diphospho-Glucuronosyltransferase
UGT1A1	Uridine 5'-Diphospho-Glucuronosyltransferase 1A1
UGT1A3	Uridine 5'-Diphospho-Glucuronosyltransferase 1A3

UGT2B7	Uridine 5'-Diphospho-Glucuronosyltransferase 2B7
UNAIDS	Joint United Nations Programme On HIV/Aids
UND	Undissolved
V	Voltage
VE	Venous Blood
V_e	Fractional Volumes Of Erythrocytes
VIR	Venous Infusion Rate
V_{max}	Maximum Velocity
V_{nl}	Neutral Lipid Volume Fraction Of Wet Tissue Weight
V_p	Fractional Volumes Of Plasma
V_{ph}	Phospholipid Volume Fraction Of Wet Tissue Weight
V_{ss}	Volume Of Distribution
V_t	Fractional Volumes Of Tissue
V_w	Water Volume Fraction Of Wet Tissue Weight
WHO	World Health Organisation
W_{Liver}	Weight Of The Liver
W_{PV}	Weight Of The Portal Vein

Publications

Stader F, Courlet P, **Kinvig H**, Penny MA, Decosterd LA, Battegay M, Siccardi M, Marzolini C. Clinical Data Combined With Modeling and Simulation Indicate Unchanged Drug-Drug Interaction Magnitudes in the Elderly. Clin Pharmacol Ther. 2021 Feb;109(2):471-484. doi: 10.1002/cpt.2017. Epub 2020 Sep 18. PMID: 32772364.

Stader F, Courlet P, **Kinvig H**, Battegay M, Decosterd LA, Penny MA, Siccardi M, Marzolini C. Effect of ageing on antiretroviral drug pharmacokinetics using clinical data combined with modelling and simulation. Br J Clin Pharmacol. 2021 Feb;87(2):458-470. doi: 10.1111/bcp.14402. Epub 2020 Jun 14. PMID: 32470203.

Stader F, **Kinvig H**, Penny MA, Battegay M, Siccardi M, Marzolini C. Physiologically Based Pharmacokinetic Modelling to Identify Pharmacokinetic Parameters Driving Drug Exposure Changes in the Elderly. Clin Pharmacokinet. 2020 Mar;59(3):383-401. doi: 10.1007/s40262-019-00822-9. PMID: 31583609.

Stader F, Siccardi M, Battegay M, **Kinvig H**, Penny MA, Marzolini C. Repository Describing an Aging Population to Inform Physiologically Based Pharmacokinetic Models Considering Anatomical, Physiological, and Biological Age-Dependent Changes. Clin Pharmacokinet. 2019 Apr;58(4):483-501. doi: 10.1007/s40262-018-0709-7. PMID: 30128967.

Stader F, **Kinvig H**, Battegay M, Khoo S, Owen A, Siccardi M, Marzolini C. Analysis of Clinical Drug-Drug Interaction Data To Predict Magnitudes of Uncharacterized Interactions between Antiretroviral Drugs and Comedications. Antimicrob Agents Chemother. 2018 Jun 26;62(7):e00717-18. doi: 10.1128/AAC.00717-18. PMID: 29686151; PMCID: PMC6021627.

Communications

Poster Presentations

Kinvig H, Stader F, Bunglawala FS, Rajoli RK, Cottura N, Howarth AE, Owen A, Marzolini C, Siccardi M. High-Dose Rifampicin for the Treatment of Leprosy in HIV Patients Taking Dolutegravir. Conference on Retroviruses and Opportunistic Infections (CROI). Virtual, March 8 – 11, 2020.

Kinvig H, Stader F, Howarth AE, Roberts O, Marzolini C, Siccardi M. Exploring the Role of Age in Transporter-Related Drug-Drug Interactions. International Workshop of Clinical Pharmacology on HIV, Hepatitis, and Other Antiretroviral Drugs. Virtual, September 29 – 30, 2020.

Kinvig H, Stader F, Roberts O, Owen A, Marzolini C, Siccardi M. The Role of OATP1B1 in Grazoprevir Drug-Drug Interactions and The Elderly. Conference on Retroviruses and Opportunistic Infections (CROI). Seattle, Washington, USA, March 4 – 7, 2019.

Abstract

Integrated Experimental and Computational Approaches for the Prediction of Drug-Drug Interactions by Hannah Mae Kinvig.

People living with HIV (PLWH) are highly susceptible to drug-drug interactions (DDIs) due to the increased risk of coinfections and comorbidities. Antiretroviral (ARV) drugs used for the treatment of HIV can be both victims and perpetrators of DDIs with potential effects on drug exposure leading to reduced efficacy and toxicity. Transporters have been identified as key mediators of drug pharmacokinetics however their role in DDIs remains unclear due to our current paucity of knowledge. The complexities surrounding the clinical management of DDIs in PLWH is further hindered by a lack of evidence-based guidance for many drug combinations. The aim of this thesis was to utilise *in vitro* and *in silico* techniques to explore the role of transporters in DDIs as well as investigate the magnitude of potential DDIs in PLWH that currently have no clinical data to support their management.

Uptake and efflux transporters facilitate the clearance of drugs in the liver however, due to the complex interplay with enzymes along with non-specific probe substrates and inhibitors, their role in clinically relevant DDIs have not been fully elucidated. *In vitro* and *in silico* techniques can be applied synergistically to investigate hepatic transporter-mediated DDIs. Chapter 2 describes the development and verification of a cryopreserved suspension primary human hepatocyte (SPHH) *in vitro* assay used to calculate the hepatic intrinsic clearance and inhibition constant (K_i) of the well-known organic anion transporting polypeptides (OATP) 1B1 and 1B3 substrate and inhibitor, pitavastatin (PIT) and rifampicin (RIF). This *in vitro* data was then utilised in Chapter 3 in a physiologically based pharmacokinetic (PBPK) model to simulate the DDI between PIT and RIF and was successfully verified against observed data. Chapter 4 applied the verified *in vitro-in silico* framework to assess the role of transporters in the complex DDI between the hepatitis C (HCV) NS3/4A protease inhibitor (PI) grazoprevir (GZR) and HIV PIs atazanavir (ATV), darunavir (DRV) and ritonavir (RTV), testing the suitability of the framework in a clinically relevant DDI scenario. Additionally, chapter 5 utilised SPHHs from elderly donors *in vitro* alongside an enzyme-linked immunosorbent assay (ELISA) to investigate the effect of age on transporter expression and activity. Furthermore, in chapter 6 an enzyme induction PBPK model was developed and verified to predict the magnitude of DDI between high dose once monthly (QMT) RIF and dolutegravir (DTG) 50mg twice-daily for the treatment of leprosy in PLWH as there is currently no evidence-based guidance to support their clinical management.

There is a demand for paralleled clinical management and research of DDIs in PLWH. These findings represent a potential *in vitro-in silico* framework utilising a non-drug specific IVIVE correction factor for the investigation of hepatic uptake transporters in DDIs. Additionally, these findings could help fill the knowledge gap on the role of older age in transporter expression and activity, providing key research in this underrepresented population. The reported findings could also help support the clinical management of DDIs in high dose QMT RIF regimens, presenting *in silico* assessment strategies for concomitant antiretroviral therapy.

Chapter 1

General Introduction

Contents

1.1 Human Immunodeficiency Virus

Human immunodeficiency virus (HIV) is a retrovirus that was first discovered in 1983, two years after the first diagnosis of acquired immune deficiency syndrome (AIDS). Between 1983 and 1984 multiple teams of scientists provided evidence for the causal link between HIV and AIDS (1). Since their discovery, 75.7 million people have been infected with HIV and 32.7 million have died from AIDS-related illnesses, globally. The amount of PLWH has increased approximately 80% since 1990 as shown in Figure 1.1, with 38 million PLWH in 2019, of which 1.8 million were children aged 0 – 14 years. Since the peak of HIV in 1998, the amount of people newly infected with HIV has decreased by 40% to 1.7 million people in 2019 (2, 3). As shown in Figure 1.2, Africa has the largest burden of HIV with over 67% of the total PLWH. However, relative to 2010 Africa has the greatest decrease in new diagnosis and AIDS-related deaths in comparison to other regions. Europe and the Eastern Mediterranean regions have the biggest increase in new diagnosis and AIDS-related deaths and make up 6.8% and 1.1% of total PLWH, respectively (4).

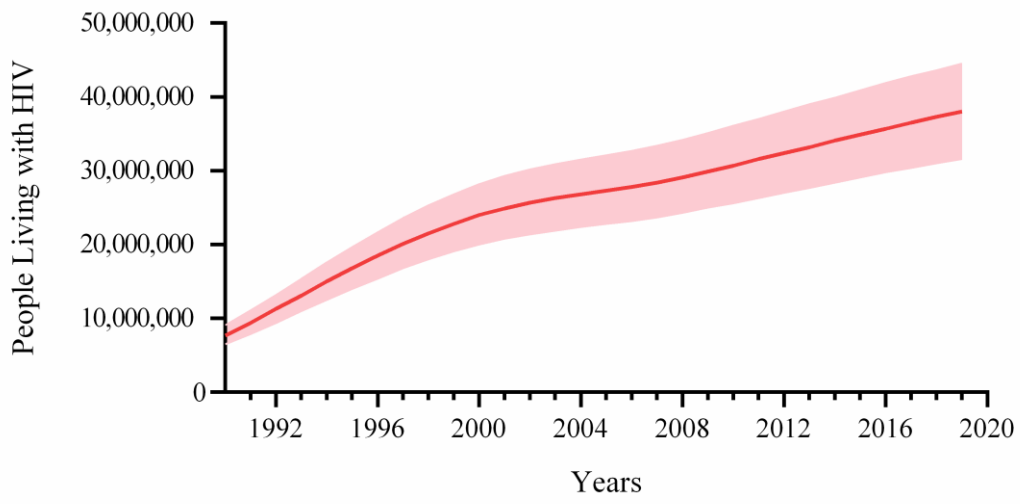

Figure 1.1 Global PLWH from 1990 to 2019, based on Joint United Nations Programme On HIV/AIDS (UNAIDS) and World Health Organisation (WHO) estimates (3). The red line represents the estimated mean with the shaded red area representing the upper and lower limits.

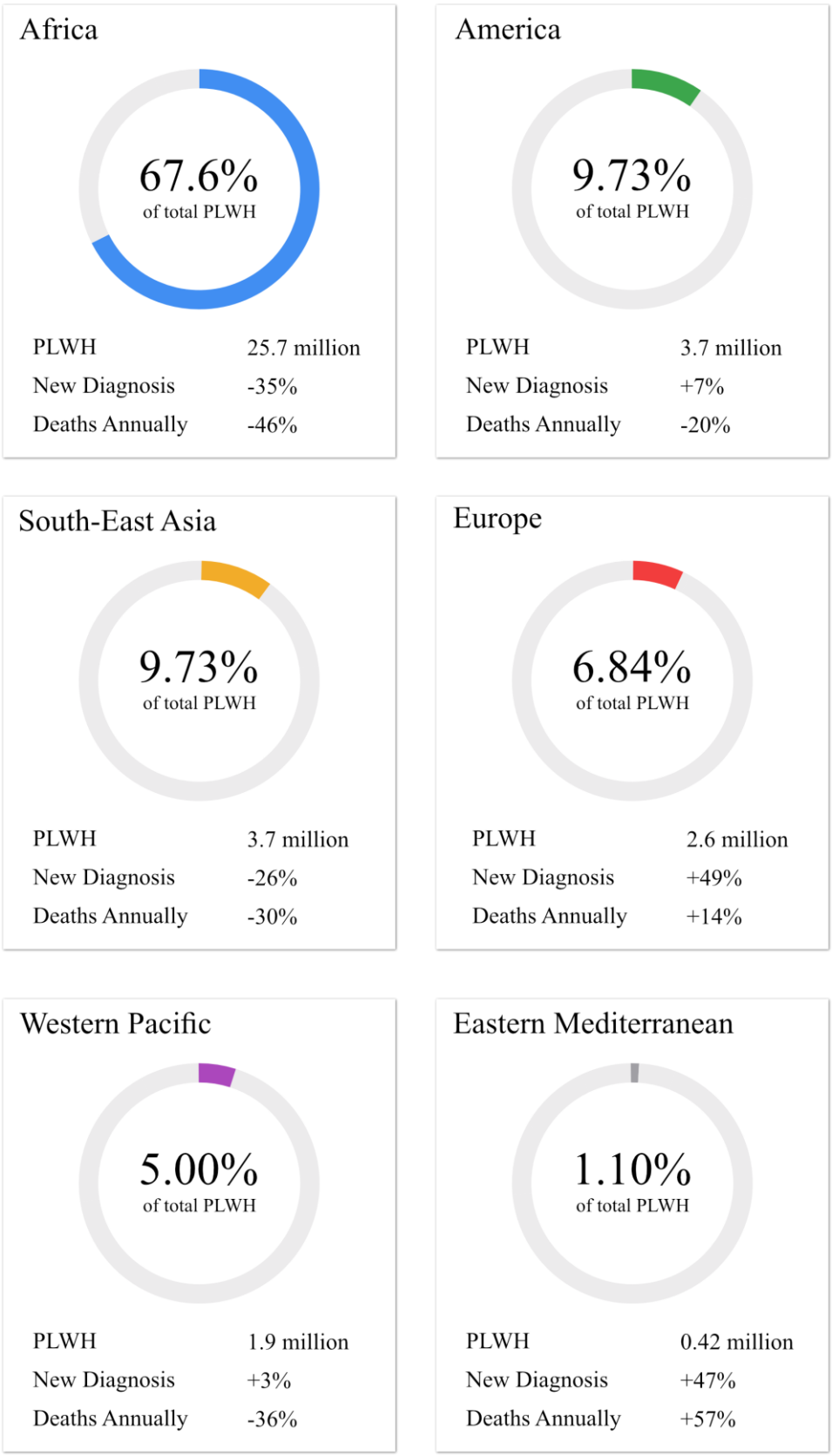

Figure 1.2 Regional breakdown of PLWH based on UNAIDS and WHO estimates (4). New diagnosis and annual deaths are relative to 2010 estimates.

HIV is transmitted through the exchange of specific bodily fluids such as blood, semen, vaginal secretions and breast milk. Additionally, HIV can be transmitted from mother to child during pregnancy. Risk factors for the acquisition of HIV include unprotected anal and vaginal sex, sexually transmitted infections, sharing injecting equipment such as needles and unsafe medical procedures. Key populations who are at high risk of acquiring HIV are men who have sex with men, people who inject drugs (PWID), people in prison, sex workers and transgender people (5).

The survival rate of PLWH has steadily increased over the past few decades with the introduction of potent antiretroviral therapy (ART). This has led to a life expectancy similar to that of the general population (6). As shown in Figure 1.3, UNAIDS and the WHO estimated that globally the amount of PLWH aged ≥50 years had more than doubled from 2010 to 2019. Older adults living with HIV (OALWH) have previously been defined as HIV-positive adults aged ≥50 years, whereas in the general population older adults are often defined as those aged ≥65 years. OALWH have a lower age cut-off due to their poorer immunological recovery and increased mortality caused by HIV-unrelated factors when compared to PLWH aged ≤50 years (7). Furthermore, in comparison to non-HIV infected adults, it has been reported that PLWH had an increased biological age (8), further justifying the lower chronological age cut-off defining OALWH.

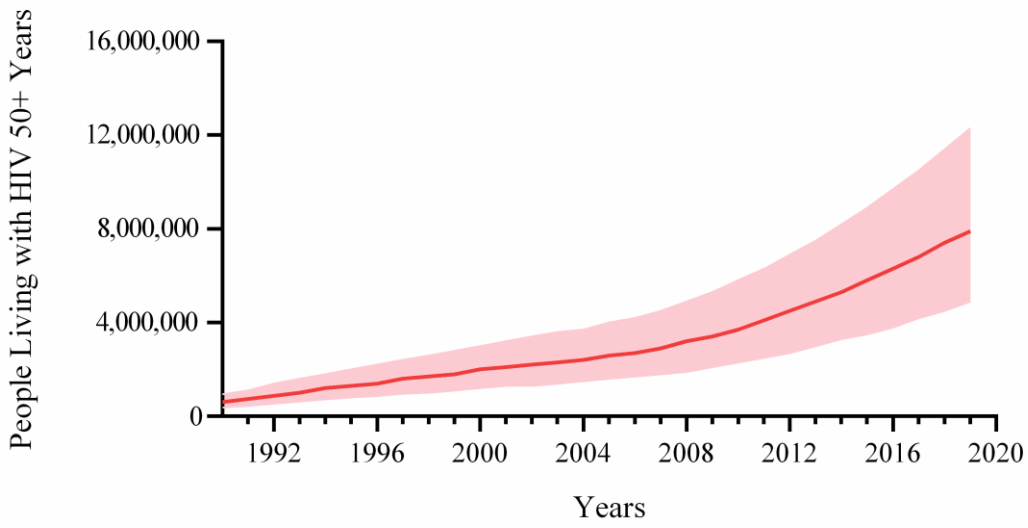

Figure 1.3 Global OALWH aged ≥50 years from 1990 to 2019, based on UNAIDS and WHO estimates (3). The red line represents the estimated mean with the shaded red area representing the upper and lower limits.

1.1.1 HIV Replication Cycle

HIV requires a host cell to replicate itself and specifically targets activated CD4 T lymphocytes as well as resting CD4 T cells, monocytes, macrophages and dendritic cells, all of which belong to the immune system (9, 10). CD4 T lymphocytes play a key role in the body's immune response and their depletion through HIV infection leaves the body incapacitated against opportunistic infections. The HIV-1 virion is spherical in shape with a lipid membrane encompassing cellular proteins and viral envelope protein complexes. The viral envelope comprises of external glycoprotein 120 (gp120) and transmembrane glycoprotein 41 (gp41) which are required for viral attachment and fusion, respectively. Within the envelope is a conical capsid containing two single strands of viral ribonucleic acid (RNA) and various enzymes and proteins necessary for the viral replication cycle. A schematic representation of the viral replication cycle is shown in Figure 1.4 which highlights each stage of HIV replication and the corresponding antiretroviral (ARV) drug classes targeting them.

First in the replication cycle is the attachment of the external gp120 on the HIV virion to CD4 receptors on the host cell. This binding leads to conformational changes that enable gp120 to interact with either the C-X-C chemokine receptor type 4 (CXCR4) or C-C chemokine receptor type 5 (CCR5) receptors on the host cell. These

interactions cause further conformational changes that enable the integration of the hydrophobic fusion peptide of the gp41 transmembrane protein into the host cell's membrane. As a result, virion fusion between the host cell and viral membranes occurs, followed by uncoating and the distribution of viral content into the cell. The newly released single-stranded viral RNA then undergoes reverse transcription producing double-stranded deoxyribonucleic acid (DNA). The double-stranded DNA is then actively transported across the nuclear pore and integration into the host genome is facilitated by the enzyme, integrase. Transcription of the proviral DNA subsequently takes place creating viral messenger RNA (mRNA) which is transferred into the cell cytoplasm from the nucleus. The viral mRNA is then translated into the encoded viral proteins followed by proteolytic cleavage via the protease enzyme. The newly produced viral contents are then assembled into a membrane-coated spherical particle at the host cell's plasma membrane for viral release to occur. The new HIV virion matures into its infectious form once released, completing the HIV replication cycle (9, 11).

There are three major stages in the progression of untreated HIV: acute HIV, asymptomatic HIV and AIDS. Figure 1.5 shows a schematic representation of the associated changes in CD4 lymphocyte count and HIV RNA copies throughout these stages. The acute stage takes place over a period of weeks after the primary infection and is characterised by symptoms such as fever and persistent generalised lymphadenopathy as well as a rapid decline in CD4 T lymphocytes and incline in HIV RNA copies until a peak is reached. The asymptomatic stage occurs for several years after the acute stage and as the name suggests PLWH in this stage may have no HIV-related symptoms. HIV replication continues at low levels whilst CD4 T lymphocytes continue to decline. The final stage, AIDS, is characterised by a CD4 T lymphocyte count of less than 200 cells per mm3 as well as the onset of opportunistic infections and a dramatic increase in HIV RNA copies. Due to the irreparable damage to the immune system caused by chronic HIV infection, those with AIDS will die within a span of 3 to 4 years unless treated (9, 12-14).

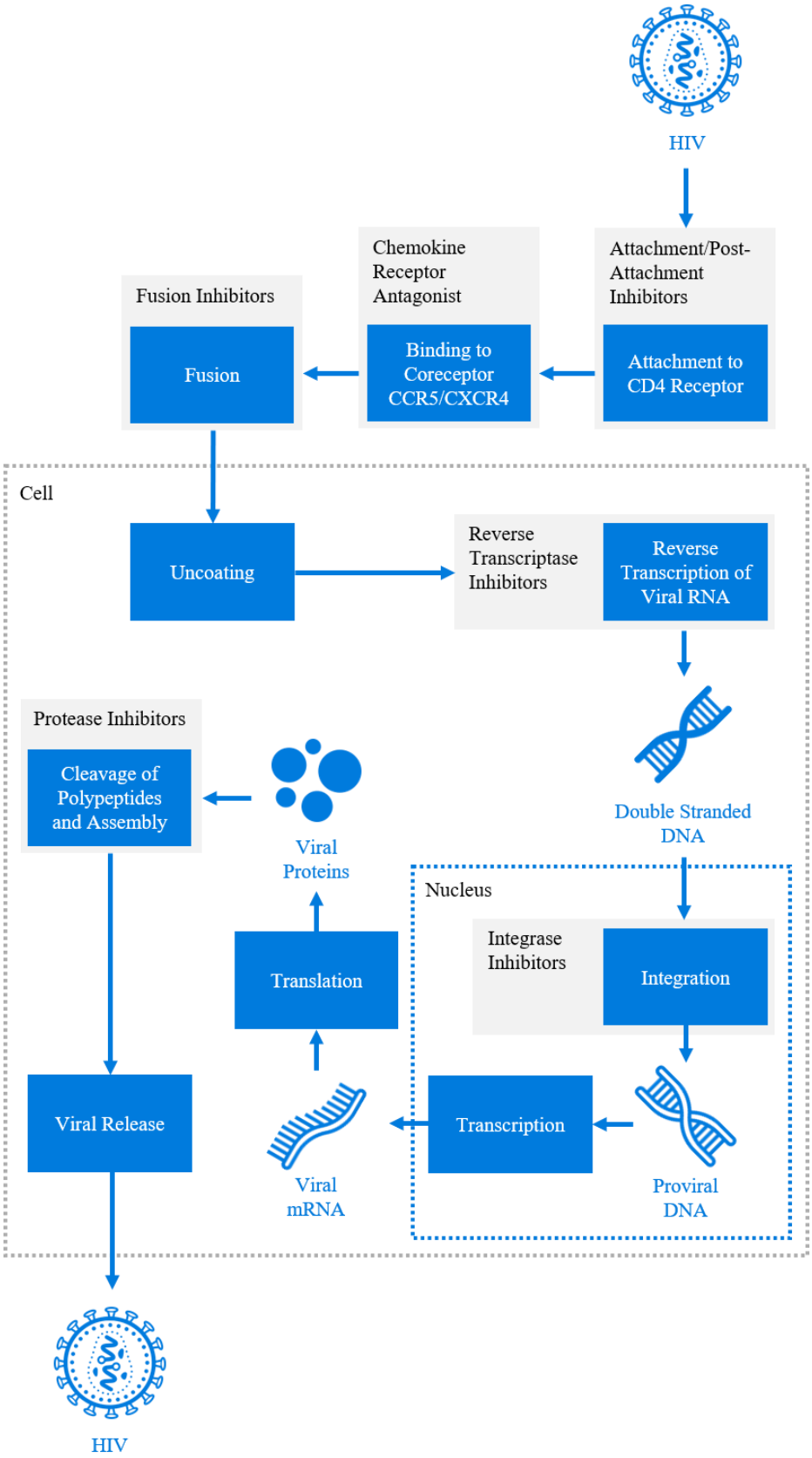

Figure 1.4 HIV replication cycle in a CD4 host cell. ARV drug classes and their corresponding sites of action are highlighted in grey boxes (9, 11, 15).

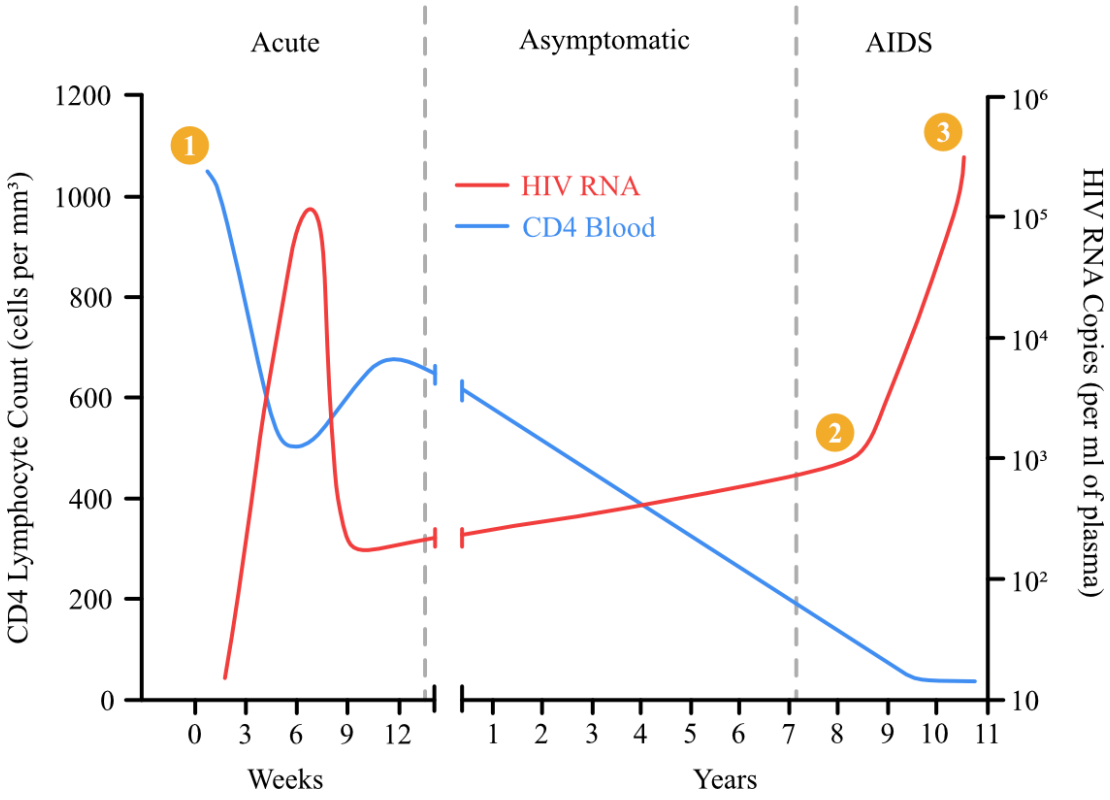

Figure 1.5 Changes in CD4 lymphocyte count and HIV RNA copies throughout the three stages of untreated HIV: acute HIV, asymptomatic HIV and AIDS. The red line represents HIV RNA copies per ml of plasma and the blue line represents CD4 lymphocyte count in cells per mm^3. Three notable events are highlighted in yellow on the graph. Numbers 1, 2 and 3 represent the primary infection, opportunistic infections and death, respectively (9, 16).

1.1.2 Antiretroviral Therapy

The WHO and UNAIDS estimated that globally in 2019 81% of PLWH knew their status, 67% were receiving ART and among those 59% were virally supressed. The WHO currently recommends that countries adopt a standard HIV testing strategy for diagnosis consisting of three HIV tests (17). HIV tests can be split into two categories: serological testing and virological testing. Serological testing involves the detection of antibodies produced as part of the immune response to HIV. These tests include ELISA, rapid tests and western blot tests. Virological testing involves the detection of viral nucleic acids or viral products via polymerase chain reaction (PCR) assays (18). It is critical to begin ART as soon as possible after a positive HIV diagnosis has been made to achieve efficient viral suppression (19). Additionally,

ARV drugs can be used in the preventative methods known as pre-exposure prophylaxis (PrEP) and post-exposure prophylaxis (PEP). Both PrEP and PEP are used by HIV-negative people who are either at high risk of HIV exposure or have had a single high risk HIV exposure, respectively (20).

There are currently nine classes of ARV drugs: attachment inhibitors, post-attachment inhibitors, chemokine receptor antagonists, fusion inhibitors, nucleoside reverse transcriptase inhibitors (NRTIs), non-nucleoside reverse transcriptase inhibitors (NNRTIs), integrase inhibitors, PIs and pharmacokinetic enhancers (15). ARV drugs that are currently licenced for the treatment of HIV can be found in Table 1.1. Each class of ARV drug, excluding pharmacokinetic enhancers, target a specific process during the HIV life cycle to prevent viral replication, as shown in Figure 1.4. There are four ARV drug classes that target the processes prior to HIV infiltration of the host cell: attachment inhibitors, post-attachment inhibitors, chemokine receptor antagonists and fusion inhibitors. Attachment inhibitors prevent HIV from entering host cells by binding to the gp120 protein located on the outer surface of the HIV envelope, thus preventing interaction with host cell surface receptors. The prodrug fostemsavir (FTR) is currently the only U.S. Food and Drug Administration (FDA) approved attachment inhibitor and is suitable for heavily treatment experienced PLWH with multidrug resistant HIV-1 (21). Post-attachment inhibitors bind to extracellular domains on the host cell preventing the conformational changes required for the interaction between gp120 and CXCR4 and CCR5 receptors, stopping HIV entry. Ibalizumab-uiyk is the first FDA approved monoclonal antibody and post-attachment inhibitor for the treatment of HIV-1 in heavily treatment experienced patients (22). Chemokine receptor antagonists prevent the binding of gp120 to chemokine receptors on the host cell. Maraviroc is currently the only FDA approved chemokine receptor antagonist and prevents the binding of gp120 to CCR5 (23). Lastly, the synthetic peptide enfuvirtide is currently the only FDA approved fusion inhibitor which blocks the conformational changes required for cell fusion by binding to viral gp41, thereby preventing viral entry (24).

There are four classes of ARV drugs that target the life cycle process after HIV infiltration of the host cell: NRTIs, NNRTIs, integrase inhibitors and PIs. These ARV classes are well established in comparison to attachment inhibitors, post-attachment inhibitors and fusion inhibitors, and form the cornerstone of first-line and second-line

ART regimens. Both NRTIs and NNRTIs prevent the production of double-stranded DNA from viral RNA by inhibiting the reverse transcription of viral RNA. Whereas NRTIs undergo intracellular phosphorylation to form their active diphosphate and triphosphate metabolites to competitively inhibit reverse transcription, NNRTIs produce their inhibitory action non-competitively. Integrase inhibitors stop the integration of viral DNA into the host chromosome via inhibition of the integrase enzyme used to catalyse covalent bond formation between viral and host DNA. Finally, PIs impede mature virion formation in the latter stages of the HIV life cycle through HIV protease binding, stopping the required cleavage and assembly of polypeptides (9, 25). In addition to the abovementioned ARV classes, there are two currently approved pharmacokinetic enhancers: cobicistat (COBI) and the PI, RTV. Both ARVs inhibit the cytochrome P450 (CYP3A4) enzyme thereby reducing the metabolism of the coadministered ARVs to attain the effective therapeutic plasma concentrations. COBI and RTV are given in combination with almost all PIs as well as the integrase inhibitor elvitegravir (26).

Table 1.1 ARV drugs currently approved for the treatment of HIV (15).

Drug Name	Brand Name	FDA Approval Date
Nucleoside Reverse Transcriptase Inhibitors (NRTIs)		
Abacavir*	Ziagen	17th December 1998
Emtricitabine (FTC)*	Emtriva	2nd July 2003
Lamivudine (3TC)*	Epivir	17th November 1995
Tenofovir Disoproxil Fumarate (TDF)*	Viread	26th October 2001
Tenofovir Alafenamide Fumarate (TAF)**	Genvoya	5th November 2015
	Odefsey	1st March 2016
	Descovy	4th April 2016
	Biktarvy	7th February 2018
	Symtuza	17th July 2018
Zidovudine (AZT, ZDV)	Retrovir	19th March 1987
Non-Nucleoside Reverse Transcriptase Inhibitors (NNRTIs)		
Doravirine (DOR)*	Pifeltro	30th August 2018
Efavirenz (EFV)*	Sustiva	17th September 1998
Etravirine (ETR)	Intelence	18th January 2008
Nevirapine (NVP)	Viramune	21st June 1996
Rilpivirine (RPV)*	Edurant	20th May 2011
Protease Inhibitors (PIs)		
Atazanavir (ATV)*	Reyataz	20th June 2003

Darunavir (DRV)*	Prezista	23rd June 2006
Fosamprenavir (FPV)	Lexiva	20th October 2003
Ritonavir (RTV)***	Norvir	1st March 1996
Saquinavir (SQV)	Invirase	6th December 1995
Tipranavir (TPV)	Aptivus	22nd June 2005
Fusion Inhibitors		
Enfuvirtide (T-20)	Fuzeon	13th March 2003
Chemokine Receptor Antagonists		
Maraviroc (MVC)	Selzentry	6th August 2007
Integrase Inhibitors		
Cabotegravir (CAB)*	Vocabria	22nd January 2021
Dolutegravir (DTG)*	Tivicay	13th August 2013
Raltegravir (RAL)	Isentress	12th October 2007
Attachment Inhibitors		
Fostemsavir (FTR)	Rukobia	2nd July 2020
Post-Attachment Inhibitors		
Ibalizumab-uiyk (IBA)	Trogarzo	6th March 2018
Pharmacokinetic Enhancers		
Cobicistat (COBI)*	Tybost	24th September 2014
Adapted from HIVinfo.NIH.gov. * - also available as part of combination HIV medicines under different brand names with different FDA approval dates, ** - only available as part of combination HIV medicines (as listed), *** - RTV is a PI however it is generally used as a pharmacokinetic enhancer in combination HIV medicines.		

Since the introduction of HIV treatment in 1987 with the NRTI zidovudine, ART has evolved from a single monotherapy to a multitude of combination therapies, allowing for treatment personalisation. Unlike the original monotherapies, combination therapies offer rapid HIV RNA reduction and improved immune functionality by targeting multiple processes in the HIV life cycle, resulting in reduced rates of HIV morbidity and mortality as well as reducing the risk of transmission (25). For adults, the WHO currently recommends the integrase inhibitor DTG alongside two NRTIs, known as an NRTI backbone, as a first-line ART regimen. Alternatively, the NNRTI efavirenz is recommended in combination with an NRTI backbone. The WHO also recommends second-line ART regimens involving DTG alongside an optimised NRTI backbone or, for PLWH failing on DTG-based regimens, PIs boosted with a pharmacokinetic enhancer in combination with an optimised NRTI backbone (27). All currently recommended first-line and second-line ART regimens are shown in Table 1.2. Current ART requires lifelong treatment for the maintenance of viral suppression. Since 2006, several single tablet once daily (QD) combination ART regimens have been produced, helping to lower pill burden and combat drug adherence issues. Drug adherence is vital to prevent viral rebound and the introduction of transmittable ARV-resistant HIV mutations (25). Alongside the development of QD single tablet regimens consisting of highly potent ARVs with minimal toxicity, long-acting ARVs have been of increasing interest with the potential to eradicate adherence issues and improve treatment accessibility. The first extended-release long acting injectable for the treatment of HIV was approved by the FDA in January 2021. Cabenuva, which consists of an injectable cabotegravir (CAB) and rilpivirine (RPV) formulation, is suitable for QMT administration with recent studies demonstrating effective viral load reduction when administered every two months (28, 29).

Table 1.2 WHO guidelines on first-Line and second-line ART regimens (27).

First-Line Regimens for Adults and Adolescents	Preferred Regimen: TDF + 3TC (or FTC) + DTG	Alternative Regimen: TDF + 3TC + EFV 400 mg	Special Circumstances: TDF + 3TC (or FTC) + EFV 600 mg AZT + 3TC + EFV 600 mg TDF + 3TC (or FTC) + PI/r TDF + 3TC (or FTC) + RAL TAF + 3TC (or FTC) + DTG Abacavir + 3TC + DTG
Second-Line Regimens for Adults and Adolescents	Failing First-Line Regimen: TDF + 3TC (or FTC) + DTG TDF + 3TC (or FTC) + EFV (or NVP) AZT + 3TC + EFV (or NVP)	Preferred Regimen: AZT + 3TC + ATV/r (or LPV/r) AZT + 3TC + DTG TDF + 3TC (or FTC) + DTG	Alternative Regimen: AZT + 3TC + DRV/r AZT + 3TC + ATV/r (or LPV/r or DRV/r) TDF + 3TC (or FTC) + ATV/r (or LPV/r or DRV/r)
Adapted from the WHO guidelines. 3TC – lamivudine, ATV/r - atazanavir/ritonavir, AZT- zidovudine, DRV/r - darunavir/ritonavir, DTG – dolutegravir, EFV – efavirenz, FTC – emtricitabine, LPV/r - lopinavir/ritonavir, NVP – nevirapine, PI/r - protease inhibitor boosted with ritonavir, RAL – raltegravir, TAF - tenofovir alafenamide, TDF - tenofovir disoproxil fumarate.			

1.2 Coinfections

PLWH have an increased risk of acquiring additional infections, known as coinfections, due to their weakened immune system as well as through shared routes of transmission (30). Coinfections can lead to increased morbidity and mortality in PLWH due to debilitated immune responses accelerating disease progression. Rates of coinfections are country and sub-population dependent with a large proportion of coinfections affecting PLWH in Africa (30). For example, in 2018 tuberculosis (TB) produced one in three AIDS-related deaths of which 84% occurred in Africa (31). Furthermore, the treatments used for coinfections can incur potential drug-drug interactions (DDIs) with ART regimens, with DDIs for both hepatitis C (HCV) and leprosy being assessed in Chapters 4 and 6.

1.2.1 Hepatitis C

HCV is a bloodborne virus that was first discovered in 1989 and was initially referred to as non-A and non-B viral hepatitis (32). Hepatitis A (HAV) and hepatitis B (HBV) were discovered in the 1960s and 1970s with a vaccine for HBV being approved for human use in 1986. Clinical descriptions of hepatitis date back to 3000 BC and was thought to spread throughout the middle ages with epidemics taking place during the 18th century (33). There were an estimated 2.3 million PLWH with past or present serological evidence of HCV coinfection in 2017, accounting for approximately 6.2% of total PLWH. The highest burden of coinfection was amongst PWID with 84% of total co

infection cases, of which Central Asia and Eastern Europe had the greatest prevalence (34). These demographics are indicative of the similar routes of transmission between HIV and HCV, such as through the sharing of injecting equipment and unsafe medical procedures as well as unscreened blood transfusions (35). Furthermore, there are seven HCV genotypes which vary in their geographical prevalence. Genotypes 1, 2 and 3 are prevalent in America, Europe and Japan with genotype 1 accounting for more than 50% of cases in these regions. South and Southeast Asia has the highest burden of genotypes 3 and 6, with genotypes 4 and 5 being predominant in Africa. To date genotype 7 has a minimal clinical impact (36).

HCV can be categorised into acute and chronic HCV. In most cases acute HCV is asymptomatic and can clear without treatment in up to 45% of all cases. If left untreated, acute HCV develops into chronic HCV with fibrosis, cirrhosis and liver failure ensuing, including hepatocellular carcinoma in some cirrhosis patients. The stages of chronic HCV are accelerated in PLWH with multiple studies demonstrating advanced progression of hepatic fibrosis and cirrhosis in PLWH co-infected with HCV when compared to HIV-negative patients (37). In comparison, the effect of HCV on HIV progression is uncertain with contradictions amongst current studies. The SWISS cohort study identified an association between HCV infection and AIDS-related deaths. On the other hand, the EuroSIDA cohort study found no difference in HIV viral load reduction or CD4 count elevation following ART initiation in PLWH co-infected with HCV vs. PLWH (38, 39). Moreover, a recent cross-sectional study of 97 patients found that PLWH co-infected with HCV had a larger HIV-1 reservoir when compared to PLWH (40).

Our understanding of the HCV replication cycle remains incomplete however considerable advancements in HCV treatment over the past 20 years have enabled up to 95% of HCV infections to be cured (35). Current treatment strategies target multiple stages in the replication cycle including the HCV lipoviroparticle, viral entry, receptor interaction, translation, viral RNA replication and viral assembly (36). The latest guidelines from 2016 for the treatment of HCV in adults moved away from the previously recommended interferon-based regimens towards the more effective direct acting antivirals (DAAs). Current regimens are based on a 12 to 24-week course of pangenotypic DAAs, such as daclatasvir/sofosbuvir and ledipasvir/sofosbuvir, depending on whether the patient has liver cirrhosis. A multitude of regimens are available, with further drugs for the treatment of HCV receiving approval after the publication of the 2016 guidelines. Although recommendations for treatment in PLWH co-infected with HCV are the same as those infected with HCV alone, special consideration must be taken in their clinical management, specifically regarding potential DDIs between ART and DAAs (37, 38, 41, 42).

1.2.2 Leprosy

Mycobacterium leprae (M. leprae) is the bacterium responsible for the infectious disease leprosy, also known as Hansen's disease, and was first discovered in 1873 by

Dr. Gerhard Armauer Hansen. Historically, written clinical descriptions as early as 1400 BC from India are widely regarded as leprosy, with the spread of the disease throughout Europe thought to take place between 1000 – 1400 AD. Since the introduction of multi-drug therapy (MDT) by the WHO in 1981, the prevalence of leprosy has decreased from an estimated 10 – 12 million cases to a reported 184,212 registered cases worldwide in 2018. India, Brazil and Indonesia have the highest prevalence of leprosy with 50%, 15% and 10% of worldwide cases, respectively (43-45). There are currently no epidemiological data on PLWH co-infected with leprosy, however there is a geographical overlap in high prevalence countries of both leprosy and HIV. Studies specifically investigating PLWH co-infected with leprosy are limited, however clinical cohort studies in Brazil and India have identified a higher prevalence of leprosy in PLWH. Additionally, a study comparing two cohorts of leprosy patients with and without HIV in the Amazon region of Brazil concluded that HIV and leprosy have independent infectious courses (46). Despite this, there remains a lack of understanding of the interplay between leprosy and HIV (47, 48).

Leprosy transmission is thought to occur through droplets from the nose and mouth between close, repeated contact with an untreated patient (49). A study in northwest Bangladesh found that the risk of developing leprosy through household contact with an untreated patient is 10-fold greater in comparison to the general population (50, 51). Leprosy has a prolonged incubation period due to the slow multiplication of *M. leprae* and can take up to 20 years to produce symptoms. The skin, nerves and nasal mucosa are primarily affected by leprosy with symptoms including skin growths and discolouration, muscle weakness and nosebleeds. Untreated leprosy can cause muscle paralysis, blindness and chronic foot ulcers (45, 49). Current WHO guidelines recommend a three-drug therapy, referred to as MDT, consisting of rifampicin (RIF), dapsone and clofazimine for 6 and 12 months for paucibacillary (PB) and multibacillary leprosy, respectively. Additionally, single dose RIF (SDR) is recommended as chemoprophylaxis in adults and children with close contact to a diagnosed leprosy patient (52). The COLEP clinical study found that SDR in close contacts reduced the risk of leprosy incidence by 57% in the first two years post contact (53). The clinical management of MDT in PLWH must be carefully evaluated due to the risk of DDIs between ARVs and RIF, dapsone and clofazimine. Whilst the majority of clinically significant DDIs revolve around the coadministration

of RIF, dapsone and clofazimine present potential clinically significant and potential weak interactions with several ARVs, particularly surrounding adverse effects (54, 55).

Although the implementation of MDT has substantially decreased the number of cases of leprosy since the 1980's, the prevalence of leprosy has plateaued over the past 10 years (43). The lack of progress towards the elimination of leprosy has challenged existing procedures used for prevention and treatment, with research efforts currently targeting early detection, contact screening, point-of-care diagnosis tests and SDR chemoprophylaxis (56, 57). Current research has explored the use of Bacillus Calmette-Guérin (BCG) vaccination alongside SDR for prevention. The MALTALEP trial identified a 42% reduction in PB leprosy amongst patients who received SDR after BCG vaccination vs. patients who received BCG vaccination alone (51). An additional clinical trial has planned to evaluate the effectiveness of SDR administered prior to BCG vaccination (58). A further aspect yet to be considered for SDR chemoprophylaxis as well as MDT is the implementation of a higher dose of RIF. Current guidelines recommend a 600mg RIF dose however a previous study demonstrated the ability of 1200mg and 1500mg SDR to reduce the rate at which *M. leprae* were rendered non-infective more effectively than 600mg and 900mg SDR. Cost associations and toxicity studies at the time of study led to the preference of 600mg SDR however recent studies exploring high dose RIF for the treatment of TB have found dosing up to 35mg/kg (2450mg for the average 70kg adult) to be safe and well tolerated (59-61).

1.3 Pharmacokinetics

The dose-exposure-response relationship of a drug is based upon two fundamental principles: pharmacokinetics and pharmacodynamics. Pharmacokinetics can be defined as the concentration-time profile of a drug in plasma, tissue or other bodily fluid that is regulated by absorption, distribution, metabolism and excretion (ADME) mechanisms in the body. Pharmacodynamics can be defined as the physiological effect of a drug on the body in relation to its plasma, tissue or other bodily fluid concentration (62). The ADME of a drug is influenced by its molecular properties as well as the route of administration. The most common route of drug administration is oral dosing with many ARVs being administered this way.

Alternative routes of administration include intravenous injection (IV), intramuscular injection (IM), subcutaneous injection (SC), transdermal and topical, all of which are used depending on the desired pharmacokinetic and pharmacodynamic outcome (63). For example, as previously mentioned the recently approved Cabenuva is an IM injectable containing extended-release CAB and RPV formulations to provide effective plasma concentrations for viral suppression over a 1 month period, lowering pill burden and increasing drug adherence for PLWH (28).

Absorption takes place following oral administration when the drug is subsequently solubilised and transported across the enterocytes of the gastrointestinal (GI) tract into the bloodstream. Several factors influence the absorption of a drug, some of which are drug and formulation dependent such as lipophilicity, particle size and polarity, and others which are physiologically dependent such as the presence of food, intestinal motility, enzyme abundance and transporter abundance. Drug absorbed from the GI tract travels via the portal vein to the liver where it is actively and passively transported across hepatocyte membranes, undergoing metabolism and biliary excretion prior to reaching the systemic circulation. This process is known as first-pass metabolism. In contrast, IV administration introduces the drug directly into the systemic circulation, bypassing the absorption and first-pass metabolism processes. Furthermore, absorption of drug from IM and SC administration is dependent on the location of administration with absorption being influenced by both drug, formulation and physiological factors such as lipophilicity and tissue vascularity (62, 63).

Drug is distributed throughout tissues and organs via the systemic circulation and again, is dependent on both drug and physiological characteristics. The flow of blood to the various tissues and organs is a major contributor to drug distribution, along with binding of drug to plasma proteins and the blood-to-plasma ratio (R). Of particular importance is the reversible binding of drug to plasma proteins as only the fraction of unbound drug in plasma (f_u) can exert its pharmacological effect as well as undergo metabolism and excretion processes (62). The f_u is dependent on a drugs physicochemical properties along with the concentration of proteins such as albumin and α-acidic glycoprotein in plasma. As previously mentioned, the liver plays a pivotal role in the metabolism and excretion of a drug, with metabolism also occurring in the GI tract. Drug metabolism can be divided into phase I and phase II metabolism whereby a drug is transformed into a more hydrophilic entity to facilitate biliary and

renal excretion. The metabolic pathway of a drug can involve a single enzyme or multiple phase I and phase II enzymes. Phase I metabolism consists of oxidative reactions carried out predominantly by the cytochrome P-450 (CYP) family of enzymes (62, 63). Phase II metabolism consists of conjugation reactions with the UDP-glucuronosyltransferases (UGT) family of enzymes being key to these processes (64). As well as facilitating drug excretion, drug metabolism can also generate the pharmacologically active metabolite from the parent drug. For example, the ARV drug tenofovir (TFV) is an NRTI that is phosphorylated intracellularly to form the active metabolite, TFV diphosphate (TFV-DP). Furthermore, due to TFV's poor membrane permeability and bioavailability, it is administered orally in the prodrug formulations TFV alafenamide (TAF) and TFV disoproxil fumarate (TDF) (65, 66). The GI tract, liver and kidneys are the predominant pathways in drug excretion where drug is removed from the body in the faeces, bile (and ultimately faeces) and urine. The kidneys are instrumental in the excretion of a drug and its metabolites and can occur through glomerular filtration from the bloodstream into the proximal tubule as well as via the interplay between tubular reabsorption and secretion from the bloodstream (63). Together, the metabolism and excretion of a drug is referred to as drug elimination (67).

There are several quantifiable parameters used to describe drug pharmacokinetics. An example of a plasma concentration-time profile after the oral administration of a drug is shown in Figure 1.6, with the processes of absorption and elimination highlighted alongside commonly used pharmacokinetic parameters. These include the area under the curve (AUC), maximum concentration (C_{max}), minimum concentration (C_{min}) and time of maximum concentration (T_{max}). In addition, the bioavailability, clearance and volume of distribution (V_{ss}) of a drug are commonly referred to pharmacokinetic parameters. The percentage of administered drug reaching the systemic circulation is known as the bioavailability of a drug and can be sub-categorised into the fraction of drug absorbed across the GI tract (F_a), fraction of drug escaping metabolism in the GI tract (F_g) and the fraction of drug escaping first-pass metabolism in the liver (F_h). Clearance defines the volume of blood cleared of drug over time with total clearance comprising most commonly as the sum of hepatic, biliary and renal clearance (63). Clearance of a drug is often referred to as apparent oral clearance (CL/F) or systemic clearance (CL_{sys}) where CL/F describes the

clearance of an orally administered drug and therefore considers the drugs bioavailability, whereas CL_{sys} does not and is associated with drugs administered through alternative routes such as IV (68). The V_{ss} is a measurement of the distribution of drug in tissue and is calculated considering f_u of drug in plasma and tissue as well as the volume of plasma and tissue, rather than being a physically quantifiable volume (63).

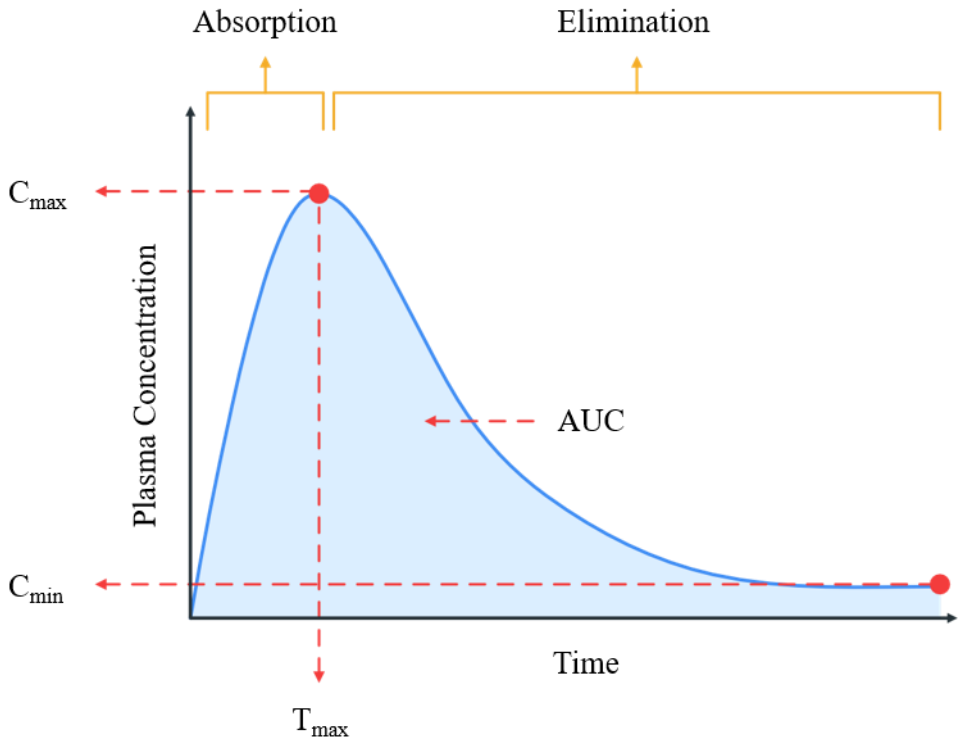

Figure 1.6 Example of a concentration-time profile after oral administration of a drug. Time is plotted on the x-axis and plasma concentration is plotted on the y-axis. Key pharmacokinetic parameters area under the curve (AUC), maximum concentration (C_{max}), minimum concentration (C_{min}) and time of maximum concentration (T_{max}) are highlighted with red dashed lines. The absorption and elimination phases are highlighted in yellow (62).

1.3.1 Transporters

Transporters are fundamental to ADME processes with our understanding of their structure, function and clinical significance vastly improving over the past 20 years thanks to a multitude of research initiatives (69). Alongside passive diffusion,

transporters facilitate the uptake and efflux of drugs across cell membranes. Although transporters are located throughout the body with varying expression profiles, those located in the liver are of significant clinical importance and will be the primary focus in this thesis. Figure 1.7 details the transporters located on the basolateral and apical membranes of human hepatocytes in the liver. Liver transporters are responsible for the directional transport of drug from the portal vein to hepatocytes and either into the bile canaliculi or back into the portal vein. Hepatic uptake transporters therefore determine the extent of liver metabolism and biliary excretion of drugs primarily transported through active uptake mechanisms, highlighting the extent of their pharmacokinetic and clinical importance. Transporters can be categorised into two major groups: the solute carrier (SLC) transporter family and the adenosine triphosphate (ATP)-binding cassette (ABC) transporter family (70). SLC transporters are primarily involved in the uptake into cells whereas ABC transporters are primarily involved in the efflux out of cells. ABC transporters utilise the hydrolysis of ATP as a source of energy for the primary active transport of drugs against their concentration gradient. In contrast, SLC transporters generally behave as either a coupled symporter or antiporter which leverage the energy produced from the electrochemical gradient of ions for the secondary active transport of drugs either in the same direction or opposite direction of the electrochemical gradient, respectively. Additionally, SLC transporters can function as a uniporter, transporting drugs down the electrochemical gradient through passive facilitated diffusion (71, 72). Whilst we still lack a comprehensive understanding of the transport processes employed by SLC transporters, three alternating access mechanisms have been suggested: rocker switch, gated-pore and elevator. Through these mechanisms the transporters are thought to undergo conformational changes from outward facing to inward facing, with the substrate binding site therefore being exposed from either the outside or inside of the cell, respectively (71, 73, 74).

Of the transporters located in the liver, the SLC organic anion transporting polypeptides 1B1 (OATP1B1; SLCO1B1) and 1B3 (OATP1B3; SLCO1B3) have been identified in the disposition of numerous drugs, with statins being a popular example (72, 74, 75). Consequently, these transporters are victim to a multitude of clinically significant DDIs, especially with ARVs, and will be discussed in more detail in section 1.4 (72). Drug-transporter relationships are complex, with drugs tending to lack

transporter specificity and their affinity towards different transporters varying along with the expression profiles of the transporters themselves. For example, PIT is a substrate of both OATP1B1 and OATP1B3 with an *in vitro* study demonstrating that OATP1B1 accounts for 90% of the total hepatic clearance of PIT and OATP1B3 for the remaining 10% (76). A meta-analysis investigating the expression levels of OATP transporters found the expression of OATP1B1 was three times greater than OATP1B3 in human liver tissue (77). This suggests that although PIT is a substrate of both transporters, it seems to have a higher affinity for OATP1B1 over OATP1B3. Interestingly, the localisation of OATP1B1 and OATP1B3 expression throughout the liver is dissimilar, with OATP1B1 being expressed equally throughout the liver and OATP1B3 being expressed largely in hepatocytes surrounding the central vein (78, 79). Additionally, the variation found in transporter expression is large with the above-mentioned meta-analysis finding for OATP1B1 from human liver tissue a range of 0.8 – 44.3 fmol/µg protein across 86 samples from 5 studies (77). Transporter expression can also vary under certain disease states such as liver fibrosis and cirrhosis, potentially resulting in altered pharmacokinetic drug profiles (79, 80). Furthermore, transporters are subject to single nucleotide polymorphisms (SNPs) which can alter their functionality. Two SNPs have been found to affect the function of OATP1B1, c.388A>G and c.521T>C, which occur in the SLCO1B1*1B, SLCO1B1*5 and SLCO1B1*15 haplotypes. Studies *in vitro* have demonstrated a reduction in the activity of OATP1B1 for all three haplotypes, with SLCO1B1*1B also showing an increase in activity (81, 82). The frequency of these SNPs differ among populations with a genetic study revealing that the haplotypes SLCO1B1*5 and SLCO1B1*15 were more frequent in European people and Asian people while SLCO1B1*1B was more frequent in sub-Saharan African people (83, 84).

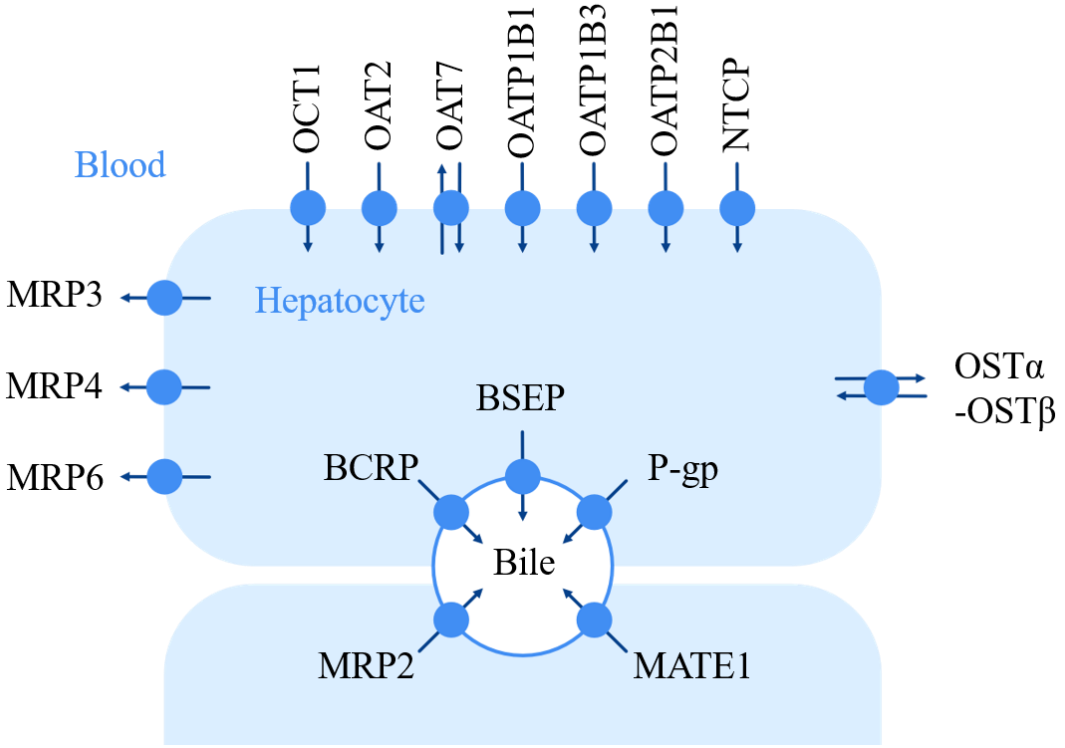

Figure 1.7 Human hepatocyte transporters located on the basolateral and apical membranes. Uptake transporters on the basolateral membrane include organic cation transporter 1 (OCT1; SLC22A1), organic anion transporter 2 (OAT2; SLC22A7), organic anion transporter 7 (OAT7; SLC22A9), OATP1B1 (SLCO1B1), OATP1B3 (SLCO1B3), organic anion transporter 2B1 (OATP2B1; SLCO2B1) and sodium/taurocholate co-transporting peptide (NTCP; SLC10A1). Efflux transporters located on the basolateral membrane include multidrug resistance-associated protein 3 (MRP3; ABCC3), multidrug resistance-associated protein 4 (MRP4; ABCC4) and multidrug resistance-associated protein 6 (MRP6; ABCC6). Additionally, located on the basolateral membrane is the dual uptake and efflux transporter organic solute transporter alpha-beta (OSTα-OSTβ; SLC51). Efflux transporters located on the apical membrane include the breast cancer resistance protein (BCRP; ABCG2), bile-salt export pump (BSEP; ABCB11), P-glycoprotein (P-gp; ABCB1), multidrug and toxin extrusion protein 1 (MATE1; SLC47A1) and multidrug resistance-associated protein 2 (MRP2; ABCC2) (70).

1.4 Drug-Drug Interactions

A DDI can be defined as the pharmacokinetic and pharmacodynamic outcome resulting from the coadministration of two or more drugs. That is, the outcome of each drug administered individually differs from when they are coadministered (85). DDIs are of significant clinical importance as they can result in ineffective pharmacologic drug concentrations as well as drug toxicity. In the example of HIV, a DDI could reduce the plasma concentration of an ARV below its minimum effective concentration (MEC) enabling viral replication to take place and potentially facilitate drug resistant mutations. Conversely, a DDI could increase the plasma concentration of an ARV above the minimum toxic concentration (MTC) or, in the case of pharmacokinetic enhancers such as RTV, the DDI could increase the plasma concentration of an ARV to achieve the pharmacologic effect threshold. DDIs are a continuously evolving clinical challenge due to the introduction of new drug regimens, high rates of comorbidities and polypharmacy, particularly in PLWH (26, 86, 87).

DDI mechanisms can be categorised into inhibition and induction and can involve both transporters and enzymes. The drugs involved in a DDI are referred to as the victim drug or perpetrator drug depending on whether they are affected by or cause the DDI, respectively. Inhibition can occur directly in an irreversible time-dependent or reversible manner, with reversible inhibition being further defined as competitive, non-competitive, uncompetitive or mixed (72, 88). The exact mechanisms of transporter inhibition remain unclear however the general principles of inhibition appear similar to enzymes, although the kinetic principles can differ. As transporters span across membranes and undergo conformational changes to become inward and outward facing, exposing the binding site on either side of the cell, they are subject to perpetrator binding from either side. So, depending on the location of the perpetrator, whether it be inside or outside of the cell, non-competitive inhibition could also exhibit uncompetitive kinetics. Furthermore, whereas in competitive enzyme inhibition increasing the substrate concentration can overcome the inhibitory effect by increasing the probability of substrate binding, this is not always true for competitive transporter inhibition as the perpetrator could competitively inhibit from the opposite side, producing non-competitive kinetics (89-91).

Irreversible inhibition occurs when the perpetrator drug has a high affinity for the binding site and will not likely dissociate once bound, whereas dissociation is highly likely in reversible inhibition. Competitive inhibition occurs when both the victim and perpetrator drug bind directly to the same site. When the inhibitor binds to a different site than the substrate this is known as non-competitive inhibition. Similarly to non-competitive inhibition, uncompetitive inhibition occurs when the inhibitor binds to a different site than the substrate however in contrast this site is only revealed after the substrate has bound. Mixed inhibition is comparable to non-competitive inhibition however the binding of either the victim or perpetrator to their respective sites reduces the binding affinity of the other. For all of the above scenarios, once the perpetrator drug has bound to the enzyme or transporter they become inactivated, preventing metabolism processes or transport across the cell membrane, respectively (92-94). A schematic representation of the four types of reversible enzyme inhibition can be found in Figure 1.8. Inhibition in enzyme-mediated DDIs can cause an increase in drug plasma concentrations as shown in Figure 1.10, while in transporter-mediated DDIs inhibition can cause either an increase or decrease in drug plasma concentrations depending on their localisation within a cell and whether they are an uptake or efflux transporter (95). Furthermore, as drugs can be substrates and/or inhibitors of both enzymes and transporters, the interplay between transporter-mediated and enzyme-mediated DDIs can produce varying effects on drug plasma concentrations. For example, the ARV PIs ATV/r, DRV/r and LPV/r have demonstrated clinically significant inhibition of OATP1B1, OATP1B3 and CYP3A4 and their coadministration is contraindicated in many scenarios. For example, GZR the HCV NS3/4A PI used in combination with elbasvir for the treatment of chronic HCV in adults is reported to be a substrate of CYP3A4, OATP1B1, OATP1B3 and P-gp. Clinical DDI studies found geometric mean ratios of GZR coadministered with ATV/r, DRV/r or LPV/r vs. GZR administered alone for AUC, C_{max} and C_{min} ranging from 5.27 – 21.7 (96).

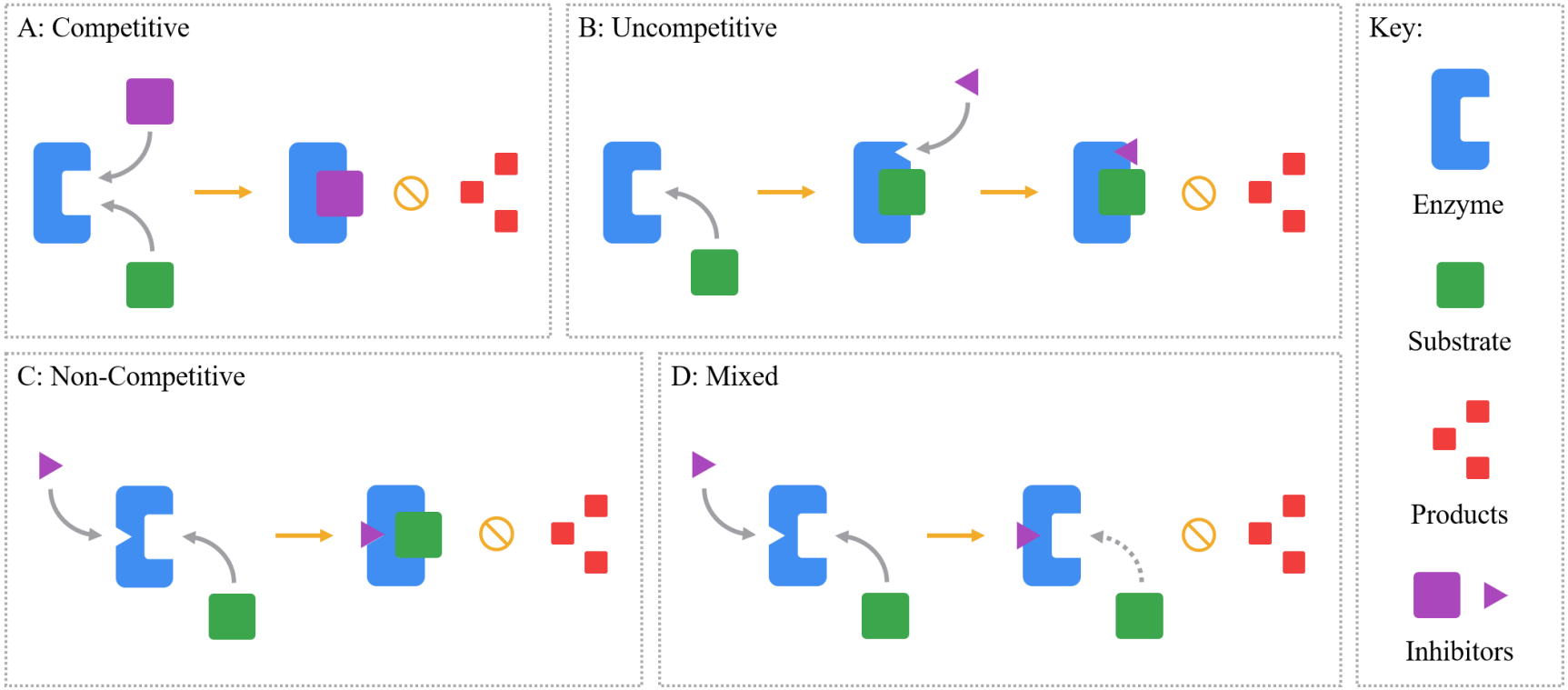

Figure 1.8 Schematic representation of the four types of reversible enzyme inhibition: competitive (A), uncompetitive (B), non-competitive (C) and mixed (D). The key details the enzyme, substrate, products and inhibitors in blue, green, red and purple, respectively. In competitive inhibition both the substrate and inhibitor bind to the same site on the enzyme. In uncompetitive inhibition the inhibitor binds to an alternate site on the enzyme that is only revealed once the substrate has bound. In non-competitive inhibition the substrate and inhibitor bind to two separate sites. In mixed inhibition the substrate and inhibitor bind to two separate sites with the binding of one reducing the binding affinity of the other (92-94, 97).

In contrast to inhibition, induction occurs indirectly. After entering the cytoplasm of a cell, the perpetrator drug binds to the ligand-binding domain on a nuclear receptor producing a ligand-receptor complex where it then translocates to the nucleus. After entering the nucleus, the complex forms homodimers or heterodimers with the retinoid X receptor via the recruitment of coactivators. These complexes are then able to modify the transcription of an enzyme or transporter by binding to specific regions of the corresponding target genes that are associated with their regulation. Thus, resulting in an increase in enzyme or transporter abundance. A schematic representation of this process can be found in Figure 1.9. Similarly to inhibition, the induction kinetics for enzymes and transporters differ with enzyme induction causing a decrease in drug plasma concentration, as shown in Figure 1.10, and transporter induction causing either an increase or decrease in drug plasma concentrations depending on their localisation within a cell and whether they are an uptake or efflux transporter. Several nuclear receptor transcription factors have been identified and their involvement in the induction of different enzymes and transporters varies. Several of these nuclear receptors such as pregnane X receptor (PXR), constitutive androstane receptor (CAR) and hepatocyte nuclear factor 4a (HNF4α) regulate CYP3A4 expression with PXR demonstrating a pivotal role. RIF is a potent inducer of several enzymes and transporters including CYP3A4, UGT1A1 and P-gp resulting in multiple clinically relevant DDIs (98, 99). For example, the integrase inhibitor dolutegravir (DTG) is reported to be majorly metabolised by UGT1A1 and CYP3A4 with minor metabolism by UGT1A3 and UGT1A9. RIF is coadministered with DTG for the treatment of TB in co-infected PLWH however due to their magnitude of DDI current guidelines recommend increasing the administration of DTG to 50mg twice daily (BID) from 50mg once daily (QD). The increased dose has proven effective in overcoming the RIF-mediated induction of UGT1A1 and CYP3A4, producing plasma concentrations similar to DTG 50mg QD that are within the effective concentration threshold to maintain viral suppression (100, 101).

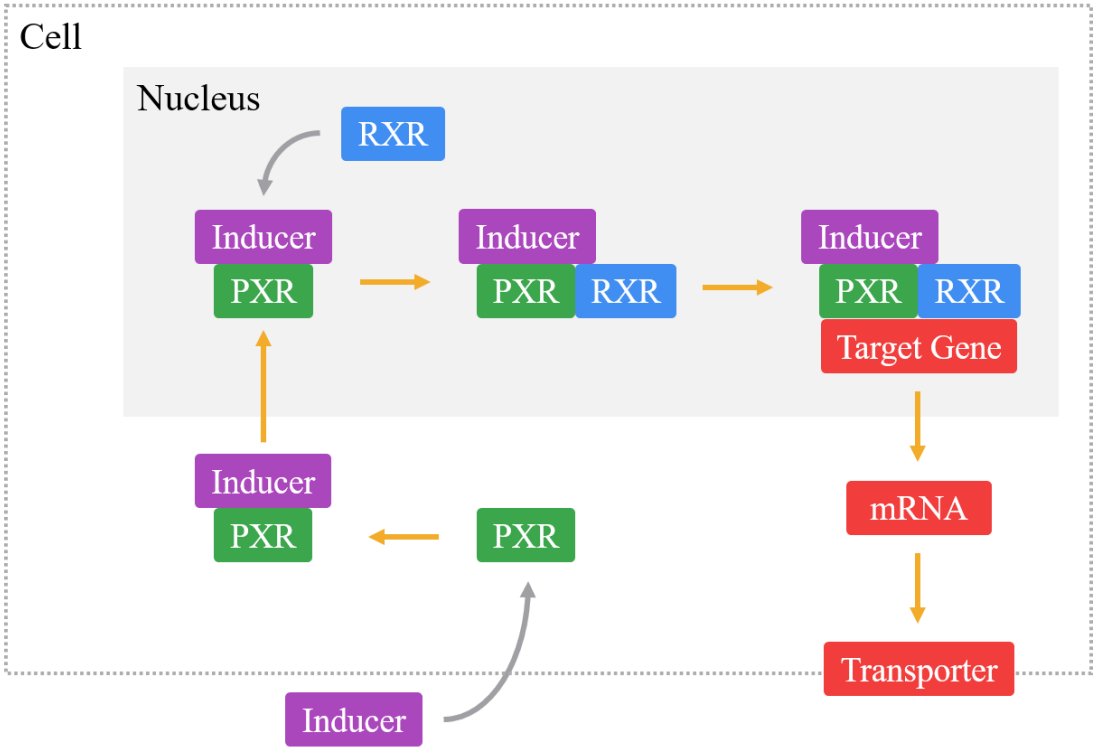

Figure 1.9 Schematic representation of the mechanism of transporter induction by the PXR nuclear receptor. The cell is represented by a grey dotted line with the nucleus represented by a grey shaded rectangle. The inducer drug, PXR and RXR are represented in purple, green and blue respectively, with the target gene, mRNA and transporter represented in red (98).

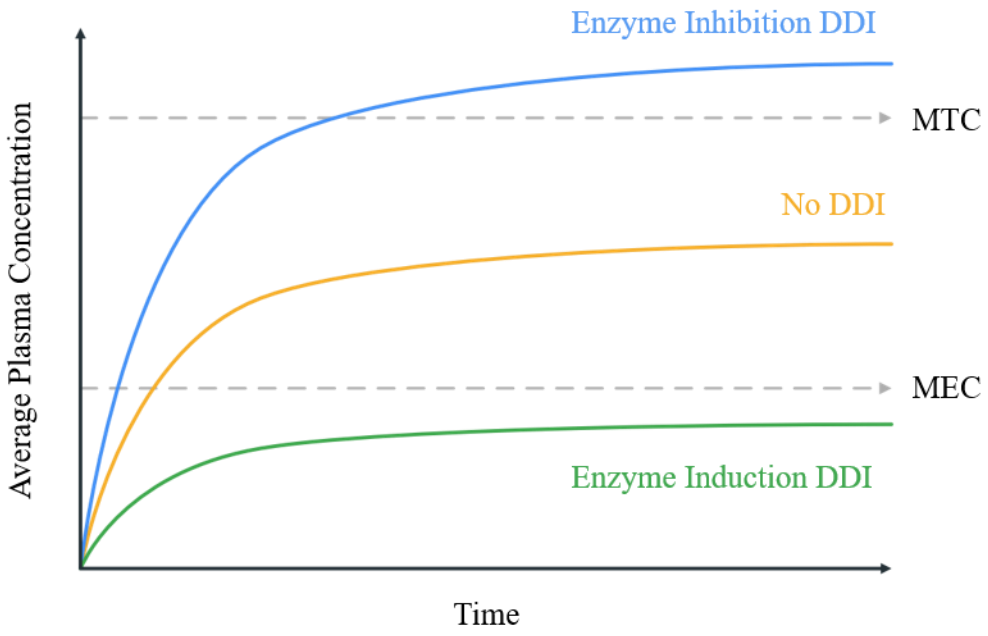

Figure 1.10 Example of the effect of enzyme-mediated DDIs on the concentration-time profile a victim drug. Time is plotted on the x-axis and the average plasma concentration is plotted on the y-axis. MTC refers to the minimum toxic concentration and MEC to the minimum effective concentration. The yellow line represents the victim drug administered alone. The blue and green lines represent the victim drug coadministered with an inhibitor perpetrator drug and an inducer perpetrator drug, respectively.

1.4.1 Older Adults Living with HIV

Despite a significant increase in OALWH over the past decade, this population remains vastly underrepresented in clinical trials leading to inadequate clinical practice guidelines and a disparity in pharmacokinetic knowledge compared to PLWH aged ≤50 years (102, 103). Clinical management of OALWH is inherently complex with comorbidities, geriatric syndromes and polypharmacy requiring simultaneous consideration. Comorbidity is defined as the co-existence of multiple chronic health conditions (104). Compared to HIV-negative matched controls, several studies have shown that OALWH have a higher burden of comorbidities and are thought to occur more frequently in this population due to a combination of factors including ART toxicity, chronic inflammation and immune dysregulation (105). Commonly occurring comorbidities include bone disease, cardiovascular disease, diabetes, kidney disease, and non-AIDS malignancies (103, 105, 106). Geriatric syndrome is the umbrella term

for clinical conditions resulting from the accumulation of multi-system impairments common in older adults. The early onset of geriatric syndromes in OALWH is thought to manifest from a combination of factors including chronic inflammation, multimorbidity and polypharmacy. A recent cross-sectional study of PLWH aged ≥50 years described frailty, difficulty with instrumental activities of daily living, cognitive impairment, depression and urinary incontinence as the most commonly occurring geriatric syndromes (107). Defined as the use of 5 or more medications (108), several studies have also demonstrated the increased rate of polypharmacy in PLWH compared to non-HIV infected adults with the prevalence of polypharmacy increasing yet again when comparing PLWH aged ≤50 years to OALWH (103, 109-114).

Over the past 10 years multiple clinical cohorts containing or designed specifically for OALWH have taken place across Europe and the US. These include but are not limited to: HOPS study (109), EuroSIDA study (111), AGEhIV study (115), POPPY study (116), COBRA study (117), GEPPO study (118), French Dat'AIDS study (110), SWISS HIV study (119) and the FUNCFRAIL study (103). Analysis of these studies have recently been published identifying the key issues hindering the clinical management of OALWH to encourage their inclusion in clinical trials and increase research efforts. Interestingly, one publication analysing several European cohorts found that there are currently no studies identifying optimal ARV regimens in OALWH. Furthermore, they found that the GEPPO study was the only study to assess ARV regimens in OALWH and that one third of participants were prescribed non-conventional ARV therapy. They discovered 68 varying ARV regimens among the 384 study participants and deduced the rate of multimorbidity and polypharmacy to be the cause of such clinical management decisions (103).

Considering the amalgamation of comorbidities, geriatric syndromes and polypharmacy in OALWH an increased risk of DDIs has been hypothesised. The POPPY study recently demonstrated an increased risk of potential DDIs in OALWH in comparison to younger PLWH in England and Ireland. They found that of the 698 PLWH aged ≥50 years, 57.3% had ≥1 potential DDI involving ARV and non-ARV drugs. Additionally, they found that for DDIs involving non-ARV drugs 36.1% of PLWH aged ≥50 years had ≥1 potential DDI (120). Similarly, a smaller study consisting of 89 PLWH aged ≥60 years in San Francisco, USA found that 70% of participants had ≥1 DDI that required therapy modification (113). In contrast, the

Swiss HIV cohort study found no statistically significant difference between potential DDIs in PLWH aged ≥65 years in comparison to PLWH aged ≤65 years. They found that among the total 996 participants 46% had ≥1 potential DDI, with PLWH aged ≥65 years having a higher rate of potential DDIs between ARV and cardiovascular drugs (119). Recently, a repository describing an aging population was produced and implemented into a physiologically-based pharmacokinetic (PBPK) model to gain further insight into the effect of ageing on ARV pharmacokinetics and DDIs. They found that elderly adults had a reduced rate of drug clearance resulting from decreased hepatic and renal blood flow and that ageing did not impact DDIs regardless of mechanism. However, it must be taken into consideration that this PBPK analysis was limited by the drugs included in the study and by our current understanding of DDI mechanisms (121-125). Furthermore, it is important to account for pharmacodynamic changes in OALWH when evaluating DDIs. For example, ageing has been reported to alter the pharmacodynamics of benzodiazepines and beta blockers, producing an increased and decreased effect in older adults compared to younger adults, respectively. These pharmacodynamic differences in older adults are thought to be caused by a change in homeostatic processes or by a change in the quantity and/or affinity of receptors (126).

To help support the clinical management of OALWH, the HIV Drug Interactions website recently published a resource for clinicians and patients containing prescribing decision trees as well as information on drug classes and common prescribing cascades to avoid (127). The HIV drug interactions website is a freely available, evidence-based drug interaction resource that uses a traffic light system to categorise drug interactions based on whether there is no clinical interaction expected (green), a potential weak interaction expected (yellow), a potential interaction expected (orange) or an interaction expected that advises against coadministering the drugs in question (red). Based on the variety of ARV regimens found to be prescribed in OALWH and the rate of polypharmacy in this population, an analysis of the HIV drug interactions website was carried out herein to understand potential DDIs in OALWH. The analysis included drug classes prescribed for commonly occurring comorbidities and geriatric syndromes found in OALWH (103, 105-108, 128) and their interactions with the four main groups of antiretrovirals: protease inhibitors (PIs), non-nucleoside reverse transcriptase inhibitors (NNRTIs),

nucleoside reverse transcriptase inhibitors (NRTIs) and entry/integrase inhibitors (129). A summary of the analysis can be found in Figure 1.11.

PIs had 58% of their drug interactions advising against coadministration or with a potential weak or potential interaction expected. Most PI drug interactions advising against coadministration involved overactive bladder agents and lipid lowering agents, of which darifenacin, lovastatin and simvastatin were the largest contributors. Of interest, several drug interactions advising against coadministration also involved saquinavir together with antidepressants and beta blockers. Drug interactions with a potential weak or potential interaction expected typically involved overactive bladder agents, antidepressants and beta blockers. Lopinavir and atazanavir were involved in several of the potential interactions expected and produced many of these interactions with beta blockers. PI drug interactions expecting no clinical interaction largely involved hypertension, lipid lowering agents and anti-diabetics. In contrast, 98% of NRTI drug interactions had no clinical interactions expected. NNRTIs and entry and integrase inhibitors were similar with 80% of their drug interactions having no clinical interactions expected and 20% advising against coadministration or with a potential weak or potential interaction expected. Of the NNRTIs, most of the drug interactions with a potential interaction expected comprised of efavirenz, etravirine and nevirapine. Regarding the entry and integrase inhibitors, elvitegravir/cobicistat/emtricitabine/tenofovir alafenamide and elvitegravir/cobicistat/emtricitabine/tenofovir disoproxil fumarate were involved in the majority of interactions advising against coadministration or with a potential weak or potential interaction expected.

A: Protease Inhibitors

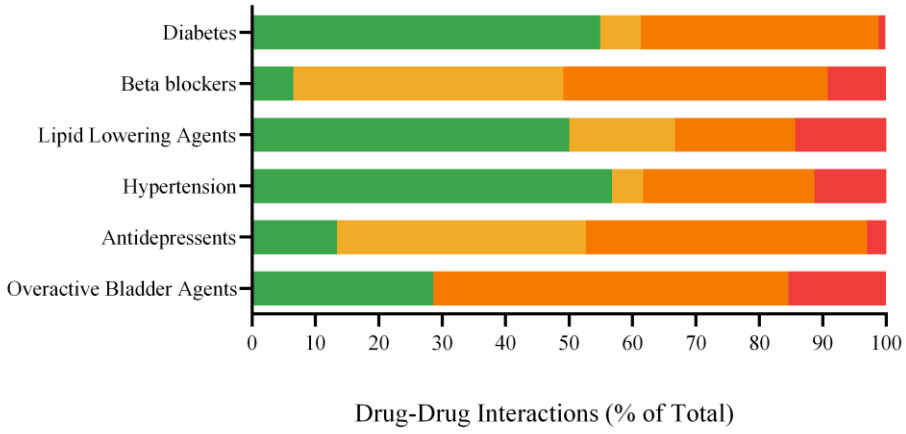

B: NNRTIs

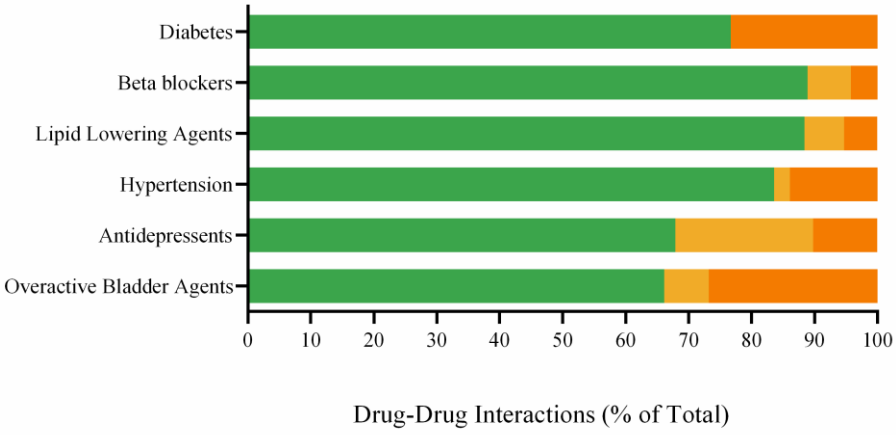

C: NRTIs

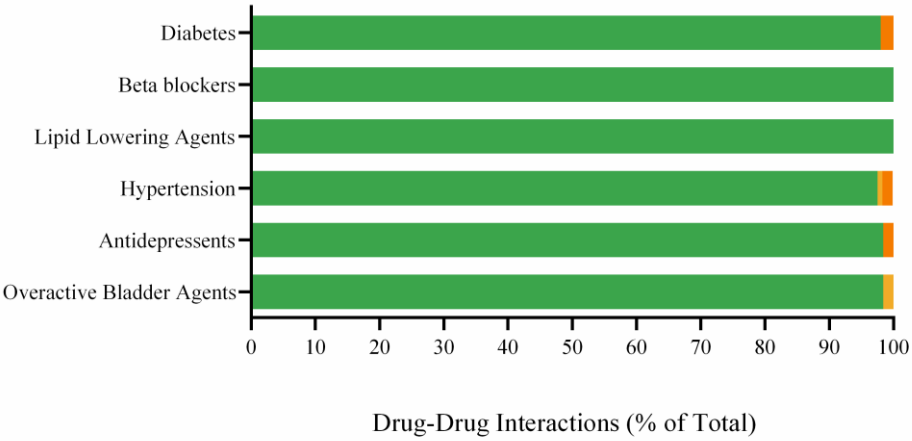

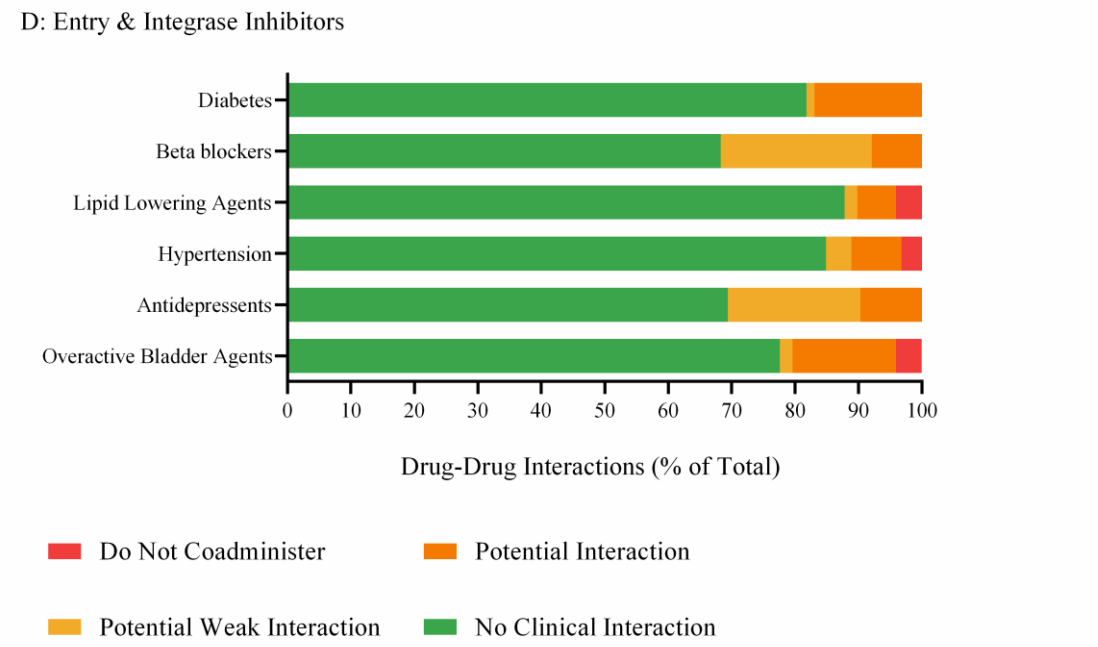

Figure 1.11 DDIs between ARV drug classes and commonly prescribed drug classes in older adults (103, 105-108, 128, 129). Graph A, B, C and D represent DDIs involving protease inhibitors (PIs), non-nucleoside reverse transcriptase inhibitors (NNRTIs), nucleoside reverse transcriptase inhibitors (NRTIs) and entry and Integrase Inhibitors, respectively. Prescribing guidance do not coadminister, potential interaction, potential weak interaction and no clinical interaction are represented in red, orange, yellow and green, respectively.

It is evident that clinical trials representative of OALWH are essential for the adaptation of current HIV clinical practice guidelines to include appropriate comorbidity, polypharmacy and geriatric assessment models, with collaboration across multiple medical and research specialities being a vital element in this process (103, 107, 130). Specifically, clinical, *in vitro* and *in silico* studies are needed to clarify the risk and magnitude of DDIs in OALWH compared to younger PLWH. These studies would improve our understanding of pharmacokinetics in OALWH and aid in the production of ARV and non-ARV drugs with lower DDI potential, helping to create more sustainable clinical management practices for OALWH in the future (106).

1.5 *In Vitro* and I*n Silico* Assessment of DDIs

In vitro and *in silico* assays can be used for the investigation of transporter pharmacokinetics with the ability to elucidate transporter-based clearance as well as magnitudes of transporter-mediated DDIs. Moreover, *in vitro-in silico* frameworks can be utilised for the extrapolation of *in vitro* assays to produce clinically meaningful data. These assays can be applied in the development of new molecular entities as well as in the exploration of transporter mechanisms to increase our knowledge base. With the clinical importance of transporters being uncovered over the past 20 years, regulatory agencies have provided guidance on clinical, *in vitro* and more recently *in silico* protocols for their investigation with a plethora of information now being available (131-133).

1.5.1 *In Vitro* Assessment of Transporter-Mediated Clearance and DDIs

There are a multitude of *in vitro* assay systems utilised for the assessment of transporters. These systems can be categorised into expression systems such as vesicular based systems or overexpressing transfected cell line systems, and whole cell systems such as hepatocytes. Different *in vitro* assay systems answer different transporter questions, with some being more appropriate than others. For example, whilst a SPHH assay can estimate hepatic clearance, it is unable to estimate biliary clearance, of which a sandwich-cultured human hepatocyte (SCHH) assay would be best suited. On the other hand, a SPHH and a plated primary human hepatocyte (PPHH) assay can both estimate hepatic clearance although each possess certain advantages and limitations. Namely, whilst both SPHH and PPHH assays benefit from cell types capable of simultaneous transporter pharmacokinetic assessment, PPHHs are impeded by decreased transporter function over the prolonged assay time-course. Overall, primary human hepatocytes enable a more physiologically accurate representation of transporter expression and function in comparison to expression systems, although they can be limited by interindividual differences across donors, as previously described in section 1.3.1. Pooled primary human hepatocyte (PHH) donor lots however, largely counteract the effect of interindividual differences in expression and activity and allow for a more realistic depiction of a population (131). Donor information such as gender, race, age, medications, history and cause of death or

surgery, depending on whether the hepatocytes were obtained from deceased or living patients, should be detailed where possible so that sources of potential variation in transporter expression and activity can be examined alongside resulting *in vitro* data. That being said, PHH suppliers often provide personalisation services so that donors with certain characteristics can be included or excluded, generating targeted *in vitro* assay systems that overcome some of the abovementioned limitations (134).

It is therefore essential to determine what data is required and what is its intended application. In general, vesicle based and transfected cell line systems are capable of estimating the kinetics of a specific transporter whilst hepatocyte or other whole cell systems are able to estimate transporter kinetics of whole processes or the combination of multiple processes simultaneously. An extensive table detailing the types of *in vitro* assays, their applications, strengths and limitations was previously published, providing a key resource for assay decision making (131). In the development of new drugs, the FDA currently recommend over-expressing cell line systems to determine whether the drug is a substrate and/or inhibitor of a transporter, with specified criteria determining the need for further *in vivo* analysis. For example, if a drug is found to be an inhibitor of OATP1B1 *in vitro*, *in vivo* studies investigating the DDI between likely coadministered drugs in the target population that are known substrates of OATP1B1 are recommended (132).

The assay systems described above can be used to assess both the uptake and efflux velocity of a substrate by a transporter as well as transporter-mediated DDIs by quantifying cell-associated drug concentrations under varying experimental conditions. To note, the term “cell-associated” rather than “intracellular” is used as it provides a more accurate description regarding drug concentrations quantified *in vitro* as drug could also be present on the outside of the cell. As this thesis focused on uptake transporters and related DDIs, the general concept of their experimental protocols are described below. Broadly speaking, transporter uptake studies consist of ≥6 concentrations of substrate drug in the presence of the cell system being used for the assay. The concentration of cell-associated drug present after a specified period of time is quantified either through liquid chromatography or radio-labelled based techniques. This data is then plotted as shown in Figure 1.12 with the ≥6 substrate concentrations plotted on the x-axis and cell-associated substrate concentration plotted on the y-axis. This assay type follows Michaelis-Menten kinetics and so the maximum velocity

(V_{max}) and Michaelis constant (K_m) can be calculated. This in turn allows for the scaling of *in vitro* data to calculate the *in vivo* intrinsic clearance, known as *in vitro-in vivo* extrapolation (IVIVE). As highlighted in the graph, the initial incline follows first-order kinetics as the rate is affected by substrate concentration whereas the plateau follows zero-order kinetics as the substrate concentration no longer effects the rate due to transporter saturation.

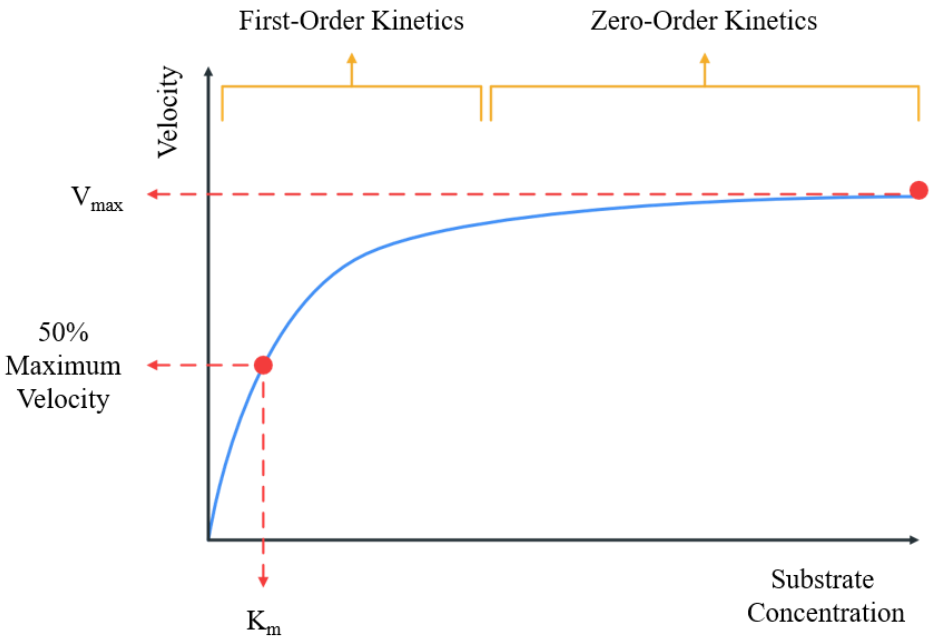

Figure 1.12 Example of a Michaelis-Menten graph of the uptake velocity of a transporter substrate. Substrate concentration is plotted on the x-axis and velocity is plotted on the y-axis. Key Michaelis-Menten parameters maximum velocity (V_{max}), 50% maximum velocity and the Michaelis-Menten constant (K_m) are highlighted with red dashed lines. First-order and zero-order kinetics are highlighted in yellow.

Similarly to uptake studies, transporter-mediated DDIs studies generally consist of ≥6 concentrations of perpetrator drug along with a constant concentration of the victim drug in the presence of the cell system being used for the assay. The concentration of cell-associated victim drug present after a specified period of time is quantified through the techniques previously described with the resulting data being plotted as shown in Figure 1.13. The ≥6 concentrations of perpetrator drug are plotted on the x-axis and the concentration of cell-associated victim drug is plotted on the y-

axis. The half maximal inhibitory concentration (IC_{50}) can then be calculated as a measure of inhibitory potency of the perpetrator for the specific victim and transporter or transporters (131-133, 135). As the IC_{50} is relative to the victim and perpetrator concentrations applied in the *in vitro* assay, the inhibition constant (K_i) is often preferred and is required for *in silico* systems. As the calculation of the K_i requires numerous, resource intensive studies it is common practice to use the IC_{50} value to calculate the K_i (136). Different equations are used for competitive, uncompetitive, non-competitive (137) and mixed inhibition (138) as shown in equations 1 – 4, respectively.

$$K_i = \frac{IC_{50}}{(S/K_m + 1)} \quad (1)$$

$$K_i = \frac{IC_{50}}{(K_m/S + 1)} \quad (2)$$

$$K_i = IC_{50} \quad (3)$$

$$K_i = IC_{50} \quad \text{or} \quad K_i = IC_{50}/2 \quad (4)$$

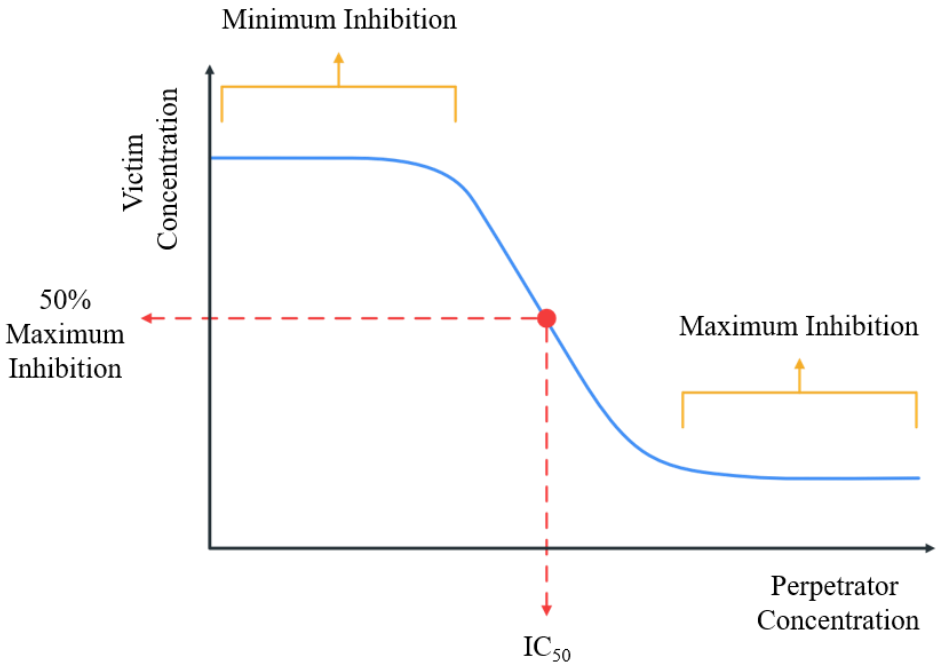

Figure 1.13 Example of a transporter-mediated DDI inhibition graph. Perpetrator concentration is plotted on the x-axis and victim concentration is plotted on the y-axis. Key inhibition parameters maximum 50% inhibition and the half maximal inhibitory concentration (IC_{50}) are highlighted with red dashed lines. Minimum and maximum inhibition are highlighted in yellow.

Although having numerous options for transporter assessment can be advantageous, it does come with certain caveats, specifically the variability in estimated pharmacokinetic parameters across laboratories. This can be particularly problematic when verifying assay system functionality as well as in the *in silico* assessment of transporters when applying previously published *in vitro* data. The underlying question in these scenarios being: which value to use? Practices across laboratories differ, for example some could use the average of all availably published values whilst others could use a singular value from a comparable assay type. Further laboratory variation is introduced when primary cell types are utilised as transporter expression varies between donors with introduction section 1.3.1 highlighting a 40-fold range being found for the expression of OATP1B1 (77). This is in addition to general assay protocol variation such as type of consumables used and natural human variation.

It is apparent that the investigation of transporters *in vitro* and *in vivo* is challenging. Transporter assay standardisation is not as comprehensive as that of enzyme based assays with there remaining a lack of specific transporter substrates and inhibitors (131, 133). However, in recent years the international transporter consortium (ITC) and FDA have highlighted several transporters which they deem clinically relevant and should be assessed during drug development. Alongside these transporters the FDA have also provided guidance on the drugs to be used for their assessment both *in vitro* and *in vivo*. Though as mentioned above, current guidance is hindered by a lack of specificity. For example, according to the FDA guidelines substrates recommended for the *in vitro* investigation of OATP1B1 are also a substrate of OATP1B3. Furthermore, some drugs are substrates of both uptake and efflux transporters found in the same cell type, for instance estrone-3-sulfate is a substrate of OATP1B1, OATP1B3 and BCRP all of which are found in hepatocytes. This is again true for *in vitro* transporter inhibitors with cyclosporine inhibiting both OATP1B1, OATP1B3 and P-gp. Additionally, some drugs are both a substrate and an inhibitor of the same transporter, for example estradiol-17β-glucuronide is both a substrate and an inhibitor of OATP1B1 and OATP1B3. Moreover, the drugs recommended by the FDA for *in vitro* investigation differ from those recommended for *in vivo* investigation (75). Differences in the *in vitro* and *in vivo* substrate and inhibitor pharmacokinetics of drugs can further complicate the analysis of assay data and is one of the challenges faced by IVIVE methods and *in silico* techniques. It is evident that the development of transporter specific substrates and inhibitors are essential for improving assessment strategies as well as expanding our current knowledge of transporters and related DDIs.

1.5.1.1 LC-MS/MS Analysis

As mentioned above, *in vitro* assays systems can utilise liquid chromatography techniques to quantify assay samples. Liquid chromatography with tandem mass spectrometry (LC-MS/MS) is a popular quantification technique used throughout academia and industry for the quantification of biological samples. Liquid chromatography, or rather reverse phase high-pressure liquid chromatography, is a separation technique that utilises a high-pressure liquid mobile phase to transport molecules through a solid stationary phase. The liquid mobile phase comprises of multiple solutions such as water, solvents as well as acid or base additives and is

hydrophilic in nature. The stationary phase consists of a column tightly packed with micron sized formulated particles that are hydrophobic in nature. Separation is driven by the hydrophilic and hydrophobic properties of the liquid mobile and solid stationary phases, respectively. In addition to the two phases, there are several other parameters that can be optimised for molecule separation including injection volume, mobile phase flow rate, column temperature and sample preparation. After separation, the molecule is detected through mass spectrometry. Mass spectrometry is a sensitive and highly selective analytical technique that quantifies the mass-to-charge (m/z) ratio of ions. A mass spectrometer consists of an ion source, a skimmer cone, one or more mass analysers, a collision cell, a detector and a vacuum system, each with specific parameters that can be optimised for ion detection. Detection occurs in a multi-step process whereby the molecule of interest is firstly ionised using either electrospray ionisation (ESI), atmospheric pressure ionisation or atmospheric pressure chemical ionisation. By utilising electric fields, a mass analyser is then able to separate the ions based on their m/z. Examples of mass analysers include quadrupole, ion trap and time-of-flight. In tandem mass spectrometry ions can then undergo fragmentation using gases such as nitrogen within a collision cell before entering a second mass analyser. This techniques allows for greater selectivity and sensitivity as well as the acquisition of structural information. Finally, the isolated ions are detected using either a point or array detector. Specialised LC-MS/MS software presents the resulting data as a chromatogram and mass spectrum (139, 140).

Quantification of unknown biological samples occurs through the application of calibration standards of known concentrations. The FDA provide recommended guidelines for the verification of LC-MS/MS methods used to quantify various molecules and sample types. A schematic diagram of the LC-MS/MS method development and FDA verification workflow is shown in Figure 1.14. Briefly, the drug of interest is solubilised in a suitable solution and directly infused into the mass spectrometer where a range of parameters are optimised for ion detection. After the selection of an appropriate liquid chromatography column and mobile phase, the chromatographic method is developed to provide suitable separation and lower limits of quantification. The accuracy and precision of the method is then analysed and if necessary, an internal standard applied. An internal standard is a substance of known concentration that is added to each sample to correct for variations and improve

quantification performance. An internal standard could either be a stable isotope version of the drug of interest or a drug with similar chemical properties. Following chromatographic method development, the technique used for sample extraction is selected based on optimal recovery of drug from the sample. Some samples may require minimal extractions procedures whilst others may require the use of liquid-liquid or solid-phase extraction to achieve adequate recovery. The FDA guidelines are then applied to verify the LC-MS/MS method. If the criteria are not met further development will be required before unknown samples can be processed (141).

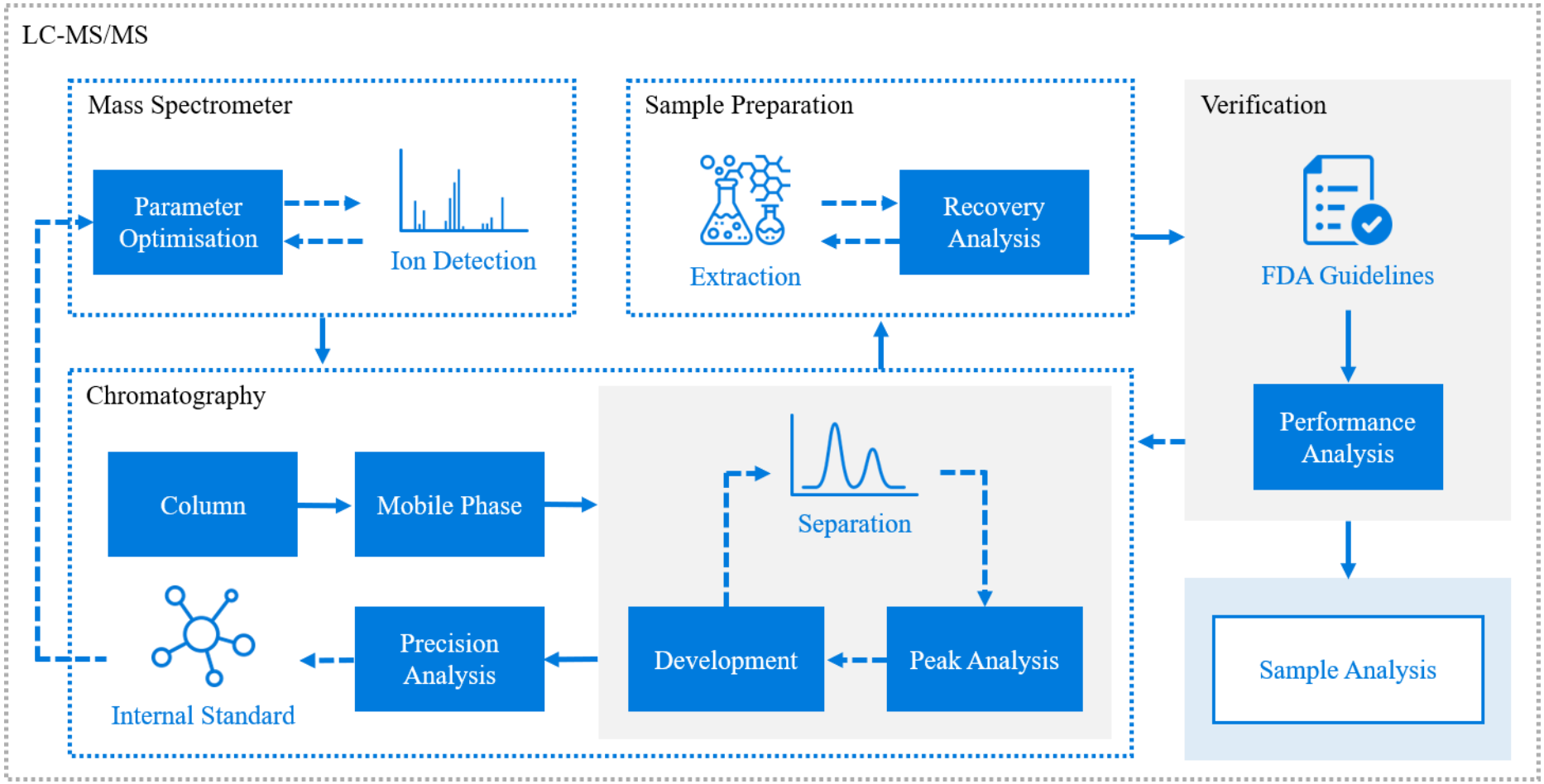

Figure 1.14 Schematic diagram of the LC-MS/MS method development and FDA verification workflow (141).

1.5.2 PBPK Modelling

PBPK modelling is an *in silico* tool that utilises mathematical equations to describe the physiological characteristics and ADME processes of the human body. The physicochemical properties of a drug can be applied within the model to predict the pharmacokinetics of drug regimens in a simulated cohort of virtual patients. Various routes of drug administration can be simulated such as oral, IV, SC, IM and transdermal. Furthermore, PBPK models can be constructed to describe specific patient characteristics such as age, gender, ethnicity and disease state and are not restricted to humans, models can also be developed for other species such as mice and rats. Both clinical and *in vitro* data are utilised in PBPK modelling and can therefore be described as a bottom-up approach. An example of a whole-body PBPK model for oral administration is shown in Figure 1.15, with both first-pass metabolism and systemic circulation being highlighted. Within the model organs and tissues are represented by compartments with the distribution of drug throughout the body being described by reactions occurring between each compartment. Reactions are defined by first-order kinetic equations and consist of parameters that are specified by constant values, including drug specific variants, or further equations known as rules. Drug variants include characteristics such as molecular weight, f_u and R. Rules provide detailed descriptions of physiological and ADME characteristics, for instance tissue-to-plasma ratios, organ weight and volume, hepatic and renal clearance as well as patient height, weight and BMI. Compartments, reactions, rules, parameters and variants work synergistically to predict pharmacokinetic parameters such as AUC, C_{max} and C_{min} which can be monitored over specified timepoints in a simulated cohort of virtual patients. Moreover, any parameter within the model can be monitored allowing for the analysis of individual processes that go beyond conventional pharmacokinetic parameters produced in clinical trials or *in vitro* investigations (63).

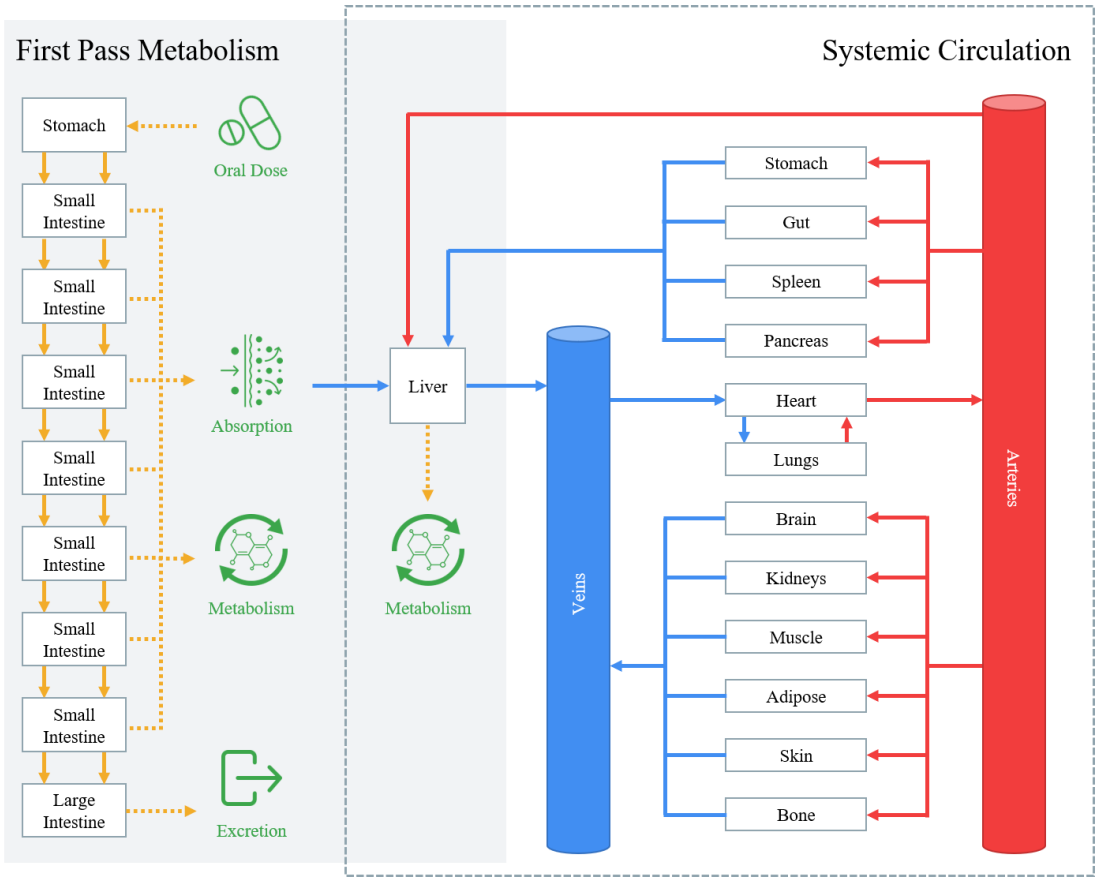

Figure 1.15 Schematic diagram of a whole-body PBPK model used to predict drug pharmacokinetics after oral administration. Organs and tissues are represented by compartments, with drug distribution represented by arrowed lines and calculated by first-order kinetic equations. Veins, arteries, and their associated reactions are highlighted in blue and red, respectively, with reactions involved in absorption, metabolism and excretion highlighted in yellow. Compartments and reactions involved in first pass metabolism are located within the grey box, with those involved in systemic circulation enclosed within the dashed line (63, 142, 143).

As described above, PBPK models can be tailored to answer specific clinical questions in a variety of populations and scenarios. As a result, PBPK modelling has proved increasingly popular in drug development as well as in the investigation of clinical scenarios absent of evidential data. In 2019, approximately 50% of all newly approved drugs contained PBPK modelling in their submission to the FDA, increasing by 30% since 2013. Of the total submissions between 2018 and 2019, 40%, 16% and 9% were concerning enzyme-mediated DDIs, transporter-mediated DDIs and

paediatrics, respectively. The remaining 35% were split across several further applications such as renal and hepatic impairment, absorption and disease. This data demonstrates the current predictive capabilities and confidence in specific PBPK modelling applications, with enzyme-mediated DDIs proving most successful in terms of regulatory acceptance. This is attributable to our expansive knowledge of enzyme function and mechanisms of DDI, experience with related PBPK models as well as the quality and quantity of available *in vitro* and clinical data used for model development and verification (144, 145). A recent analysis examining PBPK modelling over the past 20 years discovered a delay between trends in FDA submissions and publications, providing a potential insight into future regulatory applications. Specifically, they found an increase in PBPK model publications for special populations with disease, paediatric and ethnicity showing the largest rise over the past 20 years. In comparison, the study found minimal publications for transporter-related DDIs and the elderly throughout the analysed time period, identifying the need for increased efforts in both PBPK modelling and research of these two underrepresented areas (146). Encouragingly, as mentioned in introduction section 1.4.1, a PBPK model for a healthy adult population aged up to 99 years was recently developed, indicating a positive change in research initiatives in the elderly population (125).

It is interesting that despite any profound increase in publications over the past 20 years, transporter-mediated DDIs were the second most popular PBPK modelling application in FDA drug approval submissions (144-146). Lack of advancements in transporter-mediated DDI modelling has been highlighted by the FDA, with the existence of knowledge gaps and the resulting implementation of complex IVIVE methods as the current challenges in producing successful regulatory applications (144, 145). As discussed in introduction section 1.3.1 and 1.5.1, transporters play a fundamental role in the ADME of a drug and can be involved in clinically relevant DDIs. A drug can be a substrate and/or inhibitor of multiple transporters which due to issues surrounding specificity, can prove challenging to assess *in vitro*. This has an adverse downstream effect on the development of PBPK models and their ability to accurately describe mechanisms that we do not fully understand. In addition to these challenges, PBPK modelling of transporter-mediated DDIs must also consider the interplay with enzyme-mediated DDIs. This is of particular relevance in the liver and several publications have employed a permeability limited liver structure within a

whole-body PBPK model to predict such DDIs. Briefly, multiple extracellular and intracellular compartments are constructed with the extracellular compartments being connected by reactions considering blood flow rate. Active uptake and efflux as well as passive diffusion are applied in reactions linking the extracellular and intracellular compartments. Additionally, enzyme metabolism and transporter-mediate biliary CL are considered in reactions exiting the intracellular compartments. DDIs are predicted through the simulation of the perpetrator drug in a secondary model. For basolateral transporter-mediated DDIs, the concentration of perpetrator drug in the plasma or in the extracellular compartment in the liver is applied alongside the predetermined transporter K_i value in the reactions between the extracellular and intracellular liver compartments of the victim drug model. For apical transporter-mediated DDIs, the concentration of the perpetrator drug within the intracellular liver compartment is applied alongside the predetermined transporter K_i value in the reactions exiting the intracellular liver compartment of the victim drug model. Enzyme-mediated DDIs are applied similarly to apical transporter-mediated DDIs but instead consider the predetermined enzyme K_i value (147, 148). Although these models have been shown to predict drug pharmacokinetics and DDIs relatively accurately, they are limited by the application of IVIVE correction factors which differ per drug and per publication. Until further advancements in our knowledge of the underpinning mechanisms of transporters and related DDIs occur, collective efforts are required to unify IVIVE methods and rationale to improve the capabilities of our currently impeded PBPK model structures (149).

1.5.2.1 Model Workflow

PBPK model development and verification is a multi-step process and although no regulatory guidance strictly exists, verification criteria of observed vs. predicted data ratios within 0.5 – 2-fold are widely accepted (150). Figure 1.16 details the general workflow applied in PBPK model development and verification. Firstly, drug metabolism and pharmacokinetic data along with relevant clinical data are collected for the application drug as well as for any further drugs involved in the mechanistic verification of the model. Specific compartments, reactions, rules, parameters and variants describing the mechanisms involved in the model application as well as the application population are then integrated into a generic PBPK model structure alongside the collected drug data. These mechanisms are then verified using available

clinical data by simulating the corresponding dosing regimens and comparing the observed vs. predicted pharmacokinetic data values. The performance of the model can be analysed during this process and if necessary various reactions, rules, parameters and variants can be tested along with the application of correction factors. Once verified according to the above-mentioned criteria, the model can be used to predict the outcomes of the application drug (151). Furthermore, version control can be applied to the PBPK model to assist in project management, support multi-user collaboration and reduce error in model development (152).

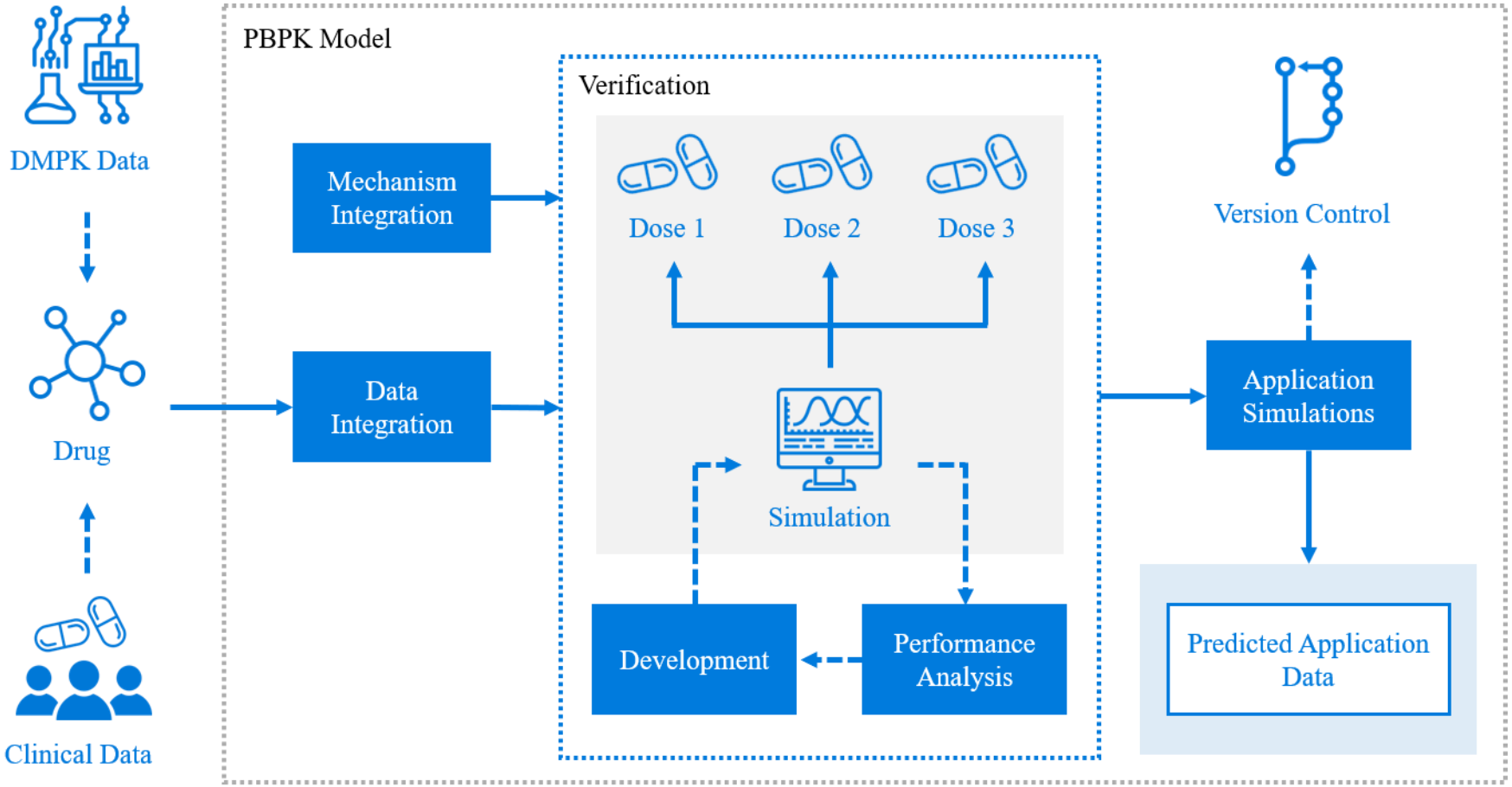

Figure 1.16 Schematic diagram of the PBPK model development and verification workflow.

1.5.2.2 Limitations

Although the data predicted by PBPK models can be used to inform clinical decisions, it must be analysed with caution and with a clear understanding of its limitations. While these limitations vary per model, they are generally based on our fundamental understanding of the ADME processes involved in the application as well as the type and quality of clinical data applied in the development and verification process. As has been highlighted in the previous sections, the mechanism involved in the ADME of a drug are complex and we often lack comprehensive knowledge of such processes making translation to mathematical frameworks particularly difficult. Additionally, the variability found *in vitro* can become a liability in IVIVE and incorporation into PBPK modelling. The appropriateness of the applied *in vitro* studies could also be called to question, with some systems showing little resemblance to physiological environments (153). Furthermore, there are several factors regarding the clinical data used for model verification that can be problematic. For example, some studies such as those used for the investigation of DDIs are conducted in as little as 5 patients producing data that is not necessarily representative of a whole population. Moreover, the available clinical data may not be generated from the population being simulated, with many studies being conducted in healthy patients aged 18 – 60 years old. The clinical data could also be from studies conducted many years ago using outdated practices in comparison to present day, resulting in potentially inaccurate data (154). A quality assessment matrix for PBPK modelling is shown in Figure 1.17 depicting the outcomes of the above-mentioned limitations. In the absence of knowledge on the ADME processes involved in a model's application, correction factors may be integrated and optimised according to the clinical data used for model verification. On the other hand, when the quality and availability of clinical data for model verification is lacking pre-clinical models can be implemented. Both scenarios, and all those in between, reduce confidence in model predictions however such PBPK modelling applications still provide valuable insight and may instigate further studies to fill the knowledge and data gap, providing vital information and allowing for improved PBPK model predictions in the future (155).

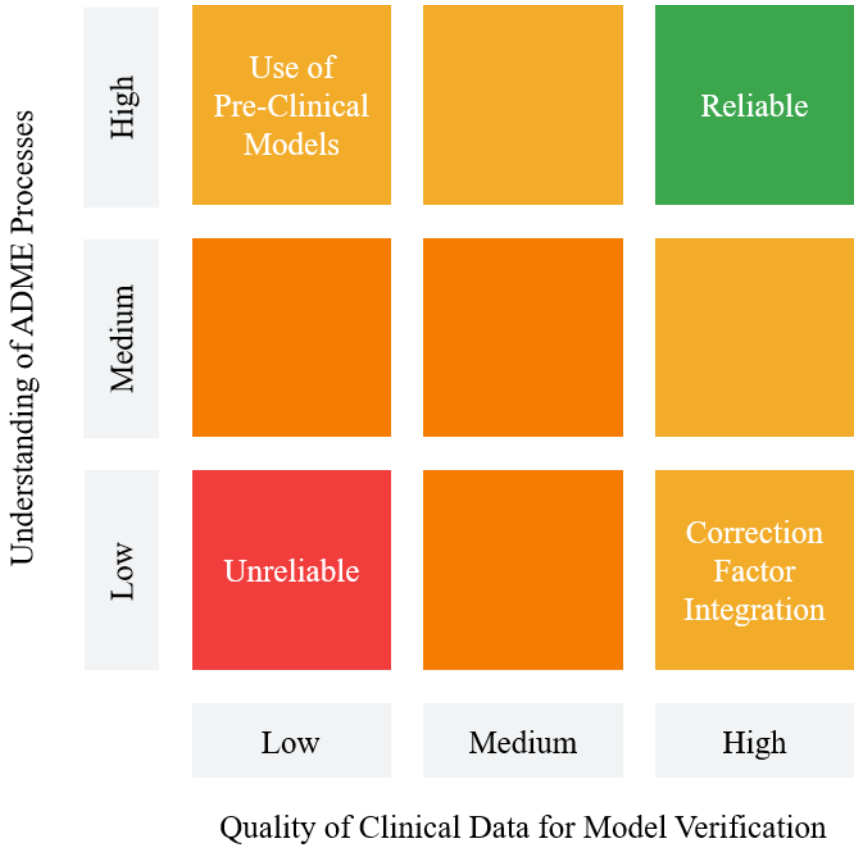

Figure 1.17 Quality assessment matrix for PBPK modelling. The reliability of a model's predictive capabilities is defined by the understanding of the implemented ADME processes as well as the quality of the clinical data used for model verification (155).

1.6 Aims

DDIs remain a key issue in the evolving clinical management of PLWH. Clinical guidance is currently impaired by the lack of understanding surrounding the mechanisms that dictate DDIs, specifically transporter-mediated DDIs. *In vitro* and *in silico* techniques can be employed synergistically to explore the role of transporters in DDIs, providing valuable information towards a more comprehensive knowledge base. Furthermore, the paucity of evidence-based guidance for ARV DDIs produces additional challenges in the clinical management of PLWH. The aim of this thesis was to identify an effective *in vitro* assay and *in silico* PBPK modelling framework to elucidate the role of hepatic uptake transporters in DDIs. Additionally, we aimed to utilise PBPK modelling to predict the outcome of HIV-related DDIs that have not been assessed clinically.

Chapter 2 aimed to establish and verify an efficient and reproducible *in vitro* assay system for the assessment of transporter-mediated hepatic intrinsic clearance and DDIs. This included the development and verification of an appropriate LC-MS/MS method. Following the verification of the *in vitro* assay system, Chapter 3 aimed to construct a PBPK model with a detailed mechanistic description of transporter-mediated uptake and passive diffusion that incorporated the *in vitro* data produced in Chapter 2. The PBPK model was verified against observed clinical data. The *in vitro-in silico* framework designed and verified in Chapter 2 and 3 was then applied in Chapter 4 to elucidate the unconfirmed role of transporters in the DDI between the HCV drug GZR and the ARV PIs ATV, DRV and RTV. In addition, the *in vitro* assay system verified in Chapter 2 was also utilised in Chapter 5 alongside a sandwich-ELISA assay to quantify the activity and expression of the hepatic uptake transporter OATP1B1 in non-elderly vs. elderly primary human hepatocyte (PHH) donors. Furthermore, the aim of Chapter 6 was to design a PBPK model to predict the magnitude of the enzyme induction-based DDI between high dose RIF QMT and DTG BID for the treatment of leprosy in PLWH. In the absence of clinical data, the aim of the PBPK model was to determine if a dose adjustment for DTG would be necessary if this treatment regimen were to be implemented in the clinical setting.

Chapter 2

Assessment of Transporter-Mediated Drug-Drug Interactions I*n Vitro* Using Suspension Cryopreserved Primary Human Hepatocytes

Contents

2.1 Introduction

PLWH are susceptible to DDIs due to the high rate of coinfections, comorbidities and complex ART regimens. Moreover, ARV drugs used for the treatment of HIV have been identified as both victims and perpetrators of several clinically relevant DDIs with the resulting changes in drug exposure leading to toxicity and reduced efficacy (156). Recent studies have highlighted the prevalence of potential DDIs in PLWH across multiple countries. A prospective cohort study of PLWH in Tanzania found that of the 1945 participants 33% had at least one potential DDI (157). An assessment of PLWH in the Swiss HIV cohort study found that 29% of the 9298 study participants had at least one potential DDI (158). Additionally, a study of PLWH in China identified that out of the 1804 participants 19.15% had at least potential DDI (159).

The liver plays an integral role in drug clearance and contains several transporters that mediate the uptake and efflux of a wide range of drugs (160, 161). Consequently, these transporters are involved in numerous DDIs and their involvement in ARV DDIs has been previously summarised (72). Specifically, OATP1B1 and OATP1B3 located exclusively on the sinusoidal membrane of hepatocytes have been identified by the FDA and ITC as clinically important transporters that should be assessed during drug development (70, 75, 162). The investigation of transporters is challenging as the mechanisms surrounding uptake and efflux are not well understood and are further complicated by their interplay with enzyme metabolism. However, strategies integrating *in vitro* and *in silico* techniques can be applied to overcome some of these challenges. The FDA and ITC published guidelines for the assessment of transporter-mediated clearance and DDIs and provide recommendations on probe substrate and inhibitor drugs for the *in vitro* assessment of clinically relevant transporters across several cell systems. Additionally, a detailed overview of *in vitro* assays for transporter assessment has been previously published, highlighting the strengths and weaknesses of each system (131).

LC-MS/MS is a routine technique that allows for the quantification of a plethora of biological molecules and is recommended in transporter assessment. Accurate and sensitive LC-MS/MS assays are produced through step-wise method development and are verified according to guidelines provided by the FDA (141). Briefly, molecules are

separated based on their polarity through liquid chromatography before being ionised and analysed by their m/z via a tandem mass spectrometer. A calibration curve of known analyte concentrations can be applied to allow the quantification of samples with unknown analyte concentrations (139).

The aim of this study was to develop and verify an *in vitro* system for the assessment of hepatic transporter intrinsic clearance ($CL_{int,T}$) and DDIs using a dual OATP1B1 and OATP1B3 probe substrate and inhibitor. Additionally, this study aimed to develop and verify a LC-MS/MS method for the quantification of the probe substrate in the *in vitro* assay (141). The *in vitro* assay can then be implemented into a PBPK model and verified against observed clinical data in Chapter 3 to generate a comprehensive *in vitro-in silico* framework for the investigation of DDIs in future chapters.

2.2 Methods

2.2.1 Materials

Accucore C18 100 x 2.1mm LC-MS/MS column (catalog no. 17126-102130) and Accucore C18 10 x 2.1mm LC-MS/MS pre-column (catalog no. 17126-012105) and LC-MS/MS grade water (H_2O_L; catalog no. 10777404) were purchased from Thermo Fisher Scientific (Hemel Hempstead, UK). LC-MS/MS grade acetonitrile (ACN_L; catalog no. 34967), LC-MS/MS grade formic acid (FA_L; catalog no. 56302), phosphate buffer saline (PBS) tablets (pH 7.2-7.6; catalog no. P4417-100TAB), Krebs-Henseleit buffer (KHB) modified (catalog no. K3753-10L) and dimethyl sulphoxide (DMSO; catalog no. D8418-50ML) were purchased from Sigma-Aldrich (Poole, UK). Cryopreserved hepatocyte recovery medium (CHRM; catalog no. CM7000) and HEPES 1M buffer (catalog no. 15630049) were purchased from Life Technologies (Paisley, UK). RIF (98% purity; catalog no. R508000) and pravastatin (PRA) sodium (98% purity; catalog no. P702000) were purchased from Toronto Research Chemicals (Ontario, Canada). PIT calcium (98% purity; catalog no. 318503) was purchased from Medkoo Biosciences (North Carolina, USA). Nucleocassettes (catalog no. 16704-000014) were purchased from Sartorius (Surrey, UK). Distilled water was produced via an Elga PureLab system (Veolia Water Technologies, High Wycombe, UK). All other materials were purchased from Thermo Fisher Scientific (Hemel Hempstead, UK) and Sigma-Aldrich (Poole, UK).

2.2.2 Primary Human Hepatocytes

Pooled donor cryopreserved SPHHs with lot no. HUE120 (catalog no. HMCS10) were purchased from Thermo Fisher Scientific (Hemel Hempstead, UK). A summary of donor characteristics can be found in Table 2.1. Lot. HUE120 SPHHs were used in the $CL_{int,T}$, DDI and toxicity studies with any remaining SPHHs from each study being utilised as the matrix for calibration and quality control (QC) standards during LC-MS/MS analysis.

Table 2.1 Summary of cryopreserved SPHH pooled donor characteristics.

Characteristics	Lot No. HUE120
n	10
Age, years Median (range)	56 (30-62)
Gender, n Male (%) Female (%)	 7 (70) 3 (30)
Race, n Caucasian (%)	 10 (100)
Reported History, n Alcohol (%) Tobacco (%) Recreational Drugs (%) Medication (%)	 8 (80) 5 (50) 4 (40) 8 (80)
n – number of patients.	

2.2.3 *In Vitro* Assay Development and Validation

The *in vitro* $CL_{int,T}$ and DDI assays were developed from similar studies described in the literature (135, 163-168) and validated by comparison to available clinical and *in vitro* data (166). A SPHH *in vitro* assay utilising PIT and RIF as the probe substrate and inhibitor for OATP1B1 and OATP1B3 were selected in accordance with the recommendations from the FDA and the ITC (70, 75) as well as considering the availability of *in vitro* and clinical data (166). Both assays were carried

out in duplicate and each contained four technical replicates per condition. The SPHH *in vitro* assays assume negligible metabolism.

2.2.3.1 Preparation of Pitavastatin and Rifampicin Stock Solutions

Stock solutions of both PIT and RIF were prepared such that the final concentrations in each cell culture plate well were between 0.1 – 300 µM with a constant DMSO concentration of 1% (vol/vol). Firstly, stock solutions of PIT (20 – 60000 µM) and RIF (20 – 60000 µM) were freshly prepared in 100% (vol/vol) DMSO through serial dilution the day before the experiment. The day of the experiment, incubation stock solutions of PIT (0.6 – 1800 µM) and RIF (0.6 – 1800 µM) were prepared in KHB (pH 7.4) with 30 µl of the corresponding DMSO stock solution being aliquoted per 1 ml of KHB. This equated to PIT and RIF incubation stock solutions containing 3% (vol/vol) DMSO in KHB. For the $CL_{int,T}$ assay where only PIT was present in each well, KHB containing 3% (vol/vol) DMSO was prepared as a substitute for RIF in order to maintain the final DMSO concentration of 1% (vol/vol).

2.2.3.2 Preparation of Suspension Primary Human Hepatocytes

Preparation of cryopreserved SPHHs took place in a class II biosafety cabinet (Baker, Maine, USA) with aseptic techniques being applied throughout (163, 169). Firstly, cryopreserved SPHHs were thawed in a 37°C water bath for 2 minutes and wiped with 70% isopropanol alcohol (IPA) before being placed in a biosafety cabinet. A wide-bore pipette was used to slowly drip the thawed hepatocytes in a circular motion into the pre-warmed CHRM media (37°C) before being centrifuged at room temperature at 100 × g for 10 minutes. The supernatant was then carefully removed and disposed of using a stripette, making sure not to disturb the pelleted SPHHs. The SPHHs were then resuspended in 8ml of pre-warmed KHB (37°C). Cell viability was determined using a NucleoCounter NC-100 apparatus (Sartorius Ltd., Epsom, UK) that utilises fluorescence based cytometry. The concentration of non-viable cells was calculated by aliquoting 150 µl of the suspension into a microcentrifuge tube and loading them into a Nucleocassette. The Nucleocassette contains propidium iodide that stains the cell nuclei of the non-viable cells due to their permeable cell membranes. The Nucleocassette was then inserted into the NucleoCounter and the number of non-viable cells was calculated through the quantification of the propidium iodide

fluorescence. The concentration of total cells was calculated by aliquoting 50 µl of the SPHH solution into a microcentrifuge tube along with 50 µl of reagent A100 and reagent B with 20 seconds of vortexing after the addition of each reagent. These reagents lyse the cells enabling the cell nuclei to be stained with propidium iodide. Again, the Nucleocassette was inserted into the NucleoCounter and the number of total cells was calculated through the quantification of the propidium iodide fluorescence (170). Equations 1 – 4 were then used to calculate the percent of viable cells, the number of viable cells/ml and the quantity of KHB required to produce a concentration of 1×10^6 cells/ml. The calculated amount of additional KHB required was then added to the SPHH solution and 100 µl was aliquoted into each well on the 24-well cell culture plate to produce a final incubation SPHH solution of 1×10^5 cells/well. Remaining SPHHs were aliquoted into microcentrifuge tubes at a concentration of 1×10^5 cells/ml, centrifuged at 2000 × g for 2 minutes at 4°C, supernatant removed and stored at -80°C for future use as the matrix for calibration, QC and blank samples during LC-MS/MS analysis.

$$\text{Cell Viability (\%)} = 100 - \left(\frac{\text{Dead Cells (cells/ml)}}{\text{Total Cells (cells/ml)} \times 3} \times 100\right) \quad (1)$$

$$\text{Cell Viability (cells/ml)} = \text{Total Cells (cells/ml)} - \text{Dead Cells (cells/ml)} \quad (2)$$

$$\text{Total Volume for } 1\times10^6 \text{ cells/ml Solution} = \frac{\text{Cell Viability (cells/ml)} \times 7.8\text{ml}}{1\times10^6 \text{ cells/ml}} \quad (3)$$

$$\text{Additional KHB Required} = \text{Total Volume for } 1\times10^6 \text{ cells/ml Solution} - 7.8\text{ml} \quad (4)$$

2.2.3.3 Pitavastatin $CL_{int,T}$ and Rifampicin DDI *In Vitro* Assays

To determine the $CL_{int,T}$ of PIT, 300µl of KHB was added to each well on the 24-well cell culture plate followed by preincubation with 100 µl KHB (0.5% vol/vol DMSO) for 5 minutes. The study was initiated with the addition of 100 µl of PIT KHB stock solution (0.5% vol/vol DMSO; 0.1 – 300 µM). To determine the magnitude of DDI between PIT and RIF, 300 µl of KHB was added to each well followed by

preincubation with RIF KHB stock solution (0.5% vol/vol DMSO; 0.1 – 300 µM) for 5 minutes. The study was initiated with the addition of 100µl PIT KHB stock solution (0.5% vol/vol DMSO; 0.1 µM). All wells had a final total volume of 600µl with all incubations taking place at 37°C on a plate shaker at 150 rpm. Both studies were terminated after 2 minutes by placing the cell culture plates on ice and aliquoting 600 µl ice-cold PBS into each well. Solutions were immediately transferred to 1.5ml microcentrifuge tubes and centrifuged at 2000 × g for 2 minutes at 4°C. Incubation solutions were then removed from each tube, cell pellets washed with 600 µl ice-cold PBS and the centrifugation process repeated. PBS wash solutions were then removed from each microcentrifuge tube and the cell pellets were stored at -80°C. Cells were lysed by a single freeze-thaw cycle (-80°C to room temperature; 18 – 25°C) prior to LC-MS/MS analysis. The *in vitro* assays were considered validated if the SPHHs demonstrated uptake of PIT as well as inhibition of PIT uptake when in the presence of RIF.

Although SPHH *in vitro* studies investigating PIT and RIF have previously been described in the literature (135, 163-168), potential toxicity of PIT and RIF with the SPHHs was assessed through a cell viability study. During the assays described above, PIT (300 µM) and RIF (300 µM) well conditions were produced, and after the termination of the 2 minute incubation, cell viability was determined as described in method section 2.2.3.2. PIT and RIF drug concentrations were deemed non-toxic if the cell viability had not substantially decrease in comparison to the cell viability calculated during the preparation of the cryopreserved SPHHs.

2.2.4 LC-MS/MS Quantification

Quantification was carried out on a TSQ Endura LC-MS/MS (Thermo Scientific, Hemel Hempstead, UK) using the Thermo Xcalibur Roadmap (version 4.0.27.42), Chromeleon Xpress and TSQ Endura Tune Application (version 2.0.1292.15) software. PRA was chosen as the internal standard (IS) for PIT due to their structural similarities and was added to calibrator, QC and unknown samples at a constant concentration to facilitate the quantification of PIT, as per convention. For use in LC-MS/MS quantification, 1mg/ml stock solutions of PIT and IS PRA in 50% (vol/vol) ACN_L in deionised H_2O (dH_2O) were freshly made every 2 weeks.

2.2.4.1 Mass Spectrometer Optimisation

Several mass spectrometer (MS) parameters were optimised for the detection of PIT and IS PRA by directly infusing 500 ng/ml solutions in 50% (vol/vol) ACN_L in dH_2O into the MS. Heated ESI was applied in positive mode to ionise the analytes and allow detection of their fragments via selective reaction monitoring (SRM) scanning. Ion spray voltage, sheath gas, auxiliary gas, ion transfer tube temperature and vaporiser temperature were optimised separately for PIT and IS PRA. The final parameter values were selected based upon the maximal detection of PIT as well as the ability to sufficiently detect the IS PRA.

2.2.4.2 Chromatographic Separation

An Accucore C18 (100 x 2.1mm) LC-MS/MS column fitted with an Accucore C18 pre-column (10 x 2.1mm) was used to achieve chromatographic separation of PIT and IS PRA. Two mobile phases, A and B, comprising of 100% H_2O_L with 0.1% FA_L and 100% ACN_L with 0.1% FA_L were used in the development of the multi-step gradient method. Solutions of 500 ng/ml PIT and IS PRA were prepared in 50% (vol/vol) ACN_L in dH_2O and 100 µl aliquoted into Chromacol fixed insert vials for analysis. The method was developed in a stepwise manner to obtain the shortest run time whilst providing efficient separation and detection of the analytes.

2.2.4.3 Sample Preparation

Once brought to room temperature, the lysed cells from the PIT $CL_{int,T}$ and RIF DDI *in vitro* assays were resuspended in 100 µl of 50% (vol/vol) ACN_L in dH_2O. These cell samples are referred to as unknown samples. To produce concentrations within the LC-MS/MS calibration curve range, all unknown samples were diluted with a ratio of 1:2 in 50% (vol/vol) ACN_L in dH_2O except for the unknown samples from the PIT 10 – 300 µM well conditions which were diluted with a ratio of 1:10. These dilution ratios were determined by quantifying one replicate per condition from one experimental replicate prior to the analysis of all remaining samples, with these samples being excluded from the final analysis. Calibration, QC and blank samples were prepared according to the FDA guidelines as described in method section 2.2.4.4 and Table 2.2 (141). At a concentration of 300 ng/ml, 300 µl of IS PRA in 100% (vol/vol) ACN_L was aliquoted into each unknown, calibration, QC and blank sample

microcentrifuge tube. Samples were then vortexed for 10 seconds and centrifuged at 13,300 × g for 10 minutes at 4°C. The resulting supernatant was carefully aliquoted into borosilicate glass tubes and dried in a Jouan RC10.22 vacuum centrifuge for 4 hours at room temperature (18 – 25°C). Once dry, samples were reconstituted in 100 µl of 50% (vol/vol) ACN_L in dH_2O, vortexed for 10 seconds and 50 µl transferred to Chromacol fixed insert vials for LC-MS/MS analysis.

2.2.4.4 Assay Verification and In-Study Guidelines

The LC-MS/MS assay was verified according to the FDA's recommended bioanalytical guidelines for industry, as described in Table 2.2. Specifically, the calibration curve, QCs, selectivity, carryover, sensitivity, accuracy, precision and carryover were assessed. Both intra-assay and inter-assay accuracy and precision were calculated using equations 5 and 6. The percent difference between the nominal and quantified concentrations were calculated within the Thermo Xcalibur Roadmap software (Hemel Hempstead, UK). Additionally, for in-study analysis, LC-MS/MS runs were kept to a maximum of 70 samples, including zero calibrators, non-zero calibrators and QC samples. Each in-study analysis quantification was therefore split up and quantified accordingly, ensuring all samples within each $CL_{int,T}$ and DDI assay replicate were within the same LC-MS/MS analysis.

$$\% \text{ Variability of Accuracy} = \frac{\text{Error}}{\text{Stated Value}} \times 100 \quad (5)$$

$$\% \text{ Variability of Precision} = \frac{\text{Standard Deviation}}{\text{Mean Assay Value}} \times 100 \quad (6)$$

2.2.5 Data Analysis

Prism v8 software (GraphPad Software Inc., La Jolla, CA, USA) was used to plot the $CL_{int,T}$ and DDI *in vitro* assay data quantified using the LC-MS/MS method described. Michaelis Menten non-linear regression analysis was applied to the PIT (0.1 – 300 µM) $CL_{int,T}$ assay data to derive the V_{max} (µmole/10^6cells/minute) and K_m (µM).

$CL_{int,T}$ (µl/10^6cells/minute) of PIT was calculated as shown in equation 7 (135) and the percent inhibition of PIT (0.1 µM) by RIF (0.1 – 300 µM) was calculated as shown in equation 8 (168). $Uptake_{substrate,inhibitor}$ and $Uptake_{substrate}$ are the total PIT (0.1 µM) uptake concentrations in the presence and absence of RIF (0.1 – 300 µM), respectively. A log(inhibitor concentration) vs. response equation and a least-squares fitting method was applied to the percent inhibition data to calculate the IC_{50} of RIF required to inhibit PIT (0.1 µM). Results from both assays were expressed as the mean ± standard deviation (SD) of two individual experimental replicates, each containing three or four technical replicates per condition, as previously described. Normality was tested using a D'Agostino & Pearson test.

$$CL_{int,T} = V_{max} / K_m \quad (7)$$

$$\% \text{ Inhibition} = 100 - (Uptake_{substrate,inhibitor} / Uptake_{substrate} \times 100) \quad (8)$$

Table 2.2 FDA recommended guidelines for LC-MS/MS verification and in-study analysis (141).

Parameters	Verification Recommendations	In-Study Analysis Recommendations
Calibration Curve	Elements: • Every verification run should contain a blank (no analyte, no IS), a zero calibrator (blank plus IS), and at least six non-zero calibrator levels covering the quantification range (including the LLOQ). • All blanks and non-zero calibrators should be in the same matrix as the study samples. • The simplest regression model should be applied to the concentration-response relationship. Acceptance Criteria: • In each verification run the non-zero calibrators should be ±15% of the nominal concentrations, except for the LLOQ which should be ±20%. • In each validation run 75% of the non-zero calibrator levels (six minimum) should meet the above criteria.	Elements: • The elements outlined for the verification runs should also be applied for the in-study analysis runs. • The regression model applied in the verification should also be used for the in-study analysis. Acceptance Criteria: • The same acceptance criteria as the verification runs should also be applied for the in-study analysis runs.

Quality Controls	Elements: • At least three verification runs should contain at least five replicates of three QC levels L (three times the LLOQ), M and H as well as the LLOQ. Acceptance Criteria: • In each verification run ≥67% of the QCs should be ±15% and LLOQ ±20% of their nominal concentrations, with ≥50% of QCs and LLOQ per level meeting this criteria.*	Elements: • Every in-study analysis should contain at least two replicates of the L, M & H QC levels. • The total number of QCs should be 5% of the unknown samples or ≥6, whichever number is greater. Acceptance Criteria: • The same acceptance criteria as the verification runs should also be applied for the in-study analysis runs.
Selectivity	Elements: • Blank samples consisting of the same matrix as the study samples from at least six individual sources should be analysed**.	Acceptance Criteria: • The same acceptance criteria as the verification runs should also be applied for the in-study analysis runs.

	Acceptance Criteria: • In each verification run the blank and zero calibrators should be free of interference at the retention times of the analyte(s) and the IS. • In each verification run the IS response in the zero calibrator should be ±5% of the average IS responses of the calibrators and QCs.	
Carryover	Elements: • The impact of carryover should be assessed. Acceptance Criteria: • In each verification run carryover should not exceed 20% of the LLOQ.	Acceptance Criteria: • The same acceptance criteria as the verification runs should also be applied for the in-study analysis runs.
Sensitivity	Elements: • Sensitivity is defined by the LLOQ (lowest non-zero standard) and should be analysed in at least three verification runs.	Acceptance Criteria: • The same acceptance criteria as the verification runs should also be applied for the in-study analysis runs.

	Acceptance Criteria: • In each verification run the LLOQ should be ≥ five times the zero calibrator.	
Accuracy and Precision	Elements: • Accuracy and precision should be analysed in at least three verification runs with L, M and H QC levels as well as the LLOQ, each with ≥ five replicates. Acceptance Criteria: • Accuracy within-run and between runs should be ±15% of the nominal concentrations, except for the LLOQ which should be ±20% (calculated as described in equation 1). • Precision within-run and between runs should be ±15% of the CV, except for the LLOQ which should be ±20% (calculated as described in equation 2).	Acceptance Criteria: • The same acceptance criteria as the verification runs should also be applied for the in-study analysis runs.

Recovery	Elements: • Recovery should be analysed from extracted samples vs. post-extracted spiked samples at L, M, and H QC level concentrations. Acceptance Criteria: • None specified***.	Acceptance Criteria: • None specified.
Only data points that fail to meet acceptance criteria may be excluded. This table was adapted from the FDA bioanalytical method validation guidelines (141). IS – internal standard, LLOQ – lower limit of quantification, QC – quality control, L – low range, M – mid range, H – high range, CV - coefficient of variation. * - within our lab we accept the L QC within ±20% of the nominal concentration, ** - within our lab, for *in vitro* assay quantification, we accept the analysis from one source, *** - within our lab we accept a recovery of analyte ≥75%.		

2.3 Results

2.3.1 LC-MS/MS Method Development and Verification

The LC-MS/MS method was successfully developed and verified according to the adapted FDA guidelines (141) as described in method section 2.2.4, with the exception of the IS selectivity criteria.

2.3.1.1 Mass Spectrometer Optimisation

The MS was successfully optimised for the maximal detection of PIT and the suitable detection of IS PRA. A summary of the optimised MS parameters as well as the detected precursor and products ions of PIT and IS PRA can be found in Table 2.3 and Table 2.4, respectively.

Table 2.3 Optimised MS parameters.

Parameter	Setting
Ion Spray Voltage (V)	Positive 4000
Sheath Gas (arb)	50
Auxiliary Gas (arb)	5
Ion Transfer Tube Temperature (°C)	350
Vaporiser Temperature (°C)	350
Parameters optimised using PIT and PRA 500 ng/ml stock solutions in 50% (vol/vol) ACN_L in dH_2O. V – voltage, arb – arbitrary unit, °C – Celsius.	

Table 2.4 PIT and PRA precursor and product ions.

Compound	Precursor (m/z)	Products (m/z)
PIT	422.183	260.04, 261.04, 262.04, 274.111, 276.111, 288.054, 290.111, 300.125, 318.111, 362.111
PRA	447.17	143.065, 241.062, 265.097, 327.111, 345.097, 385.143, 387.194, 406.25, 411.097, 429.28
Precursor and product ions determined using PIT and PRA 500 ng/ml stock solutions in 50% (vol/vol) ACN_L in dH_2O. PIT – pitavastatin, PRA – pravastatin, m/z - mass-to-charge ratio.		

2.3.1.2 Chromatographic Separation

The final multi-step mobile phase gradient is summarised in Table 2.5 and achieved a run time of 5 minutes with a flow rate of 300µl/ml and average retention times of 0.77 minutes and 0.69 minutes for PIT and IS PRA, respectively. Chromatographic representations of 10 µl injections of 500 ng/ml PIT, IS PRA and blank stock solutions in 50% (vol/vol) ACN_L in dH_2O using the optimised multi-step mobile phase gradient are shown in Figure 2.1.

Table 2.5 Chromatographic separation method.

Time (minutes)	Mobile Phase A (%)	Mobile Phase B (%)
0	95	5
0.5	95	5
1.5	5	95
3.5	5	95
3.5	95	5
5	95	5
Mobile phase A consisted of 100% H_2O_L with 0.5% FA_L and mobile phase B consisted of 100% ACN_L with 0.5% FA_L with a flow rate of 300 µl/ml and 10 µl analyte injections.		

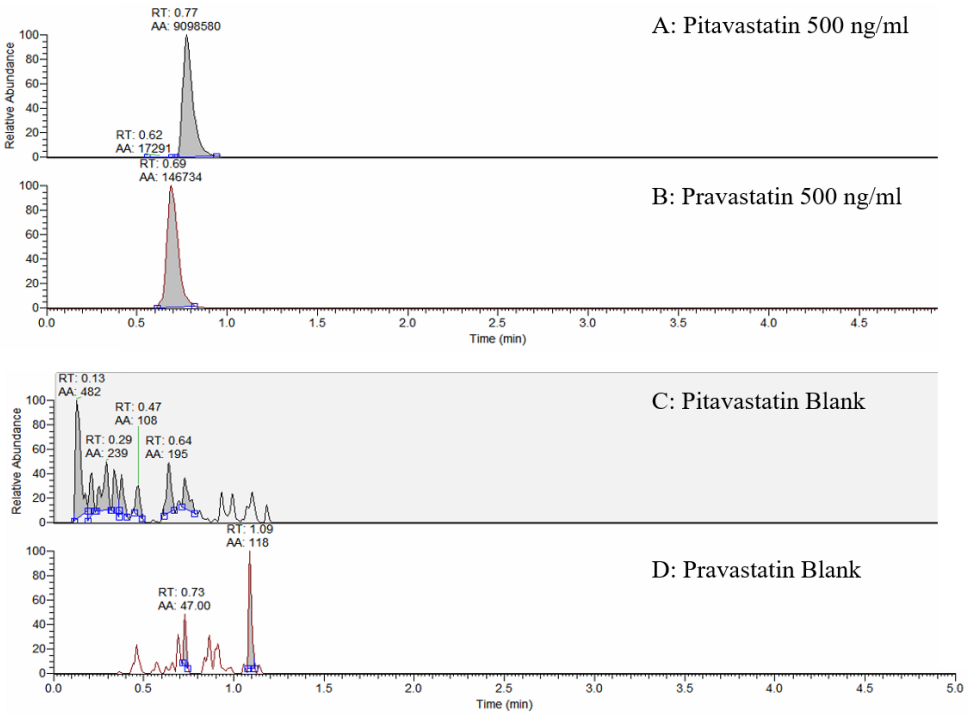

Figure 2.1 Chromatographic separation of PIT, IS PRA and blank stock solutions using the optimised MS parameters and mobile phase gradient method. Chromatograms A and B show the peaks produced by a 10 µl injection of 500 ng/ml PIT and IS PRA solutions in 50% (vol/vol) ACN_L in dH_2O, respectively. Chromatograms C and D show peaks produced by a 10 µl injection of blank solution in 50% (vol/vol) ACN_L in dH_2O for PIT and IS PRA, respectively. The grey shaded areas represent peaks detected and processed by the Thermo Xcalibur Roadmap software, with retention time (RT) and peak area (automatic integration; AA) being displayed for each detected peak.

2.3.1.3 Calibration Curve

A concentration range of 1.95 – 500 ng/ml was chosen for the calibration curve, with 1.95ng/ml being determined as the LLOQ. The LC-MS/MS method passed the calibration curve verification acceptance criteria with 100% of calibrators in two of the verification runs and 88.89% in the third verification run falling within ±15% (non-zero calibrators) and ±20% (LLOQ calibrator) of their nominal concentrations. Furthermore, the calibration curves showed good linearity over the three LC-MS/MS verification runs, with R^2 values between 0.9965 – 0.9992. A quadratic equation with a weighting of 1/X was applied in the Thermo Xcalibur Roadmap software to generate the calibration curve for PIT with IS PRA. This regression model was found to be the

simplest model that best described the signal response to calibrator concentration relationship.

2.3.1.4 Quality Controls

The LLOQ, low (L), medium (M) and high (H) QC levels were selected as 1.95 ng/ml, 5 ng/ml, 100 ng/ml and 400 ng/ml, respectively, falling within the calibration curve range. Across the three LC-MS/MS verification runs, seven of the QC levels attained 100%, four of the QC levels attained 80% and one of the QC levels attained 60% of their respective samples within ±15% (L, M and H) and ±20% (LLOQ) of their nominal concentrations.

2.3.1.5 Selectivity

Blank and zero-calibrators with the lot. HUE120 SPHHs as their matrix were used to evaluate selectivity. Both the blank and zero calibrators were free from interference at the RTs for PIT and IS PRA. As previously mentioned, the response of the zero-calibrator IS in two of the three verification runs was greater than the ±5% verification criteria. The zero-calibrator IS responses in the three verification runs were 18.60%, 3.54% and 7.23% greater than the average IS responses of the associated calibrators and QCs, respectively.

2.3.1.6 Carryover

The impact of carryover was assessed by comparing the LLOQ to the blank sample that was run after the highest calibrator concentration. No carryover was found in either of the three LC-MS/MS verification runs, with the blank samples being less than 2% of the LLOQ.

2.3.1.7 Sensitivity

Sensitivity was analysed in the three LC-MS/MS verification runs by comparing the concentration of PIT in the blank samples with the LLOQ. In all the runs, the LLOQ was at least 5 times greater than the blank sample.

2.3.1.8 Accuracy and Precision

The three LC-MS/MS verification runs contained 5 replicates of the LLOQ, L QC, M QC and H QC to allow for the assessment of accuracy and precision within and between runs. Both intra-assay and inter-assay accuracy and precision were within ±15% of their nominal values, as summarised in Table 2.6 and Table 2.7, respectively.

2.3.1.9 Recovery

Recovery was assessed across three concentrations distributed throughout the calibration curve range. The recovery of PIT for the three concentrations 1 ng/ml, 50 ng/ml and 500 ng/ml were 101.12%, 78.87% and 108.34% producing a mean recovery and standard deviation of 96.11 ± 12.54%.

Table 2.6 Summary of LC-MS/MS intra-assay accuracy and precision.

Nominal Concentration (ng/ml)	Verification Run 1		Verification Run 2		Verification Run 3	
	Variance of Accuracy (%)	Variance of Precision (%)	Variance of Accuracy (%)	Variance of Precision (%)	Variance of Accuracy (%)	Variance of Precision (%)
1.95 (LLOQ)	4.34	8.53	6.25	12.70	3.46	7.92
5 (L QC)	2.47	5.61	3.17	7.28	1.67	2.86
100 (M QC)	1.77	4.00	2.60	6.26	1.06	2.40
400 (H QC)	3.90	9.19	3.48	8.00	4.14	9.87
Data points that failed to meet the acceptance criteria were excluded. LLOQ – lower limit of quantification, QC – quality control, L – low range, M – mid range, H – high range.						

Table 2.7 Summary of LC-MS/MS inter-assay accuracy and precision.

Nominal Concentration (ng/ml)	Variance of Accuracy (%)	Variance of Precision (%)
1.95 (LLOQ)	2.74	9.96
5 (L QC)	1.54	6.03
100 (M QC)	1.32	5.29
400 (H QC)	2.25	9.16
Data points that failed to meet the acceptance criteria were excluded. LLOQ – lower limit of quantification, QC – quality control, L – low range, M – mid range, H – high range.		

2.3.2 *In Vitro* Assessment of $CL_{int,T}$ and DDI

2.3.2.1 LC-MS/MS Quantification

As described in method section 2.2.4.4, the assay samples were quantified over three separate LC-MS/MS analysis runs, with the first replicate for both $CL_{int,T}$ and DDI assays being carried out in one analysis run and the second replicate of $CL_{int,T}$ and DDI assays being carried out in two separate runs. The LC-MS/MS method was effectively applied for the quantification of PIT in the *in vitro* assays, with three exceptions to the in-study analysis verification criteria. Firstly, the IS was excluded during the quantification software processing of analysis run one due to the QC in-study analysis criteria only being met when the IS was excluded. Secondly, for analysis run two the LLOQ was 4 times greater than the blank sample rather than the criteria of 5 times greater. Thirdly, during analysis run three the Accucore C18 LC-MS/MS column began to malfunction throughout different stages of the run, producing split peaks in some of the samples, as shown in Figure 2.2. There were no further samples to repeat the LC-MS/MS analysis and so the samples with split peaks were excluded from the analysis. These included 28% of non-zero calibrators and QCs and 31% of unknown samples, with ≥50% of unknown samples per concentration condition still being included in the analysis. Nonetheless, with the exclusion of these samples the

in-study analysis verification criteria was still met except for the H QC level which had less than two replicates and the IS was 6.58% greater than the average IS responses rather than ≤5%.

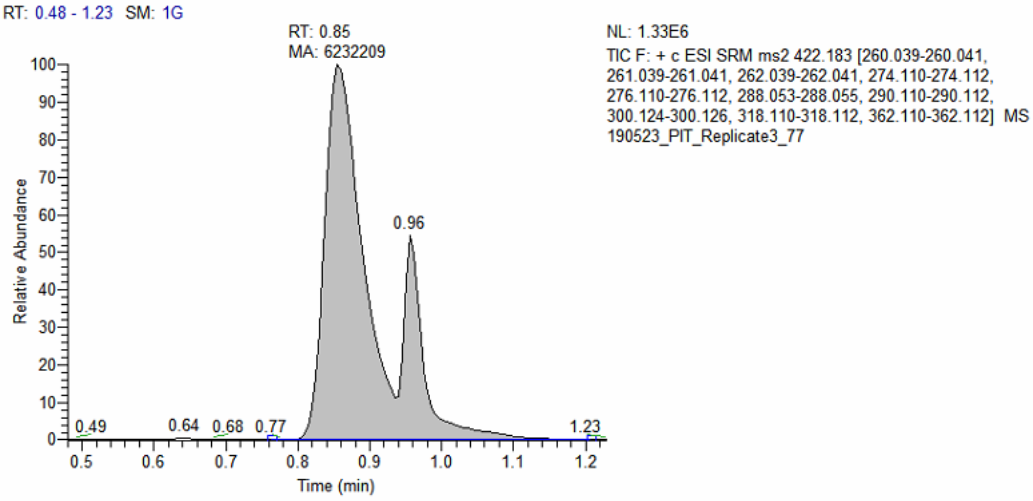

Figure 2.2 Example of the split peaking caused by the malfunctioning column during the chromatographic separation of PIT in replicate two of the DDI assay. The grey shaded area represents peaks detected and processed by the Thermo Xcalibur Roadmap software, with RT and peak area (manual integration; MA) being displayed for each detected peak.

2.3.2.2 Toxicity Study

The PIT and RIF drug concentrations used in the $CL_{int,T}$ and DDI assays were deemed non-toxic as the cell viability had decreased 2.19% and increased 0.36% in comparison to the cell viability calculated during the preparation of the cryopreserved SPHHs, respectively.

2.3.2.3 $CL_{int,T}$ of Pitavastatin and DDI with Rifampicin

A summary of the *in vitro* $CL_{int,T}$ and DDI assay with PIT and RIF can be found in Table 2.8. V_{max}, K_m and IC_{50} were calculated using Prism v8 software (GraphPad Software Inc., La Jolla, CA, USA) with the $CL_{int,T}$ and percent inhibition being calculated as described in method section 2.2.5. $CL_{int,T}$ of PIT in the lot. HUE120 SPHHs was 108.1 ± 34.38 µl/min/10^6 cells (Figure 2.3). Coincubation of RIF with PIT reduced PIT uptake by 74% with maximal inhibition at 300 µM and an IC_{50} of 0.021 µM (Figure 2.4). A D'Agostino & Pearson test for normality was conducted using

Prism v8 software (GraphPad Software Inc., La Jolla, CA, USA) for both the $CL_{int,T}$ and DDI assay data. Both the $CL_{int,T}$ and DDI assay data sets passed the normality test with p-values of 0.3601 and 0.6920, respectfully.

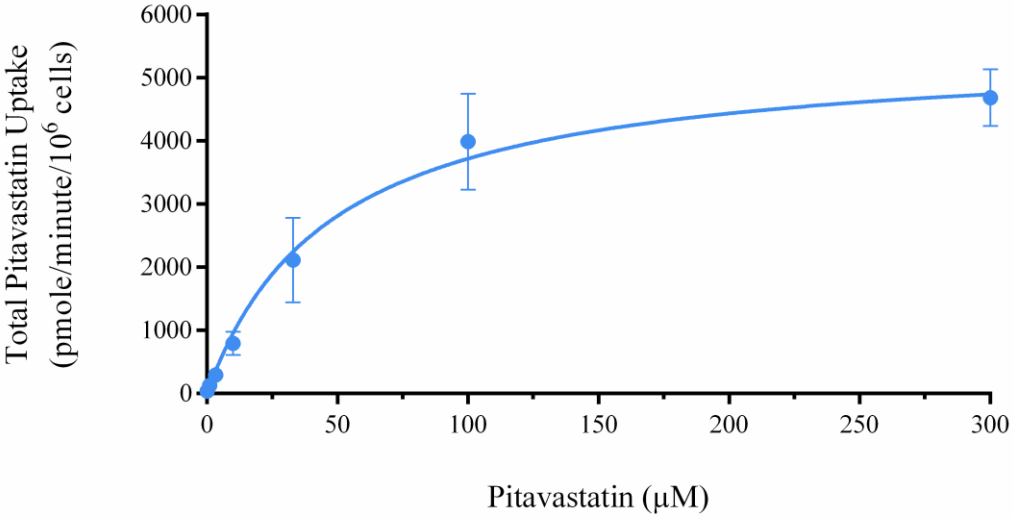

Figure 2.3 Total uptake kinetic profile of PIT (0.1 µM) measured in the lot. HUE120 SPHHs. The blue line and error bars represent the mean total PIT uptake ± SD (pmole/minute/10^6 cells) of two experimental replicates with four technical replicates.

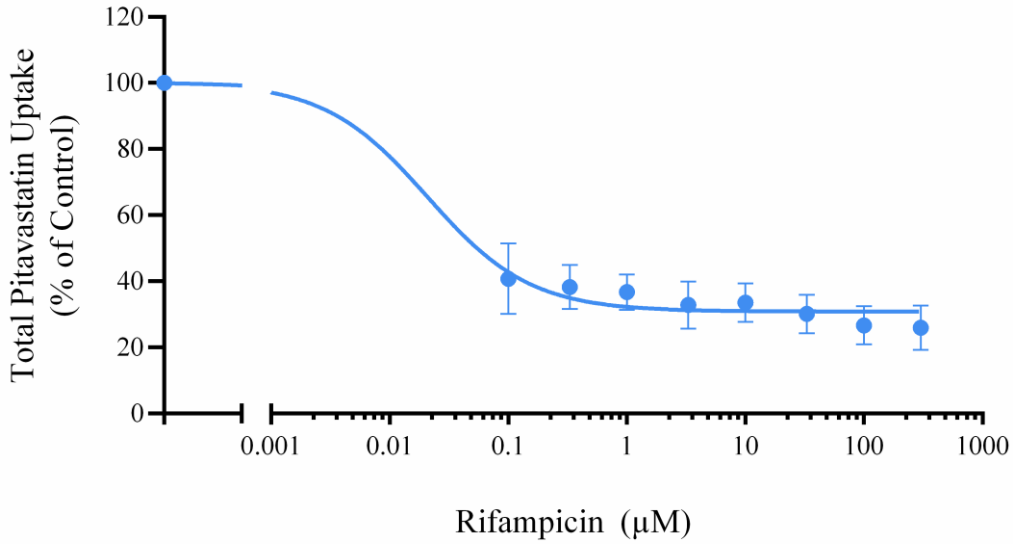

Figure 2.4 Concentration-dependent inhibition of total PIT (0.1 µM) uptake by RIF (0.1 – 300 µM) measured in the lot. HUE120 SPHHs. The blue line and error bars represent the mean inhibited total PIT uptake ± SD (% of control) of two experimental replicates with four technical replicates.

Table 2.8 Summary of the *in vitro* $CL_{int,T}$ and DDI assay with PIT and RIF.

PIT Parameter	Lot. HUE120
V_{max} (µmole/minute/10^6 cells)	5490 ± 259
K_m (µM)	50.81 ± 7.533
$CL_{int,T}$ (µl/minute/10^6 cells)	108.1 ± 34.38
RIF IC_{50} (µM)	0.021
RIF Maximum Inhibition (%)	74

V_{max}, K_m and $CL_{int,T}$ presented as mean ± SD and RIF IC_{50} and RIF maximum inhibition presented as mean of two experimental replicates with four technical replicates. PIT – pitavastatin, RIF – rifampicin, V_{max} – maximum uptake velocity, K_m – half maximum velocity concentration, $CL_{int,T}$ – hepatic transporter intrinsic clearance, IC_{50} – half maximal inhibitory concentration, SD – standard deviation.

2.4 Discussion

The mechanisms that govern drug clearance and DDIs can be investigated through an abundance of *in vitro* techniques to provide valuable information in drug discovery and the design of clinical trials (131). Recently, the importance of drug transporters in such processes has been recognised (70). In particular, the hepatic uptake drug transporters OATP1B1 and OATP1B3 have been shown to mediate the uptake of a wide range of drugs and facilitate clinically relevant DDIs (160). PHHs can be utilised *in vitro* to elucidate transporter-mediated clearance and DDIs, with the FDA and ITC providing specific guidelines and recommendations for their application (70, 162). In this study, a cryopreserved SPHH *in vitro* system was verified using the OATP1B1 and OATP1B3 probe substrate and inhibitor, PIT and RIF, for the assessment of $CL_{int,T}$ and DDI. In addition, a LC-MS/MS method was developed and verified according to FDA guidelines (141) for the quantification of PIT.

2.4.1 LC-MS/MS Quantification

The FDA guideline recommendations for the verification of bioanalytical methods were implemented herein (141). Some adaptations to the verification criteria were applied for the quantification of PIT in SPHHs and were found to be fit-for-purpose in accordance with the best practices of our laboratory. Firstly, stability was not assessed during the LC-MS/MS method verification as the stability of PIT and IS PRA has previously been described in the literature (171, 172). It was found that PIT at 0.5 ng/ml, 20 ng/ml and 320 ng/ml were stable at room temperature (18 – 25°C), refrigerated (4°C), and frozen (-20°C) as well as through two freeze-thaw cycles (-20°C to room temperature; 18-25°C). A further study demonstrated that PRA was stable when refrigerated (4°C) for 5 months (172). Secondly, the effect of dilution was not assessed as the LC-MS/MS detection of PIT across the calibration concentration range was found to be linear suggesting no impact of dilution on the quantification of PIT. Thirdly, for two of the three verification LC-MS/MS analysis runs the zero-calibrator IS response in comparison to the IS responses of the associated calibrators and QCs were 2.23% and 13.6% greater than the FDA's recommended criteria. Nonetheless, as the LC-MS/MS method was successfully verified according to all other FDA criteria, the impact of this result was believed to be insignificant.

In addition to LC-MS/MS method verification guidelines the FDA also provide acceptance criteria for in-study analysis. These criteria are largely similar to the verification criteria with the exception of the number of replicates required for QC samples. As described in Results section 2.3.2.1, there were three instances where the in-study analysis verification criteria were not met, however in view of the circumstances the processed data was considered fit-for-purpose for the following reasons. Firstly, ISs are applied in LC-MS/MS quantification to aid in the accuracy and precision of a method, yet we found that in analysis run one the IS caused the failure of the in-study analysis criteria (173). When the IS was excluded from the quantification software processing, the in-study analysis criteria were met. Although it is unclear why the IS failed during this analysis, the SD for 93.75% of conditions across the $CL_{int,T}$ and DDI assays were ≤25% of the mean and so the impact of excluding the IS in this single analysis run was thought to be insignificant.

Secondly, the zero-calibrator response was slightly higher in analysis run two resulting in a LLOQ that was 4 times greater rather than the minimum criteria of ≥5. However, as this was only a marginal difference and all other in-study verification criteria were achieved, it was deemed inconsequential. Lastly, during analysis run three split peaking was found in 28% of non-zero calibrators and QCs and 31% of unknown samples. When a peak splits it is suggestive of an issue prior to the separation of the analyte, particularly if all analytes are affected in the same way. This phenomenon is indicative of a column malfunction, specifically a void at the head of the column or a blocked frit (174). To confirm this, the column was replaced, and no further split peaking was found. Unfortunately, there were no further samples to repeat the analysis however once the samples with split peaks were removed from the analysis the in-study verification criteria were still achieved, albeit with two exceptions. Two of the three H QC level samples demonstrated split peaking and so the criteria for each QC level to contain a minimum of two samples was not met. Additionally, the IS response in the zero-calibrator was slightly higher than the accepted criteria. Overall, taking into consideration the scarcity of samples, experimental cost, data uniformity across the three analyses and the fact that all other in-study analysis criteria were met, the data produced from the LC-MS/MS quantification were satisfactory.

2.4.2 *In Vitro* Assessment of Transporter-Mediated Clearance and DDI

There are several *in vitro* assay systems outlined by the regulatory agencies for the identification of transporter-mediated clearance and DDIs, each with differing applications, strengths and limitations. These systems include membrane vesicles, recombinant cell lines expressing uptake transporters, polarised cell monolayers, PPHH, SPHHs and SCHH. This study required the identification of OATP1B1 and OATP1B3 $CL_{int,T}$ and DDIs in an *in vitro* system that closely resembled the human physiological environment. This was in part due to the implementation of the *in vitro* data into a PBPK model, as described in Chapter 3 and 4. Considering the above-mentioned criteria, a pooled cryopreserved SPHH *in vitro* assay system was selected. Unlike recombinant cell lines that overexpress the transporter of interest, such as human embryonic kidney (HEK293) cells, SPHHs provide an expression of hepatic transporters close to that found *in vivo*. Additionally, by utilising pooled donor SPHHs we can account for interindividual variability, which is an important consideration for the application of this data in PBPK modelling. Furthermore, SPHHs were selected over PPHHs as the experimental protocol is much quicker, reducing the loss of transporter activity which is considered a limitation of these *in vitro* systems (131). SPHHs have also been suggested to provide the most accurate IVIVE for the prediction of the $CL_{int,T}$ of OATP substrate drugs (175).

SPHH *in vitro* assays have been widely described in the literature (135, 163-168) and alongside the FDA's and ITC's recommended guidelines for the investigation of drugs as clinically relevant transporter substrates and inhibitors, were the basis of the assay developed and implemented herein (70, 162). One key differentiation between this study and those previously described was the omission of the *in vitro* assessment of passive uptake at 4°C. Historically passive uptake has been determined by running a parallel SPHH *in vitro* assay at 4°C, however there is much debate as to whether this method is most suitable, considering the temperature sensitivity of cell membranes (131). More recently, the use of high concentrations of OATP inhibitors to determine passive uptake have been explored (176, 177). Theoretically, coincubation with a strong inhibitor of the major OATP transporters, which are located on the sinusoidal membrane of human hepatocytes, would prevent all active uptake of an OATP substrate and therefore passive uptake would be the only mechanism of

sinusoidal membrane uptake remaining (176). This method however is dependent on our current knowledge of transporters, which is still lacking (69). One study compared multiple cellular systems at 37°C, 10°C and 4°C as well as with and without rifamycin SV, of which RIF is a derivative of, to determine passive uptake across several compounds (178). They suggested that the application of low temperatures may overestimate passive uptake whereas the use of rifamycin SV could reliably estimate passive uptake (176). Similarly, another study compared the assessment of passive uptake at 4°C against rifamycin SV inhibition in human hepatocytes and found that RIF inhibition was able to reliably estimate passive uptake (177). Considering the 74% maximal inhibition of PIT by RIF calculated in this study, passive uptake could be deemed as 26% of the total $CL_{int,T}$ with active uptake as the remaining 74%. Interestingly, this value is similar to that previously published, where the fraction of PIT transported by passive uptake was calculated through a parallel 4°C study and ranged from 0.29 – 0.37 (179). The assay described in this study was developed to work in conjunction with a PBPK model that predicts transporter-mediated clearance and DDIs *in vivo*, as described in Chapter 3. A strength of PBPK modelling is the ability to estimate parameters that are either unavailable in the literature, or experimental evaluation of the parameter is uncertain, and verify them against existing clinical pharmacokinetic data. Thus, the contribution of passive uptake to the total $CL_{int,T}$ calculated within this study will be estimated using PBPK modelling considering both the maximal inhibition calculated herein as well as the fractions determined in the literature.

The $CL_{int,T}$ of PIT determined in this assay fell within the range of values found in the literature that were documented in µl/min/10^6 cells. Table 2.9 summarises these values as well as detailing the total mean ± SD. $CL_{int,T}$ was also described in ml/min/g liver in the literature and so $CL_{int,T}$ of PIT determined in this assay was converted to ml/min/g liver based on 1.39×10^8 cells/g liver for comparison, producing a value of 15.03 ± 4.78 ml/min/g liver (180). This was similar to the value of 18.5 ± 3.8 ml/min/g liver previously reported (181). Furthermore, RIF demonstrated a substantial inhibition of PIT in the DDI *in vitro* assay in this study, which is comparable to the previously reported clinical pharmacokinetic parameters of PIT administered with and without RIF (166). However, the IC_{50} determined in this study was dissimilar to the IC_{50} previously reported, with our study presenting a much stronger level of inhibition.

Additionally, the toxicity study demonstrated minimal impact of either PIT or RIF on cell viability. The large variability of *in vitro* OATP1B1 and OATP1B3 inhibition data between studies has been recently investigated. Analysis of 21 OATP1B1 and OATP1B3 substrate and inhibitor pairs found that the most significant contributing factors to data variation were the cell system used as well as the pre-incubation and co-incubation time with the inhibitor (182). Taking this into consideration, both the SPHH donors and co-incubation time with RIF were dissimilar in this study and could explain the difference between the previously published data. Therefore, as the DDI *in vitro* assay in this study demonstrated the inhibition of PIT by RIF and alongside the results of the $CL_{int,T}$ of PIT, the experimental system described herein was deemed verified for its integration into the PBPK model described in Chapter 3.

Table 2.9 Summary of $CL_{int,T}$ of PIT.

In Vitro System	$CL_{int,T}$ (µl/min/10^6 cells)
SPHH	61.3* (76) 113* (76) 39.2* (76) 26.7** (183) 69 ± 14 (184) 66.9 ± 18.1 (175) 256 ± 40 (175)
PPHH	40.7 (185)
SCHH	53 ± 3.4 (184)
Total Mean ± SD	80.65 ± 66.23

Reference for literature values presented in brackets. Data presented as mean or mean ± SD when available. $CL_{int,T}$ – hepatic transporter intrinsic clearance, SPHH – suspension primary human hepatocytes, PPHH – plated primary human hepatocytes, SCHH – sandwich cultured human hepatocytes, SD – standard deviation, * - SD was not reported, ** - calculated from reported V_{max} (pmol/min/10^6 cells) and K_m (µM) values as described in equation 7.

2.4.3 Conclusion

This study verified the application of the SPHH *in vitro* assay alongside LC-MS/MS quantification to determine the $CL_{int,T}$ and IC_{50} of the OATP1B1 and

OATP1B3 substrate and inhibitor, PIT and RIF. Moreover, this *in vitro* system can be incorporated into a PBPK model for the verification of an *in vitro-in silico* framework as described in Chapter 3. Together this framework can be utilised to explore the role of transporters in ARV DDIs, providing knowledge for the clinical management of PLWH.

Chapter 3

Physiologically-Based Pharmacokinetic Modelling to Predict Transporter-Mediated Drug-Drug Interactions in Humans

Contents

3.1 Introduction

PBPK modelling has become an essential pharmacological tool that utilises *in vitro* and clinical data within a mathematical description of the human body for the prediction of drug pharmacokinetics. PBPK modelling can be applied in a variety of scenarios, for example it can be used to predict the pharmacokinetics of various dosing regimens during drug development (186). It can also be used to predict drug pharmacokinetics in special populations, particularly those whom clinical data may be difficult to obtain such as the elderly (187). Furthermore, PBPK modelling can be used for the investigation of DDIs mediated by enzymes and transporters, with the FDA recently providing guidance on this application (132, 188).

Transporters have been recognised as fundamental mechanisms for the ADME of a drug and regulatory agencies require their investigation during the drug development process (132, 189). Over-expressing cell lines are commonly used *in vitro* to determine if a drug is a substrate of predetermined clinically relevant transporters to aid in the design of clinical DDI studies, with the priority of understanding if dose adjustments are required or if comedication is contraindicated (70). However, due to the lack of specific transporter substrates and inhibitors and based on our currently limited understanding of transporter biology and pharmacology, it is challenging to delineate the complex interactions of the various processes involved from these studies alone (135). Understanding these intricate processes is of particular importance in PLWH who are at risk of a multitude of DDIs and as a result require extensive analysis of their drug regimens during clinical management.

PBPK modelling can be employed together with *in vitro* assays to provide comprehensive *in vitro-in silico* frameworks for the investigation of transporter-mediated clearance and DDIs. These frameworks can improve our understanding of transporter mechanisms of action and provide additional evidence-based guidance for the clinical management of PLWH. Blood flow limited descriptions of the liver have been successfully implemented in whole-body PBPK models for the assessment of transporter-mediated DDIs within the literature (147, 148). However, there is a trend in the underprediction of transporter-mediated clearance and DDIs using current *in vitro* assay systems (153, 190). This has become a major challenge in the IVIVE of transporter data for PBPK modelling applications. Consequently, drug and study

specific correction factors have become commonplace within the field of transporter pharmacokinetics, although their rationale is often lacking. It is hypothesised that these underpredictions are a result of differing transporter expression and activity *in vitro* and *in vivo* (133, 147, 179, 191-193). These convoluted IVIVE processes have limited the success of PBPK modelling in regulatory applications (145, 146).

The aim of this study was to develop and verify a whole-body PBPK model describing transporter-mediated hepatic clearance that can be applied in conjunction with the *in vitro* system developed and verified in Chapter 2 for PIT. Furthermore, this study aimed to develop and verify a minimal PBPK model for the prediction of RIF pharmacokinetics to be used alongside the whole-body PBPK model and *in vitro* system for the prediction of the transporter-mediated DDI between PIT and RIF. Additionally, we aimed to determine a SPHH specific rather than drug specific correction factor for the IVIVE of transporter data in this *in vitro-in silico* framework. The verified framework can then be used to elucidate the role of hepatic transporters in clinically relevant ARV DDIs, as described in Chapter 4.

3.2 Methods

The PBPK model was designed in Simbiology v5.8, a product of Matlab 2018a (MathWorks, Natick, MA, USA; 2018). The model was developed assuming well-stirred compartments with instant distribution of the drug and that the distribution to the compartments was blood-flow limited. Furthermore, it was assumed that there was no absorption of orally dosed drug from the large intestine. The *in vitro* $CL_{int,T}$ and IC_{50} data produced in Chapter 2 were applied in the PBPK model. All other physicochemical, pharmacokinetic, *in vitro* and *in vivo* data for PIT and RIF were sourced from literature or if unavailable were estimated via curve fitting. Virtual cohorts consisting of 100 male and female patients aged 18 – 60 years were simulated. The PBPK model was verified against observed clinical data for PIT and RIF and, where applicable, pharmacokinetic parameters and concentration time profile data were extracted from charts and graphs using the Plot Digitizer Tool (plotdigitizer.sourceforge.net).

3.2.1 Whole-Body PBPK Model

A whole-body PBPK model was applied to predict the pharmacokinetic parameters and concentration time profile of a single 1mg dose of PIT with and without a single 600mg dose of RIF (166). The physicochemical and *in vitro* data for PIT were sourced from the literature or experimentally determined, as described in Chapter 2, and can be found in Table 3.1. A schematic overview of the PBPK model utilised herein is shown in Figure 3.1 and described in the following sections.

Table 3.1 Physicochemical and *in vitro* data for pitavastatin.

Parameters	PIT
Molecular Weight (g/mol)	421.6 (194)
HBD	3 (194)
Log $P_{O:W}$	2.91 (191)

P_{app} (10^{-4} cm/s)	4.688 (191)
pK_a	5.31 (191)
Protein Binding (%)	99.6 (195)
fu_{Liver}	0.0405 (196)
PSA ($Å^2$)	90.65 (194)
R	0.55 (191)
V_{ss} (L/kg)	0.22 (191)
Water Solubility (mg/L)	3.94 (194)
$CL_{Biliary}$ (ml/minute/kg)	5.48 (197)
$CL_{int,T}$ (µL/minute/10^6 cells)	108.1^E
$CL_{int,T}$ IVIVE Correction Factor	18 (191)
$CL_{int,CYP}$ (µL/minute/mg protein)	2.5 (198)
$CL_{int,UGT}$ (µL/minute/mg protein)	15.2 (175)

Reference for literature values presented in brackets. HBD – hydrogen bond donor, Log $P_{O:W}$ - partition coefficient between octanol and water, P_{app} – apparent permeability, pK_a - logarithmic value of the dissociation constant, fu_{Liver} – fraction unbound in the liver, PSA – polar surface area, R – blood-to-plasma ratio, V_{ss} – volume of distribution at steady state (an average adult body weight of 70 kg was assumed), $CL_{Biliary}$ – biliary clearance, $CL_{int,T}$ – hepatic transporter intrinsic clearance, IVIVE – *in vitro in vivo* extrapolation, $CL_{int,CYP}$ – cytochrome P450 enzyme intrinsic clearance, $CL_{int,UGT}$ – UDP-glucuronosyltransferase enzyme intrinsic clearance, E – experimentally determined.

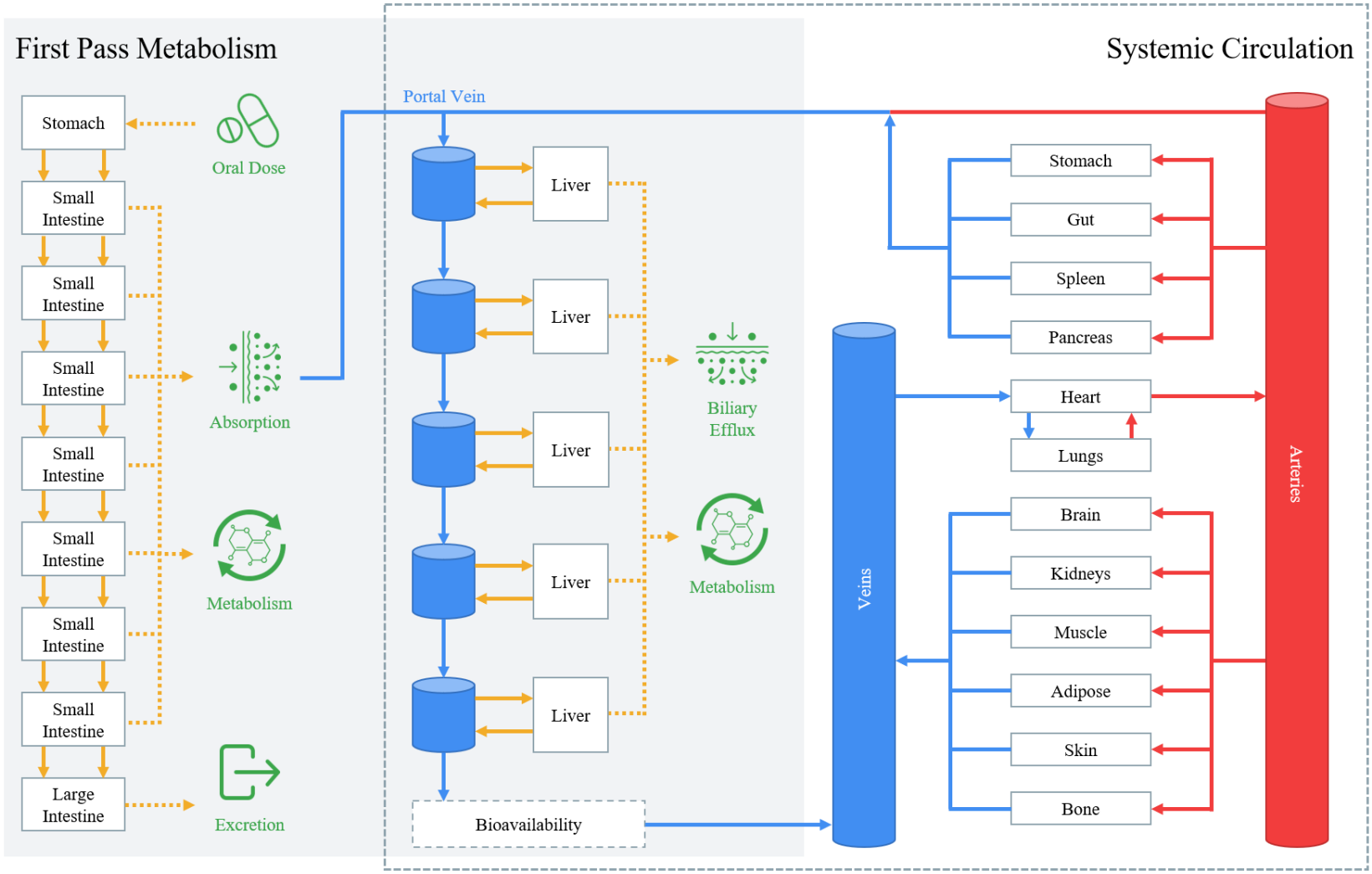
First Pass Metabolism
Systemic Circulation
Portal Vein
Stomach
Small Intestine
Small Intestine
Small Intestine
Small Intestine
Small Intestine
Small Intestine
Large Intestine
Oral Dose
Absorption
Metabolism
Excretion
Liver
Liver
Liver
Liver
Liver
Biliary Efflux
Metabolism
Bioavailability
Veins
Arteries
Stomach
Gut
Spleen
Pancreas
Heart
Lungs
Brain
Kidneys
Muscle
Adipose
Skin
Bone

Figure 3.1 Schematic diagram of the whole-body PBPK model used to predict the DDI between PIT and RIF. Each compartment represents various organs and tissues, as labelled, with each arrowed line representing a reaction described by a first-order kinetic equation to calculate the distribution of drug throughout the organs and tissues. Veins, arteries, and their associated reactions are highlighted in blue and red, respectively, with reactions involved in absorption, metabolism and excretion highlighted in yellow. Compartments and reactions involved in first pass metabolism are located within the grey box, with those involved in systemic circulation enclosed within the dashed line (63, 142, 143, 147).

3.2.1.2 Anatomy

Virtual male and female patients age 18-60 years were simulated in the PBPK model. Weight and body mass index (BMI) were defined using data from the National Center for Health Statistics as shown in Table 3.2 (199). From these predefined characteristics, the height and body surface area (BSA) were calculated using equations 1 and 2 (200, 201), with upper and lower limits applied according to the National Center for Health Statistics.

Table 3.2 Predefined male and female characteristics (199).

Parameter	Male	Female
Weight (Kg)	88.8 (0.43)	76.4 (0.42)
BMI (Kg/m^2)	28.7 (0.13)	29.2 (0.17)
Data presented as mean and standard error in brackets. Sourced from National Center for Health Statistics (199).		

$$\text{Height} = \text{Weight}/\text{BMI} \quad (1)$$

$$\text{BSA} = \text{Weight}^{0.425} \times \text{Height}^{0.725} \times 0.007184 \quad (2)$$

Height, weight, BMI and BSA were then used to determined organ weights through allometric equations 3-19 (201). Organ density values shown in Table 3.3 were then used to calculate organ volume from their weight (202). Blood flows were defined as fractions of the total cardiac output as shown in Table 3.4 (203).

$$\text{Adipose} = ((((1.20 \times \text{BMI}) + (0.23 \times \text{Age}) - 16.2) \times \text{Weight})/100) \pm 0.041 \quad (3)$$

$$\text{Blood} = 3.33 \times \text{BSA} - 0.81 \pm 0.1 \quad (4)$$

$$\text{Bones} = \exp(0.0689 + 2.67 \times \log(\text{Height})) \pm 0.166 \quad (5)$$

$$\text{Brain} = 0.405 \times \exp(-\text{Age}/629) \times (3.68 - 2.68 \times \exp(-\text{Age}/0.89)) \pm 0.084 \quad (6)$$

$$\text{Gonads} = (3.3 + 53 \times (1 - (\exp((-\text{Age}/17.5)^{5.4})))/1000 \pm 0.049 \quad (7)$$

$$\text{Heart} = \exp(-2.502 + 2.13 \times \log(\text{Height})) \pm 0.069 \quad (8)$$

$$\text{Intestines} = \exp(-1.351 + 2.47 \times \log(\text{Height})) \pm 0.049 \quad (8)$$

$$\text{Kidneys} = \exp(-2.306 + 1.93 \times \log(\text{Height})) \pm 0.14 \quad (9)$$

$$\text{Liver} = \exp(-0.6786 + 1.98 \times \log(\text{Height})) \pm 0.028 \quad (10)$$

$$\text{Lungs} = \exp(-2.092 + 2.1 \times \log(\text{Height})) \pm 0.195 \quad (11)$$

$$\text{Muscle} = 0.93 \times \text{Weight} - \text{Total Weight} \quad (12)$$

$$\text{Pancreas} = \exp(-3.431 + 2.43 \times \log(\text{Height})) \pm 0.245 \quad (13)$$

$$\text{Remaining} = \exp(-0.072 + 1.95 \times \log(\text{Height}) \pm 0.049 \quad (14)$$

$$\text{Skin} = \exp(1.64 \times \text{BSA} - 1.93) \pm 0.049 \quad (15)$$

$$\text{Spleen} = \exp(-3.123 + 2.16 \times \log(\text{Height})) \pm 0.156 \quad (16)$$

$$\text{Stomach} = \exp(-3.266 + 2.45 \times \log(\text{Height})) \pm 0.0965 \quad (17)$$

$$\text{Thymus} = 14 \times ((7.1 - 6.1 \times \exp(-\text{Age}/11.9)) \times ((0.14 + 0.86 \times \exp(-\text{Age}/10.3))))/1000 \pm 0.049 \quad (18)$$

$$\text{Total weight} = \text{Lungs} + \text{Heart} + \text{Bones} + \text{Kidneys} + \text{Stomach} + \text{Intestines} + \text{Spleen} + \text{Pancreas} + \text{Liver} + \text{Remaining} + \text{Brain} + \text{Skin} + \text{Blood} + \text{Adipose} + \text{Thymus} + \text{Gonads} \quad (19)$$

Table 3.3 Organ density in humans (202).

Organ or Tissue	Density
Adipose	0.916
Bones	1.2
Brain	1.035
Gonads	1
Heart	1.03
Intestines	1.05
Kidneys	1.05
Liver	1
Lungs	1.05
Muscle	1.041
Pancreas	1.045
Skin	1.1
Spleen	1.054
Stomach	1.05
Thymus	1

Table 3.4 Organ and tissue blood flow in humans as a fraction of cardiac output (203).

Organ or Tissue	Fraction of Cardiac Output
Adipose	0.052
Bones	0.042
Brain	0.11
Gonads	0.01
Hepatic Artery	0.12
Hepatic Vein	0.32
Intestines	0.05
Kidneys	0.175
Lungs	0.025
Muscle	0.19
Pancreas	0.05
Portal Vein	0.2
Remaining Tissue	0.01
Skin	0.06
Spleen	0.05
Stomach	0.05
Cardiac output (L/h) = $15 \times \text{Weight}^{0.75}$.	

3.2.1.3 Intestinal Absorption

A multi-compartment absorption and transit model was used to simulate the intestinal absorption of PIT. Differential equations 20-28 (143, 204) were used in the model to describe the transit of PIT in an undissolved and dissolved form from the stomach through seven small intestine compartments to the colon, with absorption occurring in the small intestine alone. Where A is the amount of drug and UND, DIS and ABS are the undissolved, dissolved and absorbed drug. ST, SI, COL, and n are the stomach, small intestine, colon, and number of compartments, respectively. K_s, K_t and K_c are the transit rates for the stomach, small intestine, and colon, respectively, and are shown in Table 3.5 (63). K_D, K_a and C_{sol} are the dissociation rate constant, absorption rate constant and soluble concentration of PIT, respectively.

Stomach Compartment:

$$\frac{dA_{UND(ST)}}{dt} = -K_s \times A_{UND(ST)} - K_D \times A_{UND(ST)} \quad (20)$$

$$\frac{dA_{DIS(ST)}}{dt} = -K_s \times A_{DIS(ST)} + K_D \times A_{UND(ST)} \quad (21)$$

Small Intestine Compartment 1:

$$\frac{dA_{UND(SI,1)}}{dt} = K_s \times A_{UND(ST)} - K_t \times A_{UND(SI,1)} - K_D \times A_{UND(SI,1)} \quad (22)$$

$$\frac{dA_{DIS(SI,1)}}{dt} = K_s \times A_{DIS(ST)} - K_t \times A_{DIS(SI,1)} + K_D \times A_{UND(SI,1)} - K_a \times C_{sol(SI,1)} \times A_{DIS(SI,1)} \quad (23)$$

$$\frac{dA_{ABS(SI,1)}}{dt} = K_a \times C_{sol(SI,1)} \times A_{DIS(SI,1)} \quad (24)$$

Small Intestine Compartment 2-7:

$$\frac{dA_{UND(SI,n)}}{dt} = K_t \times A_{UND(SI,n-1)} - K_t \times A_{UND(SI,n)} - K_D \times A_{UND(SI,n)} \quad (25)$$

$$\frac{dA_{DIS(SI,n)}}{dt} = K_t \times A_{DIS(SI,n-1)} - K_t \times A_{DIS(SI,n)} + K_D \times A_{UND(SI,n)} - K_a \times C_{sol(SI,n)} \times A_{DIS(SI,n)} \quad (26)$$

$$\frac{dA_{ABS(SI,n)}}{dt} = K_a \times C_{sol(SI,n)} \times A_{DIS(SI,n)} \quad (27)$$

Colon Compartment:

$$\frac{dA_{COL}}{dt} = K_t \times A_{UND(SI,7)} + K_t \times A_{DIS(SI,7)} - K_c \times A_{COL} \quad (28)$$

Table 3.5 Transit rates for fed and fasted states (63).

Compartment	Transit Rate Constant (per hour)	
	Fed	Fasted
Stomach (K_s)	1.02	3.96
Small Intestine (K_t)	0.57	2.1
Colon (K_c)	0.084	0.084
Values presented as per hour and were converted from per min literature values for incorporation into the PBPK model. The small intestine transit rate constant (K_t) applies to all seven compartments as described in equations 22-28.		

The soluble drug available for absorption in each small intestine compartment was calculated using equation 29 and considers the solubility of PIT ($Drug_{sol}$) as well as the concentration of dissolved drug in each compartment. K_a was calculated as described in equation 30 (143), with the apparent permeability (P_{app}) being calculated by the polar surface area (PSA) and hydrogen bond donor (HBD) values for PIT, as described in equation 31 (142). Equation 31 is transformed from the logarithmic form to the inverse logarithmic form for use in the model. The fraction of PIT available for the multi-compartment liver model (F_g) was calculated using equation 32, where Q_{gut}, $f_{u,g}$ and CL_{gut} are the blood flow to the gut, fraction unbound in the gut and metabolism based clearance of drug from the gut. As we assume that no clinically relevant PIT metabolism occurs in the gut CL_{gut}, and therefore F_g, for PIT equals 1.

$$C_{sol(SI,n)} = \max(0,\min(Drug_{sol},A_{DIS(SI,n)})) \quad (29)$$

$$K_a = \frac{P_{app} \times \text{scaling factor} \times 2}{\text{Small Intestine Radius}} \quad (30)$$

$$\log P_{app} = -2.546 - 0.011 \times PSA - 0.278 \times HBD \quad (31)$$

$$F_g = \frac{Q_{gut}}{Q_{gut} + f_{u,g} \times CL_{gut}} \quad (32)$$

3.2.1.4 Multi-Compartment Liver

A multi-compartment PBPK liver model was utilised to predict the transporter-mediated clearance of PIT, as described previously (147). The model is comprised of five portal vein and liver compartments (i) connected by blood flow with reactions describing the active and passive uptake and efflux of PIT into the liver as well as enzyme metabolism and biliary clearance of PIT. These reactions are summarised in equations 33-35 where W_{Liver}, W_{PV}, C_{Liver}, C_{PV} and C_B are the weight of the liver and portal vein and concentration of PIT in the liver compartment, portal vein compartment and blood, respectively. $CL_{int,T,a}$, $CL_{int,T,p}$, $CL_{Biliary}$ and $CL_{int,liver}$ are the active intrinsic clearance by transporters, passive diffusion, biliary clearance, and total metabolic intrinsic clearance of PIT, respectively. $f_{u,b}$, $f_{u,t}$, K_a and C_{SI} are the fraction unbound in plasma, fraction unbound in tissue, the absorption rate constant, and the concentration of PIT in the small intestine, respectively.

Liver Compartment 1-5:

$$(W_{Liver}/5) \times (dC_{Liver,i}/dt) = (CL_{int,T,a}/5) \times f_{u,b} \times C_{PV,i} + (CL_{int,T,p}/5) \times f_{u,b} \times C_{PV,i} - (CL_{int,T,p}/5) \times f_{u,t} \times C_{Liver,i} - (CL_{Biliary}/5) \times f_{u,t} \times C_{Liver,i} - (CL_{int,liver}/5) \times f_{u,t} \times C_{Liver,i} \quad (33)$$

Portal Vein Compartment 1:

$$(W_{PV,i}/5) \times (dC_{PV}/dt) = Q_{PV} \times (C_B - C_{PV,i}) - (CL_{int,T,a}/5) \times f_{u,b} \times C_{PV,i} - (CL_{int,T,p}/5) \times f_{u,b} \times C_{PV,i} + (CL_{int,T,p}/5) \times f_{u,t} \times C_{Liver,i} + K_a \times C_{SI} \quad (34)$$

Portal Vein Compartment 2-5:

$$(W_{PV,i}/5) \times (dC_{PV}/dt) = Q_{PV} \times (C_{PV,(i-1)} - C_{PV,i}) - (CL_{int,T,a}/5) \times f_{u,b} \times C_{PV,i} - (CL_{int,T,p}/5) \times f_{u,b} \times C_{PV,i} + (CL_{int,T,p}/5) \times f_{u,t} \times C_{Liver,i} \quad (35)$$

As described in Chapter 2, $CL_{int,T,a}$ and $CL_{int,T,p}$ were optimised considering the 74% inhibition of PIT by RIF *in vitro* alongside the available clinical data. This process was carried out in a stepwise manner, with $CL_{int,T,a}$ and $CL_{int,T,p}$ firstly equalling 74% and 26% of $CL_{int,T}$, respectively, with the AAFE and ratio values being calculated for predicted vs. observed data. Considering these simulations, a range of percentage values were then simulated and their AAFE and ratio values calculated. The percentage values achieving the most accurate predictions were then selected.

PIT undergoes minimal metabolism by CYP2C9 as well as UGT1A1, UGT1A3 and UGT2B7 (175, 198, 205, 206). Due to the lack of available data, the contribution of UGT enzymes to the metabolism of PIT were determined by calculating their percentage contribution to the formation of PIT lactone from an *in vitro* recombinant assay (205). The intrinsic clearance by CYP2C9, UGT1A1, UGT1A3 and UGT2B7 were then converted from µL/minute/mg protein to µl/minute/pmol using equation 36 where $CL_{int,E}$ and $Abundance_E$ are the intrinsic clearance and abundance for each enzyme. These values were then implemented into equation 37-39 in the PBPK model where $CL_{int,liverE}$, MPPGL, W_{Liver} and $CL_{int,liver}$ are the intrinsic clearance of the enzyme scaled to the whole liver, the microsomal protein per gram of liver, the liver weight and the total metabolic intrinsic clearance for the whole liver (207-210).

$$CL_{int,E}\ (\mu l/minute/pmol) = \frac{CL_{int,E}\ (\mu l/minute/mg\ protein)}{Abundance_E\ (pmol/mg)} \quad (36)$$

$$CL_{int,liverE} = (CL_{int,E} \times Abundance_E \times MPPGL \times W_{Liver}) \quad (37)$$

$$MPPGL = 10^{1.407 + 0.0158 \times Age - 0.00038 \times Age\text{^}2 + Age\text{^}3} \quad (38)$$

$$CL_{int,liver} = \Sigma CL_{int,liverE} \quad (39)$$

3.2.1.5 Drug-Drug Interactions

The inhibition of PIT by RIF was determined *in vitro* as described in Chapter 2. The IC_{50} was implemented into the PBPK model using equations 40 and 41 by firstly converting the IC_{50} value into its respective K_i value. K_i, IC_{50}, S, K_M, $f_{u,b}$ and C_{Inh} are the inhibition constant, half maximal inhibitory concentration, substrate concentration, half maximum velocity concentration, fraction unbound in blood and the concentration of inhibitor. In equations 33-35 $CL_{int,T,a}$ is divided by the resulting R-value to simulate the magnitude of the DDI (211, 212).

$$K_i = IC_{50}/(1 + S/K_M) \quad (40)$$

$$R = 1 + (f_{u,b} \times C_{Inh})/Ki \quad (41)$$

3.2.1.6 Volume of Distribution

The V_{ss} was calculated using equations 42-47 (213), with equations 46 and 47 being transformed from the logarithmic form to the inverse log form for use in equations 43 and 44. V_t, V_e and V_p are the fractional volumes of tissue, erythrocytes and plasma, respectively. $P_{t:p}$ and E:P are the adipose and non-adipose tissue:plasma partition coefficient and erythrocyte:plasma ratio. V_{nl}, V_{ph} and V_w are the neutral lipid, phospholipid and water volume fraction of wet tissue weight, where t is tissue and p is plasma. Values for the tissue composition parameters used in the V_{ss} equations can be found in Table 3.6 (213). Lastly, $D^*_{vo:w}$ is the olive oil:buffer partition coefficient of nonionised and ionised species at pH 7.4 and $P_{vo:w}$ is the n-octanol:buffer partition coefficient of nonionised species at pH 7.4.

$$V_{ss} = (\Sigma V_t \times P_{t:p}) + (V_e \times E:P) + V_p \quad (42)$$

$$P_{t:p,adipose} = \frac{(D^{*}_{vo:w} \times (V_{nlt} + 0.3 \times V_{pht})) + (1 \times (V_{wt} + 0.7 \times V_{pht}))}{(D^{*}_{vo:w} \times (V_{nlp} + 0.3 \times V_{php})) + (1 \times (V_{wp} + 0.7 \times V_{php}))} \times \frac{f_{u,p}}{1} \quad (43)$$

$$P_{t:p,non\text{-}adipose} = \frac{(P_{vo:w} \times (V_{nlt} + 0.3 \times V_{pht})) + (1 \times (V_{wt} + 0.7 \times V_{pht}))}{(P_{vo:w} \times (V_{nlp} + 0.3 \times V_{php})) + (1 \times (V_{wp} + 0.7 \times V_{php}))} \times \frac{f_{u,p}}{f_{u,t}} \quad (44)$$

$$E{:}P = (B{:}P - (1 - 0.45))/0.45 \quad (45)$$

$$\log D_{vo:w} = 1.115 \times \log P_{vo:w} - 1.35 \quad (46)$$

$$\text{Monoprotic Acid: } \log D^{*}_{vo:w} = \log D_{vo:w} - \log(1 + 10^{pH - pKa}) \quad (47)$$

Table 3.6 Tissue composition parameters (213).

Tissue	Composition (Volume Fraction of Wet Tissue Weight)		
	Water	Neutral Lipids	Phospholipids
Adipose	0.18	0.79	0.002
Bone	0.439	0.074	0.0011
Brain	0.77	0.051	0.0565
Gut	0.718	0.0487	0.0163
Heart	0.758	0.0115	0.0166
Kidney	0.783	0.0207	0.0162
Liver	0.751	0.0348	0.0252
Lung	0.811	0.003	0.009
Muscle	0.76	0.0238	0.0072
Skin	0.718	0.0284	0.0111
Spleen	0.788	0.0201	0.0198

Plasma	0.945	0.0035	0.00225
Data representative of a human weighing 70 kg.			

To obtain a V_{ss} of 0.22 (L/kg) for PIT, equations 43 and 44 were multiplied by a correction factor. The correction factor was determined by simulating a cohort of patients, as previously described, and calculating the average V_{ss}. Incremental changes were made to the correction factor and the simulations repeated until the average V_{ss} equalled 0.22 (L/kg).

3.2.1.7 Systemic Circulation

The CL_{sys} of PIT was calculated through differential equations. The lungs, arterial blood, venous blood, stomach, gut, and kidneys are described in equations 48-53, with all other non-eliminating organs and tissues being described by equation 54 (143). Liver equations were previously described in Method section 3.2.1.3. C, Q, V, $P_{t:p}$ and R are the concentration, blood flow rate, volume, tissue:plasma ratio and blood:plasma ratio, respectively. LU, AR, VE, ST, GU, KI and T are the lungs, arterial blood, venous blood, stomach, gut, kidneys and other non-eliminating organs and tissues, respectively. AIR, VIR, TIA and K_r are the arterial infusion rate, venous infusion rate, total intestinal absorption, and renal elimination rate constant, respectively.

Lungs:

$$\frac{dC_{LU}}{dt} = \frac{Q_{LU}}{V_{LU}}\left(C_{VE} - \frac{C_{LU} \times R}{P_{t:p(LU)}}\right) \quad (48)$$

Arterial Blood:

$$\frac{dC_{AR}}{dt} = \frac{1}{V_{AR}}\left(Q_{LU}\left(\frac{C_{LU} \times R}{P_{t:p(LU)}} - C_{AR}\right) + AIR\right) \quad (49)$$

Venous Blood:

$$\frac{dC_{VE}}{dt} = \frac{1}{V_{VE}}\left(\Sigma\frac{C_{LU} \times R}{P_{t:p(T)}} - Q_{LU} \times C_{VE} + VIR\right) \quad (50)$$

Stomach:

$$\frac{dC_{ST}}{dt} = \frac{1}{V_{ST}}\left(Q_{ST}\left(C_{AR} - \frac{C_{ST} \times R}{P_{t:p(ST)}}\right) + \text{Gastric Absorption}\right) \quad (51)$$

Gut:

$$\frac{dC_{GU}}{dt} = \frac{1}{V_{GU}}\left(Q_{GU}\left(C_{AR} - \frac{C_{GU} \times R}{P_{t:p(GU)}}\right) + TIA\right) \quad (52)$$

Kidneys:

$$\frac{dC_{KI}}{dt} = \frac{1}{V_{KI}}\left(Q_{KI}\left(C_{AR} - \frac{C_{KI} \times R}{P_{t:p(KI)}}\right)\right) - \frac{C_{KI} \times K_r}{P_{t:p(KI)}} \quad (53)$$

Non-Eliminating Organs and Tissues:

$$\frac{dC_T}{dt} = \frac{Q_T}{V_T}\left(C_{AR} - \frac{C_T \times R}{P_{t:p(T)}}\right) \quad (54)$$

3.2.2 Rifampicin PBPK Model

A minimal PBPK model was applied to predict the pharmacokinetic parameters and concentration time profile of a single 600mg dose of RIF (214-216). Equations 55 and 56 describe the absorption and elimination of RIF in the model where D, K_a, CL, C and V_{ss} are the dose, absorption rate constant, clearance, plasma concentration and the volume of distribution of RIF, respectively. A diagrammatic representation of the minimal RIF PBPK model is shown in Figure 3.2. The physicochemical and *in vitro* data for RIF were sourced from the literature or experimentally determined and can be found in Table 3.7.

$$\text{Absorption} = D \times K_a \quad (55)$$

$$\text{Elimination} = CL \times (C/V_{ss}) \quad (56)$$

Figure 3.2 Schematic representation of the minimal PBPK model used to predict RIF pharmacokinetics. Arrowed lines A and E represent the absorption and elimination reactions described by equations 55 and 56, respectively.

Table 3.7 Physicochemical and *in vitro* data for 600mg RIF.

Parameters	Rifampicin
Molecular Weight	822.9 (217)
Protein Binding (%)	80 (218)
V_{ss} (L/kg)	23.3 (219)
CL/F (L/h)	7.5 (219)
K_a (h^{-1})	1.15 (214)
K_i (µM)	0.021^{E}
Reference for literature values presented in brackets. V_{ss} – volume of distribution, CL/F – apparent oral clearance, K_a – absorption rate constant, K_i – inhibitor constant, E – experimentally determined.	

3.2.3 PBPK Model Verification

The whole-body PBPK model and minimal RIF PBPK model were considered successfully verified if the ratio of predicted vs. observed pharmacokinetic values for PIT, RIF and their DDI were between 0.5 – 2 (150). Where possible we aimed for the ratio of predicted vs. observed values to be within 0.75 – 1.25 to generate more accurate simulations (220). The absolute average-fold error (AAFE) for the predicted vs. observed pharmacokinetic parameters and concentration time profiles were also calculated, as defined in equation 57 (209). AAFE values between 1 – 2 were considered successfully verified however we aimed for values between 1 – 1.25. To verify the DDI between PIT and RIF, the ratio of DDI vs. drug alone were calculated (DDI_R) for both the predicted and observed values, as described in equation 58 where $drug_{DDI}$ and $drug_{sub}$ are the substrate drug parameter value in the presence of the perpetrator drug and substrate drug parameter value, respectively. The DDI_R was verified according to abovementioned criteria.

$$AAFE = 10\left|\frac{1}{N}\ \Sigma \log \frac{\text{Predicted}}{\text{Observed}}\right| \tag{57}$$

$$DDI_R = drug_{DDI} / drug_{sub} \tag{58}$$

3.3 Results

The PBPK models were successfully verified by comparing the predicted AUC, C_{max}, C_{min}, bioavailability and concentration time profiles with the observed clinical data for the oral administration of PIT, RIF and the DDI between PIT and RIF. The AAFE and ratio verification results for all drug regimens can be found in Table 3.11.

3.3.1 Whole-Body PBPK Model Verification

The whole-body PBPK model was effectively applied for the prediction of a single oral dose of PIT 1mg, with ratio and AAFE values for AUC, C_{max}, C_{min} and the concentration time profile within 0.75 – 1.25 and 1 – 1.25, respectively. The bioavailability of PIT was within the 0.5 – 2 ratio and 1 – 2 AAFE criteria. The predicted vs. observed concentration time profile and pharmacokinetic parameters can be found in Figure 3.3 and Table 3.8. As described in Method section 3.2.1.5, the V_{ss} was optimised according to the previously reported literature with the application of a correction factor value of 0.085 (191). Furthermore, equation 31 used to calculate P_{app} was unable to accurately describe the rapid absorption of PIT and was therefore replaced with the previously reported value of 4.688×10^{-4} cm/s (191). Moreover, the $CL_{int,T}$ determined *in vitro* in Chapter 2 was successfully implemented in the multi-compartment liver model with the incorporation of the previously reported IVIVE correction factor of 18 (191).

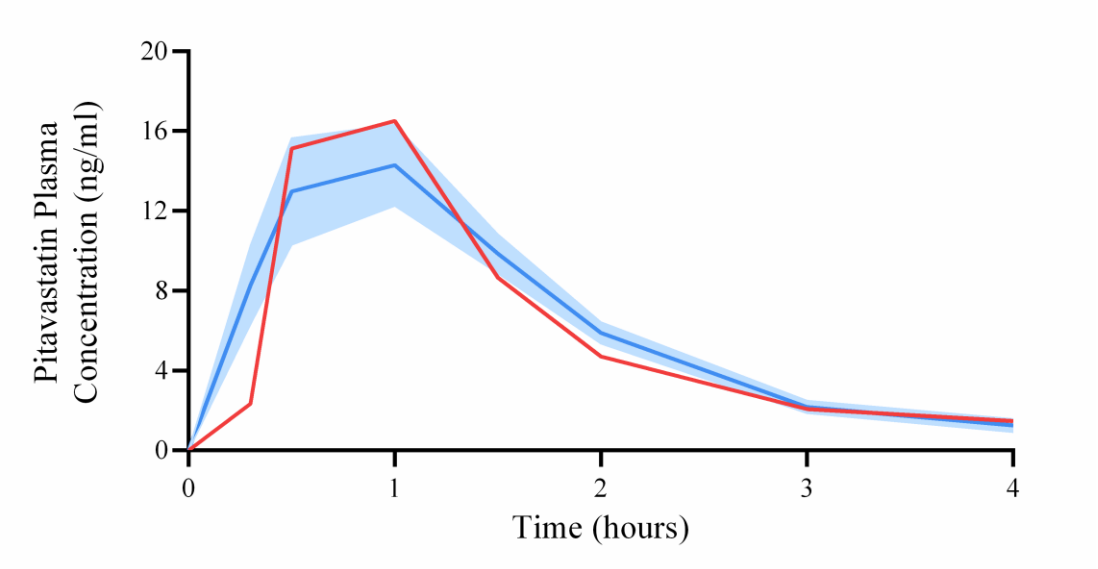

Figure 3.3 Predicted vs. observed concentration time profiles for single dose PIT 1mg. The blue line and shaded area represent the mean plasma concentration ± SD (ng/ml) of the predicted data. The red line represents the observed clinical data (ng/ml) (166).

Table 3.8 Predicted vs. observed pharmacokinetic parameters for a single dose of 1mg PIT.

Parameter	Predicted	Observed (166)
AUC_{0-4} (ng/h/ml)	25.86 ± 2.95	21 ± 7.1
C_{max} (ng/ml)	15.09 ± 2.5	16.5 ± 9.32
C_{min} (ng/ml)	1.25 ± 0.32	1.48
F (%)	32	53 (195)
Reference for observed values presented in brackets. C_{min} observed value presented as the mean (ng/ml) and was obtained from the concentration time profile. C_{min} predicted values presented as mean ± SD (ng/ml). AUC – area under the curve, C_{max} – maximum plasma concentration, C_{min} – minimum plasma concentration, F – bioavailability. AUC_{0-4} values presented as mean ± SD (ng/h/ml). C_{max} values presented as mean ± SD (ng/ml).		

3.3.2 Rifampicin PBPK Model Verification

A single oral dose of RIF 600mg was simulated and compared to the AUC_{0-24}, C_{max} and concentration time profile clinical data as shown in Figure 3.4 and Table 3.9 (221). The RIF PBPK model was successfully verified according to the criteria, with ratio and AAFE values falling within 0.75 – 1.25 and 1 – 1.25, respectively.

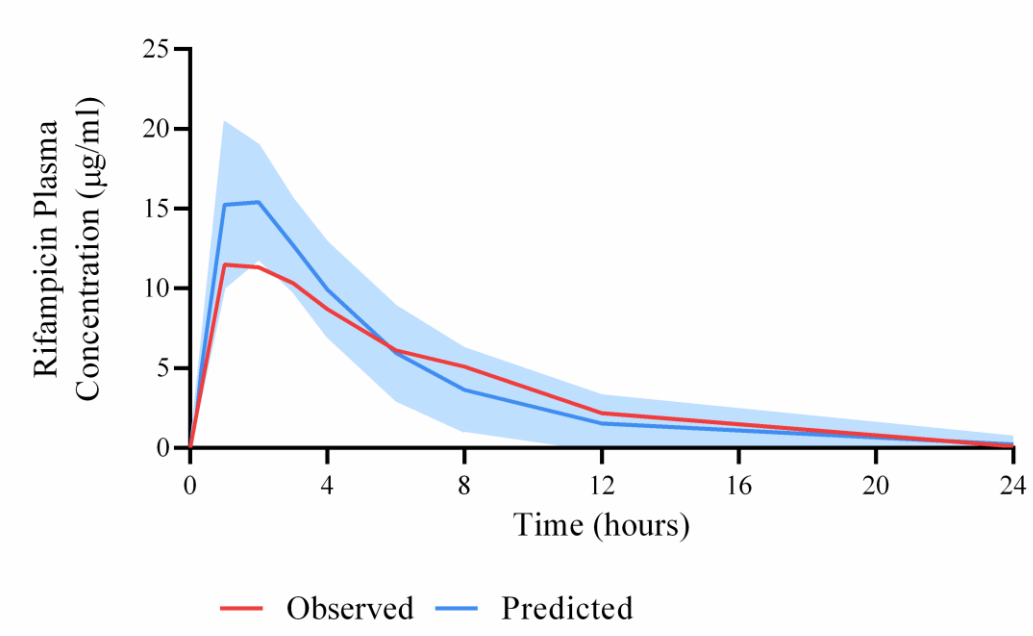

Figure 3.4 Predicted vs. observed concentration time profiles for single dose RIF 600mg. The blue line and shaded area represent the mean plasma concentration ± SD (µg/ml) of the predicted data. The red line represents the observed clinical data (µg/ml) (221).

Table 3.9 Predicted vs. observed pharmacokinetic parameters for a single dose of 600mg RIF.

Parameter	Predicted	Observed (221)
AUC_{0-24} (µg/h/ml)	93.25 ± 35.02	87.53 ± 27.2
C_{max} (µg/ml)	16.34 ± 4.7	13.07 ± 4.05
Reference for observed values presented in brackets. AUC_{0-24} values presented as mean ± standard deviation (µg/h/ml). C_{max} values presented as mean ± SD (µg/ml). AUC – area under the curve, C_{max} – maximum plasma concentration.		

3.3.3 Pitavastatin and Rifampicin Drug-Drug Interaction

The DDI between a single oral dose of PIT 1mg and a single oral dose of RIF 600mg was successfully verified with ratio and AAFE values for AUC, C_{min}, AUC DDI_R, and concentration time profile within 0.75 – 1.25 and 1 – 1.25, respectively. The C_{max}, C_{max} DDI_R and bioavailability were within the 0.5 – 2 ratio and 1 – 2 AAFE criteria. The predicted vs. observed concentration time profile and pharmacokinetic parameters can be found in Figure 3.5 and Table 3.10. As described in Method section 3.3.1.3, the optimised values for $CL_{int,T,a}$ and $CL_{int,T,p}$ that produced the most accurate predictions for the DDI between PIT and RIF were 85% and 15%, respectively.

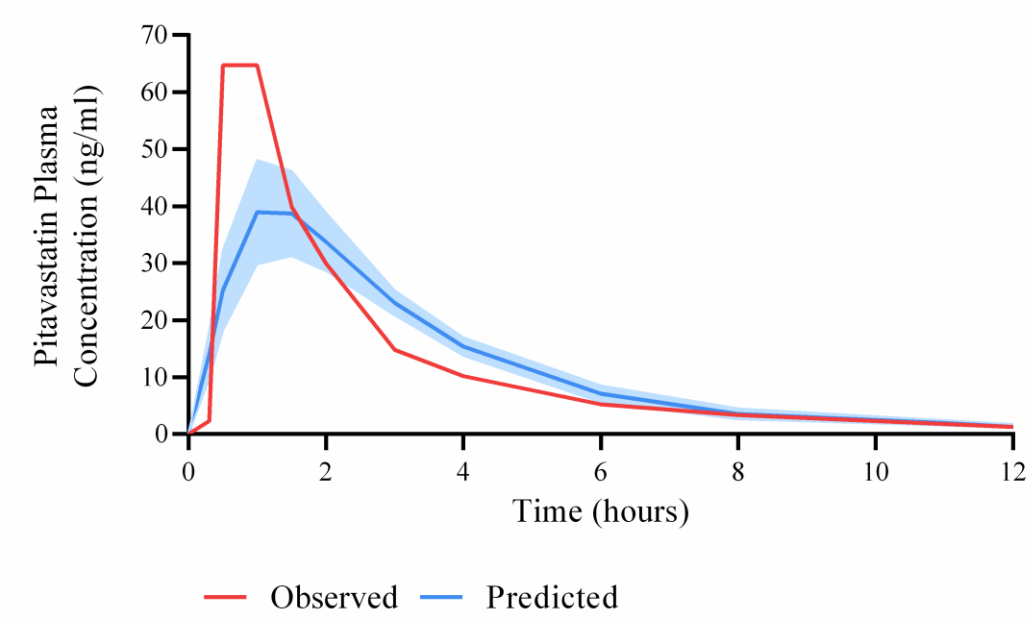

Figure 3.5 Predicted vs. observed concentration time profiles for single dose PIT 1mg coadministered with single dose RIF 600mg. The blue line and shaded area represent the mean plasma concentration ± SD (ng/ml) of the predicted data. The red line represents the observed clinical data (ng/ml) (166).

Table 3.10 Predicted vs. observed pharmacokinetic parameters for the DDI between a single dose of 1mg PIT and a single dose of RIF 600mg.

Parameter	Predicted	Observed (166)
AUC_{0-4} (ng/h/ml)	110.05 ± 19.48	118 ± 53
C_{max} (ng/ml)	40.88 ± 10.08	78.8 ± 45.3
C_{min} (ng/ml)	1.52 ± 0.31	1.26
AUC_{0-4} DDI_R	4.26	5.21
C_{max} DDI_R	2.71	4.36

Reference for observed values presented in brackets. AUC_{0-4} values presented as mean ± standard deviation (ng/h/ml). C_{max} values presented as mean ± SD (ng/ml). C_{min} observed value presented as the mean (ng/ml) and was obtained from the concentration time profile. C_{min} predicted values presented as mean ± SD (ng/ml). DDI ratios calculated as described in equation 58. AUC – area under the curve, C_{max} – maximum plasma concentration, C_{min} – minimum plasma concentration, DDI – drug-drug interaction, DDI_R – DDI ratio.

Table 3.11 PBPK model verification summary of predicted vs. observed clinical data.

Dose	Parameter	Ratio	AAFE
PIT 1mg Single Dose	AUC_{0-4}	1.23	1.23
	C_{max}	0.91	1.09
	C_{min}	0.84	1.19
	F	0.6	1.656
	Profile	-	1.19
RIF 600mg Single Dose	AUC_{0-24}	1.07	1.07
	C_{max}	1.25	1.25
	Profile	-	1.13
PIT 1mg Single Dose with RIF 600mg Single Dose	AUC_{0-4}	0.93	1.07
	C_{max}	0.52	1.93
	C_{min}	1.15	1.15
	AUC_{0-4} DDI_R	0.82	1.22
	C_{max} DDI_R	0.62	1.61
	Profile	-	1.2

PIT – pitavastatin, RIF – rifampicin, AUC – area under the curve, C_{max} – maximum plasma concentration, C_{min} – minimum plasma concentration, F – bioavailability, DDI – drug-drug interaction, DDI_R – DDI ratio, Profile – concentration time profile. Ratio and AAFE values calculated as described in Method section 3.2.3.

3.4 Discussion

The integration of *in vitro* and *in silico* methodologies can support the prediction and simulation of complex pharmacokinetics, providing important knowledge to support the clinical management of transporter-mediated DDIs as well as in drug development. PBPK modelling utilises mathematical equations alongside the compartmentalisation of organs and tissues to simulate drug pharmacokinetics in a cohort of virtual patients, providing an efficient and ethical resource of simulated clinical data. The aim of this study was to develop and verify a whole-body PBPK model detailing a multi-compartment liver that encapsulates active and passive diffusion of PIT across the sinusoidal membrane of hepatocytes, as well as describing the interplay between PIT diffusion, metabolism, and biliary excretion. Moreover, the study aimed to develop and verify a secondary minimalistic model to simulate RIF pharmacokinetics to predict the magnitude of transporter-mediated DDI between PIT and RIF. The models incorporated the *in vitro* experimental data for PIT and RIF determined in Chapter 2 for the overall verification of the *in vitro-in silico* framework for the investigation of ARV transporter-mediated DDIs in Chapter 4.

3.4.1 *In Silico* Assessment of Transporter-Mediated Clearance and DDI

A previously published multi-compartment description of the liver was integrated into the whole-body PBPK model to allow the incorporation of transporter kinetics whilst reflecting the blood-flow limited hepatic disposition of the dispersion model (147). The dispersion model has previously been described as the optimal strategy for predicting hepatic clearance. The well-stirred approach implemented for the other organs in the PBPK model assumes that there is a uniform concentration of drug throughout the organ, whereas the concept of the dispersion model applied herein considers the non-uniform concentration of drug as it travels throughout the liver. However, as the dispersion model considers enzyme metabolism as the rate limiting step rather than transporter kinetics, it is unable to be applied directly thus an adapted model is required (222, 223).

$CL_{int,T}$ of PIT and the K_i for the DDI between PIT and RIF were determined *in vitro* in Chapter 2 and applied in the multi-compartment liver model. This *in vitro-in silico* framework produced accurate predictions of single dose 1mg PIT

pharmacokinetics with ratio and AAFE values for all parameters, excluding the bioavailability, within the stringent 0.75 – 1.25 ratio and 1 – 1.25 AAFE verification criteria. The bioavailability was underpredicted however remained within the 0.5 – 2 ratio and 1 – 2 AAFE verification criteria widely accepted within the literature, demonstrating that the 5-compartment structure was suitable for PIT predictions (150). Furthermore, as this parameter is thought to be less imperative for the application of this model compared to the other pharmacokinetic parameters, which were all within the strict criteria, this underprediction was deemed acceptable. The simulated DDI magnitude tended to be underpredicted, with only the AUC, AUC DDI_R and C_{min} of single dose 1mg PIT coadministered with single dose 600mg RIF falling within the strict verification criteria. Nonetheless, the C_{max} and C_{max} DDI_R achieved the 0.5 – 2 ratio and 1 – 2 AAFE criteria.

Underprediction of transporter-mediated DDIs is commonplace within the literature (190), with a previous PIT PBPK model also describing the underprediction of the DDI between PIT and RIF in their simulations (191). Interestingly, previous models found significant underpredictions using the reported K_i value of 0.9 µM and proceeded to use an optimised K_i value of 0.09 µM to obtain more accurate predictions (191). Comparatively, the K_i value determined in the *in vitro* assay in Chapter 2 was 0.017 µM, demonstrating the suitability of the *in vitro* assay developed and used herein. Curiously, the previously published model described accurate C_{max} predictions with a C_{max} DDI_R of 1.82 compared to their documented observed C_{max} DDI_R of 2.11, though the outlined reference for the observed ratio recorded a C_{max} DDI_R of 9.2 (224). Nevertheless, this C_{max} DDI_R was comparable to that predicted here, with our predictions more accurately representing the C_{max} DDI_R described in the literature (166). It should also be noted that the previously published model used single dose 4mg PIT data obtained from healthy Chinese volunteers (224) whereas our data was sourced from a single dose 1mg PIT study in healthy Caucasians (166). This could in part explain the difference in DDI ratios found between the studies, with reports of higher OATP1B1 expression amongst Asian donors compared to Caucasian donors *in vitro* (225).

Predicting transporter-mediated DDIs is challenging. The underprediction of the C_{max} DDI_R in this study could be due to a multitude of reasons and is likely based on our lack of knowledge surrounding transporter pharmacology. Although PIT has

been reported as a specific OATP1B1 and OATP1B3 substrate, our underpredicted simulations suggest a further mechanistic pathway involved in the ADME of PIT that is affected by the RIF DDI. Consequently, this lack of understanding has led to the omission of such pathways in the PBPK model implemented herein, thus failing to capture the C_{max} DDI_R reported in the literature. As previously described (191) and as tested during the model development process in this study, decreasing the RIF K_i did not improve the accuracy of the C_{max} predictions, reinforcing the theory that RIF could potentially be inhibiting an additional pathway, increasing the absorption of PIT or altering the V_{ss} (190). Considering these scenarios, during the parameter optimisation process the effect of different V_{ss} correction factors and P_{app} values on the pharmacokinetics of PIT were analysed. V_{ss} correction factor values lower than the final optimised value produced more accurate predictions of PIT C_{max} however the resulting AUC and C_{min} values were overpredicted and outside the 0.5 – 2 ratio and 1 – 2 AAFE verification criteria and were therefore not selected. Increasing the P_{app} value had minimal impact on the C_{max} prediction. Interestingly, the equation used to calculate P_{app} was unable to capture the rapid absorption of single dose 1mg PIT and a specific value from the literature was implemented instead. It is clear that with multiple factors influencing the pharmacokinetics of PIT and with current clinical and *in vitro* data proving insufficient in combination with our current understanding, dissecting the mechanisms involved in DDIs lacks confidence. Yet, by applying these *in vitro-in silico* frameworks we can highlight areas that require further research and apply the framework step-by-step towards eliminating the knowledge gap on transporter-mediated DDIs.

3.4.1.1 Active and Passive Diffusion

The percentage contribution of active and passive diffusion to the $CL_{int,T}$ calculated *in vitro* differed from the optimised values used in the PBPK model. It was found that, although the pharmacokinetics of single dose 1mg PIT were accurately predicted, the magnitude of DDI between PIT and RIF was underestimated. When $CL_{int,T,a}$ and $CL_{int,T,p}$ were estimated as 85% and 15% of the $CL_{int,T}$ the most accurate DDI predictions were achieved. These values are comparable to that described previously for PIT, with $CL_{int,T,a}$ being calculated in the range of 80-88% to provide optimal predictions (179). In addition, a previously published study found that the *in vitro* assessment of $CL_{int,T,a}$ and $CL_{int,T,p}$ using 4°C experimental conditions were

inaccurate and concluded that passive diffusion *in vivo* is smaller than that determined using *in vitro* systems (135). The inappropriateness of the $CL_{int,T,a}$ and $CL_{int,T,p}$ values estimated *in vitro* in Chapter 2 using the maximal percent inhibition of PIT by RIF further highlights the limitations surrounding *in vitro* techniques for this purpose. PBPK modelling could therefore be a suitable alternative for the prediction of active and passive diffusion and necessitates further exploration comparing a variety of drugs and *in vitro* systems.

3.4.1.2 IVIVE Correction Factor

The use of correction factors on the IVIVE of $CL_{int,T}$ data has been described multiple times within the literature (133, 147, 179, 191-193). The underprediction of $CL_{int,T}$ from *in vitro* data remains unclear however it is thought that a reduction in transporter expression and activity through isolation and cryopreservation of hepatocytes used *in vitro* could be responsible (133). The issue with applying correction factors to the IVIVE of $CL_{int,T}$ data is that, thus far, the values applied differ between drug, cell system, PBPK model and laboratory. A previous attempt to define an average correction factor for multiple drugs using a SCHH *in vitro* assay was unsuccessful, with a geometric mean and range of 58 and 12-161, respectively (192). Nonetheless, to provide consistency the IVIVE value used in this study was chosen based on a prior PBPK model developed for the prediction of PIT pharmacokinetics (191). An additional PBPK model for PIT also assessed the application of correction factors and found similar values between 10-15 produced optimal simulations (179). It was found that the use of the previously reported correction factor of 18, which was also applied to *in vitro* SPHH data, proved successful in simulating the pharmacokinetics of PIT in this study. This suggests the potential for SPHH assay specific IVIVE correction factors to be developed and applied universally and justifies further investigation with other drugs.

3.4.2 Minimal Rifampicin PBPK Model

A minimal representation of the whole-body PBPK model for the prediction of RIF pharmacokinetics was successfully verified according to the stringent 0.75 – 1.25 ratio and 1 – 1.25 AAFE verification criteria. RIF ADME is complex and the lack of knowledge and data surrounding this topic proves challenging for the application of

whole-body PBPK models. Therefore, the use of 3-compartment PBPK models has been adopted throughout the literature and provides an effective simulation strategy (214-216), as verified in this study. A limitation of this model, which must be considered when analysing the underprediction of PIT C_{max} and the C_{max} DDI_R, is the application of RIF plasma concentration rather than liver concentration for the prediction of the DDI. As described above, the lack of data surrounding the concentration of RIF found in the liver prevents the verification of a more physiologically accurate whole-body PBPK model, which is essential for the confidence in model prediction accuracy. Taking this into consideration, it was concluded that the application of RIF plasma concentrations was suitable for this study.

3.4.3 Conclusion

This study successfully verified a multi-compartment liver PBPK model and minimal inhibitor PBPK model combined with a SPHH *in vitro* assay using OATP1B1 and OATP1B3 probe substrate and inhibitor, PIT and RIF, for the prediction of hepatic transporter-mediated clearance and DDIs. Furthermore, a novel PBPK methodology for determining hepatic passive diffusion was implemented and could provide a sustainable alternative to current *in vitro* strategies. This *in vitro-in silico* framework could be utilised for the investigation of OATP1B1 and OATP1B3 substrates in ARV DDIs, allowing us to gain an imperative insight into the mechanisms involved in these clinically relevant processes.

Chapter 4

Exploring the Role of Transporters in Grazoprevir Drug-Drug Interactions Using a Suspension Primary Human Hepatocyte *In Vitro* Assay and Physiologically-Based Pharmacokinetic Modelling

Contents

4.1 Introduction

HCV is a bloodborne virus that is estimated to effect 6.2% of PLWH worldwide. Of the estimated 2.3 million PLWH coinfected with HCV 84% were PWID (34, 226). There is an increased risk of developing chronic hepatitis in PLWH which could lead to liver-related morbidity and potentially mortality if left untreated (227). Fortunately, since the introduction of DAAs, most HCV infections can be cured with 12 – 24 week oral dose regimens (228). However, treatment of HIV-HCV coinfection must be carefully managed due to the high risk of DDIs associated with ART (229).

GZR is a HCV NS3/4A PI that is co-formulated with elbasvir for the treatment of chronic HCV (genotypes 1, 4 and 6) in adults, particularly difficult to treat adult patients such as those coinfected with HIV (230). GZR is reported to be metabolised by CYP3A4 and transported by OATP1B1, OATP1B3 and P-gp and as a result, its coadministration with several ARV drugs is contraindicated (231). Boosted PIs, such as ATV and DRV coadministered with RTV (ATV/r and DRV/r) are recommended in combination with an optimised NRTI backbone as preferred second-line regimens for PLWH (27). Coadministration of GZR with ATV/r and DRV/r are not recommended due to clinical DDI studies demonstrating geometric mean ratios (with/without) of AUC, C_{max} and C_{min} between 5.27 and 11.64. It has been deduced that according to these DDI studies, alongside further DDI studies with GZR and CYP3A4, OATP1B1, OATP1B3 and P-gp inhibitors, OATP1B1 and OATP1B3 play a significant role in the magnitude of the DDI between GZR, ATV/r and DRV/r (231). However, due to the unspecific nature of the inhibitors used in the DDI studies alongside the lack of *in vitro* data, the precise contribution of OATP1B1 and OATP1B3 to the overall DDI magnitude is unknown.

Strategies incorporating both *in vitro* and *in silico* techniques can be utilised alongside observed clinical data for the investigation of the mechanisms underpinning DDIs. By delineating the involvement of each pathway in the overall magnitude of DDI we can improve our understanding of their functionality and interplay with one another. This is of particular importance with transporters considering our current deficit of knowledge. Moreover, these practices allow us to verify the *in vitro* and *in silico* techniques we apply for the prediction of unknown DDI scenarios, which is an

integral step towards building reliable systems and identifying research objectives for their refinement.

The aim of this study was to utilise the *in vitro-in silico* framework developed and verified in Chapter 2 and 3 to elucidate the role of OATP1B1 and OATP1B3 in the DDI between GZR and ATV, DRV and RTV. Furthermore, this study aimed to verify the SPHH specific IVIVE correction factor identified in Chapter 2 and 3 to generate a rationale for correction factor application in the *in vitro* assessment of transporters. This data will help provide key information on our understanding of transporter-mediated clearance and DDIs and evaluate the application of the *in vitro-in silico* framework in a clinically relevant ARV DDI scenario.

4.2 Methods

4.2.1 Materials

Materials used for the $CL_{int,T}$, DDI and toxicity *in vitro* studies were previously described in Chapter 2. Additionally, GZR (96% purity; catalog no. M424985) was purchased from 2BScientific (Oxfordshire, UK) and ATV (≥98% purity; catalog no. SML1796), DRV (≥98% purity; catalog no. SML0937) and RTV (≥98% purity; catalog no. SML0491) were purchased from Sigma-Aldrich (Poole, UK). Pooled donor cryopreserved SPHHs with lot no. HUE120 (catalog no. HMCS10; Thermo Fisher Scientific, Hemel Hempstead, UK) were used as detailed in Chapter 2, Method section 2.2.2. Likewise, a summary of donor characteristics can be found in Chapter 2, Table 2.1.

4.2.2 Grazoprevir $CL_{int,T}$ and Protease Inhibitor DDI *In Vitro* Assay

The $CL_{int,T}$ and DDI *in vitro* assay was previously described in detail in Chapter 2, Method section 2.2.3. To obtain a comprehensive pharmacokinetic profile the GZR DDIs with ATV, DRV and RTV were assessed individually as well as ATV and DRV in their boosted form with RTV, thereby replicating the clinically relevant DDI scenario. GZR, ATV/r and DRV/r assays were carried out in duplicate with a single replicate of the ATV, DRV and RTV assays, all of which had 4 technical replicates per condition and were designed based on the assumption that two assays could be carried out per vial of cryopreserved SPHHs. PIT and the DDI between PIT and RIF were utilised as experimental controls owing to their successful verification of the *in vitro* assay in Chapter 2.

Briefly, DMSO 100% (vol/vol) stock solutions were freshly prepared the day before the experiment with KHB (pH 7.4) stock solutions containing 3% (vol/vol) DMSO being prepared the day of the experiment. The concentrations for each drug in the DMSO stock solution, KHB stock solution and the final cell culture plate well conditions are outlined in Table 4.1. Concentration ranges for each drug were established based on their solubility in KHB and were tested prior to the *in vitro* assays. To note, a 1:1 ratio for well conditions containing ATV/r and DRV/r was applied. Concentrations of the control drugs were selected to clearly demonstrate transporter-

uptake and inhibition in the SPHHs. Additionally, in the $CL_{int,T}$ assay where only GZR was present in each well, KHB containing 3% (vol/vol) DMSO was prepared as an inhibitor substitute to maintain the final DMSO concentration of 1% (vol/vol). Furthermore, SPHHs were prepared so that the final incubation solution suspension equalled 1×10^5 cells/well. Any remaining SPHHs were used as the matrix for verification and calibrator samples during LC-MS/MS analysis. A schematic representation and description of the experimental protocol can be found in Figure 4.1.

Table 4.1 Drug stock solution and final well condition concentrations.

Drug	DMSO Stock (µM)	KHB Stock (µM)	Well Condition (µM)
GZR	6.6 – 20000	0.198 – 600	0.033 – 100
ATV	1.32 – 4000	0.0198 – 60	0.0033 – 10
DRV	4 – 13200	0.06 – 198	0.01 – 33
RTV	4 – 13200	0.06 – 198	0.01 – 33
ATV/r	1.32 – 4000	0.0198 – 60	0.0033 – 10
DRV/r	4 – 13200	0.06 – 198	0.01 – 33
PIT*	20	0.6	0.1
RIF*	2000	60	10

DMSO and KHB stock solutions were prepared using serial dilutions. Stock solutions were prepared so that the final well conditions consisted of a constant DMSO concentration of 1% (vol/vol). A 1:1 ratio for well conditions containing ATV/r and DRV/r was applied. DMSO – dimethyl sulfoxide, KHB – Krebs-Henseleit buffer (pH 7.4), GZR – grazoprevir, ATV – atazanavir, DRV – darunavir, RTV – ritonavir, ATV/r – atazanavir and ritonavir, DRV/r – darunavir with ritonavir, PIT – pitavastatin, RIF – rifampicin, * - control drugs.

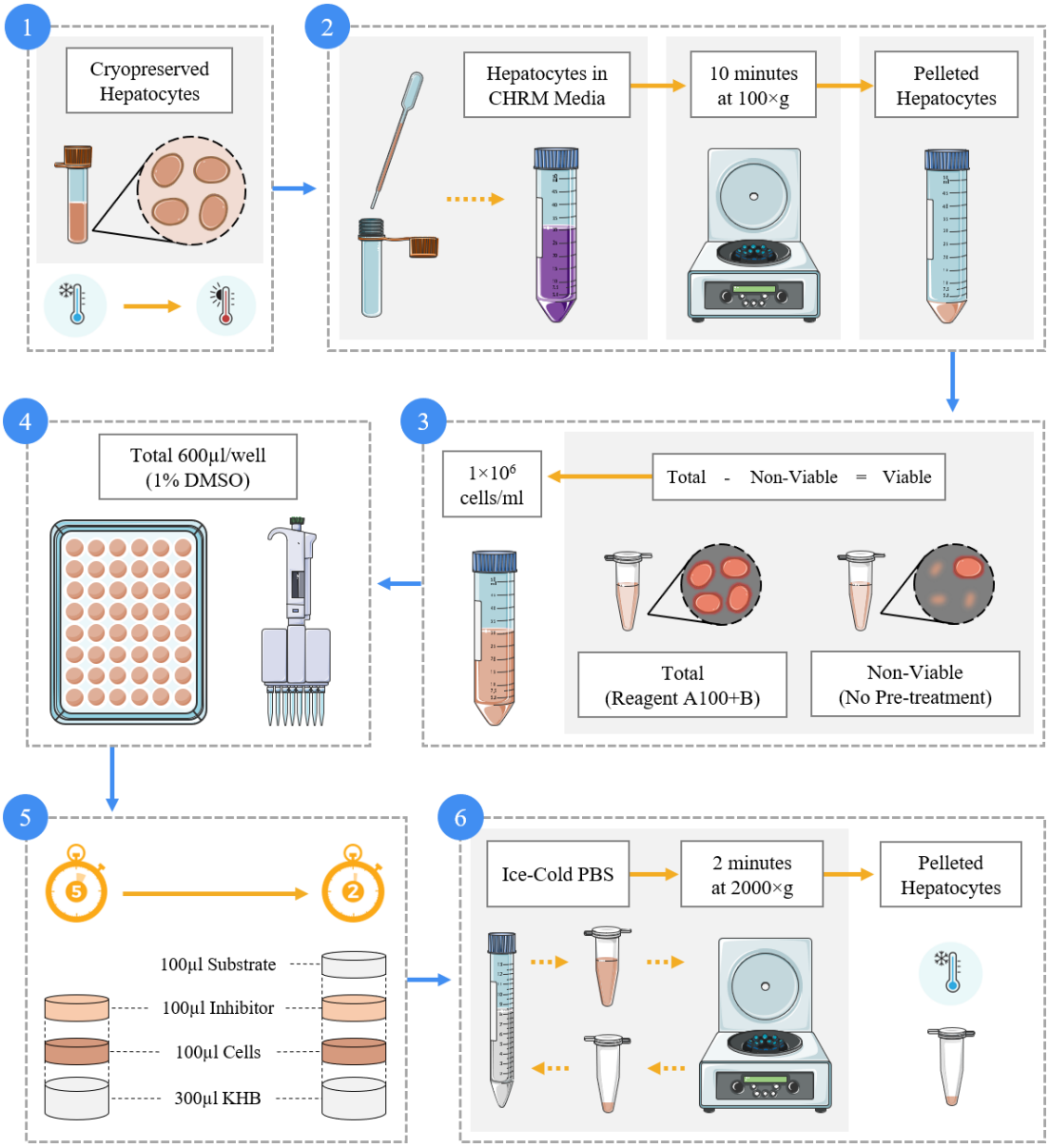

Figure 4.1 Schematic diagram detailing the protocol for the SPHH $CL_{int,T}$ and DDI transporter assay. Step 1 – thaw cryopreserved SPHHs in a 37°C water bath for 2 minutes; Step 2 - using a wide-bore pipette tip, slowly transfer thawed SPHHs into pre-warmed CHRM media (37°C) and centrifuge at room temperature at 100 × g for 10 minutes before removing the CHRM media supernatant; Step 3 – resuspend pelleted SPHHs in 8ml of pre-warmed KHB (pH 7.4; 37°C) and, using a nucleocounter alongside reagent A100 and B, count the total and non-viable cells to determine the viable cells and adjust the concentration of SPHHs to 1×10^6 cells/ml; Step 4 – aliquot cells, KHB and pre-prepared inhibitor stock solutions into their corresponding wells; Step 5 – incubate for 5 minutes before initiating assays with the addition of pre-prepared substrate stock solutions and incubating for 2 minutes at 37°C on a plate

shaker at 150 rpm; Step 6 – terminate assay incubations with the addition of 600 µl ice-cold PBS and transfer well solutions to microcentrifuge tubes before centrifuging at 2000 × g for 2 minutes at 4°C followed by the removal of the supernatant and again, add 600 µl ice-cold PBS and repeat centrifugation and removal process before storing the pelleted SPHHs at -80°C.

4.2.3 LC-MS/MS Quantification

GZR quantification was carried out on a TSQ Endura LC-MS/MS (Thermo Scientific, Hemel Hempstead, UK) using the Thermo Xcalibur Roadmap (version 4.0.27.42), Chromeleon Xpress and TSQ Endura Tune Application (version 2.0.1292.15) software. GZR 1 mg/ml stock solutions in 100% (vol/vol) LC-MS/MS grade methanol were freshly made every 2 weeks and stored at 4°C for use in LC-MS/MS analysis.

4.2.3.1 Mass Spectrometer Optimisation

GZR 500 ng/ml solution in 50% (vol/vol) ACN_L in dH_2O was directly infused into the mass spectrometer using heated electron spray ionisation in positive mode for the optimisation of ion spray voltage, sheath gas, auxiliary gas, ion transfer tube temperature and vaporiser temperature. Ionised analytes and their fragments were detected using SRM scanning.

4.2.3.2 Chromatographic Separation

Chromatographic separation of GZR was carried out using an Accucore C18 (100 x 2.1mm) LC-MS/MS column fitted with an Accucore C18 pre-column (10 x 2.1mm). A multi-step gradient method consisting of two mobile phases was developed using GZR 500 ng/ml solution in 50% (vol/vol) ACN_L in dH_2O aliquoted into Chromacol fixed insert vials to obtain an efficient and effective separation of GZR.

4.2.3.3 Sample Preparation

Samples were prepared as described in Chapter 2, Method section 2.2.4.3, excluding the use of the IS. For the $CL_{int,T}$ assay samples, one replicate per condition was quantified prior to the analysis of all remaining samples to determine appropriate

dilution ratios for the analysis of GZR concentrations within the LC-MS/MS calibration curve range. GZR 10 – 100 µM well conditions were diluted with a 1:10 ratio whilst all unknown samples were diluted with a 1:2 ratio in 50% (vol/vol) ACN_L in dH_2O. All GZR calibrator and blank samples were prepared in accordance with the FDA guidelines (141).

4.2.3.4 Assay Verification

The LC-MS/MS method for the quantification of GZR was verified considering the calibration curve, quality controls, selectivity, carryover, sensitivity, accuracy, precision and carryover. Guidelines adapted from the FDA for method verification and in-study analysis verification were described in detail in Chapter 2, Table 2.2, and were applied herein (141).

4.2.4 *In Vitro* Assay Data Analysis

The $CL_{int,T}$ and DDI *in vitro* assay data quantified using the GZR LC-MS/MS method were processed using Prism v8 software (GraphPad Software Inc., La Jolla, CA, USA). Michaelis Menten non-linear regression analysis was applied to the GZR (0.033-100 µM) $CL_{int,T}$ assay data to derive the V_{max} (µmole/10^6cells/minute) and K_m (µM) whilst a log(inhibitor concentration) vs. response equation and a least-squares fitting method was applied to the DDI assay data to calculate the IC_{50}. $CL_{int,T}$ and the percentage inhibition of GZR by the inhibitors was calculated as previously described in Chapter 2, Method section 2.2.5. Furthermore, a D'Agostino & Pearson test was used to assess the normality of all datasets.

4.2.5 Grazoprevir I*n Silico* Assessment using PBPK Modelling

The GZR *in vitro* $CL_{int,T}$ data was integrated into the PBPK model (Simbiology v5.8, a product of Matlab 2018a; MathWorks, Natick, MA, USA; 2018) described in detail in Chapter 3, Method section 3.2.1, to simulate GZR pharmacokinetics. All equations were applied as previously outlined, except for the olive oil:buffer partition coefficient of nonionised and ionised species at pH 7.4 ($D^*_{vo:w}$) which was calculated using Equation 1 and further transformed from the logarithmic form to the inverse log form for model implementation (213). The logarithmic value of the dissociation constant for acid and base are pK_a1 and pK_a2, respectively.

$$\text{Zwitterionic: } LogD^{*}_{vo:w} = LogD_{vo:w} - Log(1 + 10^{-pKa2 + pH + pKa1 - pH}) \quad (1)$$

A virtual cohort of 100 male and female patients aged 18 – 60 years were simulated with physicochemical and pharmacokinetic data for GZR being sourced from the literature or via curve fitting when data were unavailable or inadequate. A summary of the physicochemical and *in vitro* data utilised in the GZR PBPK model can be found in Table 4.2. Clinically observed pharmacokinetic data and concentration time profile for GZR 200mg QD (96) were utilised for PBPK model verification, with data being extracted from graphs when necessary using the Plot Digitizer Tool (plotdigitizer.sourceforge.net). Verification was carried out as described in Chapter 3, Method section 3.2.3, with both the stringent 0.75 – 1.25 ratio and 1 – 1.25 AAFE criteria (220) as well as the widely recognised 0.5 – 2 ratio and 1 – 2 AAFE (150) criteria being employed.

Table 4.2 Physicochemical and *in vitro* data for GZR.

Parameter	GZR
Molecular Weight (g/mol)	766.903 (232)
HBD	0.012 (232)
Log $P_{O:W}$	4.7 (233)
pK_a (Strongest Acidic)	3.77 (232)
pK_a (Strongest Basic)	1.79 (232)
Protein Binding (%)	98.8 (232)
PSA ($Å^2$)	205.69 (232)
R	0.7 (234)
V_{ss} (L)	1250 (101)
F (%)	27 (101)

Water Solubility (mg/L)	0.0097 (232)
$CL_{int,T}$ (µL/minute/10^6 cells)	E
$CL_{int,T}$ IVIVE Correction Factor	18 (191)
$CL_{int,CYP3A4}$ (%)	20 (231)

Reference for literature values presented in brackets. GZR – grazoprevir, HBD – Hydrogen bond donor, Log $P_{O:W}$ - Partition coefficient between octanol and water, pK_a - logarithmic value of the dissociation constant, PSA – polar surface area, R – blood-to-plasma drug ratio, V_{ss} – volume of distribution, F – bioavailability, $CL_{,int,T}$ – total hepatic transporter intrinsic clearance, IVIVE – in vitro in vivo extrapolation, $CL_{int,CYP}$ – Cytochrome P450 enzyme intrinsic clearance, E – experimentally determined *in vitro*.

4.3 Results

4.3.1 LC-MS/MS Method Development and Verification

The GZR LC-MS/MS method was successfully developed and verified as described in Method section 4.2.3.4 with each verification parameter detailed below.

4.3.1.1 Mass Spectrometer Optimisation

The MS parameters were optimised for the maximum detection of GZR. A summary of the finalised MS parameters can be found in Table 4.3, including the product and precursor ions used for the detection of GZR.

Table 4.3 Optimised MS parameters.

Parameter	Setting
Ion Spray Voltage (V)	Positive 4000
Sheath Gas (arb)	50
Auxiliary Gas (arb)	9
Ion Transfer Tube Temperature (°C)	350
Vaporiser Temperature (°C)	350
Precursor Ion (m/z)	767.34
Product Ions (m/z)	189.04, 191.111, 285.151, 326.103, 489.262, 537.347, 646.405, 739.458
Parameters optimised using grazoprevir 500ng/ml stock solutions in 50% (vol/vol) ACN_L in dH_2O. V – voltage, arb – arbitrary unit, °C – Celsius, m/z - mass-to-charge ratio.	

4.3.1.2 Chromatographic Separation

A multi-step mobile phase gradient was optimised for the separation of GZR and is summarised in Table 4.4. GZR was separated using two mobile phases over 6 minutes with a flow rate of 300 µl/min and an average retention time of 3.61 minutes. Mobile phase A consisted of 100% H_2O_L with 0.5% FA_L and mobile phase B consisted of 100% ACN_L with 0.5% FA_L. Example chromatograms of 10 µl injections of 500 ng/ml GZR and blank stock solutions in 50% (vol/vol) ACN_L in dH_2O are shown in Figure 4.2.

Table 4.4 Chromatographic separation method.

Time (minutes)	Mobile Phase A (%)	Mobile Phase B (%)
0	95	5
0.1	95	5
0.3	10	90
4.1	5	95
5	5	95
5	95	5
6	95	5
Mobile phase A consisted of 100% H_2O_L with 0.5% FA_L and mobile phase B consisted of 100% ACN_L with 0.5% FA_L with a flow rate of 300 µl/ml and 10 µl analyte injections.		

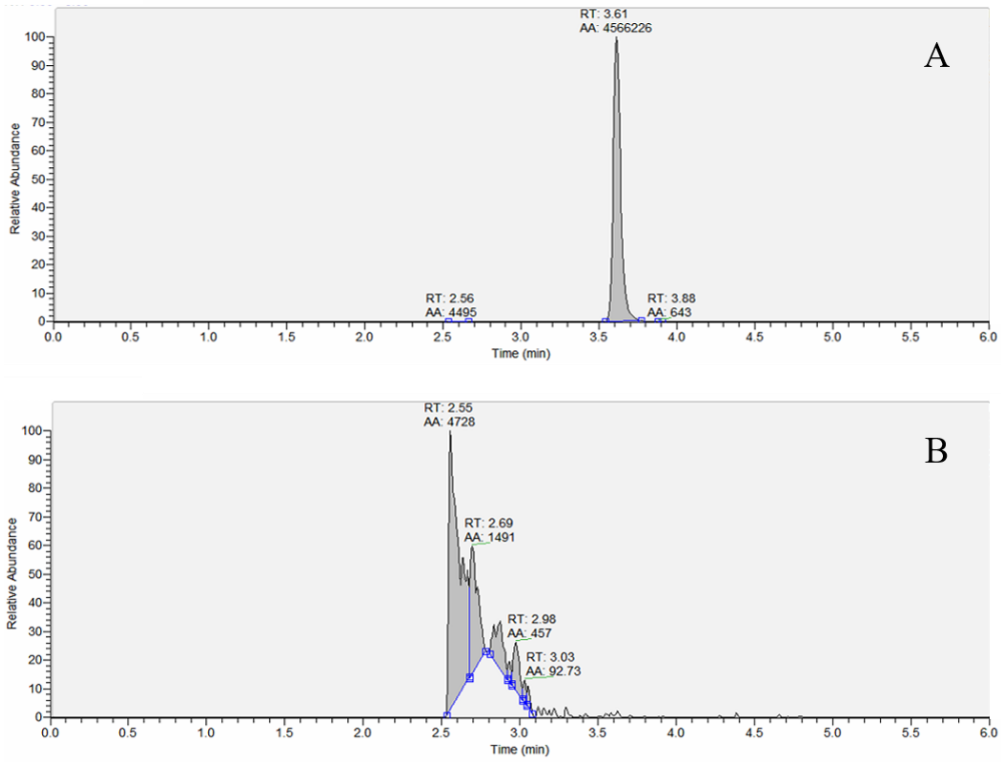

Figure 4.2 Chromatographic separation of GZR and blank stock solution using the optimised MS parameters and mobile phase gradient method. Chromatogram A shows the peak produced by a 10 µl injection of 500 ng/ml GZR solution in 50% (vol/vol) ACN_L in dH_2O. Chromatogram B shows the peak produced by a 10 µl injection of blank solution in 50% (vol/vol) ACN_L in dH_2O for GZR. The grey shaded areas represent peaks detected and processed by the Thermo Xcalibur Roadmap software, with RT and peak area (automatic integration; AA) being displayed for each detected peak.

4.3.1.3 Calibration Curve

A calibration curve with a concentration range of 1.95 – 500 ng/ml was chosen, with 1.95 ng/ml being established as the LLOQ. The LC-MS/MS method met the calibration curve verification criteria with two verification runs obtaining 100% of calibrators and one verification run obtaining 88.89% of calibrators within ±15% (non-zero calibrators) and ±20% (LLOQ calibrator) of their nominal concentrations. R^2 values of 0.9964 – 0.9998 were achieved by applying a quadratic equation with 1/X weighting and demonstrated good linearity of the LC-MS/MS method. In accordance

with the verification criteria, this regression model was found to be the simplest model that best described the signal response to calibrator concentration relationship.

4.3.1.4 Quality Controls

The LLOQ, low (L), medium (M) and high (H) QC levels were selected as 1.95 ng/ml, 5 ng/ml, 100 ng/ml and 400 ng/ml, respectively. In total, verification run one, two and three produced 93.33%, 86.67% and 66.67% of QC levels within ±15% (M and H QC) and ±20% (LLOQ and L QC) of their nominal concentrations.

4.3.1.5 Carryover

The blank sample following the 500 ng/ml calibrator was compared to the LLOQ calibrator to evaluate the effect of carryover on sample analysis. In all verification runs the blank was less than 1% of the LLOQ, satisfying the verification criteria.

4.3.1.6 Sensitivity and Selectivity

To assess sensitivity, the concentration of GZR in a blank sample was compared to the concentration of GZR in the LLOQ calibrator, with the LLOQ being at least 5 times greater in all three verification runs. Additionally, blank and zero calibrators with a SPHH (lot. HUE120) matrix were free from interference at GZR's RT, as shown in Figure 4.2, demonstrating suitable selectivity of the LC-MS/MS method.

4.3.1.7 Accuracy and Precision

Accuracy and precision were assessed within and between verification runs for LLOQ, L QC, M QC and H QC calibrators. Inter-assay and intra-assay accuracy and precision variance for all calibrators were within ±15% of their nominal values as show in Table 4.5 and 4.6, respectively.

4.3.1.8 Recovery

The recovery of GZR across 1 ng/ml, 50 ng/ml and 500 ng/ml concentrations were 104.94%, 101.85% and 110.78% producing a mean recovery and standard deviation of 105.86 ± 3.7%, achieving the verification criteria.

Table 4.5 Summary of LC-MS/MS intra-assay accuracy and precision.

Nominal Concentration (ng/ml)	Verification Run 1		Verification Run 2		Verification Run 3	
	Variance of Accuracy (%)	Variance of Precision (%)	Variance of Accuracy (%)	Variance of Precision (%)	Variance of Accuracy (%)	Variance of Precision (%)
1.95 (LLOQ)	0.40	0.94	1.61	3.53	2.12	4.74
5 (L QC)	2.18	5.13	2.37	5.23	3.13	6.44
100 (M QC)	1.85	4.57	1.47	3.68	3.94	7.15
400 (H QC)	1.13	2.59	3.20	6.87	1.57	2.78
Data points that failed to meet the acceptance criteria were excluded. LLOQ – lower limit of quantification, QC – quality control, L – low range, M – mid range, H – high range.						

Table 4.6 Summary of LC-MS/MS inter-assay accuracy and precision.

Nominal Concentration (ng/ml)	Variance of Accuracy (%)	Variance of Precision (%)
1.95 (LLOQ)	1.17	4.57
5 (L QC)	2.00	7.60
100 (M QC)	1.44	5.67
400 (H QC)	1.38	4.95
Data points that failed to meet the acceptance criteria were excluded. LLOQ – lower limit of quantification, QC – quality control, L – low range, M – mid range, H – high range.		

4.3.2 $CL_{int,T}$ Primary Human Hepatocyte *In Vitro* Assay

4.3.2.1 LC/MS-MS Quantification

The LC-MS/MS method was successfully applied for the quantification of GZR with assay samples being analysed across eight LC-MS/MS analysis runs. Seven of the LC-MS/MS analysis runs passed the in-study analysis verification criteria. One analysis run passed the in-study criteria albeit with one exception; one of the QC concentration levels had 33% of calibrators attaining ±15% of their nominal values rather than the required 50%, with one calibrator being marginally below the criteria.

4.3.2.2 Toxicity Study

The GZR, ATV, DRV, RTV, ATV/r and DRV/r drug concentrations used in the $CL_{int,T}$ and DDI assays were deemed non-toxic as the cell viability had decreased 1.25%, 0.73%, 2.94%, 7.68% 15.39% and 10.6% in comparison to the cell viability calculated during the preparation of the cryopreserved SPHHs, respectively.

4.3.2.3 $CL_{int,T}$ of Grazoprevir and DDI with Protease Inhibitors

A summary of the $CL_{int,T}$ *in vitro* assay data can be found in Table 4.7 with the uptake kinetic profile of GZR being shown in Figure 4.3. V_{max} and K_m were calculated

using Prism v8 software (GraphPad Software Inc., La Jolla, CA, USA) and $CL_{int,T}$ was calculated by dividing V_{max} by K_m. The DDI *in vitro* assay is summarised in Table 4.8 with Figures 4.4 – 4.8 detailing the concentration-dependent inhibition of GZR by ATV, ATV/r, DRV, DRV/r and RTV, respectively. Due to the irregularity of the DDI between GZR, ATV and DRV, the IC_{50} and maximal percent inhibition was not calculated. All data sets were tested for normality using the D'Agostino & Pearson test. Excluding the dataset for the DDI between GZR and ATV/r which had a p-value of 0.0422, all datasets passed the normality test with p-values between 0.0583 – 0.9832.

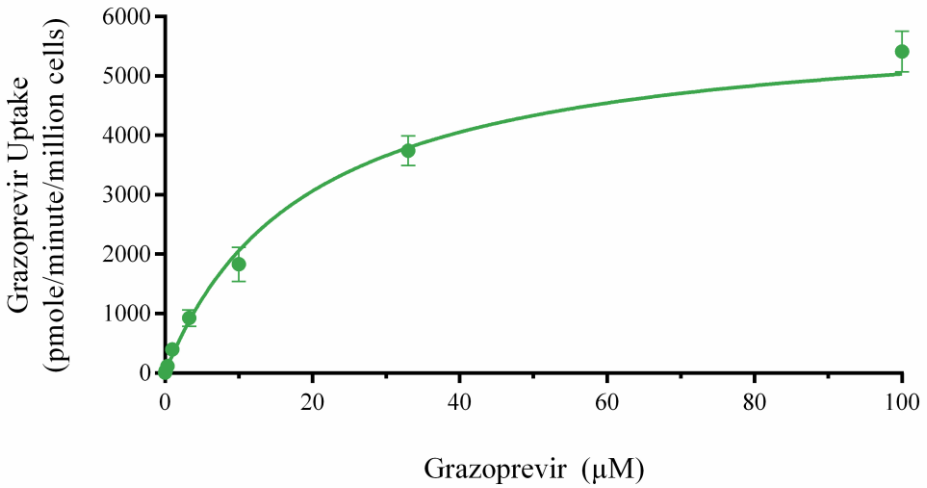

Figure 4.3 Total uptake kinetic profile of GZR (0.033 – 100 µM) measured in the lot. HUE120 SPHHs. The green line and error bars represent the mean total GZR uptake ± SD (pmole/minute/10^6 cells) of two experimental replicates with four technical replicates.

Table 4.7 Summary of the GZR $CL_{int,T}$ *in vitro* assay.

GZR Parameter	Lot. HUE120
V_{max} (µmole/minute/10^6 cells)	5999 ± 220.63
K_m (µM)	23.54 ± 2.43
$CL_{int,T}$ (µl/minute/10^6 cells)	254.84 ± 90.83
Data presented as the mean ± SD of two experimental replicates with three or four technical replicates as described in method section 4.2.3.3. GZR – grazoprevir, V_{max} – maximum uptake velocity, K_m – half maximum velocity concentration, $CL_{int,T}$ – hepatic intrinsic clearance, SD – standard deviation.	

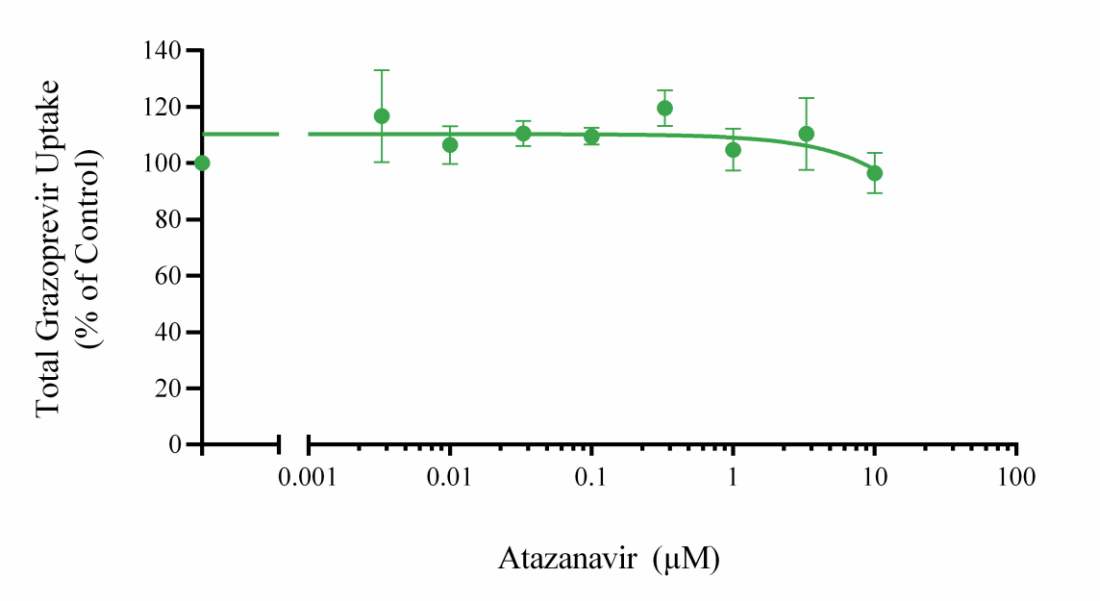

Figure 4.4 Concentration-dependent inhibition of total GZR (0.1 µM) uptake by ATV (0.0033 – 10 µM) measured in the lot. HUE120 SPHHs. The green line and error bars represent the mean inhibited total GZR uptake ± SD (% of control) of two experimental replicates with four technical replicates.

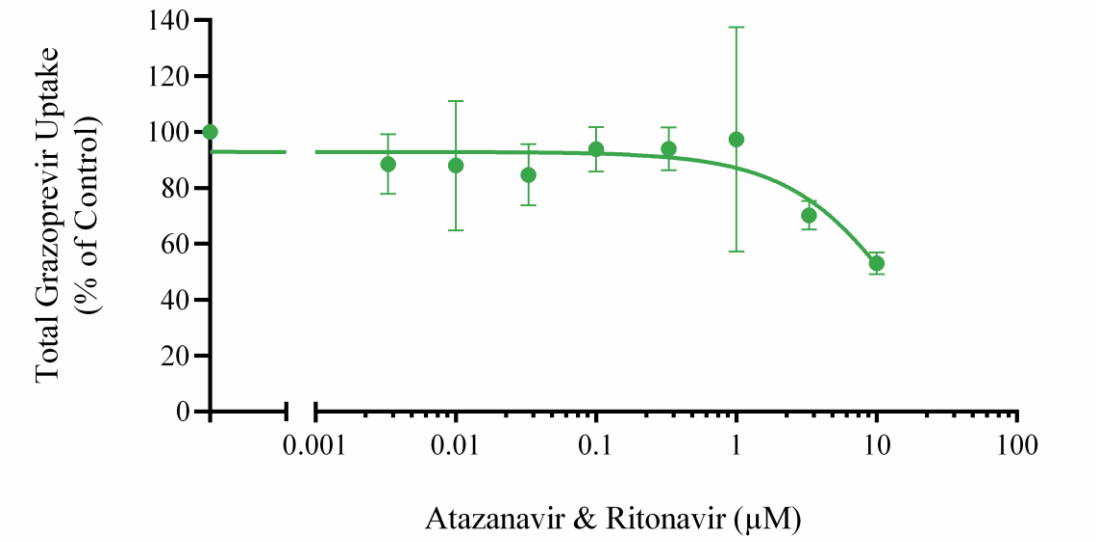

Figure 4.5 Concentration-dependent inhibition of total GZR (0.1 µM) uptake by ATV/r (1:1 ATV:RTV; 0.0033 – 10 µM) measured in the lot. HUE120 SPHHs. The green line and error bars represent the mean inhibited total GZR uptake ± SD (% of control) of two experimental replicates with four technical replicates.

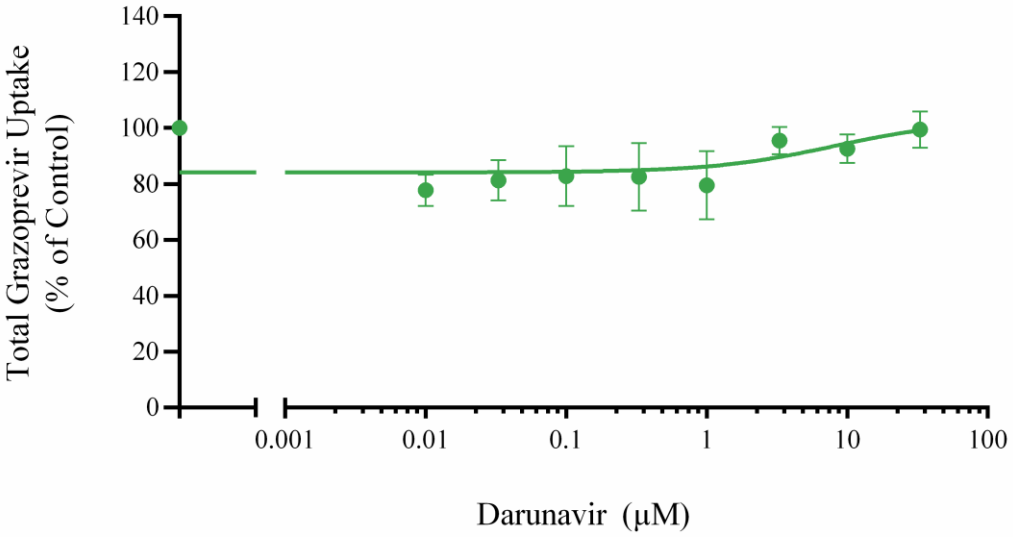

Figure 4.6 Concentration-dependent inhibition of total GZR (0.1 µM) uptake by DRV (0.01 – 33 µM) measured in the lot. HUE120 SPHHs. The green line and error bars represent the mean inhibited total GZR uptake ± SD (% of control) of two experimental replicates with four technical replicates.

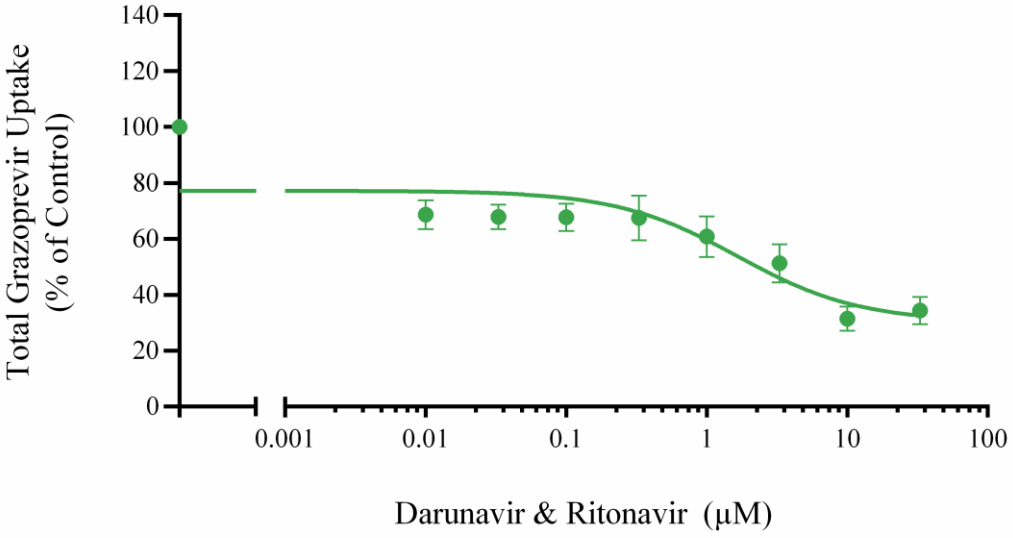

Figure 4.7 Concentration-dependent inhibition of total GZR (0.1 µM) uptake by DRV/r (1:1 DRV:RTV; 0.01 – 33 µM) measured in the lot. HUE120 SPHHs. The green line and error bars represent the mean inhibited total GZR uptake ± SD (% of control) of two experimental replicates with four technical replicates.

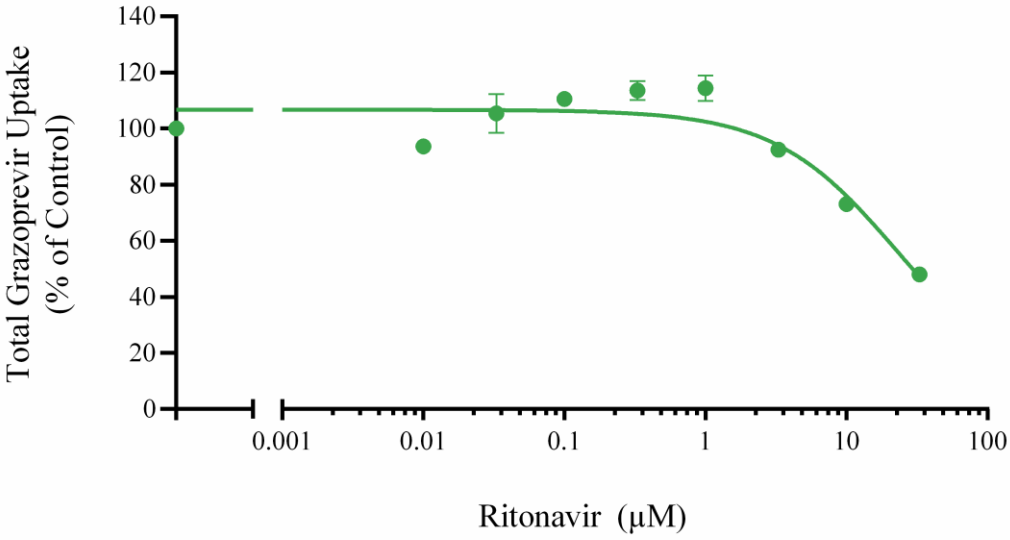

Figure 4.8 Concentration-dependent inhibition of total GZR (0.1 µM) uptake by RTV (0.01 – 33 µM) measured in the lot. HUE120 SPHHs. The green line and error bars represent the mean inhibited total GZR uptake ± SD (% of control) of two experimental replicates with four technical replicates.

Table 4.8 Summary of the DDI *in vitro* assay with GZR, ATV, DRV and RTV.

GZR Parameter	IC_{50} (µM)	Maximal Inhibition (%)
ATV	NC	NC
ATV/r	20.76	46.98
DRV	NC	NC
DRV/r	1.66	68.56
RTV	22.89	52.01

Data calculated from two experimental replicates with four technical replicates. GZR – grazoprevir, ATV – atazanavir, ATV/r – atazanavir with ritonavir, DRV – darunavir, DRV/r – darunavir with ritonavir, RTV – ritonavir, IC_{50} - half maximal inhibitory concentration, SD – standard deviation, NC – not calculated due to unsuitable data.

4.3.3 Grazoprevir PBPK model

The PBPK model was successfully verified for the simulation of steady state GZR 200mg QD. Ratio and AAFE values for C_{min}, T_{max}, bioavailability and the concentration-time profile were within the stringent 0.75 – 1.25 and 1 – 1.25 verification criteria, respectively. AUC and C_{max} achieved the 0.5 – 2 ratio and 1 – 2 AAFE criteria. A summary of the predicted vs. observed pharmacokinetic data and the concentration-time profile are shown in Table 4.9 and Figure 4.9, respectively. The GZR $CL_{int,T}$ determined *in vitro* was successfully implemented into the multi-compartment liver model with the application of the IVIVE correction factor and active and passive percent contribution values verified in Chapter 3. However, due to the unsuitable nature of the *in vitro* GZR DDI data, the PBPK model was not developed or verified for the simulation of the DDI between GZR, ATV/r and DRV/r.

During model development, five parameters were optimised via curve fitting to achieve the most accurate simulations of GZR pharmacokinetics. Firstly, a correction factor of 0.4 was applied to the V_{ss}. Secondly, due to the lack of data surrounding GZR metabolism and biliary excretion, these parameters were optimised alongside the pharmacokinetic profile to achieve 20% metabolism mediated by CYP3A4, as specified in the literature (231). A value of 0.26 µl/min/pmol was estimated for CYP3A4 intrinsic clearance ($CL_{int,CYP3A4}$) with $CL_{biliary}$ being estimated as 0.004 ml/min/kg. Thirdly, the equation for P_{eff} was unable to capture the absorption of GZR and so this parameter was estimated to be 0.001 cm/s. Lastly, alongside P_{eff} optimisation, fasted rather than fed intestinal transit rates were applied in the PBPK model to achieve an accurate absorption profile, contrary to the GZR clinical study which administered GZR to participants after a moderate-fat breakfast.

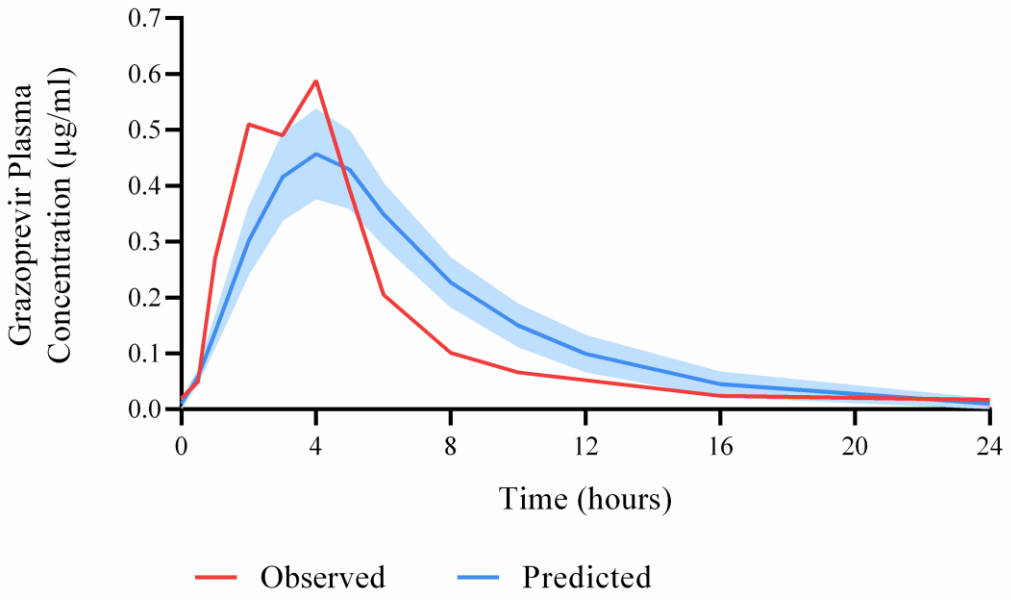

Figure 4.9 Predicted vs. observed concentration time profiles for steady state GZR 200mg QD. The blue line and shaded area represent the mean plasma concentration ± SD (µg/ml) of the predicted data. The red line represents the observed clinical data (µg/ml) (96).

Table 4.9 Predicted vs. observed pharmacokinetic parameters, ratio and AAFE values for steady state GZR 200mg QD.

Parameter	Predicted	Observed (96)	Ratio	AAFE
AUC (µg/h/ml)	3.58 ± 0.62	2.54	1.41	1.41
C_{max} (µg/ml)	0.46 ± 0.08	0.63	0.73	1.37
C_{min} (µg/ml)	0.01 ± 0.008	0.012	0.83	1.20
T_{max} (h)	4	3	1.33	1.33
F (%)	24.13	27 (101)	0.89	1.12
Profile	-	-	-	1.08

Reference for observed values presented in brackets. Observed values for AUC, C_{max} and C_{min} presented as mean ± SD. Observed values for T_{max} and F presented as the mean. Observed AUC is AUC_{0-24}. Predicted values presented as the mean (SD not provided). Predicted AUC is $AUC_{0-\infty}$. Predicted values converted from µM/h (AUC) and µM (C_{max} and C_{min}) to µg/h/ml and µg/ml, respectively. Ratio and AAFE values calculated as described in Chapter 3, Method section 3.2.3. AUC – area under the curve, C_{max} – maximum plasma concentration, C_{min} – minimum plasma concentration, T_{max} – time taken to reach maximum concentration, F – bioavailability, Profile – concentration time profile.

4.4 Discussion

The clinical management of PLWH requires a comprehensive knowledge of multiple disease areas, special populations and polypharmacy, specifically how co-medicated drugs interact with one another. Unlike enzyme-mediated DDIs our knowledge of transporter-mediated DDIs is lacking, generating research initiatives to fulfil the demand for further evidence-based guidance. Currently, there is a paucity of transporter specific substrates, inhibitors and inducers available for the assessment of DDIs *in vitro* and *in vivo* (235). As a result, an array of DDI combinations are studied in clinical trials to determine any significant interactions, with the mechanisms of action being surmised as a secondary objective. In this study the *in vitro-in silico* framework developed and verified in Chapter 2 and 3 was used to explore the role of transporters in the DDI between GZR, ATV/r and DRV/r and further our understanding of their mechanisms of action. Additionally, we evaluated the capabilities of the framework and an SPHH specific IVIVE correction factor in a clinically relevant scenario involving ARV drugs.

4.4.1 LC-MS/MS Quantification

The verification criteria adapted from the FDA guidelines were applied successfully for the verification of the GZR LC-MS/MS method. Both GZR stability and the effect of dilution were not assessed in this study as they had previously been evaluated and were in accordance with the methodology applied herein (236, 237). Additionally, an IS was not applied as the accuracy and precision of the developed method proved adequate without the use of an IS. Unlike the method verification, one of the eight in-study analysis's verification presented one exception to the criteria. As previously described, one QC level had 33% of calibrators, rather than 50%, achieving the criteria. However, this was due to a single QC level replicate being ±20.96% of their nominal value rather than ±15%. As all other criteria were attained and the availability of sample was limited, the impact was deemed insignificant and the data from the assay was used in this study.

4.4.2 *In Vitro* Assessment of $CL_{int,T}$ and DDI

The $CL_{int,T}$ assay demonstrated the uptake of GZR into the SPHHs, however the DDI assay data for ATV and DRV appeared to be irregular based on previous assumptions made in the literature (231). According to previous DDI studies the magnitude of interaction between GZR, ATV/r and DRV/r is substantial and has been assumed to be predominantly caused by the inhibition of OATP1B1 and OATP1B3. It was therefore predicted that the *in vitro* assay would result in a low IC_{50} value and a high maximal percent inhibition of GZR by ATV and DRV. Yet, the data produced herein demonstrated little to no inhibition of GZR by ATV and DRV, even at high concentrations, and only under ATV/r and DRV/r conditions could an IC_{50} be calculated. The data for the DDI assay involving ATV/r was also found not to be normal according to the D'Agostino & Pearson test, whereas all other datasets were normal. The test results for normality were however only marginally outside of the criteria for normal data. Conversely, the data produced from the DDI assay between GZR and RTV was as expected based on the literature (96), with no inhibition of OATP1B1 or OATP1B3 expected at physiologically relevant concentrations. RTV demonstrated up to 50% maximal inhibition of GZR uptake at higher RTV concentrations, showing that the mechanism involved in GZR uptake into hepatocytes can be inhibited in this *in vitro* assay system. Moreover, the PIT and RIF controls applied in the *in vitro* assays showed uptake of PIT and inhibition of PIT uptake by RIF demonstrating suitable functionality of the SPHHs. Additionally, the toxicity study demonstrated minimal impact of any of the drugs or drug combinations on cell viability.

There are two rational explanations for this phenomenon. Firstly, and potentially more likely, the results obtained for the DDI between GZR, ATV(/r) and DRV(/r) are false negatives. False negative results can occur in cell-based *in vitro* assays because of the passive permeability or solubility properties of a drug and are considered limitations of these systems (238). Based on these two elements, GZR as well as ATV and DRV could have produced a false negative result. Recombinant cell line *in vitro* studies showed similar uptake of GZR (1 µM) in both MDCKII cells stably transfected with OATP1B1 and control MDCKII cells, suggesting a high passive diffusion of GZR into the cells. In contrast, the uptake of GZR in MDCKII cells stably transfected with OATP1B3 was much greater than in control MDCKII cells,

suggesting a lower passive diffusion (231). As described in the Chapter 2 discussion section, passive diffusion is established through PBPK modelling in this *in vitro-in silico* framework rather than through temperature driven *in vitro* studies, and so the contribution of passive diffusion to the $CL_{int,T}$ determined herein cannot be concluded. Furthermore, both ATV (239) and DRV (240) are lipophilic drugs and during the DDI *in vitro* assay it was found that maximum concentrations of 10 µM and 33 µM could be solubilised in 1% DMSO in KHB solution, respectively. The lipophilic properties of ATV and DRV could of resulted in non-specific binding, producing lower than expected concentrations during the assay and potentially producing a false negative result (241). Although, it must be taken into consideration that RTV is also a lipophilic drug and the results for its DDI study were as anticipated (242).

Secondly, an alternative mechanism besides the inhibition of OATP1B1 and OATP1B3 could be the predominant cause of the DDI found between GZR, ATV/r and DRV/r. Clinical DDI study data provided in the Clinical Pharmacology and Biopharmaceutics Review for Zepatier (GZR and elbasvir brand name) can be found in Table 4.10 (231). The inhibitory profiles of ATV, DRV and RTV as well as those present in further DDI clinical studies are shown in Table 4.11. GZR has been described as a substrate of CYP3A4, OATP1B1, OATP1B3, P-gp and potentially BCRP (231) and the data presented in Tables 4.10 and 4.11 indicate that all of the above described mechanisms are potentially inhibited in the DDI between GZR, ATV/r and DRV/r. The data from the RIF DDI clinical study alone suggests that OATP1B1 and OATP1B3 transport of GZR has been inhibited. Additionally, considering that cyclosporine is reported to inhibit CYP3A4, OATP1B1, OATP1B3, P-gp and BCRP and that the ratio of DDI was greater than with RIF, it would suggest that all pathways may be involved. Consequently, a mechanism of action that we are yet to comprehend could be the only viable explanation if considering a DDI mechanism besides OATP1B1 and OATP1B3.

Table 4.10 Clinical GZR DDI study data (231).

Coadministered Drug	GZR Regimen	Geometric Mean Ratio of GZR PK With/Without Coadministered Drug		
		AUC	C_{max}	C_{24}
ATV/r 300mg/100mg QD	GZR 200mg QD	10.58	6.24	11.64
DRV/r 600mg/100mg QD	GZR 200mg QD	7.50	5.27	8.05
LPV/r 400mg/100mg QD	GZR 200mg QD	12.86	7.31	21.70
Ketoconazole 400mg QD	GZR 100mg S	3.02	1.13	-
Cyclosporine 400mg S	GZR/EBR 200mg/50mg QD	15.21	17.00	3.39
RIF 600mg S	GZR 200mg QD	8.35	6.52	1.62
RIF 600mg S (IV)	GZR 200mg S	10.21	10.94	1.77

Data sourced from the Clinical Pharmacology and Biopharmaceutics Review for Zepatier (231). Data presented as the mean AUC, C_{max} and C_{24} of GZR with coadministered drug/without coadministered drug. All doses were orally administered unless stated otherwise. PK – pharmacokinetics, AUC – area under the curve, C_{max} – maximum plasma concentration, C_{24} – plasma concentration at 24 hours, GZR – grazoprevir, ATV – atazanavir, ATV/r – atazanavir with ritonavir, DRV – darunavir, DRV/r – darunavir with ritonavir, RTV – ritonavir, LPV – lopinavir, RIF – rifampicin, QD – once daily, S – single dose, IV - intravenous.

Table 4.11 Inhibitory profiles of clinical DDI study drugs.

Perpetrator	Transporter	Enzyme
ATV (243)	BCRP, P-gp, MRPs, OATPs	CYP3A4, UGT1A1, CYP2C8
DRV (244)	P-gp, BCRP, MATE1, OATP1B1, OATP1B3 (with COBI), OATPs	CYP3A4, CYP2D6 (observed with RTV or COBI)
RTV (245)	P-gp, MRP1, OATP-C, BCRP	CYP3A, CYP2D6
LPV (246, 247)	BCRP, OATP1B1	CYP3A
Ketoconazole (75)	-	CYP3A4
Cyclosporine (75)	P-gp, OATP1B1, OATP1B3, BCRP	CYP3A4
RIF SD (75, 248)	OATP1B1, OATP1B3	-

Reference for each drug presented in brackets. ATV – atazanavir, DRV – darunavir, RTV – ritonavir, LPV – lopinavir, RIF – rifampicin, COBI – cobicistat, SD – single dose, BCRP – breast cancer resistance protein, P-gp – P-glycoprotein, MRPs – multidrug resistance proteins, OATPs – organic anion transporter protein, MATE1 – multidrug and toxin extrusion 1, OATP1B1 - organic anion transporter protein B1, OATP1B3 - organic anion transporter protein B3, MRP1 – multidrug resistance protein 1, OATP-C - organic anion transporter protein B1, CYP3A4 – cytochrome P450 3A4, UGT1A1 - UDP-glucuronosyltransferase 1A1, CYP2C8 - cytochrome P450 2C8, CYP2D6 - cytochrome P450 2D6.

4.4.3 *In Silico* Assessment of $CL_{int,T}$ and DDI

The $CL_{int,T}$ of GZR determined *in vitro* was successfully applied to the PBPK model developed and verified in Chapter 3, with all pharmacokinetic parameters achieving either the 0.75 – 1.25 or 0.5 – 2 ratio and 1 – 1.25 or 1 – 2 AAFE criteria. The IVIVE correction factor applied in the PIT PBPK model in Chapter 3 was also found to be suitable for GZR, suggesting that a SPHH specific IVIVE correction factor value could be used in this *in vitro-in silico* framework, although extensive testing with further drugs would be required. Additionally, the verification of the IVIVE correction factor would benefit from experimentally determined values for GZR CYP3A4 metabolism and $CL_{biliary}$ as these were fitted based on percentage literature data and so their accuracy cannot be confirmed. Similarly to the PIT PBPK model, the equation for P_{eff} was unable to predict the absorption of GZR. The fed intestinal transit rate values also contributed to the incorrect prediction of GZR absorption based on the concentration time profile for steady state GZR 200mg. Alternative values were applied as per convention and considering that the application of this PBPK is based around liver transporter-mediated clearance and DDIs, these parameter optimisations were deemed appropriate.

Unfortunately, due to the irregular data obtained from the *in vitro* DDI assays between GZR, ATV/r and DRV/r it was concluded that implementation of these values into the PBPK model for their clinical simulation was inappropriate. PBPK modelling is a powerful *in silico* tool however model predictions are limited by the data used to build them and the inclusion of potentially false negative *in vitro* data creates a lack of confidence in any resulting simulated data. This being especially true for complex DDIs like that between GZR, ATV/r and DRV/r were three drugs are interacting in conjunction with one another across multiple enzyme and transporter pathways. As a result, the additional verification of PBPK modelling for the determination of active and passive $CL_{int,T}$ described in Chapter 3 could also not be completed.

4.4.4 Conclusion

Based upon the above arguments it is clear that further *in vitro* studies are required to produce conclusive evidence of the contribution of OATP1B1 and OATP1B3 in the DDI between GZR, ATV/r and DRV/r. Such *in vitro* studies could

include the SPHH GZR DDI assay with RIF to identify the potentially more specific *in vitro* inhibition of OATP1B1 and OATP1B3 by RIF. They could also include the use of recombinant over expressing cell lines for DDI assessment, as utilised previously for the assessment of GZR uptake in OATP1B1-MDCKII and OATP1B3-MDCKII cells (231). If false negative results are disproven, additional concepts such as time-based transporter inhibition should also be explored (133). Furthermore, the secondary aim of this study to verify the *in vitro-in silico* framework in a clinically relevant ARV scenario was not achieved, thus requiring future studies to be completed before the framework can be confidently used in the analysis of transporter-mediated DDIs.

Chapter 5

The Impact of Age on OATP1B1 Expression and Activity

Contents

5.1 Introduction

Since the introduction of potent ART over the past few decades, the survival rate of PLWH has steadily increased, leading to a life expectancy approaching that of the general population (6). UNAIDS estimated the worldwide total of PLWH ≥50 years old had increased from 7.9% in 1990 to 20.8% in 2019 (249). Furthermore, a recent European modelling study projected that by 2030, 73% of PLWH in Europe will be aged ≥50 years old with 40% of those aged ≥65 years old (105). There is an emergent need to understand the role of age-associated changes in ARV pharmacokinetics as these demographic changes have led to complex clinical scenarios that involve factors not only related to HIV infection but also to ageing. Yet, OALWH remain vastly underrepresented in clinical trials leading to a paucity of pharmacokinetic knowledge and insufficient clinical practice guidelines for this population (102). Moreover, an increased risk of DDIs in OALWH has been hypothesised due to their high prevalence of polypharmacy and age-related comorbidities (105, 250).

PBPK modelling has been utilised to overcome some of the clinical limitations experienced in OALWH (121, 187, 251). The reported PBPK model identified differences in drug exposure between non-elderly and elderly adults and were suggested to be caused by age-related physiological changes such as decreased hepatic and renal blood flow, resulting in reduced rates of drug clearance (251). Additionally, it has been suggested that ageing does not impact the magnitude of DDIs regardless of DDI mechanism or drugs involved, however this PBPK analysis was limited by the number of drugs included in the study representing each DDI mechanism of action (121). Furthermore, our limited understanding of the mechanisms that underpin transporter-mediated DDIs introduces challenges in the analysis of such studies. Although several advancements have been made to address the knowledge gap relating to transporters over the past few years, the impact of age on clinically relevant transporters such as OATP1B1 has yet to be comprehensively studied (69). Existing literature regarding the expression of OATP1B1 is contradictory, stating both a weak correlation (77) and no correlation between age and OATP1B1 expression (252). Moreover, where donor information was available, it was found that a limited number of donors aged ≥65 years old (10.5%) and ≥70 years old (3.5%) were included in the analysis (77).

In vitro techniques can be applied to investigate the effect of age on OATP1B1 expression and activity by utilising PHHs from donors across multiple age groups. Commercially available sandwich-ELISA kits have been produced for the quantification of several transporters and provide a more accessible approach in comparison to the resource and skill intensive LC-MS/MS technique commonly applied for protein quantification (253). The SLCO1B1 ELISA kit utilises antigen interactions between SLCO1B1 and antibody-SLCO1B1 alongside a horseradish peroxidase (HRP) colorimetric system for the detection of SLCO1B1 antigen targets. By implementing a calibration curve with known SLCO1B1 concentrations, the concentration of unknown samples of SLCO1B1 can be quantified (254). Additionally, SPHHs can be utilised *in vitro* to assess transporter-mediated clearance and DDIs, with FDA guidelines identifying probe substrate and inhibitors for a range of clinically relevant transporters (75, 131, 132).

The aim of this study was to quantify the expression of the hepatic uptake drug transporter OATP1B1 using a commercially available sandwich-ELISA kit. We also aimed to apply the SPHH *in vitro* assay developed in Chapter 2 to quantify the $CL_{int,T}$ and IC_{50} for the OATP1B1 probe substrate and inhibitor, PIT and RIF, in non-elderly adults (30 – 62 years), elderly adults (70 – 80 years) and mixed age adults (18 – 74 years). This work aimed to further understand the role of age in the expression and activity of OATP1B1 and expand our current knowledge of transporters to help support the clinical management of DDIs in OALWH.

5.2 Methods

5.2.1 Materials

Materials used for the $CL_{int,T}$, DDI and LC-MS/MS *in vitro* studies were previously described in Chapter 2. Additionally, the Human SLCO1B1 ELISA Kit (catalog no. MBS9323360) was purchased from MyBioSource (California, USA). Pierce BCA Protein Assay Kit (catalog no. 23227), Mem-PER^{TM} Plus Membrane Protein Extraction Kit (catalog no. 89842), Trypan blue (catalog no. 15250061) were purchased from Thermo Fisher Scientific (Hemel Hempstead, UK). All other materials were purchased from Thermo Fisher Scientific (Hemel Hempstead, UK) and Sigma-Aldrich (Poole, UK).

5.2.2 Cryopreserved Primary Human Hepatocytes

Pooled cryopreserved SPHH with lot no. HUE120 (catalog no. HMCS10; non-elderly) and HUE50-0 (catalog no. HMCS50; mixed-age) were purchased from Thermo Fisher Scientific (Hemel Hempstead, UK). Individual cryopreserved SPHH with lot no. IGG, JCM, KQF, TJP (catalog no. F00995; elderly) and MNO (catalog no. M00995; elderly) were purchased from BioIVT (West Sussex, UK). A summary of donor characteristics can be found in Table 5.1. The non-elderly (30 – 62 years), mixed-age (18 – 74 years) and elderly (70 – 80 years) SPHHs were all used in the quantification of OATP1B1 by sandwich ELISA. However, only the individual elderly SPHH donor aged 80 years old (lot no. MNO) was used in the *in vitro* PIT and RIF $CL_{int,T}$ and DDI study as this was the only elderly donor previously qualified for transporter uptake studies. Data from the non-elderly SPHH $CL_{int,T}$ and DDI study in Chapter 2 were used for comparison analysis in this chapter.

Table 5.1 Summary of primary human hepatocyte donor characteristics.

Characteristics	Non-Elderly	Mixed-Age	Elderly
n	10	50	5
Age, years Median (range)	56 (30-62)	52.5 (18-74)	77 (70-80)
Gender, n Male (%) Female (%)	7 (70) 3 (30)	24 (48) 26 (52)	1 (20) 4 (80)
Race, n Caucasian (%) African American (%) Asian (%) Hispanic (%)	10 (100) 0 (0) 0 (0) 0 (0)	43 (86) 4 (8) 2 (4) 1 (2)	5 (100) 0 (0) 0 (0) 0 (0)
Reported History, n Alcohol (%) Tobacco (%) Recreational Drugs (%) Medication (%)	8 (80) 5 (50) 4 (40) 8 (80)	32 (64) 31 (62) 23 (46) 31 (62)	2 (40) 3 (60) 0 (0) 3 (60)
Non-elderly – lot no. HUE120, Mixed-age – lot no. HUE50-0, Elderly – lot no. IGG, JCM, KQF, TJP and MNO, n – number of patients.			

5.2.3 OATP1B1 Quantification by Sandwich ELISA

OATP1B1 expression in the non-elderly, mixed-age and elderly SPHHs were quantified using a SLCO1B1 ELISA kit (MyBioSource, California, USA). The kit has a sensitivity of 0.1 ng/ml and detection range of 0.625 – 20 ng/ml (254). Firstly, the SPHH samples were thawed and resuspended in KHB (pH 7.4) at a concentration of $1x10^6$ cells/ml as previously described in Chapter 2. ELISA wash solution was diluted 1:20 with dH_2O and all reagents were brought to room temperature (18 – 25°C). Three technical replicates of each SPHH sample were generated by aliquoting 750µl of each suspension into microcentrifuge tubes. The remaining SPHHs were stored at -80°C and used as described in method section 5.2.3.1. The SPHHs were then centrifuged at 2000 × g for 2 minutes at 4°C and the resulting supernatant was removed. Cell pellets were washed with 1ml of ice-cold PBS before centrifugation was repeated. The supernatant was removed and 75 µl of ice-cold PBS was aliquoted into each microcentrifuge tube and the cell pellet resuspended. On ice, each sample was passed slowly through a 30 gauge needle ten times followed by centrifugation at 14,000 × g for 20 minutes to pellet the cell debris. A control sample of SPHHs was prepared as described above, stained with trypan blue and visually inspected under a microscope to confirm cell lysis (255).

Following the above sample preparation, 50 µl of supernatant was aliquoted into the ELISA plate wells, producing a final relative concentration of $5×10^5$ cells/well. Similarly, 50 µl of pre-prepared standard and blank solutions were added in duplicate to the ELISA plate wells and 100 µl of HRP-conjugate reagent was aliquoted into each well. The ELISA plate was then covered with a closure plate membrane and incubated at 37°C for 1 hour. Following incubation, the ELISA plate was manually washed by disposing the incubation mixtures into a waste container and filling each well with wash solution and leaving to stand for 1 minute. The wash solution was then disposed of into a waste container before being inverted and hit onto absorbent paper towels until no moisture was present. This process was repeated four times and once completed, 50 µl of Chromogen solution A and B were successively aliquoted into each well. The ELISA plate was then covered to protect the Chromogen solutions from light and incubated at 37°C for 15 minutes. Finally, 50 µl of stop solution was aliquoted into each well and the ELISA plate was left to stand for 5 minutes. A GENios

microplate reader (Tecan, Männedorf, Switzerland) was then used to read the optical density of each well at 450nm.

5.2.3.1 Data Analysis

Prism v8 software (GraphPad Software Inc., La Jolla, CA, USA) was used to plot the sandwich ELISA standard curve absorbance data and interpolate the unknown OATP1B1 values in ng/ml for the non-elderly, mixed-age and elderly SPHH samples. In order to normalise OATP1B1 expression to fmol/µg total membrane protein, a Pierce BCA Protein Assay Kit (Thermo Fisher Scientific, Hemel Hempstead, UK) was used to quantify the total membrane protein content in each sample. Membrane and membrane-associated proteins were firstly isolated from the hepatocyte samples using a Mem-PER^{TM} Plus Membrane Protein Extraction Kit (Thermo Fisher Scientific, Hemel Hempstead, UK). The remaining SPHHs from the sandwich ELISA were brought to room temperature (18 – 25°C) and 5ml was aliquoted into 15ml centrifuge tubes. For elderly hepatocyte donor lot no. TJP and IGG, only 1.5ml and 2.5ml were available for analysis, respectively. SPHH samples were centrifuged at 300 × g for 5 minutes at 4°C and the supernatant was removed before the cell pellets were washed with 3 ml of wash solution. This process was repeated, and the cell pellets were resuspended in 1.5 ml of wash solution before being transferred to microcentrifuge tubes. SPHH samples were centrifuged at 300 × g for 5 minutes at 4°C and supernatant removed before 750 µl of permeabilization buffer was added. Cell pellets were resuspended via brief vortexing and incubated with constant mixing for 10 minutes at 4°C. The now permeabilised cells were centrifuged at 16,000 × g for 15 minutes at 4°C and the supernatant containing cytosolic proteins was carefully transferred to new microcentrifuge tubes. Immediately before use, 50 µl of protease/phosphatase inhibitor cocktail was added to 5 ml of solubilisation buffer and 500 µl aliquots of buffer were added to each sample. The cell pellets were resuspended in the solubilisation buffer and incubated with constant mixing for 30 minutes at 4°C. SPHH samples were then centrifuged at 16,000 × g for 15 minutes at 4°C and supernatant containing solubilised membrane and membrane-associated proteins were transferred to new microcentrifuge tubes in preparation for the Pierce BCA protein assay.

To quantify the total membrane protein content, 25µl of each membrane protein sample were aliquoted in triplicate into a 96-well cell culture plate. Albumin

standards were diluted with PBS as described in the Pierce BCA protein assay kit protocol (256), producing a detection range of 25 – 2000 µg/ml. Similarly, 25 µl of albumin standards and blank PBS were aliquoted into the 96-well cell culture plate. A working reagent was produced by mixing 10 ml of kit reagent A with 200 µl of kit reagent B and 200 µl of the working reagent was added to each well. The plate was mixed thoroughly on a plate shaker for 30 seconds before being incubated for 30 minutes at 37°C. Following incubation, the plate was cooled to room temperature over 30 minutes. A GENios Tecan microplate reader was used to read the optical density of each well at 562nm.

Prism v8 software (GraphPad Software Inc., La Jolla, CA, USA) was used to plot the Pierce BCA protein assay standard curve absorbance data and interpolate the unknown total membrane protein values in µg/ml for the non-elderly, mixed-age and elderly SPHHs. The OATP1B1 sandwich ELISA data was then normalised to fmol/µg total membrane protein using equation 1. Statistical analysis of the OATP1B1 expression data was also carried out using Prism v8 software (GraphPad Software Inc., La Jolla, CA, USA). Due to the lack of data points normality was unable to be tested and therefore statistical significance between the non-elderly, mixed-age and elderly SPHH's OATP1B1 expression values were assessed using a Mann-Whitney (non-parametric) test.

$$\text{OATP1B1 (fmol/µg total membrane protein)} = \frac{\text{OATP1B1 (fmol/ml)}}{\text{Total Membrane Protein (µg/ml)}} \quad (1)$$

5.2.4 *In Vitro* Pitavastatin and Rifampicin $CL_{int,T}$ and DDI Study

The *in vitro* PIT and RIF $CL_{int,T}$ and DDI assays were adapted from literature (135, 163-168) and previously described in detail in Chapter 2. Both assays were carried out in duplicate and each contained four technical replicates per condition. Briefly, stock solutions of PIT and RIF were freshly prepared in 100% (vol/vol) DMSO the day before the experiment. The day of the experiment, incubation solution concentrations of the probe substrate PIT (0.1 – 300 µM) and probe inhibitor RIF (0.1

– 300 µM) were prepared in KHB (pH 7.4) through serial dilution, providing a constant DMSO final concentration of 1% (vol/vol) per well. Cryopreserved SPHHs were then thawed, resuspended in KHB at a concentration of 1×10^6 cells/ml and aliquoted into 24-well cell culture plates to produce a final incubation solution suspension of 1×10^5 cells/well. To determine the $CL_{int,T}$ of PIT, cells were preincubated with KHB for 5 minutes and the study was initiated with the addition of PIT (0.1 – 300 µM). To determine the magnitude of DDI between PIT and RIF, cells were preincubated with RIF (0.1 – 300 µM) for 5 minutes and the study was initiated with the addition of PIT (0.1 µM). All incubations took place at 37°C on a plate shaker at 150rpm. Both studies were terminated after 2 minutes by placing the 24-well plates on ice and aliquoting ice-cold PBS into each well. Solutions were immediately transferred to microcentrifuge tubes followed by centrifugation at 2000 × g for 2 minutes at 4°C. Incubation solutions were then removed from each tube, cell pellets washed with ice-cold PBS and the centrifugation process repeated. Cell pellets were stored at -80°C followed by a single freeze-thaw cycle (-80°C to room temperature; 18 – 25°C) to lyse the cells in preparation for LC-MS/MS analysis.

5.2.4.1 Quantification of Pitavastatin by LC-MS/MS

PIT concentrations were determined using a TSQ Endura LC-MS/MS (Thermo Scientific, Hemel Hempstead, UK) and validated chromatographic method previously described in Chapter 2. To summarise, lysed cell pellet samples were resuspended in 100 µl of 50% (vol/vol) ACN in dH_2O and pre-determined dilutions carried out accordingly. At a concentration of 300 ng/ml, 300 µl of IS PRA in 100% (vol/vol) ACN were aliquoted into each microcentrifuge tube. Samples were vortexed for 10 seconds and centrifuged at 13,300 × g for 10 minutes at 4°C. The resulting supernatant was aliquoted into borosilicate glass tubes and dried in a vacuum centrifuge for 4 hours at room temperature (18 – 25°C). Once dry, 100 µl of 50% (vol/vol) ACN in dH_2O was aliquoted into each glass tube, vortexed for 10 seconds and 50 µl transferred to LC-MS/MS vials for analysis. Standard, QC and blank samples were prepared in a similar manner in accordance with FDA guidelines (141). Chromatographic separation of PIT and IS PRA was achieved using an Accucore C18 (100 x 2.1mm) LC-MS/MS column fitted with an Accucore C18 pre-column (10 x 2.1mm). Mobile phases comprising of 100% H_2O_L with 0.1% FA_L and 100% ACN_L with 0.1% FA_L were applied in a multi-step gradient method over 5 minutes with a flow rate of 300 µl/ml,

as described in Chapter 2. Heated ESI was applied in positive mode to ionise the samples and allow detection of the breakdown products via SRM scanning.

5.2.4.2 Data Analysis

Prism v8 software (GraphPad Software Inc., La Jolla, CA, USA) was used to plot the $CL_{int,T}$ and DDI *in vitro* assay data for both the non-elderly SPHHs and individual elderly SPHH donor aged 80 years old. Michaelis Menten non-linear regression analysis was applied to the PIT (0.1 – 300 µM) $CL_{int,T}$ assay data to derive the V_{max} (µmole/10^6cells/minute) and K_m (µM). $CL_{int,T}$ (µl/10^6cells/minute) of PIT was then calculated as shown in equation 2 (135). The percent inhibition of PIT (0.1 µM) by RIF (0.1 – 300 µM) was calculated as shown in equation 3 (168), were $Uptake_{substrate,inhibitor}$ and $Uptake_{substrate}$ are the total PIT (0.1 µM) uptake concentrations in the presence and absence of RIF (0.1 – 300 µM), respectively. A log(inhibitor concentration) vs. response equation and a least-squares fitting method was applied to the percent inhibition data to derive IC_{50} of RIF required to inhibit PIT (0.1 µM).

$$CL_{int,T} = V_{max} / K_m \quad (2)$$

$$\% \text{ Inhibition} = 100 - (Uptake_{substrate,inhibitor} / Uptake_{substrate} \times 100) \quad (3)$$

Results from both assays were expressed as the mean ± SD of two individual experimental replicates, each containing three or four technical replicates for each condition as described in method section 5.2.4.1. Statistical analysis of the $CL_{int,T}$ and DDI *in vitro* assay were also carried out using Prism v8 software (GraphPad Software Inc., La Jolla, CA, USA). Normality was tested using a D'Agostino & Pearson test and the statistical significance between the non-elderly and individual elderly SPHH donor's $CL_{int,T}$ and IC_{50} values were assessed using an unpaired t-test.

5.3 Results

5.3.1 OATP1B1 Quantification by Sandwich ELISA

OATP1B1 expression in the non-elderly (30 – 62 years), mixed-age (18 – 74 years) and elderly (70 – 80 years) SPHHs were successfully quantified using a SLCO1B1 sandwich ELISA kit. Cell lysis was confirmed via visual inspection with a trypan blue stain. The Pierce BCA protein assay kit determined a mean ± SD total membrane protein yield of 3.57 ± 0.55 mg/100mg liver tissue across all samples. For both the SLCO1B1 sandwich ELISA kit and Pierce BCA protein assay kit the average of each standard was calculated from one independent experiment that contained two technical replicates for each condition, as described in method section 5.2.3. Furthermore, the average absorbance reading for the blank samples was deducted from each calibration and unknown sample prior to analysis, as per convention. The standard curve obtained from the SCLO1B1 sandwich ELISA kit and Pierce BCA protein assay kit can be found in Figure 5.1 and Figure 5.2, respectively. The mean ± SD of the non-elderly, mixed-age and elderly SPHHs were calculated from one independent experiment that contained three technical replicates for each condition, as described in method section 5.2.3.

Using the yield of total membrane protein, OATP1B1 expression was normalised to fmol/µg total protein. OATP1B1 expression in the 70 year old female, 74 year old female, 77 year old female, 78 year old female and 80 year old male SPHHs were 0.811 ± 0.042 fmol/µg total protein, 0.333 ± 0.039 fmol/µg total protein, 0.458 ± 0.036 fmol/µg total protein, 0.438 ± 0.069 fmol/µg total protein and 0.277 ± 0.023 fmol/µg total protein, respectively (Figure 5.3). OATP1B1 expression in the non-elderly, mixed-age and mean of the individual elderly SPHHs were 0.845 ± 0.102 fmol/µg total protein, 0.619 ± 0.062 fmol/µg total protein and 0.463 ± 0.191 fmol/µg total protein, respectively (Figure 5.4). When compared to the non-elderly, OATP1B1 expression in the mixed-age and elderly SPHHs were 27% ($p=0.2$) and 45% ($p=0.0172$) lower, respectively. Additionally, when compared to the mixed-age SPHHs, OATP1B1 expression in the elderly SPHHs was 25% lower ($p=0.1299$).

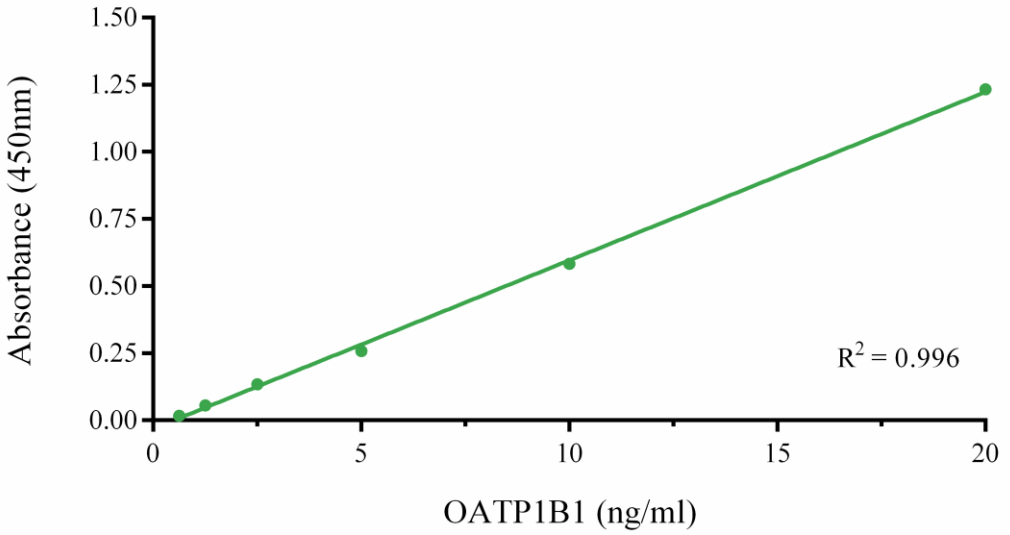

Figure 5.1 Standard curve produced by the OATP1B1 ELISA kit. Data presented as the average OATP1B1 concentration from two technical replicates (ng/ml).

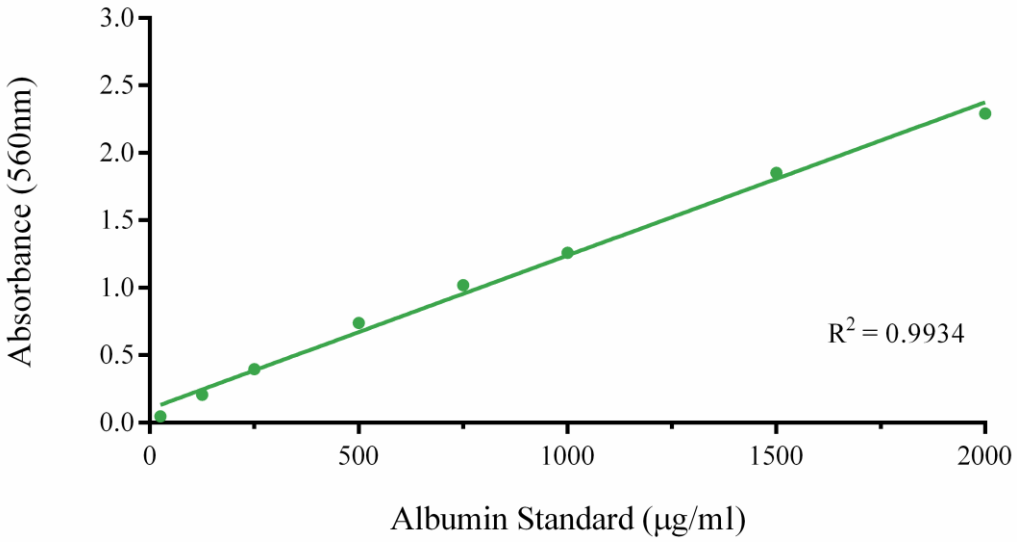

Figure 5.2 Standard curve produced by the Pierce BCA Protein Assay kit. Data presented as the average albumin concentration from two technical replicates (µg/ml).

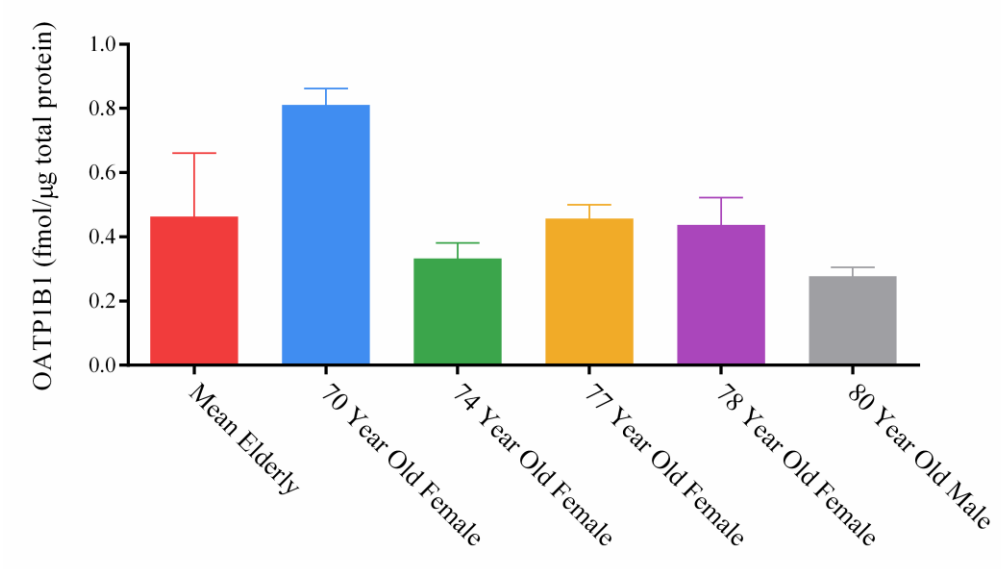

Figure 5.3 OATP1B1 expression determined by sandwich ELISA in elderly PHH. The red, blue, green, yellow, purple and grey bars and error bars represent the mean OATP1B1 expression (fmol/µg protein) ± SD of three technical replicates from the mean elderly, 70-year old female, 74-year old female, 77-year old female, 78-year old female and 80-year old male PHH, respectively.

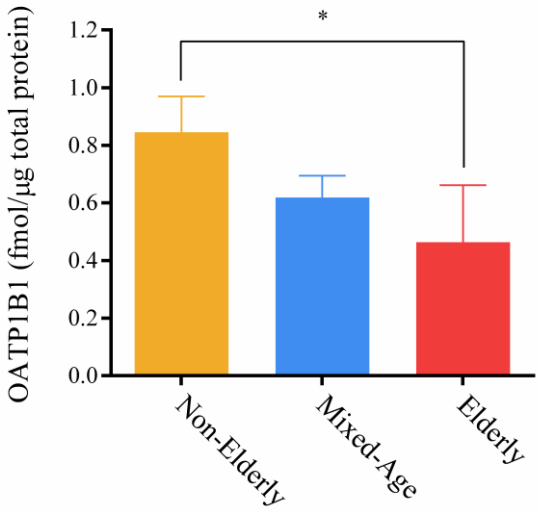

Figure 5.4 OATP1B1 expression determined by sandwich ELISA in non-elderly (30 – 62 years), mixed-aged (18 – 74 years) and elderly (70 – 80 years) SPHHs. The yellow, blue and red bars and error bars represent the mean OATP1B1 expression (fmol/µg protein) ± SD of three technical replicates from the non-elderly, mixed-age and elderly SPHHs, respectively. Statistical significance between non-elderly, mixed-age and elderly SPHHs was assessed using a Mann-Whitney test (* = p-value ≤0.05).

5.3.2 *In Vitro* Assessment of $CL_{int,T}$ and DDI

A summary of the *in vitro* $CL_{int,T}$ and DDI assay with PIT and RIF can be found in Table 5.2. The mean ± SD of each PIT parameter was calculated from two independent experiments that contained three or four technical replicates for each condition, as described in method section 5.2.4. Samples were successfully quantified using the previously verified LC-MS/MS method for PIT described in Chapter 2. V_{max}, K_m and IC_{50} were calculated using Prism v8 software (GraphPad Software Inc., La Jolla, CA, USA) and $CL_{int,T}$ were calculated as described in method section 5.2.4. $CL_{int,T}$ of PIT in the non-elderly and individual 80 year old SPHHs were 108.1 ± 34.38 µl/min/10^6 cells and 53.57 ± 20.67 µl/min/10^6 cells, respectively (Figure 5.5). Coincubation of RIF with PIT reduced PIT uptake by 74% (maximal inhibition at 300 µM; IC_{50} 0.021 µM) and 85% (maximal inhibition at 10 µM; IC_{50} 0.29 µM) in the non-elderly and individual 80 year old SPHHs, respectively (Figure 5.6). A D'Agostino & Pearson test for normality was conducted using Prism v8 software (GraphPad Software Inc., La Jolla, CA, USA) for both the $CL_{int,T}$ and DDI assay data. All data sets passed the normality test with p-values in the range of 0.0732 – 0.6917. Unpaired t-tests were carried out to assess if there were statistical significance between the non-elderly and individual 80 year old SPHHs in both the $CL_{int,T}$ and DDI assays. The unpaired t-tests determined that, although the $CL_{int,T}$ was 50.44% lower in the individual 80 year old SPHHs compared to the non-elderly SPHHs, by convention this difference was not statistically significant with a p-value of 0.1945. Conversely, it was found that the difference in IC_{50} between the non-elderly SPHHs and individual 80 year old SPHHs was very statistically significant with a p-value of 0.0071.

Table 5.2 Summary of the *in vitro* $CL_{int,T}$ and DDI assay with PIT and RIF.

PIT Parameter	Non-Elderly*	Male 80 Years
V_{max} (µmole/minute/10^6 cells)	5490 ± 259	4826 ± 348.9
K_m (µM)	50.81 ± 7.533	90.08 ± 16.88
$CL_{int,T}$ (µl/minute/10^6 cells)	108.1 ± 34.38	53.57 ± 20.67
RIF IC_{50} (µM)	0.021	0.29
RIF Maximum Inhibition (%)	74	85

V_{max}, K_m and $CL_{int,T}$ presented as mean ± SD and RIF IC_{50} and RIF maximum inhibition presented as mean of two experimental replicates with four technical replicates. Non-elderly – lot no. HUE120, Male 80 Years – lot no. MNO, RIF – rifampicin, V_{max} – maximum uptake velocity, K_m – half maximum velocity concentration, $CL_{int,T}$ – hepatic transporter intrinsic clearance, IC_{50} – half maximal inhibitory concentration, SD – standard deviation. * - Data produced in Chapter 2.

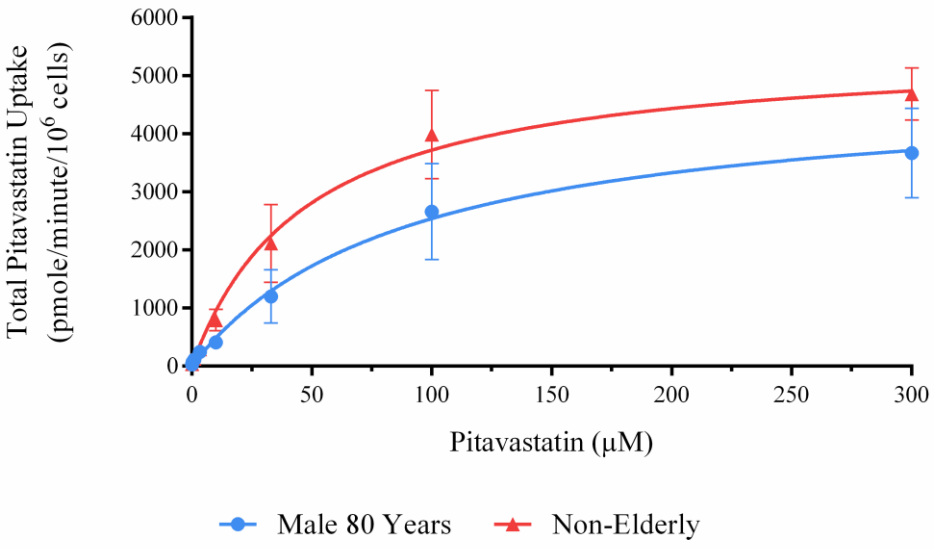

Figure 5.5 Total uptake kinetic profile of PIT (0.1 µM) measured in the individual 80 year old and non-elderly SPHHs. The blue and red lines and error bars represent the mean total PIT uptake ± SD (pmole/minute/10^6 cells) of two experimental replicates with four technical replicates in the individual 80 year old and the non-elderly SPHHs, respectively.

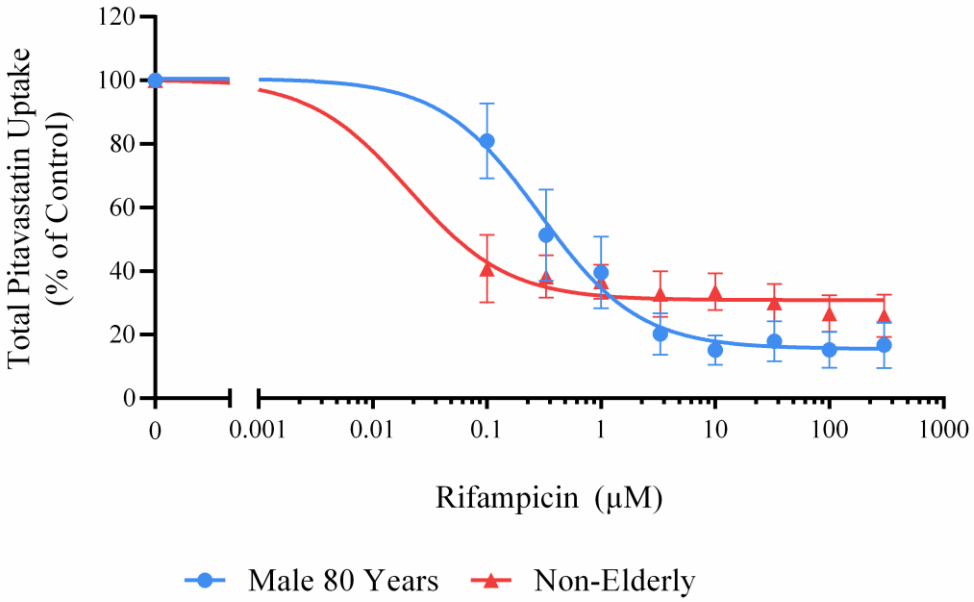

Figure 5.6 Concentration-dependent inhibition of total PIT (0.1 µM) uptake by RIF (0.1 – 300 µM) measured in the individual 80 year old and non-elderly SPHHs. The blue and red lines and error bars represent the mean inhibited total PIT uptake ± SD (% of control) of two experimental replicates with four technical replicates in the individual 80 year old and non-elderly SPHHs, respectively.

5.4 Discussion

The demographic of PLWH is changing (6, 105, 249), introducing new clinical scenarios in an ageing population that is underrepresented in clinical trials, practice guidelines and research (102). Moreover, a higher burden of DDIs is hypothesised in OALWH due to the manifestation of comorbidities, geriatric syndromes and polypharmacy found in this population (105). When clinical data is scarce, *in vitro* techniques can be utilised to elucidate the mechanisms and magnitudes that govern DDIs. Transporters play a vital role in the ADME of several drugs and as a result are involved in numerous DDIs (70). However, to our knowledge there are no *in vitro* studies investigating the effect of age on transporter-related DDIs. In this study, the impact of age on the hepatic uptake transporter OATP1B1 was determined through the quantification of OATP1B1 expression and activity in non-elderly, mixed-age and elderly cryopreserved SPHHs.

5.4.1 OATP1B1 Expression

Using the SLCO1B1 ELISA kit, a decrease in the expression of OATP1B1 was found with increased age. The non-elderly SPHHs presented the highest OATP1B1 expression with the expression in the mixed-age SPHHs and elderly SPHHs being 27% and 45% lower, respectively. There was a statistically significant difference in OATP1B1 expression between the non-elderly and elderly SPHHs whereas the mixed-age SPHHs did not show a statistically significant difference when compared to either of the other age groups. Interestingly, within the elderly SPHH group, the youngest SPHH donor aged 70 years had the highest OATP1B1 expression whilst the eldest SPHH donor aged 80 years had the lowest. Moreover, the 70-year-old SPHH donor had an OATP1B1 expression similar to that of the non-elderly SPHHs. When compared to the mean of the four other elderly SPHHs, the OATP1B1 expression in the 70 year old SPHH donor was 54% higher. Post-transcriptional and post-translational mechanisms have been suggested to control the expression of OATP1B1 with a study demonstrating no significant correlation between the mRNA and protein expression level of OATP1B1 from human liver bank and SPHH samples (257). These mechanisms have previously been reported to be disrupted with age and could provide an explanation for the decrease in OATP1B1 expression found herein. However, post-

transcriptional and post-translational mechanisms are currently poorly understood and further studies are required to improve our knowledge on the genetic and molecular basis of ageing (82, 258).

Existing literature on the expression of OATP1B1 is contradictory with two individual meta-analysis studies stating both a significant but weak positive correlation (77) and no correlation between age and OATP1B1 expression (252). However, when exclusion criteria were not applied to the study where no correlation was found, a significant positive correlation was observed between age and OATP1B1 expression. Interestingly, in this meta-analysis a significant but weak positive correlation was found between age and OATP2B1 (252). Investigating the relationship between age and transporter expression data is challenging, and several factors must be considered when analysing the existing literature as well as the current study. Firstly, the availability of high-quality PHH samples for the elderly is low and only a limited number of elderly patients have been included in these studies. For example, from the two above-mentioned meta-analysis studies only one provided individual donor information and it was found that just 3.75% (n=3) were ≥70 years old (77). Furthermore, during the current study it was found that there were no pooled donor SPHHs available exclusively from donors ≥70 years old. Moreover, there were few individual SPHHs from donors ≥70 years old, limiting the amount of elderly SPHH donors utilised in this study to five. Larger sample sizes of donors ≥70 years old are required to make definitive conclusions on the correlation between OATP1B1 expression and age.

Secondly, the inclusion of non-Caucasian donors must be taken into consideration as an increased expression of OATP1B1 has previously been reported in Asian and African American donors (225). The mixed-age SPHHs used in this study included non-Caucasian donors as a pooled SPHH lot consisting solely of Caucasian donors in the required age range was unobtainable. Additionally, the meta-analysis study that found a significant but weak positive correlation between OATP1B1 and age did not state the exclusion of non-Caucasian hepatocyte donors in their selection criteria and no data on the demographics of the samples included in their study were provided. In contrast, the meta-analysis study that found no correlation applied exclusion criteria omitting non-Caucasian donors. Thirdly, a large variation in OATP1B1 expression has been described throughout the literature (77, 135, 252). In

comparison to the previously published meta-analysis studies, the mean OATP1B1 expression level in this study was 86% and 96% lower (77, 252). Yet, the value determined herein was within the range of values previously reported for SPHHs (77). In contrast, a further study quantifying OATP1B1 expression in PHHs and liver tissue reported values 82% and 84% lower than that found in this study, respectively (135). To note, the yield of total membrane protein determined in this study (3.57 mg/100mg liver tissue) was comparable to that reported in the literature (3.7 mg/100mg liver tissue), providing reassurance in the accuracy of unit normalisation considering protein levels (259).

Fourthly, the quantification technique used in this study differed from those in the meta-analysis studies, with these studies predominantly consisting of data produced via proteomic LC-MS/MS quantification. Historically, western blotting was used to determine semiquantitative transporter expression data but they were limited by the lack of recombinant standards of membrane proteins and transporter specific antibodies available (252). Proteomics techniques utilising LC-MS/MS were therefore developed providing robust and quantitative transporter expression data however these techniques require expensive specialist equipment and skilled personnel, restricting accessibility (253). Recently, ELISA kits for the quantification of transporters have been developed as a more accessible alternative to proteomic LC-MS/MS techniques. These kits produce accurate and reliable results as demonstrated by the manufacturer although, to our knowledge, are yet to be described in practice in the literature (254). In addition, the sample preparation techniques varied between this study and the meta-analysis studies, with this study being limited to mechanical cell lysis techniques due to the compatibility of the SLCO1B1 ELISA kit. The above described differences in quantification and sample preparation techniques could explain the large variation in OATP1B1 expression levels. Contrariwise, the smaller study that reported an 82% and 84% lower OATP1B1 level in comparison to this study also used proteomic LC-MS/MS quantification, suggesting that the large variation may not be caused by the quantification or sample preparation technique used (135). Further studies are warranted to compare the quantification of OATP1B1 expression by ELISA vs. proteomic based LC-MS/MS methodologies in order to confirm the suitability of the simpler and more accessible ELISA technique.

Lastly, all donors in this study had reported alcohol, tobacco, recreational drug and medication history although no information on underlying disease were provided. Of the two previously published meta-analysis studies, that which found no correlation between age and OATP1B1 expression applied exclusion criteria to form a healthy Caucasian sub database by removing non-Caucasian donors and those with underlying disease from their initial database (252). Whereas the other meta-analysis study did not (77). Previous reports have suggested a link between disease state and transporter expression with a previous study describing a reduction in OATP1B1 expression in donors with fatty liver disease compared to donors with a normal liver appearance (252). Furthermore, neither meta-analysis studies provided information on reported alcohol, tobacco, recreational drug or medication history of the included donors (77, 252). Lifestyle factors such as these are associated with increased biological age in comparison to chronological age and their contribution towards OATP1B1 expression is currently unknown. Future studies analysing the relationship between biological age and OATP1B1 expression would be of great interest as they would allow for the consideration of the effect of health and lifestyle factors on transporter expression. Previous studies have demonstrated that telomere length decreases with age and could therefore be used as a biomarker of biological ageing in such future studies (260, 261).

5.4.2 OATP1B1 Activity

Utilising the $CL_{int,T}$ and DDI *in vitro* assay developed in Chapter 2, a marked reduction in PIT $CL_{int,T}$ was found in the individual 80 year old SPHH donor in comparison to the non-elderly SPHHs. However, this decrease was found not to be statistically significant. This suggests that, although OATP1B1 expression in the 80 year old SPHH donor was 68% lower than that of the non-elderly SPHHs, there was no significant alteration in transporter function with increased age. However, a statistically significant 93% decrease in IC_{50} value was found in the non-elderly SPHHs when compared to the 80 year old SPHH donor. Though, the maximal percent inhibition of PIT by RIF was 11% greater in the 80 year old SPHH donor compared to the non-elderly SPHHs. The IC_{50} values indicate that the magnitude of transporter-mediated DDIs in elderly adults may be less pronounced in comparison to non-elderly adults. This potentially less pronounced DDI in the elderly implies that although the function of hepatic uptake was not altered with age, the mechanisms that govern

transporter-mediated DDIs may be. Several factors must be taken into consideration when analysing this data and due to these limitations, further studies are required before we are able to draw definitive conclusions on the impact of age on OATP1B1 activity.

Firstly, as described for the OATP1B1 expression study, the biggest limitation of the $CL_{int,T}$ and DDI *in vitro* study was the small number of available elderly SPHH donors. Only one of the five elderly SPHH donors sourced for this analysis had previously been qualified for transporter uptake studies and although this donor was the eldest, it is unclear whether other elderly donors would produce similar results. Secondly, a large variation was found for the IC_{50} value of the non-elderly SPHHs in comparison to a previous study which reported an IC_{50} value for the inhibition of PIT by RIF of 2.2 ± 0.3 µM (166). The main differences between these studies were the period of time the assay was carried out for and the quantification technique used. Incubation times utilised for the *in vitro* assessment of transporter-mediated DDIs have been identified as significant contributing factors towards inter-study variation (182). Additionally, it must be noted that the previously published study did not provide demographic data for the PHH donors used (166). It is therefore unclear whether the difference in IC_{50} between the non-elderly SPHHs and the 80 year old SPHH donor is caused by age or from experimental variation. However, as discussed in Chapter 3 the IC_{50} produced in non-elderly SPHHs in this study proved accurate in simulating the DDI between PIT and RIF using PBPK modelling. Furthermore, a previously published PBPK model described an underprediction in the DDI between RIF and PIT unless a 10-fold decrease in the K_i value was applied (191). The resulting K_i value was similar to that produced in this study suggesting that the *in vitro* assay system used herein produces accurate IC_{50} values. Thirdly, the 80 year old SPHH donor had no report of alcohol, tobacco or recreational drug history and one reported medication history whilst the non-elderly SPHHs had between 40 – 80% of donors with reported alcohol, tobacco, recreational drug and medication history. As described in section 5.4.1, the contribution of these factors towards OATP1B1 activity is unclear. Lastly, the $CL_{int,T}$ and DDI *in vitro* study was limited by the use of one OATP1B1 probe substrate and inhibitor. Although both PIT and RIF are recommended by current FDA guidelines, a comparison between multiple probe substrate and inhibitors with varying

OATP1B1 sensitives would provide valuable information for the determination of the relationship between age and OATP1B1 activity (75).

Literature comparing non-elderly vs. elderly $CL_{int,T}$ and DDI are scarce and to our knowledge there is only one study comparing the clinical DDI between an OATP1B1 substrate and an ARV OATP1B1 inhibitor among different age groups (123). This study found no difference in the magnitude of DDI between rosuvastatin (ROS) and DRV/r in non-elderly adults ≤60 years old compared to OALWH with a mean age and SD of 67.7 ± 5.3 years. However, there are two limitations of the study that must be considered. Firstly, the data for the two age groups were obtained from separate studies. Secondly, in contrast to the study containing OALWH, the non-elderly data were obtained from HIV-negative patients who were on a different ROS and DRV/r dosing regimen. Larger clinical studies are required to comprehensively assess the impact of age on OATP1B1 activity.

5.4.3 Conclusion

This study determined a statistically significant decrease in OATP1B1 expression with increased age however, there was no statistically-significant decrease in the $CL_{int,T}$ of PIT suggesting no significant alteration of the transporter function with aging. Furthermore, a statistically significant decrease in the RIF IC_{50} value was found in non-elderly SPHHs when compared to the individual 80 year old SPHH donor which implies that transporter-mediated DDIs in elderly adults could potentially be less pronounced in comparison to non-elderly adults. However, due to the limitations of this study further *in vitro* investigations with larger PHH sample sizes including a wider range of substrates and inhibitors are warranted to verify these observations. This data could generate improved PBPK modelling verification strategies allowing for greater confidence in transporter-mediated DDI predictions in the elderly. Overall, this could provide support for the clinical management of transporter-related DDIs in OALWH.

Chapter 6

High Dose Rifampicin for the Treatment of Leprosy in People Living with HIV Taking Dolutegravir

Contents

6.1 Introduction

RIF represents a pivotal component of several anti-infective therapies however there have been no advances in the application of RIF for the treatment of TB as well as in other indications such as leprosy over the past 40 years. Of late, there has been a growing interest in the use of higher doses of RIF, particularly for shortening TB therapy and to overcome resistance (262). Recent studies focusing on the safety and efficacy of high dose RIF demonstrated that doses of up to 35 mg/kg were safe and well tolerated (59-61). In the case of leprosy, a previous study demonstrated that single RIF doses of 1200 mg and 1500 mg were more efficient at reducing the rate at which *M. leprae* were rendered non-infective than 600 mg and 900 mg (60). However, due to cost associations and toxicity studies at the time, a lower dose of 600 mg RIF QMT was prioritised in the MDT regimen which consists of 100 mg dapsone QD and 300 mg QMT and 50 mg QD clofazimine (52, 60, 61).

At the end of 2018 the WHO reported 184,212 registered cases and 208,619 new cases of leprosy worldwide, with approximately 75% of these cases being reported in India (50%), Brazil (15%) and Indonesia (10%) (43). Previously published studies have indicated a higher prevalence of leprosy in PLWH (47), however large cohort studies encompassing HIV and leprosy are lacking (48). It is clear that there is a geographical overlap of PLWH and people infected with leprosy. Despite the limited epidemiological data, it is fair to postulate that DDIs between ART and the MDT regimen used for the treatment of leprosy could occur in a clinical setting. Both dapsone and clofazimine have the potential to produce weak and clinically significant interactions with ARVs. Dapsone is unlikely to cause pharmacokinetic interactions with ARVs however it may increase the risk of adverse effects such as peripheral neuropathy. Clofazimine could increase the risk of QT prolongation when coadministered with ARVs such as ATV however as clofazimine is a moderate CYP3A4 inhibitor it could also cause potentially weak and significant interactions with CYP3A4 substrates such as maraviroc (54, 55). In comparison, RIF produces several clinically significant DDIs due to its potent induction of CYP3A4, UGT1A1 and P-gp which are involved in the metabolism and transport of several ARV drugs (54, 98, 99, 156). RIF also shares overlapping hepatotoxicity profiles with ARVs, increasing the risk of adverse effects during coadministration (55). Specifically, the

ARV drug DTG which is used in the first-line treatment of HIV is metabolised largely by UGT1A1 and CYP3A4 with minor metabolism by UGT1A3 and UGT1A9 (263). There are currently no data on how to manage the potential DDI between DTG and high dose RIF QMT for the treatment of PLWH coinfected with leprosy.

In the absence of such data, PBPK modelling can be applied to predict the magnitude of DDIs, providing evidence-based guidance for their clinical management. PBPK models predict drug pharmacokinetics through the mathematical description of ADME processes. Moreover, mechanisms of DDIs can be simulated by applying our knowledge of their functionality alongside *in vitro* and clinical data. In the example of enzyme induction, previously published equations have described the change in enzyme abundance by considering the basal enzyme abundance level, the maximum fold increase by the inducer, the concentration of inducer that achieves half maximal induction as well as the concentration of the inducer at the site of DDI. These equations however are only applicable for steady state induction interactions (63). Further equations have been developed to incorporate the relationship between enzyme transcription and translation, considering the activation of nuclear receptors by the inducer as well as the synthesis and degradation of mRNA and enzyme. Such equations allow for the simulation of induction over time, rather than at steady state alone (264).

The aim of this chapter was to develop and verify a whole-body PBPK model capable of simulating the induction effect of single dose RIF on CYP3A4 and UGT1A1. The verified PBPK model aimed to predict the magnitude of DDI between RIF 1200mg QMT and DTG 50mg BID and determine if DTG dose adjustments would be necessary. These findings may provide support for the clinical management of PLWH coinfected with leprosy as well as in other DDI scenarios involving the administration of high dose RIF on a non-daily basis. Additionally, these findings could aid in the design of DDI clinical studies investigating high dose RIF for the treatment of other indications such as TB.

6.2 Methods

All PBPK models described herein were designed in Simbiology v5.8, a product of Matlab 2018a (MathWorks, Natick, MA, USA; 2018). Virtual cohorts consisting of 100 male and female patients aged 18 – 60 years were simulated. The PBPK models were developed for DTG, midazolam (MDZ), nifedipine (NIF), raltegravir (RAL) and RIF, and verified against observed clinical data, respectively. Physicochemical, pharmacokinetic, *in vitro* and *in vivo* data were sourced from literature or if unavailable were estimated via curve fitting. Where applicable, pharmacokinetic parameters and concentration time profile data were extracted from charts and graphs using the Plot Digitizer Tool (plotdigitizer.sourceforge.net).

6.2.1 Rifampicin PBPK Model

A minimal PBPK model was developed to predict the pharmacokinetic parameters and concentration time profile of RIF, as previously described in Chapter 3 (214). In addition to the prediction of RIF 600mg QD, the model was expanded to predict single dose RIF 1200mg. The physicochemical and *in vitro* data for both doses of RIF can be found in Table 6.1. Due to the lack of observed clinical data surrounding the V_{ss} and CL/F of higher doses of RIF, these parameters were estimated by curve fitting with the observed data (265). As literature suggests a non-linear decrease in CL/F value with increasing RIF doses, a value smaller than 7.5 L/h was targeted (219).

Table 6.1 Physicochemical and *in vitro* data for 600mg and 1200mg RIF.

Parameters	RIF 600mg	RIF 1200mg
Molecular Weight	822.9 (217)	822.9 (217)
Protein Binding (%)	80 (218)	80 (218)
V_{ss} (L/kg)	23.3 (219)	E
CL/F (L/h)	7.5 (219)	E
CYP3A4 EC_{50} (µM)	1.18 (264)	1.18 (264)
UGT1A1 EC_{50} (µM)	0.321 (266)	0.321 (266)
Reference for literature values presented in brackets. V_{ss} – volume of distribution, CL/F – apparent oral clearance, CYP3A4 – cytochrome P450 3A4, UGT1A1 - uridine diphosphate glucuronosyltransferase 1A1, EC_{50} – concentration at half maximum induction, E - the value was estimated.		

6.2.2 Whole-Body PBPK Model

A whole-body PBPK model was developed to predict the pharmacokinetic parameters and concentration time profiles of DTG, MDZ, NIF and RAL. The anatomy, intestinal absorption, intestinal metabolism and systemic distribution was previously described in Chapter 3. In contrast to Chapter 3 which implemented hepatic transporter-related clearance mechanisms using multiple blood flow limited compartments, hepatic clearance was estimated using equations 1 – 4 in a single well-stirred compartment (207-209):

$$CL_{int,liverE} = (CL_{int,E} \times Abundance_{E} \times MPPGL \times W_{Liver}) \quad (1)$$

$$MPPGL = 10^{1.407 + 0.0158 \times Age - 0.00038 \times Age\text{^}2 + Age\text{^}3} \quad (2)$$

$$CL_{int,liver} = \Sigma\ CL_{int,liverE} \quad (3)$$

$$\text{Total Hepatic Clearance} = \frac{(Q_{hv} \times f_u/R \times CL_{int,liver})}{(Q_{hv} + CL_{int,liver} \times f_u/R)} \quad (4)$$

Where $CL_{int,liverE}$, $CL_{int,E}$, $Abundance_E$, MPPGL and W_{Liver} are the intrinsic clearance of the enzyme scaled to the whole liver, the intrinsic clearance of the enzyme, enzyme abundance, microsomal protein content per gram of liver and weight of the liver in kg. $CL_{int,liver}$ represents the sum of all $CL_{int,liverE}$ values for each enzyme involved in the drug's metabolism. Q_{hv}, f_u and R are the hepatic blood flow, the unbound fraction of drug and the blood-to-plasma ratio. Due to the complexity of DTG's metabolic pathway, the $CL_{int,liverE}$ of CYP3A4, UGT1A1, UGT1A3 and UGT1A9 were determined using reported CL/F fractions, as previously described (267, 268). The $CL_{int,E}$ values for DTG were then estimated via retrograde modelling as previously described (269). For MDZ, NIF and RAL $CL_{int,E}$ values for CYP3A4 and UGT1A1 were sourced from the literature. Additionally, for MDZ and NIF the monoprotic equation described in Chapter 3 was utilised for the calculation of the olive oil:buffer partition coefficient of nonionised and ionised species at pH 7.4 ($D^*_{vo:w}$). In contrast, the zwitterionic $D^*_{vo:w}$ equation was applied for DTG and RAL, as described in Chapter 4. These equations were applied accordingly towards the calculation of the V_{ss}.

6.2.3 CYP3A4 and UGT1A1 Induction Model

A dynamic PBPK model for the RIF based induction of CYP3A4 and UGT1A1 via the PXR nuclear receptor was defined using previously described equations (264). The equations assume negligible intestinal induction and are therefore only applied in the liver. As per convention, induction of mRNA and enzyme was evaluated as the fold increase over the observed value on day 0.

$$RNA^I = RNA / RNA_0 \quad (5)$$

$$ENZYME^{I} = ENZYME / ENZYME_0 \quad (6)$$

$$p = ENZYME_0 / K_{i,NF} \quad (7)$$

$$q = \frac{(k_{rna,pxr} \times k_{enzyme,syn})}{(k_{rna,deg} \times k_{enzyme,deg} \times ENZYME_0)} \quad (8)$$

$$\frac{dPXR_{act}}{dt} = \frac{1 + p}{1 + p \times ENZYME^{I}} \times \frac{RIF}{EC_{50} + RIF} - k_{inact,pxr} \times PXR_{act} \quad (9)$$

$$\frac{dRNA^{I}}{dt} = k_{rna,deg} \times (1 + q \times PXR_{act} - RNA^{I}) \quad (10)$$

$$\frac{dENZYME^{I}}{dt} = k_{enzyme,deg} \times (RNA^{I} - ENZYME^{I}) \quad (11)$$

Where RNA^{I}, RNA, RNA_0, $ENZYME^{I}$, ENZYME and $ENZYME_0$ are the fold change value, induction value and baseline value of mRNA and enzyme, respectively. $K_{i,NF}$, PXR_{act}, $k_{inact,pxr}$, RIF and EC_{50} are the constant for negative feedback inhibition, normalised amount of activated PXR, inactivation rate constant for activated PXR, RIF plasma concentration and RIF concentration at half maximum induction, respectively. $k_{rna,pxr}$, $k_{enzyme,syn}$, $k_{rna,deg}$ and $k_{enzyme,deg}$ are the rate constants for PXR-mediated mRNA synthesis, enzyme synthesis, mRNA degradation and enzyme degradation, respectively. When simulating RIF DDIs, $Abundance_E$ in equation 1 was multiplied by the $ENZYME^{I}$ value to account for the RIF induced fold change in enzyme level over time.

6.2.4 PBPK Model Verification

The PBPK model was considered successfully verified if the ratio of predicted vs. observed values for each drug and DDI pharmacokinetic parameter were between 0.5 – 2 (150). However, where possible we strived for the ratio of predicted vs. observed values to be within 0.75 – 1.25 or 0.5 – 1.5 to allow for more accurate results (220). The AAFEs for the predicted vs. observed pharmacokinetic parameters and the concentration time profiles were also calculated, as defined in equation 12 (209), and

were considered successfully verified if the value was within 1 – 2. Similarly to the ratio of predicted vs. observed, we strived for the AAFE value to be within 1 – 1.25 or 1 – 1.5 to produce greater accuracy. The more stringent evaluation of the concentration time profiles using AAFE evaluation compared to the commonly accepted visual inspection reinforces more accurate results (150, 270). For the DDIs, the percentage of DDI vs. drug alone ($DDI_{\%}$) were also calculated for both the predicted and observed values, as defined in equation 13. The $DDI_{\%}$ was verified as outlined above.

$$AAFE = 10\left|\frac{1}{N}\ \Sigma \log \frac{\text{Predicted}}{\text{Observed}}\right| \tag{12}$$

$$DDI_{\%} = (drug_{DDI} / drug_{sub}) \times 100 \tag{13}$$

Where AAFE, $drug_{DDI}$ and $drug_{sub}$ are the absolute average-fold error, substrate drug parameter value in the presence of the perpetrator drug and substrate drug parameter value, respectively.

6.2.5 PBPK Model Development

6.2.5.1 Whole-Body PBPK Model

Physicochemical and *in vitro* data for DTG, MDZ, NIF and RAL were sourced as previously described and a summary can be found in Table 6.4. These were applied in the whole-body PBPK model with hepatic clearance equations constructed according to the metabolic pathway of each drug. To obtain the most accurate predictions, a correction factor was estimated and applied to the predicted V_{ss} of each drug via curve fitting and considering their respective literature V_{ss} values. This process was carried out in a stepwise manner. Initially, simulations for each drug were carried out with no correction factor applied to the V_{ss}. As described in method section 6.2.4, AAFE and ratio values were calculated for predicted vs. observed and based upon these results a range of V_{ss} correction factor values to obtain the most accurate predictions were estimated. Three V_{ss} correction factor values within the estimated range were applied and simulations for each drug were performed. Again, AAFE and ratio values were calculated for predicted vs. observed data and the V_{ss} correction

factor with the most accurate predictions was selected. Furthermore, fed and fasted intestinal transit rates were applied according to the clinical data, unless stated otherwise.

6.2.5.2 CYP3A4 Induction PBPK Model

The RIF PBPK model together with the induction model described in method sections 6.2.1 and 6.2.3 were firstly simulated with the previously published induction parameters to predict the CYP3A4 fold change induction profile following repeated oral administration of RIF 600mg QD (264). These models in conjunction with the whole-body PBPK model described in method section 6.2.2 were used to predict the DDI dosing regimens of MDZ and NIF as well as the extended CYP3A4 fold change induction profile following 28 days repeated oral dosing of RIF 600mg QD and 28 days after the last dose of RIF. The predicted vs. observed $DDI_{\%}$ values were calculated as described in method section 6.2.4 and the ratio and AAFE values were used to analyse whether the previously published induction parameters required further optimisation to accurately simulate the extended CYP3A4 fold change induction profile. Specifically, timepoints were assigned to each of the observed clinical datasets for NIF and MDZ and the CYP3A4 fold change at each timepoint were calculated. Timepoints 1 – 5 correspond to hours 8 – 32, 648 – 672, 816 – 840, 984 – 1008 and 1320 – 1344, respectively. The ratio and AAFE results were used to assess whether no change, an increase or a decrease in the CYP3A4 fold change induction profile was required at each of the corresponding timepoints.

To optimise the CYP3A4 fold change induction profile, alternative values for each of the induction parameters were sourced from the available literature, as shown in Table 6.2. Where data was not available, induction parameters were estimated via curve fitting to observed MDZ and NIF data. Firstly, the effect of each of the induction parameters, $K_{inact,pxr}$, $K_{enzyme,deg}$, $K_{rna,deg}$, q and p, on the CYP3A4 fold change induction profile were determined by simulating a range of values. Secondly, utilising the above information the CYP3A4 fold change induction profile was optimised in a stepwise manner by either estimating induction parameter values or, when available, applying alternative values from the literature. Induction parameter values were estimated similarly to that described for V_{ss} optimisation in method section 6.2.5.1. Briefly, a range of values were initially estimated through test simulations and three values

selected based upon visual inspection. Simulations for each value were conducted and AAFE and ratio values of the $DDI_{\%}$ were calculated for predicted vs. observed data. The parameter value with the most accurate predictions was selected. Again, for the available literature values the ratio and AAFEs of the $DDI_{\%}$ were calculated and the values providing the most accurate predictions were selected. Lastly, the MDZ and NIF optimised induction parameter values were further verified using the observed DTG clinical data.

Table 6.2 CYP3A4 induction parameter values.

Parameter	Original Values (264)	Alternative Values
$k_{inact,pxr}$ (h^{-1})	0.0527	E
$k_{rna,deg}$ (h^{-1})	0.0530	0.0756 (271)
$K_{enzyme,deg}$ (h^{-1})	0.0282	0.0096 (272), 0.005 - 0.07 (273)
q	4.34	E
p	0.313	E
Reference for literature values presented in brackets. $k_{inact,pxr}$ - inactivation rate constant for activated PXR, $k_{rna,deg}$ – rate constant for mRNA degradation, $K_{enzyme,deg}$ – rate constant for enzyme degradation, p – equation 9, q – equation 10, E – estimated value.		

6.2.5.3 UGT1A1 Induction PBPK Model

Unlike CYP3A4, there are no previously published induction PBPK models or UGT1A1 fold change induction profiles available. Therefore, the UGT1A1 induction PBPK model could not be developed or verified in the same manner as the CYP3A4 induction PBPK model. However, as UGT1A1 has been reported to be induced via the same PXR mechanism as CYP3A4 (274), induction equations 5-11 described in method section 6.2.3 were utilised. The UGT1A1 fold change induction profile was optimised as described for CYP3A4, with two exceptions. Firstly, the value estimated for $k_{inact,pxr}$ via the CYP3A4 optimisation process was applied in the UGT1A1

induction equations. Secondly, the UGT1A1 p value was calculated by determining $K_{i,NE}$ from the estimated CYP3A4 p value and applying it to the p equation for UGT1A1.

Alternative induction parameter values sourced from the literature are shown in Table 6.3. A reported UGT1A1 fold change *in vitro* value of 2.8 ± 0.81 was targeted during induction parameter optimisation (274). Observed RAL clinical data was used to verify the predicted UGT1A1 fold change induction profile, as described in method section 6.2.4. In addition, the AAFE and ratio value for the predicted vs. observed UGT1A1 fold change value was calculated and verified using the previously described criteria.

Table 6.3 UGT1A1 induction parameter values.

Parameter	Original Values (264)	UGT1A1 Values
$k_{inact,pxr}$ (h^{-1})	0.0527	E_{CYP3A4}
$k_{rna,deg}$ (h^{-1})	0.0530	0.0385 (275), 0.0756 (271)
$K_{enzyme,deg}$ (h^{-1})	0.0282	0.0144 (271), 0.0243 (275), 0.0729 (276)
q	4.34	E
p	0.313	C
Reference for literature values presented in brackets. $k_{inact,pxr}$ - inactivation rate constant for activated PXR, $k_{rna,deg}$ – rate constant for mRNA degradation, $K_{enzyme,deg}$ – rate constant for enzyme degradation, p – equation 9, q – equation 10, E_{CYP3A4} – CYP3A4 estimated value, E – estimated value, C – calculated value.		

6.2.6 Prediction of Once Monthly Rifampicin with Dolutegravir

Once optimised and verified, the RIF and whole-body induction PBPK models were applied to predict the currently approved DTG dosing strategy during the coadministration of RIF 600mg QD. The current dosing strategy simulations consisted

of 35 days of repeated oral administration of DTG 50mg BID with a single oral administration of RIF 1200mg on day 7. The pharmacokinetic parameter's C_{max}, C_{avg} and C_{min} mean ± SD were calculated and compared to the minimum target concentration of 4 x PA-IC_{90} of DTG (0.256 µg/ml) (277). The predicted data was used to determine if the current dosing guidelines for DTG coadministered with RIF would be suitable for RIF 1200mg QMT or if an alteration in the dose of DTG would be required (278).

Table 6.4 Physicochemical and *in vitro* data for DTG, MDZ, NIF and RAL.

Parameters	DTG	MDZ	NIF	RAL
Molecular Weight (g/mol)	419.4 (279)	325.8 (280)	346.3 (281)	444.4 (282)
HBD	2 (279)	0 (280)	1 (281)	3 (282)
Log $P_{o:w}$	2.2 (279)	3.89 (280)	2.49 (281)	-0.39 (282)
P_{app} (10^{-6} cm/s)	40.17 (283)	37.9 (284)	250 (285)	6.6 (286)
pK_a	-0.51, 8.2 (279)	6.57 (280)	3.93 (287)	-1.5 (282), 6.7 (286)
Protein Binding (%)	98.9 (279)	97 (280)	98 (281)	83 (282)
PSA ($Å^2$)	99.18 (279)	30.18 (280)	110.45 (281)	150.02 (282)
R	0.535 (220)	0.53 (288)	0.67 (289)	0.6 (286)
V_d (L/kg)	0.25 (279)	1 – 3.1 (280)	0.71 (289)	0.4 – 2 (290)
Water Solubility (mg/L)	95 (291)	9.87 (280)	5.9 (292)	5.39×10^4 (293)

CL/F (L/h)	0.9 (294)	103 ± 53 (295)	20.5 (289)	39.1 (296)
CYP3A4 (ml/min/mg protein)	–	0.584 ± 0.065 (297)	0.21 ± 0.01 (298)	–
UGT1A1 (ml/min/10^6 hepatocytes)	–	–	–	12.4 (286)

Reference for literature values presented in brackets. DTG – dolutegravir, MDZ – midazolam, NIF – nifedipine, RAL – raltegravir, HBD – Hydrogen bond donor, Log $P_{o:w}$ – Partition coefficient between octanol and water, P_{app} – apparent permeability, pK_a - logarithmic value of the dissociation constant, PSA – polar surface area, R – blood-to-plasma drug ratio, V_d – volume of distribution (an average adult body weight of 70 kg was assumed), CL/F – apparent oral clearance, CYP3A4 – cytochrome P450 3A4, UGT1A1 - uridine diphosphate glucuronosyltransferase 1A1.

6.3 Results

The PBPK model was successfully verified by comparing the predicted AUC, C_{max} and C_{min} pharmacokinetic parameters and concentration time profiles with the observed clinical data for the oral administration of each of the validation drugs and DDIs outlined in the method section. A summary of the AAFE and ratio verification results can be found in Tables 6.11 and 6.12.

6.3.1 Rifampicin Verification

Verification of the RIF PBPK model was carried out using available AUC_{0-24} and C_{max} observed clinical data for the oral administration of RIF 600mg QD (219) as well as digitised C_{max} and C_{min} observed clinical data from the available concentration time profile for the oral administration of single dose RIF 1200mg (265). Due to the lack of observed clinical data, both the CL/F and V_{ss} for single dose RIF 1200mg were estimated as described in method section 6.2.1. The estimated values for V_{ss} and CL/F were 23.3 ± 6.96 L/kg and 3 ± 0.9 L/h, respectively. The predicted vs. observed concentration time profiles are shown in Figures 6.1 and 6.2. The predicted vs. observed AUC_{0-24} (µg×h/ml), C_{max} (µg/ml) and C_{min} (µg/ml) can be found in Table 6.5. AAFE and ratio values for the predicted vs observed pharmacokinetic parameters and concentration time profiles of RIF 600mg QD and single dose RIF 1200mg were within the stringent 0.75 – 1.25 ratio and 1 – 1.25 AAFE verification criteria.

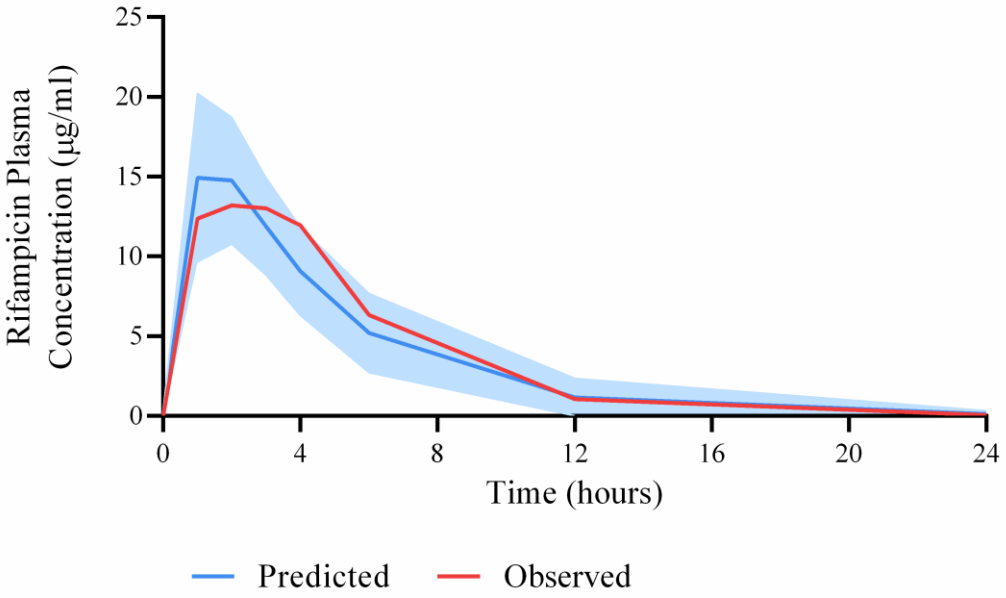

Figure 6.1 Predicted vs. observed concentration time profiles for RIF 600mg QD. The blue line and blue shaded area represent the mean plasma concentration ± SD (µg/ml) of the predicted data. The red line represents the observed clinical data (µg/ml) (219).

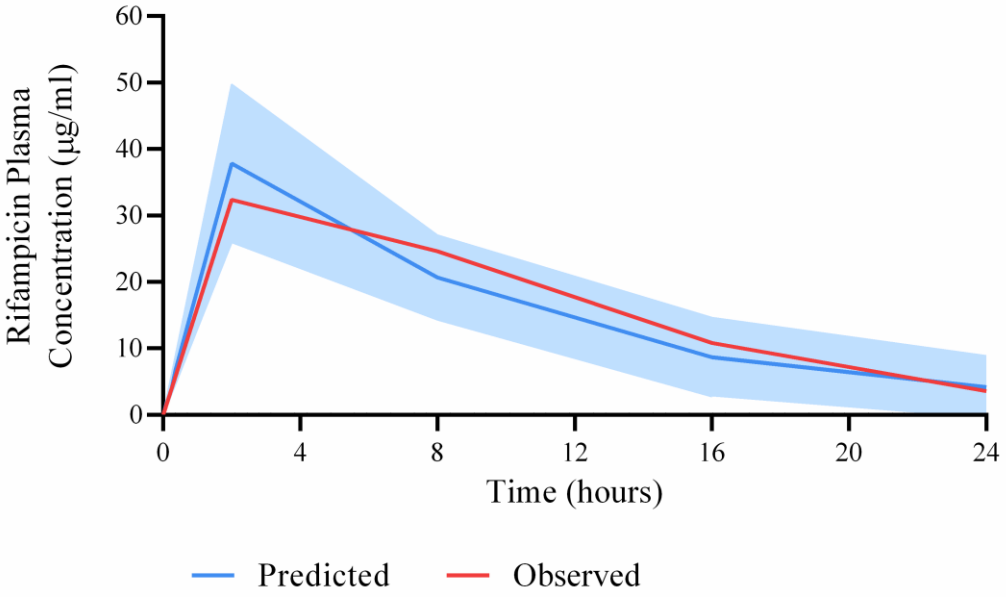

Figure 6.2 Predicted vs. observed concentration time profiles for single dose RIF 1200mg. The blue line and blue shaded area represent the mean plasma concentration ± SD (µg/ml) of the predicted data. The red line represents the observed clinical data (µg/ml) (265).

Table 6.5 Predicted vs. observed RIF pharmacokinetic parameters.

Drug Regimen	Parameter	Predicted	Observed
RIF 600mg QD	AUC_{0-24}	90.73 ± 40.48	79.7 (219)
	C_{max}	17.23 ± 7.67	15.6 (219)
Single Dose RIF 1200mg	C_{max}	38.44 ± 11.73	32.38 (265)
	C_{min}	4.15 ± 4.7	3.56 (265)

AUC_{0-24} values presented as mean ± SD (µg/h/ml). C_{max} and C_{min} values presented as mean ± SD (µg/ml). RIF – rifampicin, AUC – area under the curve, C_{max} – maximum plasma concentration, C_{min} – minimum plasma concentration.

6.3.2 CYP3A4 Induction Model Optimisation and Verification

6.3.2.1 Published CYP3A4 Induction Model

Utilising the verified RIF PBPK model and previously published induction model and parameters described in method section 6.2.1 and 6.2.3 (264), the CYP3A4 fold change induction profile following repeated oral administration of RIF 600mg QD was predicted, as shown in Figure 6.3. An AAFE value of 1.055 was calculated for the predicted vs observed CYP3A4 fold change induction profile, which was within the acceptable criteria.

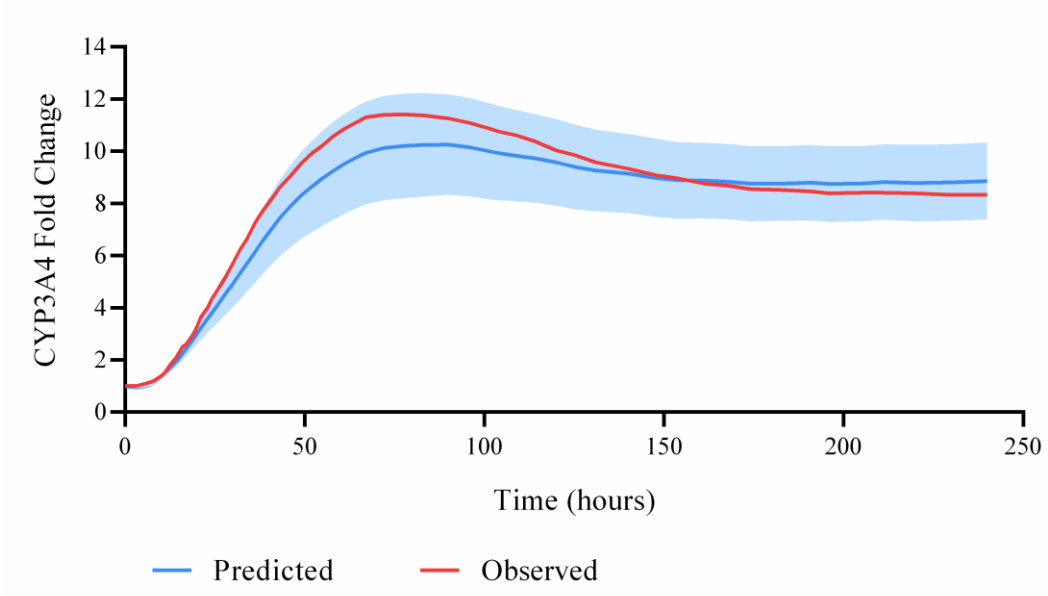

Figure 6.3 Predicted vs. observed CYP3A4 fold change following repeated oral administration of RIF 600mg QD. The blue line and blue shading represent the mean CYP3A4 fold change ± SD predicted using previously published induction parameters. The red line represents the published CYP3A4 fold change (264).

The $DDI_{\%}$ were calculated using available $AUC_{0\text{-}24}$ and C_{max} observed clinical data for the oral administration of NIF 10mg and NIF 10mg coadministered with RIF 1200mg (299) as well as MDZ 2mg QD (300) and MDZ 2mg QD 0, 1, 2 and 4 weeks after the last dose of coadministered RIF 600mg QD (301). As described in method section 6.2.5.2, the RIF induction model in conjunction with the whole-body PBPK model were used to predict the above-mentioned dosing regimens as well as the extended CYP3A4 fold change induction profile. The predicted $DDI_{\%}$ was calculated and the predicted vs. observed ratios and AAFEs were determined. A summary of the results can be found in Table 6.6. The ratio and AAFE results for timepoints 1, 3 and 4 were generally greater than the 0.75 – 1.25 ratio and 1 – 1.25 AAFE verification criteria. Timepoint 2 and 5 were within the stringent criteria. From these results it was concluded that further optimisation of the extended CYP3A4 fold change induction profile would be required to ensure the most accurate results for the model's application.

Table 6.6 Analysis of predicted vs observed clinical data as a percentage of DDI vs drug alone using previously published induction parameters.

Drug	Dose (mg)	RIF Dose (mg)	Timepoint	CYP3A4 Fold Change	Ratio		AAFE	
					AUC	C_{max}	AUC	C_{max}
NIF	10 S	1200 S	1	1.12	1.76	1.13	1.76	1.13
MDZ Week 0	2 QD	600 QD	2	9.03	1.07	1.18	1.07	1.18
MDZ Week 1	2 QD	600 QD	3	1.96	1.60	1.89	1.60	1.89
MDZ Week 2	2 QD	600 QD	4	1.01	1.41	1.75	1.41	1.75
MDZ Week 4	2 QD	600 QD	5	1.00	0.98	0.98	1.02	1.02

RIF – rifampicin, NIF – nifedipine, MDZ – midazolam, S – single dose, QD – once daily, AAFE – absolute average fold error, AUC – area under the curve, C_{max} – maximum plasma concentration, timepoint 1 – 8 – 32 hours, timepoint 2 – 648 – 672 hours, timepoint 3 – 816 – 840 hours, timepoint 4 – 984 – 1008 hours, timepoint 5 – 1320 – 1344 hours.

6.3.2.2 CYP3A4 Induction Model Optimisation

Based on the results in Table 6.6, an increase in CYP3A4 fold change at timepoints 1, 3 and 4 and no change at timepoint 2 and 5 were required to optimise the CYP3A4 fold change induction profile to obtain more accurate predictions. The effect of each of the induction parameters, $K_{inact,pxr}$, $K_{enzyme,deg}$, $K_{rna,deg}$, q and p on the extended CYP3A4 fold change induction profile were determined, as described in method section 6.2.5.2. An increase in $K_{inact,pxr}$ resulted in a decrease in CYP3A4 fold change across all timepoints in the CYP3A4 fold change induction profile. A decrease in $K_{enzyme,deg}$ caused a decrease in the CYP3A4 fold change at timepoints 1 and 2 whilst increasing the CYP3A4 fold change at timepoints 3 and 4. Timepoint 5 remained the same. Increasing $K_{rna,deg}$ caused an increase in CYP3A4 fold change at timepoint 1 and a decrease at timepoints 2, 3 and 4 with timepoint 5 remaining the same. An increase in q resulted in an increase in CYP3A4 fold change across all timepoints in the CYP3A4 fold change induction profile. Finally, an increase in p had minimal effect on timepoint 1 and 5 and decreased CYP3A4 fold change at timepoints 2, 3 and 4.

The CYP3A4 fold change induction profile was optimised in a stepwise manner utilising the above findings alongside the MDZ and NIF observed clinical data, as described in method section 6.2.5.2. The optimised parameter values for $K_{inact,pxr}$, $K_{enzyme,deg}$, $K_{rna,deg}$, q and p were 0.1 h^{-1}, 0.0096 h^{-1} (272), 0.0756 h^{-1} (271), 14 and 3, respectively. The resulting CYP3A4 fold change induction profile following 28 days repeated oral administration of rifampicin 600mg QD and 28 days after the last RIF dose can be found in Figure 6.4. A comparison of the optimised vs. published CYP3A4 fold change induction profile can be found in Figure 6.5. The CYP3A4 fold change values for timepoints 1 – 5 were 1.35 vs 1.12, 7.69 vs 9.03, 3.54 vs 1.96, 1.51 vs 1.01 and 1.02 vs 1.00 for optimised vs. published, respectively (264).

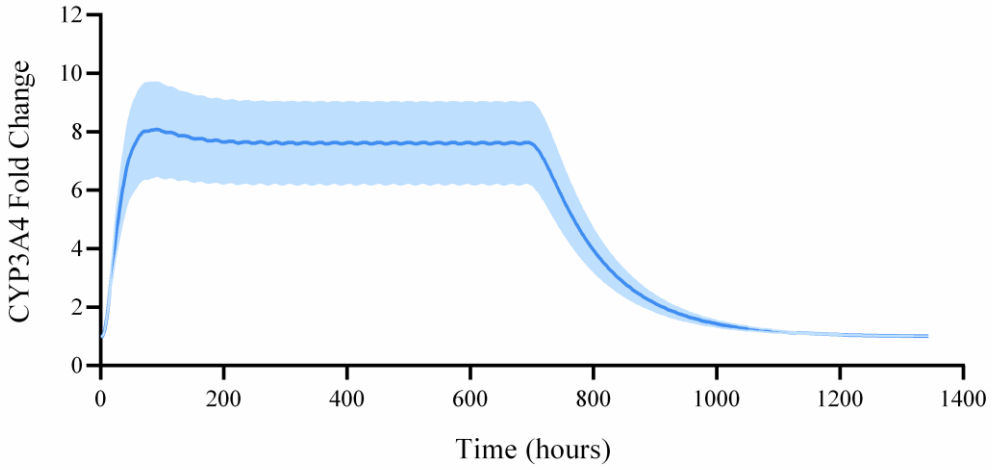

Figure 6.4 Predicted CYP3A4 fold change following 28 days repeated oral administration of RIF 600mg QD and 28 days after the last RIF dose, using the optimised induction parameters. Data expressed as mean fold change ± SD.

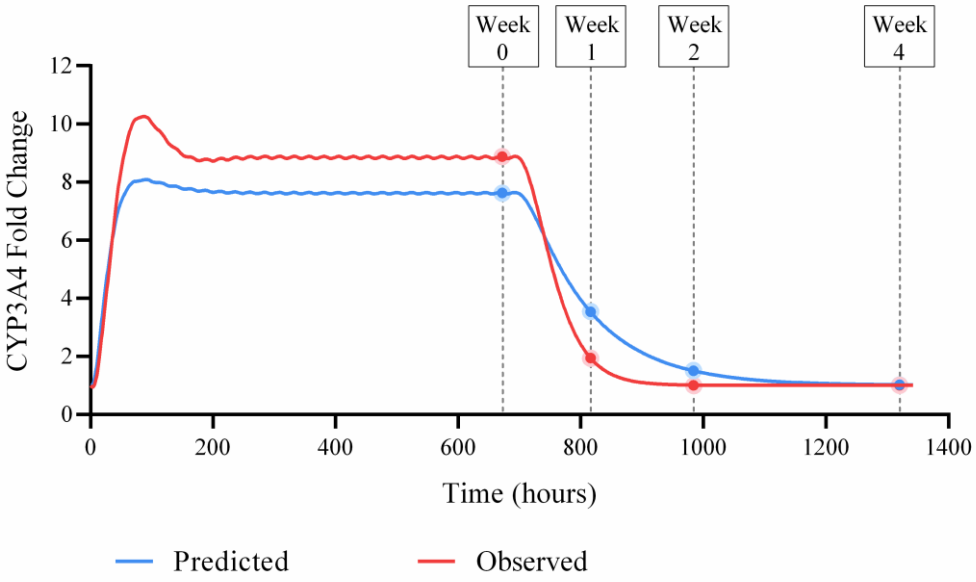

Figure 6.5 Predicted vs. observed CYP3A4 fold change following 28 days repeated oral administration of RIF 600mg QD and 28 days after the last RIF dose. The blue line represents the mean CYP3A4 fold change predicted using induction parameters optimised with observed clinical MDZ data (301). The red line represents the mean CYP3A4 fold change predicted using previously published induction parameters (264). Weeks 0, 1, 2 and 4 after the last dose of RIF are highlighted by blue and red circles for predicted and observed induction profiles, respectively.

6.3.2.3 Midazolam Verification

The MDZ PBPK model was verified using available AUC_{0-24} and C_{max} observed clinical data for the oral administration of MDZ 2mg QD (300) and MDZ 2mg QD 0, 1, 2 and 4 weeks after the last dose of coadministered RIF 600mg QD. To note, MDZ 2mg QD values were used for MDZ 2mg QD 4 weeks after the last dose of RIF as described in the literature (301). An estimated correction factor of 0.125 was applied to the predicted V_{ss} as described in the method section 6.2.5.1. The predicted vs. observed V_{ss} was 0.42 L/kg vs. 1 L/kg (280). Additionally, the fed intestinal transit rate values were applied to achieve optimal simulation performance. In contrast, the MDZ and RIF DDI clinical study stated participants fasted prior to administration and the MDZ 2mg QD clinical study did not state fed or fasted prior to administration. The predicted vs. observed concentration time profiles are shown in Figure 6.6. The predicted vs. observed AUC_{0-24} (ng×h/ml) and C_{max} (ng/ml) can be found in Table 6.7. Approximately 68% of the predicted parameters were within the 0.75 – 1.25 and 1 – 1.25 ratio and AAFE verification criteria, respectively. A further 24% achieved the 0.5 – 1.5 ratio and 1 – 1.5 AAFE criteria, with most of these involving the $DD_{\%}$ for MDZ 2mg QD 0 and 1 week after the last RIF dose. The concentration time profile for MDZ 2mg QD 4 weeks after the last RIF dose was within the 1 – 2 AAFE verification criteria, whereas for 1 and 2 weeks after the last RIF dose the concentration time profile AAFE value did not meet the criteria. However, upon visual inspection the simulations proved very accurate up to 6 hours after MDZ administration.

A

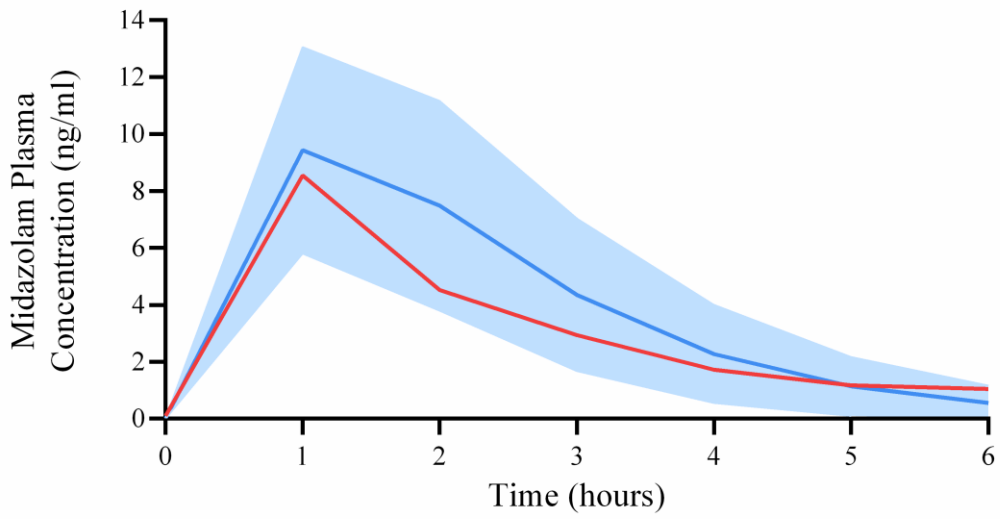
Midazolam Plasma Concentration (ng/ml)
14
12
10
8
6
4
2
0
0
1
2
3
4
5
6
Time (hours)

B

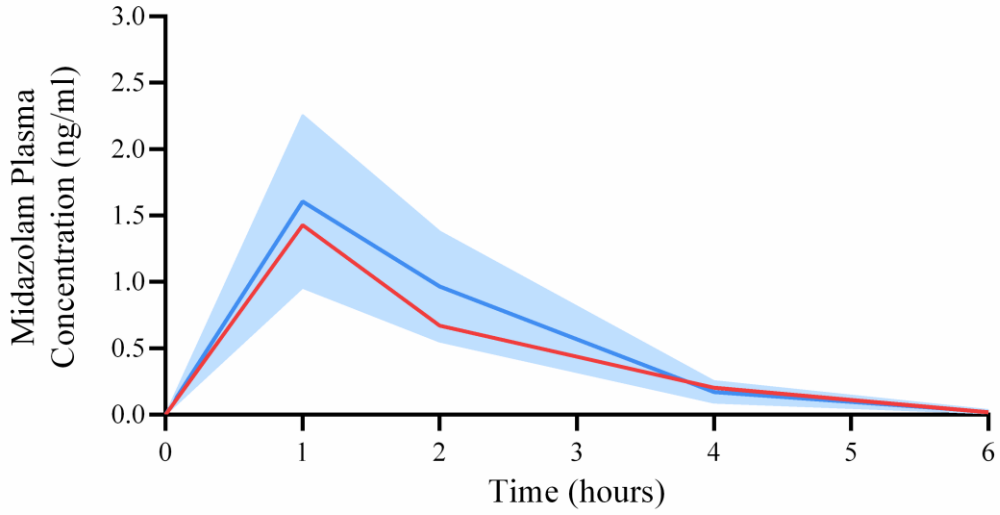
Midazolam Plasma Concentration (ng/ml)
3.0
2.5
2.0
1.5
1.0
0.5
0.0
0
1
2
3
4
5
6
Time (hours)

C

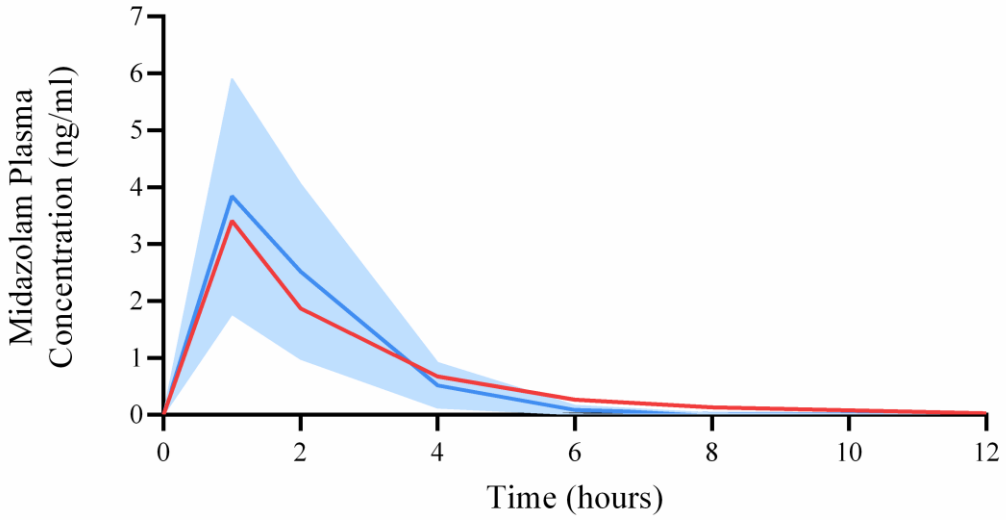
Midazolam Plasma Concentration (ng/ml)
0
1
2
3
4
5
6
7
0
2
4
6
8
10
12
Time (hours)

D

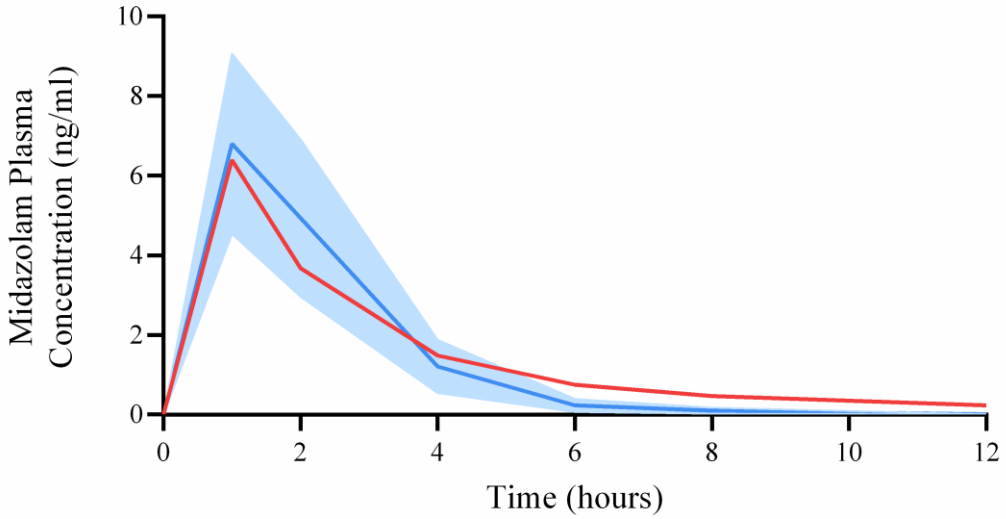
Midazolam Plasma Concentration (ng/ml)
0
2
4
6
8
10
0
2
4
6
8
10
12
Time (hours)

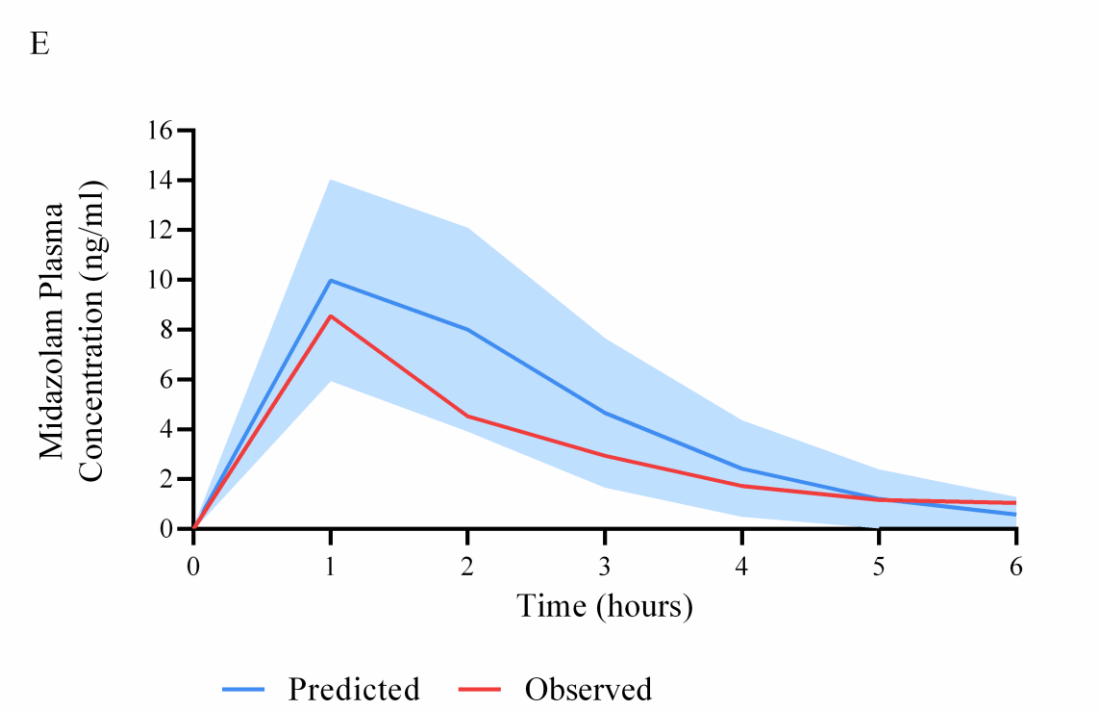

Figure 6.6 Predicted vs. observed concentration time profiles for MDZ 2mg QD (A) and MDZ 2mg QD 0 (B), 1 (C), 2 (D) and 4 (E) weeks after the last RIF 600mg QD dose. Blue lines and blue shaded areas represent the mean plasma concentration ± SD (ng/ml) of the predicted data. Red lines represent the observed clinical data (ng/ml) from each of their respective studies (300, 301).

Table 6.7 Predicted vs. observed MDZ pharmacokinetic parameters.

Drug Regimen	Parameter	Predicted	Observed
MDZ 2mg QD	AUC_{0-24}	26.25 ± 13.19	23.48 ± 11.55 (300)
	C_{max}	9.43 ± 3.62	10.33 ± 3.1 (300)
MDZ 2mg QD/RIF 600mg QD Week 0	AUC_{0-24}	3.90 ± 1.56	2.64 (301)
	C_{max}	1.61 ± 0.65	1.33 (301)
MDZ 2mg QD/RIF 600mg QD Week 1	AUC_{0-24}	9.41 ± 5.46	8.2 (301)
	C_{max}	3.845 ± 2.07	3.31 (301)

MDZ 2mg QD/RIF 600mg QD Week 2	AUC_{0-24}	17.71 ± 7.02	17.44 (301)
	C_{max}	6.8 ± 2.27	6 (301)
MDZ 2mg QD/RIF 600mg QD Week 4	AUC_{0-24}	28.99 ± 15.83	23.48 ± 11.55 (300)
	C_{max}	9.98 ± 4.01	10.33 ± 3.1 (300)
Reference for observed values presented in brackets. AUC_{0-24} values presented as mean ± standard deviation (ng×h/ml). C_{max} values presented as mean ± standard deviation (ng/ml). MDZ – midazolam, RIF – rifampicin, AUC – area under the curve, C_{max} – maximum plasma concentration.			

6.3.2.4 Nifedipine Verification

The NIF PBPK model was verified using available AUC_{0-24} and C_{max} observed clinical data for the oral administration of single dose NIF 10mg and single dose NIF 10mg coadministered with single dose RIF 1200mg (299). An estimated correction factor of 0.15 was applied to the predicted V_{ss} as described in the method section 6.2.5.1. The predicted vs. observed V_{ss} was 0.28 L/kg vs. 0.71 L/kg (289). Additionally, the fed intestinal transit rate values were applied to achieve optimal simulation performance, whereas the observed clinical data stated study participants fasted prior to administration. The predicted vs observed concentration time profiles are shown in Figure 6.7. The predicted vs. observed AUC_{0-24} (µg×h/ml) and C_{max} (µg/ml) can be found in Table 6.8. All single dose NIF 10mg parameters achieved the ratio and AAFE criteria of 0.75 – 1.25 and 1 – 1.25, respectively. For single dose NIF 10mg coadministered with single dose RIF 1200mg the C_{max} and the $DDI_{\%}$ for C_{max} fell within the 0.75 – 1.25 and 1 – 1.25 criteria for ratio and AAFE whilst the AUC and the $DDI_{\%}$ for AUC fell within 0.5 – 1.5 and 1 – 1.5 for ratio and AAFE, respectively.

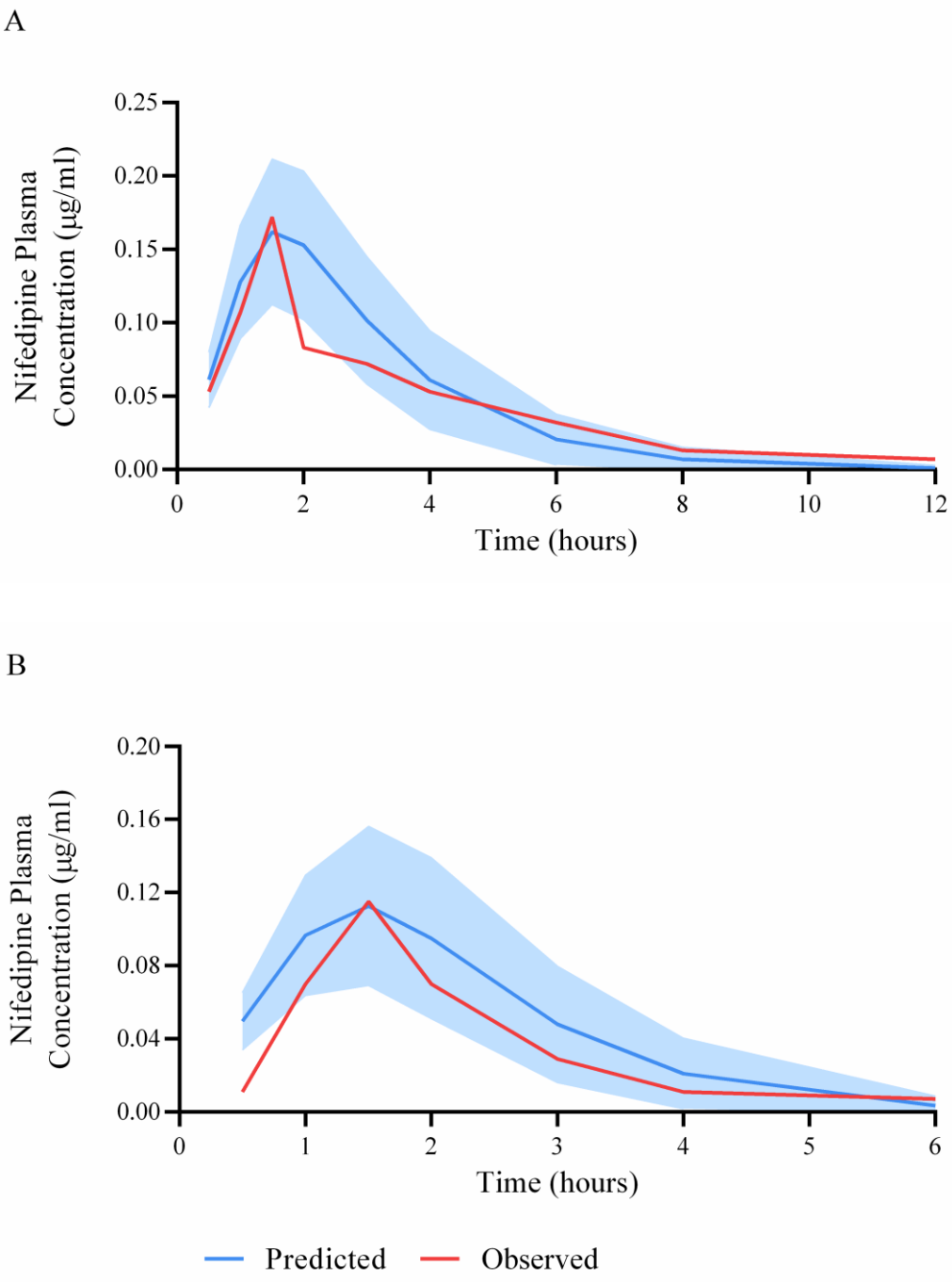

Figure 6.7 Predicted vs. observed concentration time profiles for single dose NIF 10mg (A) and single dose NIF 10mg coadministered 8 hours after single dose RIF 1200mg (B). Blue lines and blue shaded areas represent the mean plasma concentration ± SD (µg/ml) of the predicted data. Red lines represent the observed clinical data (µg/ml) (299).

Table 6.8 Predicted vs. observed NIF pharmacokinetic parameters.

Drug Regimen	Parameter	Predicted	Observed (299)
NIF 10mg	AUC_{0-24}	0.54 ± 0.22	0.57 ± 0.014
	C_{max}	0.16 ± 0.05	0.17 ± 0.006
NIF 10mg/RIF 1200mg	AUC_{0-24}	0.28 ± 0.16	0.21 ± 0.016
	C_{max}	0.11 ± 0.04	0.12 ± 0.008

Reference for observed values presented in brackets. AUC_{0-24} values presented as mean ± standard deviation (µg/h/ml). C_{max} values presented as mean ± standard deviation (µg/ml). All drug regimens were single dose. NIF – nifedipine, RIF – rifampicin, AUC – area under the curve, C_{max} – maximum plasma concentration.

6.3.3 UGT1A1 Induction Model Optimisation and Verification

6.3.3.1 UGT1A1 Induction Model Optimisation

Due to the lack of literature data surrounding the induction of UGT1A1 by RIF, the complete UGT1A1 fold change induction profile could not be verified and was instead verified against a singular steady state fold change value. Induction parameters were optimised according to the observed clinical data for RAL 400mg QD and RAL 400mg QD coadministered with RIF 600mg QD, as described in method section 6.2.5.3. The $DDI_{\%}$ was calculated for both predicted and observed data and the ratio and AAFE were determined. The optimised UGT1A1 induction parameter values for $K_{inact,pxr}$, $K_{enzyme,deg}$, $K_{rna,deg}$, q and p were 0.1 h^{-1}, 0.0144 h^{-1} (271), 0.0756 h^{-1} (271), 0.2 and 0.272, respectively. The resulting UGT1A1 fold change induction profile following 28 days repeated oral administration of rifampicin 600mg QD and 28 days after the last RIF dose can be found in Figure 6.8. The maximum UGT1A1 fold change was 1.75 ± 0.25 vs. 2.28 ± 0.81 (274) for predicted vs. observed, respectively. This corresponded to a ratio value of 0.77 and AAFE value of 1.3, achieving the 0.75 – 1.25 and 1 – 1.25 criteria, respectively.

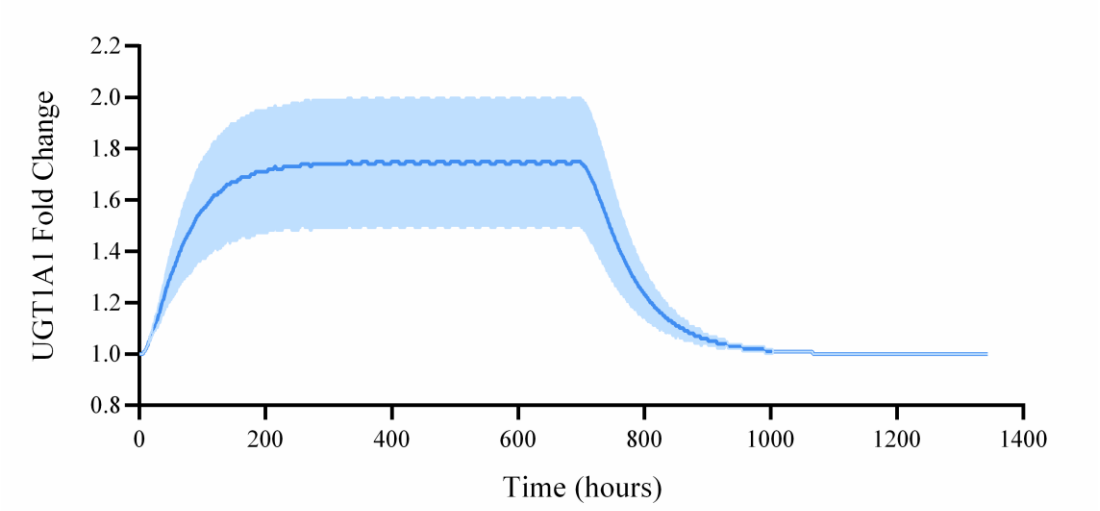

Figure 6.8 Predicted UGT1A1 fold change following 28 days repeated oral administration of RIF 600mg QD using the optimised induction parameters. Data expressed as mean fold change ± SD.

6.3.3.2 Raltegravir Verification

The RAL PBPK model was verified using available AUC_{0-24} and C_{max} data for the oral administration of RAL 400mg QD and RAL 400mg QD coadministered with RIF 600mg QD (302). As described in the method section 6.2.5.1, an estimated correction factor of 0.6 was applied to the predicted V_{ss}. The predicted vs. observed V_{ss} was 0.22 L/kg vs. 0.4 L/kg (290). The predicted vs. observed concentration time profiles can be found in Figure 6.9. The predicted vs. observed AUC_{0-24} (µg×h/ml) and C_{max} (µg/ml) pharmacokinetic parameters can be found in Table 6.9. The AUC for both RAL 400mg QD and RAL 400mg QD coadministered with RIF 600mg QD were within the 0.5 – 1.5 and 1 – 1.5 criteria for ratio and AAFE, respectively. The C_{max} and $DDI_{\%}$ for both AUC and C_{max} were within the stringent criteria of 0.75 – 1.25 and 1 – 1.25 for ratio and AAFE, respectively. The concentration time profile for RAL 400mg QD was within the 1 – 1.5 criteria for AAFE whilst RAL 400mg QD coadministered with RIF 600mg was within the 1 – 2 criteria.

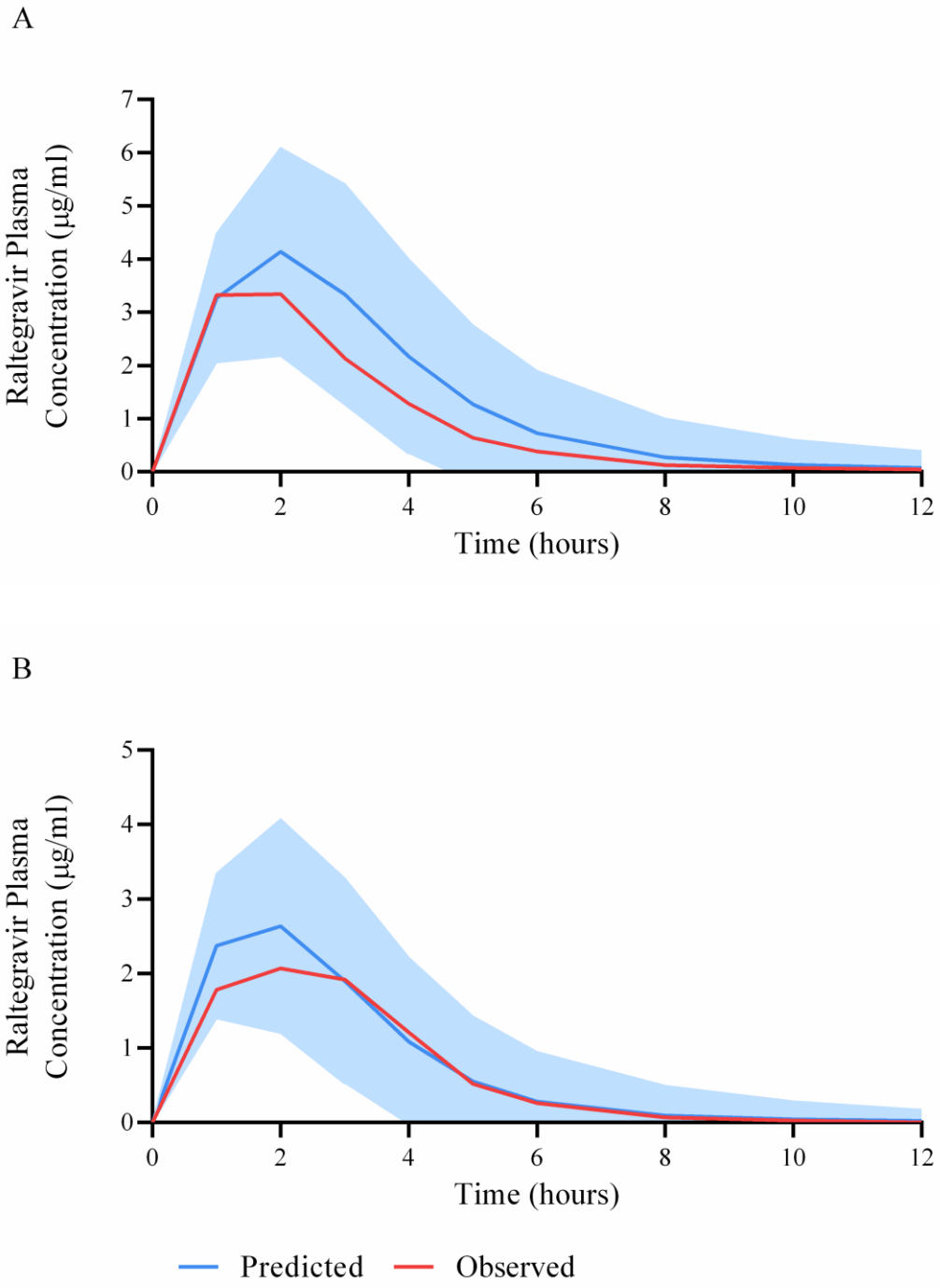

Figure 6.9 Predicted vs. observed concentration time profiles for RAL 400mg QD (A) and RAL 400mg QD coadministered with RIF 600mg QD (B). Blue lines and blue shaded areas represent the mean plasma concentration ± SD (µg/ml) of the predicted data. Red lines represent the observed clinical data (µg/ml) (302).

Table 6.9 Predicted vs. observed RAL pharmacokinetic parameters.

Drug Regimen	Parameter	Predicted	Observed (302)
RAL 400mg QD	AUC_{0-24}	16.5 ± 13.15	12.25
	C_{max}	4.14 ± 1.96	3.83
RAL 400mg QD/RIF 600mg QD	AUC_{0-24}	9.46 ± 7.93	7.34
	C_{max}	2.64 ± 1.43	2.37
Reference for observed values presented in brackets. AUC_{0-24} values presented as mean ± SD (µg/h/ml). C_{max} values presented as mean ± SD (µg/ml). NIF – nifedipine, RIF – rifampicin, AUC – area under the curve, C_{max} – maximum plasma concentration.			

6.3.4 Dolutegravir Verification

The DTG PBPK model was verified using the optimised induction parameters for both CYP3A4 and UGT1A1. Observed AUC_{0-24}, C_{max} and C_{min} clinical data for the oral administration of DTG 50mg QD, DTG 50mg QD coadministered with 600mg RIF (303), DTG 50mg BID and DTG 50mg BID coadministered with 600mg RIF (100) were utilised. An estimated correction factor of 0.08 was applied to the predicted V_{ss} as described in the method section 6.2.5.1. The predicted vs. observed V_{ss} was 0.16 L/kg vs. 0.25 L/kg (279). Furthermore, the fasted intestinal transit rate values were applied to achieve optimal simulation performance, whereas the observed clinical data stated study participants ate a meal prior to administration. The predicted vs. observed concentration time profiles are shown in Figures 6.10 and 6.11. The predicted vs. observed AUC_{0-24}, C_{max}, and C_{min} can be found in Table 6.10. Around 50% of the predicted pharmacokinetic parameters and concentration time profiles were with the 0.75 – 1.25 ratio and 1 – 1.25 AAFE criteria. Approximately 38% were within the 0.5 – 1.5 ratio and 1 – 1.5 AAFE criteria with the remaining 12% being within 0.5 – 2 and 1 – 2 for ratio and AAFE, respectively. Moreover, the combined CYP3A4 and UGT1A1 induction models were considered successfully optimised by meeting the verification criteria.

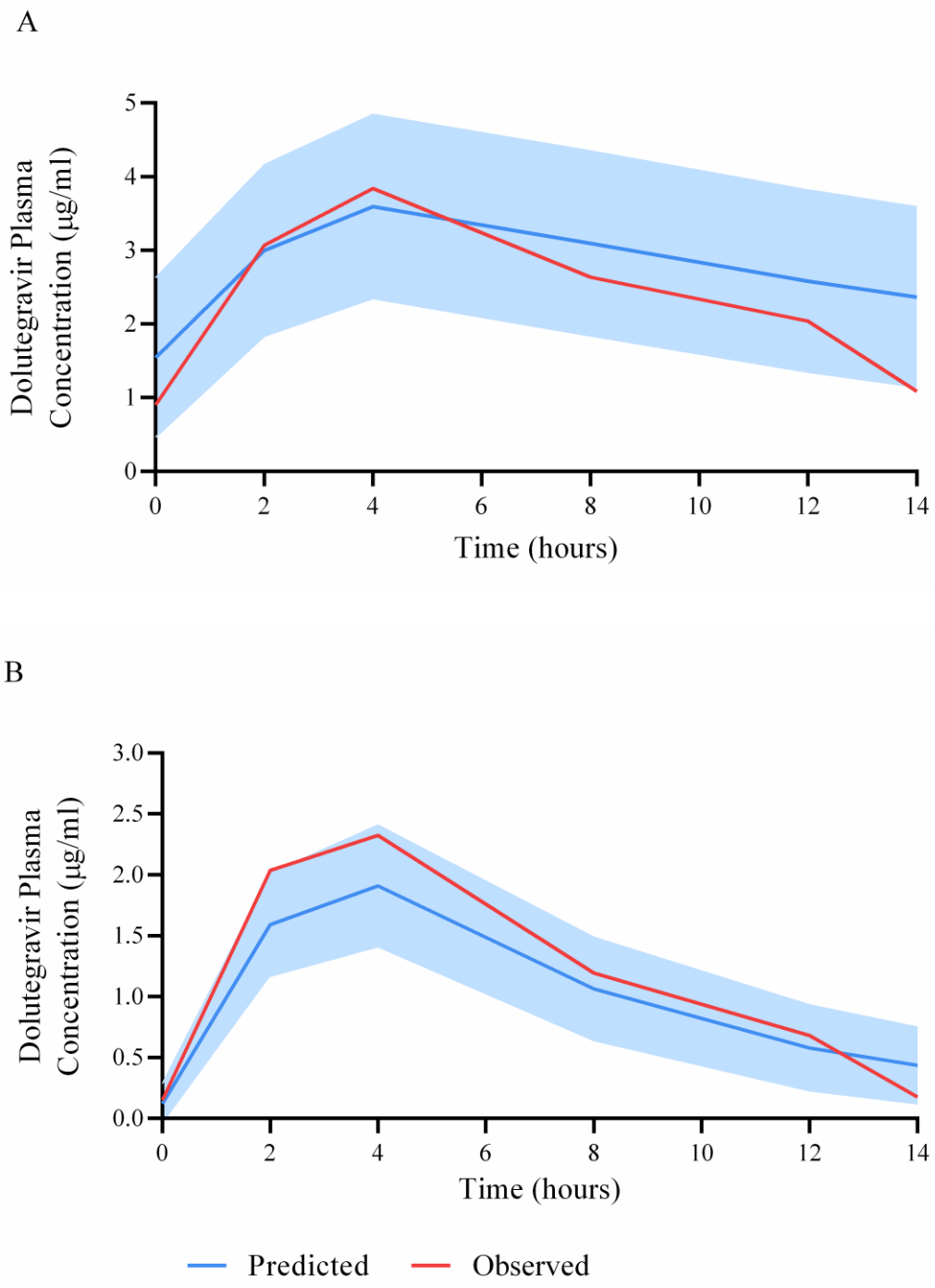

Figure 6.10 Predicted vs. observed concentration time profiles for DTG 50mg QD (A) and DTG 50mg QD coadministered with RIF 600mg QD (B). Blue lines and blue shaded areas represent the mean plasma concentration ± SD (ng/ml) of the predicted data. Red lines represent the observed clinical data (ng/ml) (303).

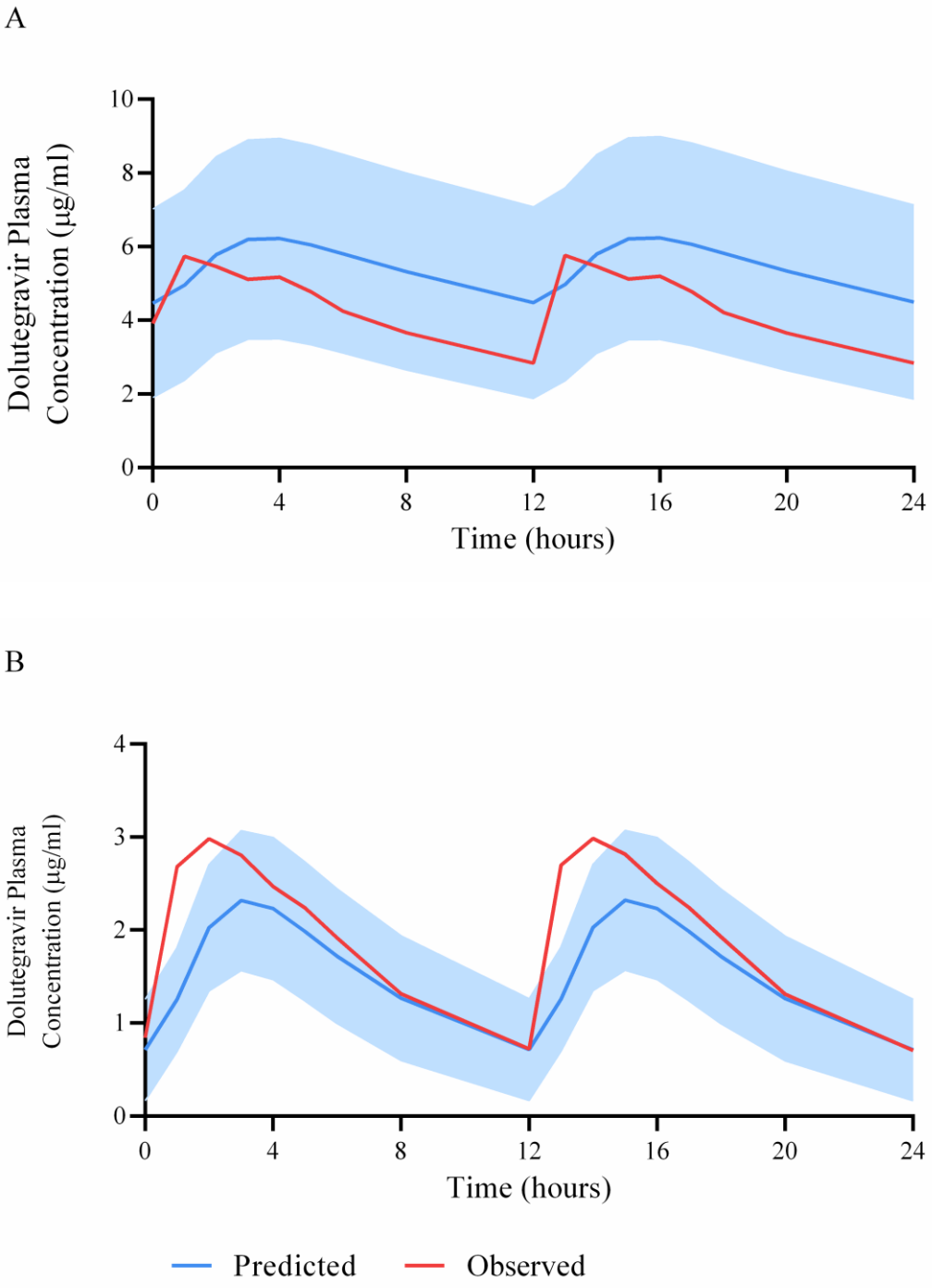

Figure 6.11 Predicted vs. observed concentration time profiles for DTG 50mg BID (A) and DTG 50mg BID coadministered with RIF 600mg QD (B). Blue lines and blue shaded areas represent the mean plasma concentration ± SD (ng/ml) of the predicted data. Red lines represent the observed clinical data (ng/ml) (100).

Table 6.10 Predicted vs. observed DTG pharmacokinetic parameters.

Drug Regimen	Parameter	Predicted	Observed
DTG 50mg QD	AUC_{0-24}	53.97 ± 21.69	52.1 (303)
	C_{max}	3.60 ± 1.25	3.97 (303)
	C_{min}	1.56 ± 1.11	1.06 (303)
DTG 50mg QD/RIF 600mg QD	AUC_{0-24}	17.66 ± 6.81	22.75 (303)
	C_{max}	1.91 ± 0.50	2.57 (303)
	C_{min}	0.12 ± 0.16	0.156 (303)
DTG 50mg BID	AUC_{0-24}	112.76 ± 46.82	92.7 (100)
	C_{max}	6.22 ± 2.72	5.55 (100)
	C_{min}	4.49 ± 2.63	2.41 (100)
DTG 50mg BID/RIF 600mg QD	AUC_{0-24}	35.66 ± 20.61	42.6 (100)
	C_{max}	2.32 ± 0.75	3.13 (100)
	C_{min}	0.71 ± 0.55	0.67 (100)

Reference for observed values presented in brackets. AUC_{0-24} values presented as mean ± SD (µg/h/ml). C_{max} and C_{min} values presented as mean ± SD (µg/ml). DTG - dolutegravir, RIF – rifampicin, AUC – area under the curve, C_{max} – maximum plasma concentration, C_{min} – minimum plasma concentration.

Table 6.11 PBPK model verification summary of predicted vs. observed clinical data.

Drugs	Dose (mg)	Ratio				AAFE				
		AUC	C_{max}	C_{min}	C_{avg}	AUC	C_{max}	C_{min}	C_{avg}	Profile
RIF	600 QD	1.14	1.10	-	-	1.14	1.10	-	-	1.11
RIF	1200 SD	-	1.19	1.17	-	-	1.19	1.17	-	1.02
RAL	400 QD	1.35	1.08	-	-	1.35	1.08	-	-	1.62
RAL/RIF	400 QD/600 QD	1.29	1.11	-	-	1.29	1.11	-	-	1.43
NIF	10 S	0.94	0.96	-	-	1.06	1.04	-	-	1.21
NIF/RIF	10 S/1200 S	1.33	0.94	-	-	1.33	1.06	-	-	1.42
MDZ	2 QD	1.12	1.91	-	-	1.12	1.10	-	-	1.11
MDZ/RIF Week 0	2 QD/600 QD	1.50	1.23	-	-	1.50	1.23	-	-	1.13
MDZ/RIF Week 1	2 QD/600 QD	1.15	1.15	-	-	1.15	1.15	-	-	3.72
MDZ/RIF Week 2	2 QD/600 QD	1.02	1.13	-	-	1.02	1.13	-	-	3.30

MDZ/RIF Week 4	2 QD/600 QD	1.23	0.97	-	-	1.23	1.06	-	-	1.98
DTG	50 QD	1.04	0.91	1.47	-	1.04	1.10	1.47	-	1.31
DTG/RIF	50 QD/600 QD	0.78	0.76	0.77	-	1.28	1.31	1.30	-	1.01
DTG	50 BID	1.22	1.12	1.86	-	1.22	1.12	1.86	-	1.23
DTG/RIF	50 BID/600 QD	0.84	0.74	1.06	-	1.19	1.35	1.06	-	1.24

Ratio data presented as predicted vs observed. AAFE data calculated as previously described in method section 6.2.4, equation 12. RAL – raltegravir, RIF – rifampicin, NIF – nifedipine, MDZ – midazolam, DTG – dolutegravir, S – single dose, QD – once daily, BID – twice daily, AAFE – absolute average fold error, AUC – area under the curve, C_{max} – maximum plasma concentration, C_{min} – minimum plasma concentration, C_{avg} – average plasma concentration, Profile – concentration time profile.

Table 6.12 PBPK model verification of predicted vs observed clinical data as a percentage of DDI vs drug alone.

Drug	Dose (mg)	RIF Dose (mg)	Ratio			AAFE		
			AUC	C_{max}	C_{min}	AUC	C_{max}	C_{min}
RAL	400 QD	600 QD	0.96	1.03	-	1.05	1.03	-
NIF	10 S	1200 S	1.45	0.98	-	1.45	1.02	-
MDZ Week 0	2 QD	600 QD	1.34	1.35	-	1.34	1.35	-
MDZ Week 1	2 QD	600 QD	1.02	1.26	-	1.02	1.26	-
MDZ Week 2	2 QD	600 QD	0.91	1.24	-	1.10	1.24	-
MDZ Week 4	2 QD	600 QD	1.10	1.06	-	1.10	1.06	-
DTG	50 QD	600 QD	0.68	0.84	0.53	1.48	1.19	1.90
DTG	50 BID	600 QD	0.69	0.61	0.57	1.45	1.63	1.76

Ratio data presented as predicted vs observed. AAFE data calculated as previously described in method section 7.2.4, equation 12. RAL – raltegravir, RIF – rifampicin, NIF – nifedipine, MDZ – midazolam, DTG – dolutegravir, S – single dose, QD – once daily, BID – twice daily, AAFE – absolute average fold error, AUC – area under the curve, C_{max} – maximum plasma concentration, C_{min} – minimum plasma concentration.

6.3.5 Once Monthly Rifampicin Coadministered with Dolutegravir

The verified DTG PBPK model together with the CYP3A4 and UGT1A1 induction PBPK model were used to predict 35 days repeated oral administration of DTG 50mg BID with single dose RIF 1200mg administration on day 7. The predicted CYP3A4 and UGT1A1 fold change induction profiles following the administration of single dose RIF 1200mg can be found in Figures 6.12 and 6.13, respectively. Predicted C_{max}, C_{avg} and C_{min} as well as the minimum target concentration of 4 x PA-IC_{90} of DTG (0.256 µg/ml) (277) are shown in Figure 6.14. The predicted C_{max}, C_{avg} and C_{min} mean values for DTG 50mg BID coadministered with single dose RIF 1200mg were above 4 x PA-IC_{90} of DTG throughout the simulation time period. However, these pharmacokinetic parameter values were substantially reduced after the administration of RIF 1200mg and took up to 28 days to return to their steady state values. The maximum CYP3A4 and UGT1A1 fold changes were 10.5-fold and 1.4-fold and were reached 56 hours and 57 hours after RIF 1200mg administration, respectively. When considering the predicted SD, the C_{min} ± SD for DTG 50mg BID coadministered with RIF 1200mg QMT fell below 4 x PA-IC_{90} of DTG on days 1, 2, 3 and 4 after RIF administration. A summary of the results are shown in Table 6.13.

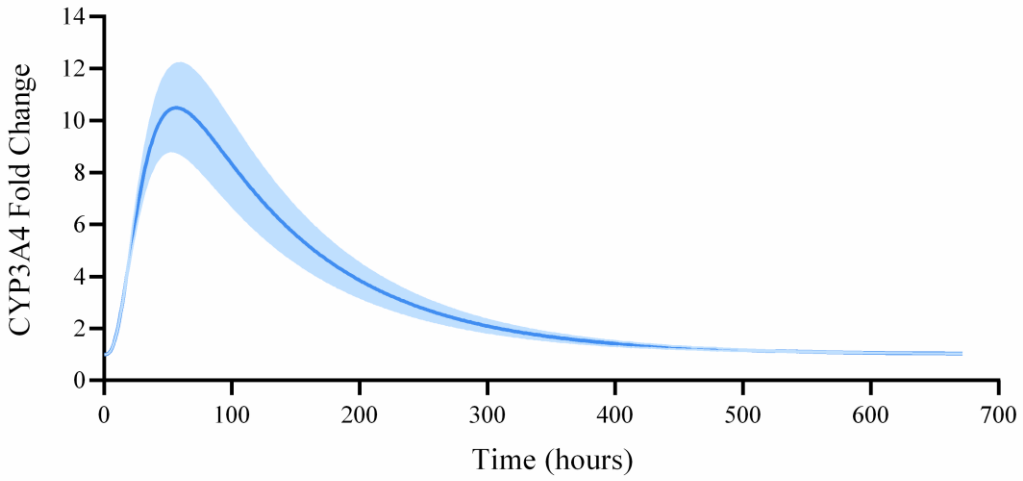

Figure 6.12 Predicted CYP3A4 fold change following the administration of single dose RIF 1200mg. Data expressed as mean fold change ± SD.

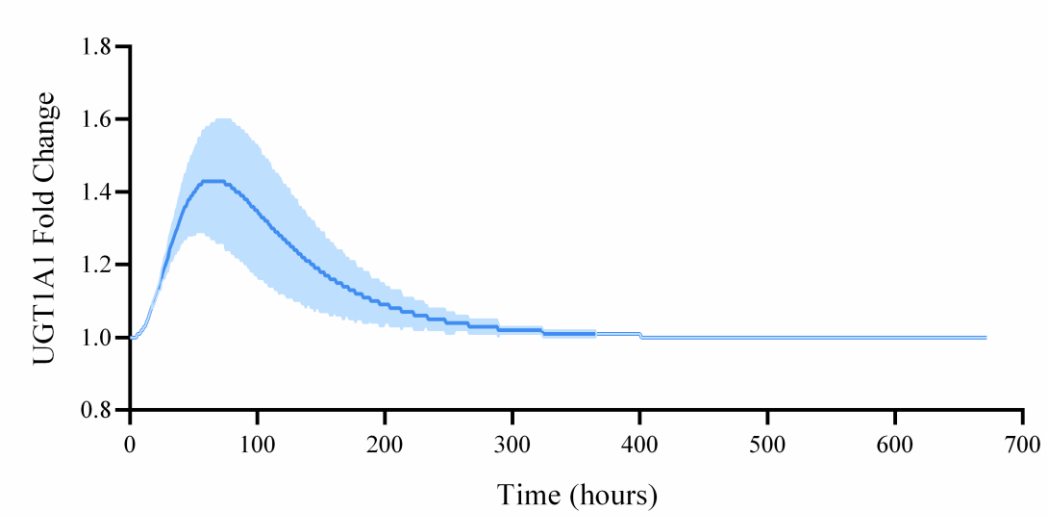

Figure 6.13 Predicted UGT1A1 fold change following the administration of single dose RIF 1200mg. Data expressed as mean fold change ± SD.

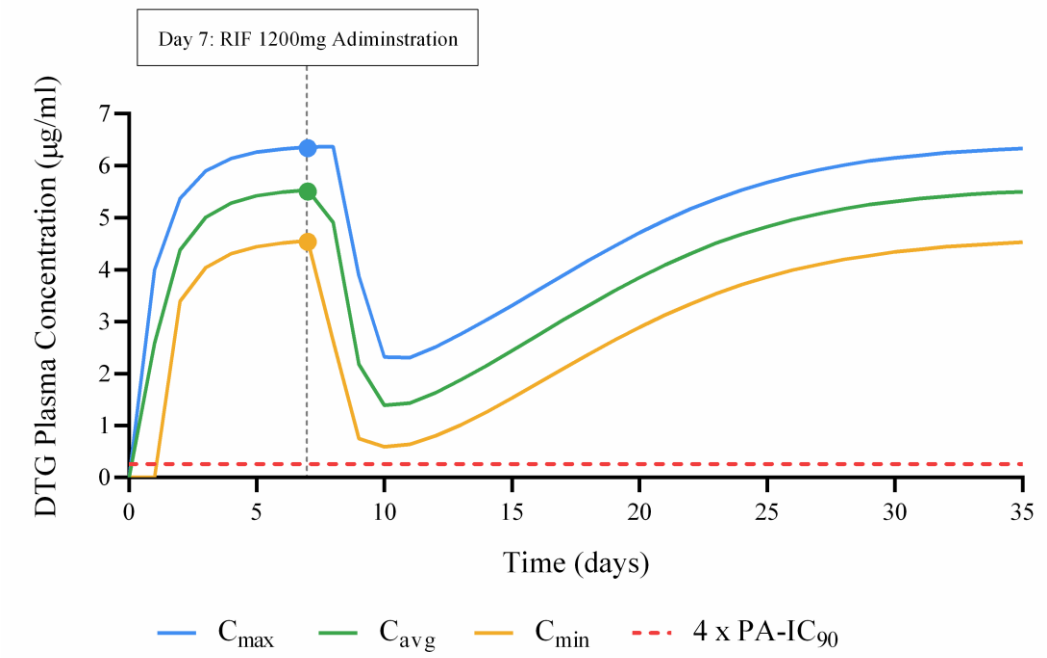

Figure 6.14 Predicted concentration time profile for DTG following 35 days repeated oral administration of DTG 50mg BID with single dose RIF 1200mg administration on day 7. The blue, green and yellow lines represent the mean C_{max}, C_{avg}, and C_{min} (µg/ml) of DTG, respectively. The blue, green and yellow circles represent the administration of RIF on day 7. The red dashed line represents the minimum target concentration of 4 x PA-IC_{90} of DTG (0.256 µg/ml) (277).

Table 6.13 Predicted DTG C_{min} following 35 days oral administration of DTG 50mg BID with single dose RIF 1200mg administration on day 7.

Days After RIF Dose	DTG C_{min} (µg/ml)
0	2.63 ± 1.97
1	0.75 ± 0.75
2	0.59 ± 0.54
3	0.64 ± 0.55
4	0.80 ± 0.61
5	1.01 ± 0.71
6	1.26 ± 0.82
7	1.53 ± 0.94

DTG C_{min} values are presented as mean ± SD. Cells highlighted in purple represent C_{min} concentrations ± SD that fell below 4 x PA-IC_{90} of DTG (0.256 µg/ml). RIF – rifampicin, DTG – dolutegravir, C_{min} – minimum plasma concentration.

6.4 Discussion

The implementation of higher doses of RIF across several clinical scenarios has been of growing interest recently. RIF is a potent inducer of several enzymes and the magnitude of DDIs resulting from higher doses is unknown (99). PBPK modelling is a powerful tool that can be used to elucidate unknown clinical scenarios, aid in the design of clinical studies and provide direct insight to clinicians during such investigative periods. In this study, a dynamic PBPK model describing the combined induction of CYP3A4 and UGT1A1 by RIF was developed and verified to predict the magnitude of DDI between RIF 1200mg QMT and DTG 50mg BID for the treatment of leprosy in PLWH.

6.4.1 Minimal Rifampicin PBPK Model

Owing to the lack of knowledge and data surrounding RIF ADME, it is common practice to adopt less mechanistically correct designs when predicting RIF pharmacokinetics via PBPK modelling (214-216). Although the minimal RIF PBPK model employed in this study does not describe the complexities of RIF ADME, it was able to predict RIF pharmacokinetic and concentration time profile data within the strict 0.75 – 1.25 ratio and 1 – 1.25 AAFE verification criteria. The model utilised published data on protein binding, CL/F and V_{ss} and when data were unavailable, estimated these parameters according to observed clinical data.

6.4.2 CYP3A4 Induction Model

A dynamic PBPK model that accounts for the variations in the level of enzyme activity over time was selected for this study as the prediction of QMT RIF induction rather than steady state RIF induction was required. Most dynamic models consider the induction of enzyme synthesis to occur in a concentration dependent manner, however previous studies have described a delay in the time taken for mRNA to reach its maximum level after the administration of RIF (264, 304, 305). Therefore, a more complex model with mathematical descriptions of enzyme transcription and translation dynamics was required. A paper was recently published comparing the current mathematical models describing the dynamics of PXR-mediated CYP3A4 gene regulation (306). Therein, two models were highlighted that specifically

described RIF induction, of which only one described RIF-induced DDIs (264, 305). The induction equations and optimised parameters reported in the RIF induction DDI model were chosen for the induction model implemented in this study and as described in results section 6.3.2.1, the CYP3A4 fold change induction profile was well replicated in conjunction with the minimal RIF PBPK model (264).

For the verification of the CYP3A4 induction model, drugs solely metabolised by CYP3A4 were required. Unfortunately, there were no clinical data for the DDI between single dose RIF coadministered with a CYP3A4 substrate drug at steady state, reflecting the required application of this model. Furthermore, there was a limited amount of clinical data for DDIs with doses of RIF greater than 600mg. In the absence of this data, two clinical studies were identified that would allow for an alternative verification of the CYP3A4 induction model and parameters: single dose NIF 10mg coadministered with single dose RIF 1200mg (299) and MDZ 2mg QD coadministered with RIF 600mg QD and up to 4 weeks after the discontinuation of RIF (300, 301). The single dose NIF DDI dataset comprised of data for the first 24 hours of the DDI with RIF and so its objective was to verify the delay in the fold change of mRNA after the initial administration of RIF. The MDZ DDI dataset provided both data for the RIF DDI at steady state, but more importantly for the RIF DDI after its discontinuation, thus verifying the duration of the induction effect beyond 24 hours. The whole-body PBPK model together with the minimal RIF PBPK model and CYP3A4 induction PBPK model with previously optimised parameters were used to predict the abovementioned DDI datasets, as described in method section 6.2.5.2. It was concluded that, due to the AAFE and ratio values being suboptimal, the induction parameters required further optimisation to generate more accurate predictions.

Optimising induction parameters is challenging. There remains a lack of consensus on the parameter values used to described CYP3A4 induction (273). This is largely due to the absence of key parameter values as well as discrepancies between the values that are available and the clinical datasets used to verify them. For example, as previously described and demonstrated in this study, the rate of enzyme degradation is a major determinant of the induction profile (273). CYP3A4 degradation rates between 0.005 h^{-1} and 0.07 h^{-1} have previously been reported using a multitude of *in vitro* methods, of which several differing values have been implemented into PBPK models (264, 306, 307). Previous studies have described how values of or similar to

0.03 h^{-1} have improved PBPK model predictions in comparison to smaller values (264, 307). However, we found that through our optimisation process, the previously published value of 0.0096 h^{-1} provided the most accurate predictions (272). It must be noted that the published value was optimised with the same clinical MDZ data used in this study. Thus, it cannot necessarily be concluded that one value is more appropriate than the other without verifying them against a range of clinical datasets. Furthermore, there were limited or no data available for the rate constants for PXR-mediated CYP3A4 mRNA synthesis, CYP3A4 synthesis, CYP3A4 mRNA degradation as well as the constant for negative feedback inhibition and the inactivation rate constant for activated PXR. Thus, these parameters were mostly estimated. Nevertheless, the CYP3A4 PBPK induction model was successfully verified largely to the stricter criteria if not the widely accepted verification criteria range, albeit with two exceptions. The AAFE values for the concentration time profile of MDZ 2mg QD 1 and 2 weeks after the last RIF dose were outside the 1 – 2 criteria. After visual inspection it can be seen that this was due to minimal differences in the tail end of the profiles. Considering the accuracy of the rest of the profile alongside the pharmacokinetic parameters achieving the strict verification criteria, these AAFE values were deemed acceptable.

6.4.3 UGT1A1 Induction Model

To our knowledge, this is the first dynamic PBPK model to predict PXR-mediated induction of UGT1A1 by RIF. Owing to the even more sparsely available data surrounding UGT1A1 induction, the verification process was limited in comparison to the CYP3A4 induction model. UGT1A1 is induced via the same PXR mechanism as CYP3A4 and so the same induction equations were implemented (274). Having said that, RIF has previously been described to induce CYP3A4 more efficiently than UGT1A1 and so this was taken into consideration whilst optimising the induction parameters (99).

There were several similarities between the optimisation process of UGT1A1 and CYP3A4. Firstly, drugs solely metabolised by UGT1A1 were required. Again, there were no clinical data for the DDI between single dose RIF coadministered with a UGT1A1 substrate drug at steady state. Nor were there clinical data available reflecting the datasets used in the CYP3A4 induction model. Hence clinical data for

the DDI between RAL 400mg QD and RIF 600mg QD (302) at steady state along with *in vitro* data of the fold change of UGT1A1 mRNA (274) were employed for the verification of the UGT1A1 induction model. Secondly, the same iterative process for optimising parameters was employed, albeit with two exceptions. The value for $k_{inact,pxr}$ was assumed to be the same for both CYP3A4 and UGT1A1 because of the paucity of information surrounding this process. With the CYP3A4 induction parameters being optimised against a larger more coherent clinical dataset, the value for $k_{inact,pxr}$ was estimated during the optimisation of the CYP3A4 induction model. The value for p was determined by calculating $K_{i,NF}$ from the estimated CYP3A4 p value and applying it to the p equation for UGT1A1. Once more assuming it to be the same for both CYP3A4 and UGT1A1 and optimising the value via the CYP3A4 induction model with a similar rationale. Nonetheless, the UGT1A1 induction model was successfully verified against the RAL data sets. Interestingly, the predicted steady state fold induction of UGT1A1 using the abovementioned parameters was approximately 23% lower than the reported literature value. That being said, with the UGT1A1 induction model being verified against steady state DDI data we must be cautious when analysing the predicted data from any future applications.

6.4.4 Predicting Dolutegravir Drug-Drug Interactions

Verification of the combined CYP3A4 and UGT1A1 induction PBPK model was carried out with clinical data for DTG 50mg QD and DTG 50mg BID coadministered with RIF 600mg QD. Although the combined models were successfully verified, only 50% were within the strict criteria. It was found that the model tended to overpredict the magnitude of induction for RIF 600mg QD with both DTG regimens, specifically regarding the C_{min}. Three factors should be considered regarding this overprediction. Firstly, as described in method section 6.2.2, there were no available *in vitro* data for the metabolic pathways of DTG. In the absence of such data the fraction of DTG metabolised by UGT1A1, CYP3A4, UGT1A3 and UGT1A9 determined from the detection of radioactive metabolites in a human mass balance study were implemented (268). However, it was found that by using these fractions the clearance of DTG was underpredicted. The abovementioned study advised that due to the instability of the UGT metabolite, the fraction metabolised by UGT could be underestimated. The fractions relating to UGT1A3, UGT1A9 and the remaining

uncategorised fraction were collated with the UGT1A1 fraction and the DTG regimens simulated. The pharmacokinetic and concentration time profile predictions proved most accurate using this method and due to the lack of available data, was deemed to be justified. Although, based on the observed overprediction of DDI between DTG and RIF, neither of these enzyme parameters may be accurate.

Secondly, as described in method section 6.2.5.1, to obtain the most accurate predictions a correction factor was estimated and applied to the predicted V_{ss} of DTG. During this process it was found that the optimal correction factor for the DTG regimens alone and with RIF differed. These findings suggest a potential alteration in DTG's V_{ss} during the DDI with RIF. Information regarding DTG V_{ss} is limited and topics divulging such changes in V_{ss} can be controversial. For example, previous studies have described the ability of a drug to be displaced in the presence of another drug with a higher protein binding affinity (308). For highly protein bound drugs, even the smallest of changes in unbound concentration can lead to alterations in the drugs V_{ss} (309). However, this phenomenon was not observed for NIF or MDZ which are also highly protein bound. This concept also suggests that RIF would be the effected drug, not DTG. Taking this into consideration alongside the insufficient clinical data, the V_{ss} correction factor estimated for optimal predictions of both DTG with and without RIF was selected. However, it should be acknowledged that this factor contributed towards the overprediction of C_{min} in the DTG 50mg QD and DTG 50mg BID regimens.

Lastly, the DDI magnitude overprediction could also be due in part to the limited optimisation and verification of the UGT1A1 induction model as UGT1A1 contributes towards at least 51% of DTG's overall metabolism (267). However, as this study has identified, future experimentation to expand upon the currently available UGT1A1 induction and DTG metabolism data is required to further refine this model. Nonetheless, the predictions made by this model for unknown clinical scenarios provide a valuable insight and their analysis should take this overprediction into careful consideration.

6.4.5 High Dose Rifampicin for the Treatment of Leprosy in PLWH Taking Dolutegravir

As previously described, the verified DTG PBPK model together with the CYP3A4 and UGT1A1 induction PBPK model were used to predict repeated oral administration of DTG 50mg BID with single dose RIF 1200mg for the treatment of leprosy in PLWH. There were substantial reductions in the mean C_{max}, C_{avg} and C_{min} values and interestingly, it took up to 28 days for these pharmacokinetic parameters to return to their steady state values. Despite this, the mean values remained above 4 x PA-IC_{90} of DTG. Though when considering the predicted SD, the C_{min} ± SD for DTG 50mg BID fell below 4 x PA-IC_{90} of DTG for the initial days after single dose RIF 1200mg administration. As mentioned previously, the models used in this application tend to overpredict the magnitude of DDI between RIF 600mg QD and DTG 50mg BID and so it is acceptable to describe these DDI predictions as the "worst-case scenario". However, if doses greater than 1200mg were to be implemented for the treatment of leprosy, these predictions indicate that the resulting DDI may have the potential to produce C_{max}, C_{avg} and C_{min} values below 4 x PA-IC_{90} of DTG. Although it must be noted that the pharmacokinetic profiles of differing doses of RIF are not linear and so a direct extrapolation cannot be made from these predictions (219). Furthermore, higher doses of RIF for the treatment of leprosy have previously been avoided partly due to reports of adverse reactions and drug toxicity associated with intermittent dosing of RIF at higher doses (60, 61). However, these studies only considered once or twice weekly dosing of RIF and so adverse reactions for once monthly dosing would require further investigation. Additionally, a previously reported static model predicted a 3-fold change in DTG AUC when coadministered with clofazimine (310). However, as the effect of RIF induction on CYP3A4 is believed to be the dominating DDI mechanism, the impact of clofazimine CYP3A4 inhibition is thought to be insignificant in the coadministration of DTG and leprosy MDT although further confirmatory studies are required.

6.4.6 Conclusion

While both the CYP3A4 and UGT1A1 induction models were successfully verified, the lack of *in vitro* and *in vivo* data for model optimisation and verification

remains a limitation of this study and careful consideration must be taken when analysing these predictions. Specifically, analysis must acknowledge the tendency to overpredict DTG DDIs with RIF. Nevertheless, the model predicted that no further dosage adjustments were required to maintain the plasma concentration of DTG above the acceptable criteria when coadministered with higher doses of RIF for the treatment of leprosy in PLWH. This study provides useful evidence-based guidance towards the clinical management of DDI scenarios yet to be investigated in clinical trials. Furthermore, this study highlighted the experimental parameter data that is missing to create a comprehensive mathematical model for RIF time-based enzyme induction, particularly regarding enzymes other than CYP3A4.

Chapter 7

General Discussion

Contents

7.1 DDIs in People Living with HIV

ART for the treatment of HIV is continuously evolving, with the latest ARVs being characterised by more favourable pharmacodynamic and pharmacokinetic profiles (311). However, DDIs remain a key issue in the clinical management of PLWH. Currently, ART regimens consist of multiple ARVs targeting different stages of the HIV replication cycle and PLWH can receive different combinations of ARVs due to resistance or specific clinical characteristics, generating an expansive range of potential DDIs (103, 312). This is exacerbated by the high rate of comorbidities and polypharmacy found in different sub-populations and considering the increased life expectancy of PLWH, new and complex clinical scenarios are emerging as a product of older age (87). Furthermore, with the introduction of LA ARVs for the treatment of HIV and the development of alternative administration strategies for ART, having a deep understanding of the role of DDIs and their mechanisms of action is important now more than ever (313). In particular, with the cessation of treatment not being as simple under some of the abovementioned applications it is imperative that we have a detailed knowledge of the potential for an adverse DDI to occur. This also applies to innovations in the treatment of other infectious diseases and morbidities, with conventional treatment strategies being replaced as research and technology advances.

It is clear that the landscape of HIV is changing and the underrepresentation of sub-populations as well as pharmacokinetic mechanisms in research is hindering our ability to make optimised, well-informed clinical decisions for all PLWH. Specifically, there continues to be a paucity of knowledge surrounding transporters despite their substantial role in drug pharmacokinetics and DDIs (69). This gap is underpinned by the inability of current assessment techniques to efficiently extrapolate *in vitro* data and evaluate individual transporters on both an *in vitro* and clinical level (131, 133). Additionally, DDI guidelines for OALWH as well as PLWH with uncommon clinical scenarios are lacking due to their limited inclusion in clinical studies (102, 103). The overall aim of this thesis was to develop and verify an efficient *in vitro-in silico* framework to delineate the role of transporters in DDIs and assess the robustness of the framework in a clinically relevant ARV DDI scenario. Moreover, this thesis aimed to apply *in vitro* and *in silico* techniques to investigate DDI mechanisms in currently underrepresented sub-populations of PLWH.

7.2 Integrated Experimental and Computational Approaches for the Prediction of DDIs

Several transporters are located in the liver and mediate multiple DDIs involving ARVs (70, 72). Since their recognition as clinically relevant entities in the ADME of numerous drugs, their investigation is a prerequisite for the drug approval process (132). However, as described above, current *in vitro* assessment applications are unable to accurately quantify the role of transporters in such DDIs. This inability largely occurs for three reasons: non-specific transporter substrates, inhibitors and inducers, inconsistent IVIVE methods and a limited mechanistic understanding of transporters. Furthermore, the interplay between transporters and enzymes in the liver adds another layer of complexity during their analysis. *In vitro* techniques can be used together with *in silico* systems to overcome some of these limitations and provide an insight into the mechanisms and magnitudes of transporter-mediated DDIs in the liver (131, 153).

An *in vitro-in silico* framework was developed and verified in Chapter 2 and 3 for the investigation of hepatic transporters in a clinically relevant ARV DDI in Chapter 4. Whilst the framework was able to adequately predict the $CL_{int,T}$ of the OATP1B1 and OATP1B3 probe substrate during verification, there was a tendency to slightly underpredict the DDI with the probe inhibitor. However, these predictions demonstrated improvements over previous assessment applications. Most notably was the ability for the *in vitro* system to quantify a more accurate IC_{50} value for the probe substrate and inhibitor, which proved efficient at overcoming the large underpredictions of transporter DDIs previously reported (190, 191). The *in vitro-in silico* framework was also able to implement an assay specific rather than drug specific IVIVE correction factor for the $CL_{int,T}$ across two different drugs. Furthermore, the implementation of PBPK modelling to estimate passive hepatic uptake demonstrated an effective and sustainable alternative to the quantification of passive uptake *in vitro*. Unfortunately, the *in vitro* system proved ineffective at quantifying the contribution of hepatic transporters in the DDI involving ATV/r and DRV/r. In contrast to the DDI between the probe substrate and inhibitor, significant underpredictions were determined with ATV/r and DRV/r. Although the cause is unconfirmed, it is likely a

false positive result potentially stemming from the physicochemical properties of the drugs and incompatibility with the SPHH *in vitro* system.

As discussed, current *in vitro* and clinical transporter-mediated DDI assessment strategies are limited by the implementation of non-specific victim and perpetrator drugs. This exposes data analysis to the misinterpretation of results as well as the partial understanding of the DDI outcomes, especially considering the interplay between multiple transporters and enzymes in the ADME of a drug. The identification of transporter specific probes is essential for the advancement of transporter pharmacology however this task is particularly challenging considering our current knowledge gap surrounding transporter biology. Endogenous biomarkers have been of increasing interest as prospective transporter substrates in DDI assessment and may offer improved specificity. Whilst endogenous biomarker research remains in the early stages, studies thus far have highlighted their possible application within the initial phases of drug development. With the possibility of quantifying multiple endogenous biomarkers from a single study as opposed to conducting multiple *in vitro* and clinical DDI studies, their application could alleviate some of the complexities of DDI assessment (314, 315).

Moreover, the justifications behind current IVIVE methodologies are ambiguous. Correction factors for the extrapolation of *in vitro* transporter data are commonplace amongst the literature, however they tend to be drug rather than assay specific with one study reporting up to 100-fold variation amongst 7 drugs using SCHHs (192). Although the application of IVIVE correction factors have been thought to account for differences in the transporter expression and activity between *in vitro* and *in vivo* systems, these large, drug specific variations seem to represent a relevant barrier for a reliable application of predictive systems. Interestingly, the drugs with higher active and passive intrinsic clearance values in the abovementioned study had higher IVIVE correction factor values. This was also documented in a study analysing multiple experiments whereby underpredictions increased with increasing *in vitro* clearance values (316). A further paper investigating the potential causes of IVIVE inaccuracies described the incorrect estimation of hepatic blood flow to be a contributing factor towards the underprediction of high clearance drugs through IVIVE (153). These findings could provide logical reasoning behind the variation in IVIVE correction factors and present opportunities for improved extrapolation systems. For

example, specific IVIVE correction factors could be generated for low, medium and high clearance drugs within each cell system.

Furthermore, variation resulting from *in vitro* systems continues to be an issue in transporter assessment, concerning both expression and activity (153, 182). The application of different cell systems with various protocols, incubation times, drug concentrations, donor characteristics and quantification techniques all contribute towards the large variation reported in the literature. Although recommendations have been published by the FDA and ITC in recent years, a consensus on standardised experimental protocols, including IVIVE correction factors, and improved access to large donor pools from an array of populations is key to understanding the authenticity of the currently observed variations (70, 132). By refining current *in vitro* methodologies, the predictive capabilities of PBPK modelling can be exploited, providing sustainable and ethical research strategies for the assessment of transporters.

7.2.1 Older Adults Living with HIV

As the population of OALWH increases, clarity is required on the effect of age on transporter-mediated DDIs. The current omission of OALWH in clinical studies and research compounds their already challenging clinical management. Specifically, there are limited *in vitro* studies investigating transporters in older adults, with the available literature assessing transporter expression remaining inconclusive (77, 252). PBPK modelling has recently been employed to fill the knowledge gap on pharmacokinetics in OALWH, providing a mathematical description of the physiological changes occurring with older age. Although initial predictions concluded no difference in DDI magnitude with older age irrespective of DDI mechanism, the model verification process was limited by minimal transporter DDI clinical and *in vitro* data (123).

The expression and activity of the clinically relevant OATP1B1 transporter was quantified in Chapter 5 presenting preliminary data on the impact of age on transporters. The *in vitro* assay developed and verified in Chapter 2 was implemented alongside a commercially available SLCO1B1 sandwich ELISA kit. It was found that OATP1B1 expression tended to decrease with increased age although this did not correspond to decreased $CL_{int,T}$. Interestingly, a lesser magnitude of DDI between the

OATP1B1 probe substrate and inhibitor was found with increased age, suggesting DDIs could be less pronounced in older adults. However, due to the lack of available elderly hepatocyte donors the findings cannot be classified as definitive. A much larger pool of donors with further substrate and inhibitor combinations are required to generate conclusive evidence on the above-mentioned relationship between age and transporters. Furthermore, utilising the previously published repository, the PBPK model developed as part of the *in vitro-in silico* framework could be expanded to include physiological descriptions of older adults (187). IVIVE of the data produced from this study could then be carried out using the PBPK model, allowing us to understand the clinical impact of potentially lower magnitudes of DDIs in older adults.

Future studies correlating age and transporter expression and activity could encompass the assessment of biological age vs. chronological age. Biological age differs to chronological age in that it considers genetic and epigenetic changes resulting from ageing, lifestyle and disease (317). Biological age can be quantified through multiple techniques with recent studies recommending a combination of assessments involving telomere length, DNA methylation and functional tests such as the frailty index (318). Recently, artificial intelligence has been applied to decipher the abundance of age-related data, providing exciting opportunities for the identification and assessment of age-related biomarkers (319). Of interest, a previously published study found that HIV infection caused an increase in the biological age of blood and brain tissue (8). Moreover, it is plausible that a multitude of factors are attributable to the large variation in transporter data found amongst the literature as well as the contradictory findings surrounding the effect of age on transporter expression and function. For example, a previous study identified a correlation between HIV infection and both enzyme and efflux transporter expression in the intestine (320). However, to what extent different diseases impact transporters has yet to be identified. These unknowns are problematic in the analysis of transporter studies with the identification of causative factors proving difficult to justify. Therefore, research initiatives comparing transporter expression and function against a quantifiable measurement of the combined effect of age, disease and lifestyle would be invaluable in improving our understanding of transporters.

7.2.2 Prediction of Novel Induction-Based DDIs

The induction effect of high, single dose RIF has not been clinically assessed and based on current trends towards the application of higher doses of RIF it is important for us to understand the clinical impact potential DDIs may have. RIF QMT is given as a part of the treatment regimen for leprosy and DDIs involving ARVs are possible due to the geographical overlap in the incidence of leprosy and HIV alongside reported cases of coinfection from smaller studies. However, owing to the lack of data identifying the scale of coinfection, clinical DDI studies have not taken place and there is little guidance for such scenarios. PBPK modelling was employed in Chapter 6 to investigate the magnitude of DDI in the potential coadministration of high dose RIF QMT and the first-line ARV DTG. This involved the mathematical description of CYP3A4 and UGT1A1 induction via the interaction between RIF and the PXR nuclear receptor. Whilst induction mechanisms were successfully developed and verified, providing a first attempt towards the simulation of non-daily induction effects of RIF, the PBPK model was limited by the lack of *in vitro* data for specific induction parameters as well as DTG ADME. This resulted in the overprediction of the magnitude of DDI between DTG and RIF during the verification process and thus the likelihood of overprediction in the application simulations. However, the simulation of overpredictions of DDI magnitudes is preferential to underpredictions so that if anything the worst-case scenario is known.

Quantifying the parameters involved in the mechanisms of enzyme induction *in vitro* could improve the reliability and accuracy of the PBPK model's DDI predictions. Although parameter estimations can provide relative accuracy, the estimation of multiple parameters facilitates over and under prediction with uncertainty as to which parameter could be at fault. Furthermore, having an extensive *in vitro* assessment of DTG metabolism would help improve the current model, allowing for greater confidence in the parameter values applied. Similarly, a comprehensive verification of the UGT1A1 model with further clinical and *in vitro* data would help eliminate any uncertainty in the prediction of the induction magnitudes. To summarise, the most accurate and reliable model simulations are obtained from the implementation of legitimised *in vitro* and *in vivo* data.

As discussed, higher doses of RIF are being investigated for the treatment of TB and several clinical studies have been carried out or are currently underway (59, 262, 321-323). Data from a phase 2b clinical trial in Uganda was recently released at the virtual conference on retroviruses and opportunistic infections (vCROI) 2021 assessing the DDI between DTG 50mg BID and RIF QD dosed at 35mg/kg (324). The study found that the magnitude of DDI was like that of RIF 10mg/kg and the reduction of DTG's C_{min} did not exceed the minimal therapeutic concentration required for HIV treatment. This data suggests that the PXR induction mechanism is potentially saturable at these concentrations of RIF. The new data could be used to recalibrate the PBPK model and simulate a 35mg/kg dose of RIF. Moreover, further studies would be required to define the effectiveness of high doses of RIF for the treatment of leprosy although improvements in treatment outcomes are assumed based on previous studies investigating doses up to 1500mg (60).

7.3 Conclusion

In summary, an *in vitro-in silico* framework was established for the investigation of transporter-mediated DDIs. An accessible platform for the quantification of transporter expression was tested and applied in conjunction with the developed *in vitro* techniques to investigate the impact of age on transporters. Additionally, *in silico* methods were utilised to simulate the mechanisms of PXR-mediated induction to identify potential DDIs. These studies intended to provide information towards the advancement of current *in vitro* and *in silico* DDI assessment strategies and present considerations for the clinical management of PLWH, particularly those with minimal evidence-based guidance.

Bibliography

1. Schmid S. The discovery of HIV-12018 17/02/2021. Available from: https://www.nature.com/articles/d42859-018-00003-x.
2. UNAIDS. Global HIV & AIDS statistics — 2020 fact sheet: UNAIDS; 2020 [Available from: https://www.unaids.org/en/resources/fact-sheet].
3. UNAIDS. AIDS info Geneva, Switzerland: UNAIDS; 2019 [Available from: http://aidsinfo.unaids.org/].
4. WHO. Latest HIV estimates and updates on HIV policies uptake. Geneva, Switzerland: World Health Organisation; 2020.
5. WHO. HIV/AIDS Geneva, Switzerland: World Health Organisation; 2020 [Available from: https://www.who.int/news-room/fact-sheets/detail/hiv-aids].
6. Gueler A, Moser A, Calmy A, Gunthard HF, Bernasconi E, Furrer H, et al. Life expectancy in HIV-positive persons in Switzerland: matched comparison with general population. AIDS. 2017;31(3):427-36.
7. Sánchez-Conde M, Díaz-Alvarez J, Dronda F, Brañas F. Why are people with HIV considered “older adults” in their fifties? European Geriatric Medicine. 2019;10(2):183-8.
8. Horvath S, Levine AJ. HIV-1 infection accelerates age according to the epigenetic clock. J Infect Dis. 2015;212(10):1563-73.
9. Maartens G, Celum C, Lewin SR. HIV infection: epidemiology, pathogenesis, treatment, and prevention. Lancet. 2014;384(9939):258-71.
10. Chaplin DD. Overview of the immune response. J Allergy Clin Immunol. 2010;125(2 Suppl 2):S3-23.
11. Kirchhoff F. HIV life cycle: overview. In: Hope TJ, Stevenson M, Richman D, editors. Encyclopedia of AIDS. New York, NY: Springer New York; 2013. p. 1-9.
12. Deeks SG, Overbaugh J, Phillips A, Buchbinder S. HIV infection. Nature Reviews Disease Primers. 2015;1(1):15035.
13. WHO. WHO clinical staging of HIV disease in adults, adolescents and children. Geneva, Switzerland: World Health Organisation; 2007.
14. NIH. The stages of HIV infection 2020 [Available from: https://hivinfo.nih.gov/understanding-hiv/fact-sheets/stages-hiv-infection#:~:text=The%20three%20stages%20of%20HIV,one%20stage%20to%20the%20next.].

15. NIH. FDA-approved HIV medicines 2021 [Available from: https://hivinfo.nih.gov/understanding-hiv/fact-sheets/fda-approved-hiv-medicines].
16. Landi A, Mazzoldi A, Andreoni C, Bianchi M, Cavallini A, Laurino M, et al. Modelling and control of HIV dynamics. Comput Methods Programs Biomed. 2008;89(2):162-8.
17. WHO. Consolidated guidelines on HIV testing services. Geneva, Switzerland: World Health Organisation; 2019.
18. WHO. WHO recommendations on the diagnosis of HIV infection in infants and children. Geneva, Switzerland: World Health Organisation; 2010.
19. Saag MS. HIV 101: fundamentals of antiretroviral therapy. Top Antivir Med. 2019;27(3):123-7.
20. CDC. Pre-Exposure Prophylaxis (PrEP) and Post-Exposure Prophylaxis (PEP) 2020 [Available from: https://www.cdc.gov/hiv/clinicians/prevention/prep-and-pep.html#:~:text=Syndicate-,Pre%2DExposure%20Prophylaxis%20(PrEP)%20and,Post%2DExposure%20Prophylaxis%20(PEP)&text=PrEP%20is%20a%20prevention%20method,contact%20or%20injection%20drug%20use].
21. Lataillade M, Lalezari JP, Kozal M, Aberg JA, Pialoux G, Cahn P, et al. Safety and efficacy of the HIV-1 attachment inhibitor prodrug fostemsavir in heavily treatment-experienced individuals: week 96 results of the phase 3 BRIGHTE study. Lancet HIV. 2020;7(11):e740-e51.
22. Beccari MV, Mogle BT, Sidman EF, Mastro KA, Asiago-Reddy E, Kufel WD. Ibalizumab, a novel monoclonal antibody for the management of multidrug-resistant HIV-1 infection. Antimicrobial agents and chemotherapy. 2019;63(6).
23. Dorr P, Westby M, Dobbs S, Griffin P, Irvine B, Macartney M, et al. Maraviroc (UK-427,857), a potent, orally bioavailable, and selective small-molecule inhibitor of chemokine receptor CCR5 with broad-spectrum anti-human immunodeficiency virus type 1 activity. Antimicrobial agents and chemotherapy. 2005;49(11):4721-32.
24. Chen RY, Kilby JM, Saag MS. Enfuvirtide. Expert Opin Investig Drugs. 2002;11(12):1837-43.
25. Pau AK, George JM. Antiretroviral therapy: current drugs. Infect Dis Clin North Am. 2014;28(3):371-402.

26. Marzolini C, Gibbons S, Khoo S, Back D. Cobicistat versus ritonavir boosting and differences in the drug-drug interaction profiles with co-medications. J Antimicrob Chemother. 2016;71(7):1755-8.
27. WHO. Update of recommendations on first- and second-line antiretroviral regimens. Geneva, Switzerland: World Health Organisation; 2019.
28. Overton ET, Richmond G, Rizzardini G, Jaeger H, Orrell C, Nagimova F, et al. Long-acting cabotegravir and rilpivirine dosed every 2 months in adults with HIV-1 infection (ATLAS-2M), 48-week results: a randomised, multicentre, open-label, phase 3b, non-inferiority study. Lancet. 2021;396(10267):1994-2005.
29. FDA. FDA approves first extended-release, injectable drug regimen for adults living with HIV 2021 [Available from: https://www.fda.gov/news-events/press-announcements/fda-approves-first-extended-release-injectable-drug-regimen-adults-living-hiv].
30. Chang CC, Crane M, Zhou J, Mina M, Post JJ, Cameron BA, et al. HIV and co-infections. Immunol Rev. 2013;254(1):114-42.
31. WHO. TB HIV fact sheet Geneva, Switzerland: World Health Organisation; 2018 [Available from: https://www.who.int/tb/areas-of-work/tb-hiv/tbhiv_factsheet.pdf].
32. Choo QL, Kuo G, Weiner AJ, Overby LR, Bradley DW, Houghton M. Isolation of a cDNA clone derived from a blood-borne non-A, non-B viral hepatitis genome. Science. 1989;244(4902):359-62.
33. Trepo C. A brief history of hepatitis milestones. Liver Int. 2014;34 Suppl 1:29-37.
34. WHO. Global hepatitis report, 2017. Geneva, Switzerland: World Health Organisation; 2017.
35. WHO. Hepatitis C Geneva, Switzerland: World Health Organisation; 2020 [Available from: https://www.who.int/news-room/fact-sheets/detail/hepatitis-c].
36. Scheel TK, Rice CM. Understanding the hepatitis C virus life cycle paves the way for highly effective therapies. Nat Med. 2013;19(7):837-49.
37. Bishop OT. Chapter 4.3 - Hepatitis C and HIV coinfection in developing countries. In: Kamal SM, editor. Hepatitis C in Developing Countries: Academic Press; 2018. p. 135-55.
38. WHO. Guidelines for the screening care and treatment of persons with chronic hepatitis C infection. Geneva, Switzerland: World Health Organisation; 2016.

39. Rockstroh JK. Influence of viral hepatitis on HIV infection. J Hepatol. 2006;44(1 Suppl):S25-7.

40. López-Huertas MR, Palladino C, Garrido-Arquero M, Esteban-Cartelle B, Sánchez-Carrillo M, Martínez-Román P, et al. HCV-coinfection is related to an increased HIV-1 reservoir size in cART-treated HIV patients: a cross-sectional study. Scientific Reports. 2019;9(1):5606.

41. Childs K, Taylor C, Dieterich D, Agarwal K. Directly acting antivirals for hepatitis C virus arrive in HIV/hepatitis C virus co-infected patients: from 'mind the gap' to 'where's the gap?'. AIDS. 2016;30(7):975-89.

42. Zoratti MJ, Siddiqua A, Morassut RE, Zeraatkar D, Chou R, van Holten J, et al. Pangenotypic direct acting antivirals for the treatment of chronic hepatitis C virus infection: A systematic literature review and meta-analysis. EClinicalMedicine. 2020;18:100237.

43. WHO. Weekly epidemiological record2019; 94:[389-412 pp.].

44. Bennett BH, Parker DL, Robson M. Leprosy: steps along the journey of eradication. Public Health Rep. 2008;123(2):198-205.

45. WHO. Leprosy Geneva, Switzerland: World Health Organisation; 2019 [Available from: https://www.who.int/news-room/fact-sheets/detail/leprosy].

46. Pires CA, Juca Neto FO, de Albuquerque NC, Macedo GM, Batista Kde N, Xavier MB. Leprosy reactions in patients coinfected with HIV: clinical aspects and outcomes in two comparative cohorts in the Amazon region, Brazil. PLoS Negl Trop Dis. 2015;9(6):e0003818.

47. Massone C, Talhari C, Ribeiro-Rodrigues R, Sindeaux RH, Mira MT, Talhari S, et al. Leprosy and HIV coinfection: a critical approach. Expert Rev Anti Infect Ther. 2011;9(6):701-10.

48. Ukwaja KN. Interactions between leprosy and human immunodeficiency virus: more questions than answers. J Neurosci Rural Pract. 2015;6(2):135-6.

49. CDC. Hansen's disease (leprosy): Centers for Disease Control and Prevention; 2017 [Available from: https://www.cdc.gov/leprosy/index.html].

50. Moet FJ, Schuring RP, Pahan D, Oskam L, Richardus JH. The prevalence of previously undiagnosed leprosy in the general population of northwest Bangladesh. PLOS Neglected Tropical Diseases. 2008;2(2):e198.

51. Richardus R, Alam K, Kundu K, Chandra Roy J, Zafar T, Chowdhury AS, et al. Effectiveness of single-dose rifampicin after BCG vaccination to prevent leprosy

in close contacts of patients with newly diagnosed leprosy: A cluster randomized controlled trial. Int J Infect Dis. 2019;88:65-72.

52. WHO. Guidelines for the diagnosis, treatment and prevention of leprosy. New Delhi: World Health Organisation; 2018.

53. Moet FJ, Pahan D, Oskam L, Richardus JH, Group CS. Effectiveness of single dose rifampicin in preventing leprosy in close contacts of patients with newly diagnosed leprosy: cluster randomised controlled trial. BMJ. 2008;336(7647):761-4.

54. Interactions HD. Interaction report Liverpool, UK: Liverpool Drug Interaction Group; 2021 [Available from: https://www.hiv-druginteractions.org/downloads/ajd45jg-4er5-67oy-ur43-009ert.pdf?interaction_ids%5B%5D=103233&interaction_ids%5B%5D=103236&interaction_ids%5B%5D=78667&interaction_ids%5B%5D=67179&interaction_ids%5B%5D=93294&interaction_ids%5B%5D=93297&interaction_ids%5B%5D=130532&interaction_ids%5B%5D=130535&interaction_ids%5B%5D=78673&interaction_ids%5B%5D=71008&interaction_ids%5B%5D=118192&interaction_ids%5B%5D=118195&interaction_ids%5B%5D=102522&interaction_ids%5B%5D=102525&interaction_ids%5B%5D=101811&interaction_ids%5B%5D=101814&interaction_ids%5B%5D=123878&interaction_ids%5B%5D=123906&interaction_ids%5B%5D=123115&interaction_ids%5B%5D=123143&interaction_ids%5B%5D=95532&interaction_ids%5B%5D=95535&interaction_ids%5B%5D=98444&interaction_ids%5B%5D=98447&interaction_ids%5B%5D=97112&interaction_ids%5B%5D=97115&interaction_ids%5B%5D=78681&interaction_ids%5B%5D=69592&interaction_ids%5B%5D=116570&interaction_ids%5B%5D=116573&interaction_ids%5B%5D=81783&interaction_ids%5B%5D=81786&interaction_ids%5B%5D=115835&interaction_ids%5B%5D=115838&interaction_ids%5B%5D=99246&interaction_ids%5B%5D=99249&interaction_ids%5B%5D=99982&interaction_ids%5B%5D=99985&interaction_ids%5B%5D=100229&interaction_ids%5B%5D=100232&interaction_ids%5B%5D=78428&interaction_ids%5B%5D=67040&interaction_ids%5B%5D=85259&interaction_ids%5B%5D=85262&interaction_ids%5B%5D=85968&interaction_ids%5B%5D=85971&interaction_ids%5B%5D=78676&interaction_ids%5B%5D=70910&interaction_ids%5B%5D=87097&interaction_ids%5B%5D=87100&interaction_ids%5B%5D=96379&interaction_ids%5B%5D=96382&interaction_ids%5B%5D=128787&interaction_ids%5B%5D=128790&interaction_ids%5B%5D=78478&interaction_ids%5B%5D=70386&interaction_ids%5B%5D=78665&interaction_ids%5B%5D=701

38&interaction_ids%5B%5D=124744&interaction_ids%5B%5D=124747&interaction_ids%5B%5D=94807&interaction_ids%5B%5D=94810&interaction_ids%5B%5D=78666&interaction_ids%5B%5D=67151&interaction_ids%5B%5D=78677&interaction_ids%5B%5D=70998&interaction_ids%5B%5D=78680&interaction_ids%5B%5D=76462&interaction_ids%5B%5D=78594&interaction_ids%5B%5D=67041&interaction_ids%5B%5D=78675&interaction_ids%5B%5D=76463&interaction_ids%5B%5D=88756&interaction_ids%5B%5D=88759&interaction_ids%5B%5D=78635&interaction_ids%5B%5D=77701&interaction_ids%5B%5D=78669&interaction_ids%5B%5D=67181&interaction_ids%5B%5D=78678&interaction_ids%5B%5D=71065&interaction_ids%5B%5D=78679&interaction_ids%5B%5D=71066&interaction_ids%5B%5D=78671&interaction_ids%5B%5D=69338&interaction_ids%5B%5D=78674&interaction_ids%5B%5D=69729&report_id=Leprosy%20HIV].

55. Semvua HH, Kibiki GS, Kisanga ER, Boeree MJ, Burger DM, Aarnoutse R. Pharmacological interactions between rifampicin and antiretroviral drugs: challenges and research priorities for resource-limited settings. Ther Drug Monit. 2015;37(1):22-32.

56. Steinmann P, Reed SG, Mirza F, Hollingsworth TD, Richardus JH. Innovative tools and approaches to end the transmission of *Mycobacterium leprae*. Lancet Infect Dis. 2017;17(9):e298-e305.

57. Richardus JH, Tiwari A, Barth-Jaeggi T, Arif MA, Banstola NL, Baskota R, et al. Leprosy post-exposure prophylaxis with single-dose rifampicin (LPEP): an international feasibility programme. Lancet Glob Health. 2021;9(1):e81-e90.

58. Dos Santos DS, Duppre NC, Sarno EN, Pinheiro RO, Sales AM, Nery J, et al. Chemoprophylaxis of leprosy with rifampicin in contacts of multibacillary patients: study protocol for a randomized controlled trial. Trials. 2018;19(1):244.

59. Boeree MJ, Diacon AH, Dawson R, Narunsky K, du Bois J, Venter A, et al. A dose-ranging trial to optimize the dose of rifampin in the treatment of tuberculosis. Am J Respir Crit Care Med. 2015;191(9):1058-65.

60. Levy L, Shepard CC, Fasal P. The bactericidal effect of rifampicin on *M. leprae* in man: a) single doses of 600, 900 and 1200 mg; and b) daily doses of 300 mg. Int J Lepr Other Mycobact Dis. 1976;44(1-2):183-7.

61. Aquinas M, Allan WG, Horsfall PA, Jenkins PK, Hung-Yan W, Girling D, et al. Adverse reactions to daily and intermittent rifampicin regimens for pulmonary tuberculosis in Hong Kong. Br Med J. 1972;1(5803):765-71.

62. Mehrotra N, Gupta M, Kovar A, Meibohm B. The role of pharmacokinetics and pharmacodynamics in phosphodiesterase-5 inhibitor therapy. Int J Impot Res. 2007;19(3):253-64.
63. Peters SA. Physiologically-based pharmacokinetic (PBPK) modeling and simulations: principles, methods, and applications in the pharmaceutical industry. New Jersey: John Wiley & Sons, Inc.; 2012.
64. Sanchez-Dominguez CN, Gallardo-Blanco HL, Salinas-Santander MA, Ortiz-Lopez R. Uridine 5'-diphospho-glucronosyltrasferase: its role in pharmacogenomics and human disease. Exp Ther Med. 2018;16(1):3-11.
65. Birkus G, Bam RA, Willkom M, Frey CR, Tsai L, Stray KM, et al. Intracellular activation of tenofovir alafenamide and the effect of viral and host protease inhibitors. Antimicrobial agents and chemotherapy. 2016;60(1):316-22.
66. Ray AS, Fordyce MW, Hitchcock MJ. Tenofovir alafenamide: A novel prodrug of tenofovir for the treatment of human immunodeficiency virus. Antiviral Res. 2016;125:63-70.
67. Doogue MP, Polasek TM. The ABCD of clinical pharmacokinetics. Ther Adv Drug Saf. 2013;4(1):5-7.
68. Di L, Kerns EH. Chapter 19 - Pharmacokinetics. In: Di L, Kerns EH, editors. Drug-Like Properties (Second Edition). Boston: Academic Press; 2016. p. 267-81.
69. Giacomini KM, Galetin A, Huang SM. The international transporter consortium: summarizing advances in the role of transporters in drug development. Clin Pharmacol Ther. 2018;104(5):766-71.
70. International Transporter C, Giacomini KM, Huang SM, Tweedie DJ, Benet LZ, Brouwer KL, et al. Membrane transporters in drug development. Nature reviews Drug discovery. 2010;9(3):215-36.
71. Bai X, Moraes TF, Reithmeier RAF. Structural biology of solute carrier (SLC) membrane transport proteins. Mol Membr Biol. 2017;34(1-2):1-32.
72. Moss DM, Siccardi M, Marzolini C. Mechanisms of drug interactions II: transport proteins. In: Pai MP, Kiser JJ, Gubbins PO, Rodvold KA, editors. Drug Interactions in Infectious Diseases: Mechanisms and Models of Drug Interactions. Cham: Springer International Publishing; 2018. p. 49-85.
73. Colas C, Ung PM, Schlessinger A. SLC transporters: structure, function, and drug discovery. Medchemcomm. 2016;7(6):1069-81.

74. Liu X. SLC family transporters. In: Liu X, Pan G, editors. Drug Transporters in Drug Disposition, Effects and Toxicity. Singapore: Springer Singapore; 2019. p. 101-202.

75. FDA. Drug development and drug interactions: table of substrates, inhibitors and inducers 2020 [Available from: https://www.fda.gov/drugs/drug-interactions-labeling/drug-development-and-drug-interactions-table-substrates-inhibitors-and-inducers#table4-1].

76. Hirano M, Maeda K, Shitara Y, Sugiyama Y. Contribution of OATP2 (OATP1B1) and OATP8 (OATP1B3) to the hepatic uptake of pitavastatin in humans. The Journal of pharmacology and experimental therapeutics. 2004;311(1):139-46.

77. Badee J, Achour B, Rostami-Hodjegan A, Galetin A. Meta-analysis of expression of hepatic organic anion-transporting polypeptide (OATP) transporters in cellular systems relative to human liver tissue. Drug Metab Dispos. 2015;43(4):424-32.

78. Alam K, Crowe A, Wang X, Zhang P, Ding K, Li L, et al. Regulation of organic anion transporting polypeptides (OATP) 1B1- and OATP1B3-mediated transport: an updated review in the context of OATP-mediated drug-drug interactions. Int J Mol Sci. 2018;19(3).

79. Li TT, An JX, Xu JY, Tuo BG. Overview of organic anion transporters and organic anion transporter polypeptides and their roles in the liver. World J Clin Cases. 2019;7(23):3915-33.

80. Thakkar N, Slizgi JR, Brouwer KLR. Effect of liver disease on hepatic transporter expression and function. J Pharm Sci. 2017;106(9):2282-94.

81. Kalliokoski A, Neuvonen PJ, Niemi M. SLCO1B1 polymorphism and oral antidiabetic drugs. Basic Clin Pharmacol Toxicol. 2010;107(4):775-81.

82. Romaine SP, Bailey KM, Hall AS, Balmforth AJ. The influence of SLCO1B1 (OATP1B1) gene polymorphisms on response to statin therapy. Pharmacogenomics J. 2010;10(1):1-11.

83. Lee HH, Ho RH. Interindividual and interethnic variability in drug disposition: polymorphisms in organic anion transporting polypeptide 1B1 (OATP1B1; SLCO1B1). Br J Clin Pharmacol. 2017;83(6):1176-84.

84. Pasanen MK, Neuvonen PJ, Niemi M. Global analysis of genetic variation in SLCO1B1. Pharmacogenomics. 2008;9(1):19-33.

85. Ciracì R, Tirone G, Scaglione F. The impact of drug–drug interactions on pulmonary arterial hypertension therapy. Pulmonary Pharmacology & Therapeutics. 2014;28(1):1-8.
86. Pai MP, Kiser JJ, Gubbins PO, Rodvold KA. Introduction to drug-drug interactions. In: Pai MP, Kiser JJ, Gubbins PO, Rodvold KA, editors. Drug Interactions in Infectious Diseases: Mechanisms and Models of Drug Interactions. Cham: Springer International Publishing; 2018. p. 1-13.
87. Back D, Marzolini C. The challenge of HIV treatment in an era of polypharmacy. J Int AIDS Soc. 2020;23(2):e25449.
88. Filppula AM, Parvizi R, Mateus A, Baranczewski P, Artursson P. Improved predictions of time-dependent drug-drug interactions by determination of cytosolic drug concentrations. Sci Rep. 2019;9(1):5850.
89. Deves R, Krupka RM. A new approach in the kinetics of biological transport. The potential of reversible inhibition studies. Biochim Biophys Acta. 1978;510(1):186-200.
90. Deves R, Krupka RM. A simple test for the sidedness of binding of transport inhibitors. Biochim Biophys Acta. 1990;1030(1):24-31.
91. Krupka RM. The kinetics of transport inhibition by noncompetitive inhibitors. J Membr Biol. 1983;74(3):175-82.
92. Berg JM, Tymoczko JL, Stryer L. Biochemistry. 5th ed. New York: W H Freeman; 2002.
93. Waldrop GL. A qualitative approach to enzyme inhibition. Biochem Mol Biol Educ. 2009;37(1):11-5.
94. Pelley JW. 4 - Enzymes and energetics. In: Pelley JW, editor. Elsevier's Integrated Review Biochemistry (Second Edition). Philadelphia: W.B. Saunders; 2012. p. 29-37.
95. Shugarts S, Benet LZ. The role of transporters in the pharmacokinetics of orally administered drugs. Pharm Res. 2009;26(9):2039-54.
96. Feng HP, Caro L, Fandozzi C, Chu X, Guo Z, Talaty J, et al. Pharmacokinetic interactions between the hepatitis c virus inhibitors elbasvir and grazoprevir and HIV protease inhibitors ritonavir, atazanavir, lopinavir, and darunavir in healthy volunteers. Antimicrobial agents and chemotherapy. 2019;63(4).

97. Engelking LR. Chapter 6 - enzyme kinetics. In: Engelking LR, editor. Textbook of Veterinary Physiological Chemistry (Third Edition). Boston: Academic Press; 2015. p. 32-8.
98. Urquhart BL, Tirona RG, Kim RB. Nuclear receptors and the regulation of drug-metabolizing enzymes and drug transporters: implications for interindividual variability in response to drugs. J Clin Pharmacol. 2007;47(5):566-78.
99. Chen J, Raymond K. Roles of rifampicin in drug-drug interactions: underlying molecular mechanisms involving the nuclear pregnane X receptor. Ann Clin Microbiol Antimicrob. 2006;5:3.
100. Dooley KE, Sayre P, Borland J, Purdy E, Chen S, Song I, et al. Safety, tolerability, and pharmacokinetics of the HIV integrase inhibitor dolutegravir given twice daily with rifampin or once daily with rifabutin: results of a phase 1 study among healthy subjects. J Acquir Immune Defic Syndr. 2013;62(1):21-7.
101. Merck & Co. I. Zepatier: highlights of prescribing information. Whitehouse Station, NJ: Author; 2019.
102. Gutierrez-Valencia M, Martinez-Velilla N, Vilches-Moraga A. Polypharmacy in older people: time to take action. Eur Geriatr Med. 2019;10(1):1-3.
103. Milic J, Russwurm M, Cerezales Calvino A, Brañas F, Sánchez-Conde M, Guaraldi G. European cohorts of older HIV adults: POPPY, AGEhIV, GEPPO, COBRA and FUNCFRAIL. European Geriatric Medicine. 2019;10(2):247-57.
104. Masnoon N, Shakib S, Kalisch-Ellett L, Caughey GE. What is polypharmacy? A systematic review of definitions. BMC Geriatr. 2017;17(1):230.
105. Montejano R, de Miguel R, Bernardino JI. Older HIV-infected adults: complex patients—comorbidity (I). European Geriatric Medicine. 2019;10(2):189-97.
106. Smit M, Brinkman K, Geerlings S, Smit C, Thyagarajan K, Sighem A, et al. Future challenges for clinical care of an ageing population infected with HIV: a modelling study. Lancet Infect Dis. 2015;15(7):810-8.
107. Greene M, Covinsky KE, Valcour V, Miao Y, Madamba J, Lampiris H, et al. Geriatric syndromes in older HIV-infected adults. J Acquir Immune Defic Syndr. 2015;69(2):161-7.
108. Inouye SK, Studenski S, Tinetti ME, Kuchel GA. Geriatric syndromes: clinical, research, and policy implications of a core geriatric concept. J Am Geriatr Soc. 2007;55(5):780-91.

109. Palella FJ, Hart R, Armon C, Tedaldi E, Yangco B, Novak R, et al. Non-AIDS comorbidity burden differs by sex, race, and insurance type in aging adults in HIV care. AIDS. 2019;33(15):2327-35.
110. Allavena C, Hanf M, Rey D, Duvivier C, BaniSadr F, Poizot-Martin I, et al. Antiretroviral exposure and comorbidities in an aging HIV-infected population: The challenge of geriatric patients. PloS one. 2018;13(9):e0203895.
111. Pelchen-Matthews A, Ryom L, Borges AH, Edwards S, Duvivier C, Stephan C, et al. Aging and the evolution of comorbidities among HIV-positive individuals in a European cohort. AIDS. 2018;32(16):2405-16.
112. Darque A, Enel P, Ravaux I, Petit N, Retornaz F. Drug interactions in elderly individuals with the human immunodeficiency virus. J Am Geriatr Soc. 2012;60(2):382-4.
113. Greene M, Steinman MA, McNicholl IR, Valcour V. Polypharmacy, drug-drug interactions, and potentially inappropriate medications in older adults with human immunodeficiency virus infection. J Am Geriatr Soc. 2014;62(3):447-53.
114. Ware D, Palella FJ, Jr., Chew KW, Friedman MR, D'Souza G, Ho K, et al. Prevalence and trends of polypharmacy among HIV-positive and -negative men in the multicenter AIDS cohort study from 2004 to 2016. PloS one. 2018;13(9):e0203890.
115. Schouten J, Wit FW, Stolte IG, Kootstra NA, van der Valk M, Geerlings SE, et al. Cross-sectional comparison of the prevalence of age-associated comorbidities and their risk factors between HIV-infected and uninfected individuals: the AGEhIV cohort study. Clin Infect Dis. 2014;59(12):1787-97.
116. Bagkeris E, Burgess L, Mallon PW, Post FA, Boffito M, Sachikonye M, et al. Cohort profile: the Pharmacokinetic and clinical Observations in PeoPle over fiftY (POPPY) study. Int J Epidemiol. 2018;47(5):1391-2e.
117. De Francesco D, Wit FW, Cole JH, Kootstra NA, Winston A, Sabin CA, et al. The 'COmorBidity in Relation to AIDS' (COBRA) cohort: design, methods and participant characteristics. PloS one. 2018;13(3):e0191791.
118. Nozza S, Malagoli A, Maia L, Calcagno A, Foca E, De Socio G, et al. Antiretroviral therapy in geriatric HIV patients: the GEPPO cohort study. J Antimicrob Chemother. 2017;72(10):2879-86.
119. Courlet P, Livio F, Guidi M, Cavassini M, Battegay M, Stoeckle M, et al. Polypharmacy, drug-drug interactions, and inappropriate drugs: new challenges in the aging population with HIV. Open Forum Infect Dis. 2019;6(12):ofz531.

120. Halloran MO, Boyle C, Kehoe B, Bagkeris E, Mallon P, Post FA, et al. Polypharmacy and drug-drug interactions in older and younger people living with HIV: the POPPY study. Antivir Ther. 2019;24(3):193-201.

121. Stader F, Courlet P, Kinvig H, Battegay M, Decosterd LA, Penny MA, et al. Effect of ageing on antiretroviral drug pharmacokinetics using clinical data combined with modelling and simulation. Br J Clin Pharmacol. 2020.

122. Stader F, Courlet P, Kinvig H, Penny MA, Decosterd LA, Battegay M, et al. Clinical data combined with modeling and simulation indicate unchanged drug-drug interaction magnitudes in the elderly. Clin Pharmacol Ther. 2021;109(2):471-84.

123. Stader F, Decosterd L, Stoeckle M, Cavassini M, Battegay M, Saldanha SA, et al. Aging does not impact drug--drug interaction magnitudes with antiretrovirals. AIDS. 2020;34(6):949-52.

124. Stader F, Kinvig H, Penny MA, Battegay M, Siccardi M, Marzolini C. Physiologically based pharmacokinetic modelling to identify pharmacokinetic parameters driving drug exposure changes in the elderly. Clin Pharmacokinet. 2019.

125. Stader F, Siccardi M, Battegay M, Kinvig H, Penny MA, Marzolini C. Repository describing an aging population to inform physiologically based pharmacokinetic models considering anatomical, physiological, and biological age-dependent changes. Clinical Pharmacokinetics. 2018.

126. Livio F, Marzolini C. Prescribing issues in older adults living with HIV: thinking beyond drug-drug interactions with antiretroviral drugs. Ther Adv Drug Saf. 2019;10:2042098619880122.

127. Interactions HD. Prescribing in elderly PLWH Liverpool, UK: Liverpool Drug Interaction Group; 2019 [Available from: https://liverpool-hiv-hep.s3.amazonaws.com/prescribing_resources/pdfs/000/000/006/original/Aging_2019_Jul.pdf?1562148203].

128. Xu Y, Chen X, Wang K. Global prevalence of hypertension among people living with HIV: a systematic review and meta-analysis. J Am Soc Hypertens. 2017;11(8):530-40.

129. Interactions HD. Prescribing resources Liverpool, UK: Liverpool Drug Interaction Group; 2020 [Available from: www.hiv-druginteractions.org/prescribing-resources].

130. Brañas F, Guaraldi G, Sánchez-Conde M. HIV and aging: time to bridge the gap between clinical research and clinical care. European Geriatric Medicine. 2019;10(2):165-7.

131. Brouwer KL, Keppler D, Hoffmaster KA, Bow DA, Cheng Y, Lai Y, et al. In vitro methods to support transporter evaluation in drug discovery and development. Clin Pharmacol Ther. 2013;94(1):95-112.

132. FDA. *In vitro* metabolism- and transporter- mediated drug-drug interaction studies guidance for industry. In: Administration FaD, editor. Silver Spring, MD: Food and Drug Administration; 2017.

133. Zamek-Gliszczynski MJ, Lee CA, Poirier A, Bentz J, Chu X, Ellens H, et al. ITC recommendations for transporter kinetic parameter estimation and translational modeling of transport-mediated PK and DDIs in humans. Clin Pharmacol Ther. 2013;94(1):64-79.

134. BioIVT. LIVERPOOL cryosuspension hepatocytes: BioIVT; [Available from: https://bioivt.com/liverpool-cryosuspension-hepatocytes].

135. Bosgra S, van de Steeg E, Vlaming ML, Verhoeckx KC, Huisman MT, Verwei M, et al. Predicting carrier-mediated hepatic disposition of rosuvastatin in man by scaling from individual transfected cell-lines in vitro using absolute transporter protein quantification and PBPK modeling. European journal of pharmaceutical sciences : official journal of the European Federation for Pharmaceutical Sciences. 2014;65:156-66.

136. Burlingham BT, Widlanski TS. An intuitive look at the relationship of K_i and IC_{50}: a more general use for the dixon plot. Journal of Chemical Education. 2003;80(2):214.

137. Cer RZ, Mudunuri U, Stephens R, Lebeda FJ. IC_{50}-to-K_i: a web-based tool for converting IC_{50} to K_i values for inhibitors of enzyme activity and ligand binding. Nucleic Acids Res. 2009;37(Web Server issue):W441-5.

138. Haupt LJ, Kazmi F, Ogilvie BW, Buckley DB, Smith BD, Leatherman S, et al. The reliability of estimating K_i values for direct, reversible inhibition of cytochrome P450 enzymes from corresponding IC_{50} values: a retrospective analysis of 343 experiments. Drug Metab Dispos. 2015;43(11):1744-50.

139. Pitt JJ. Principles and applications of liquid chromatography-mass spectrometry in clinical biochemistry. Clin Biochem Rev. 2009;30(1):19-34.

140. CHROMacademy. LC-MS introduction Lanarkshire, Scotland: Crawford Scientific; [Available from: https://www.chromacademy.com/channels/lc-ms-training-courses/principles/lc-ms-introduction/].

141. FDA. Bioanalytical method validation guidance for industry: U.S. Department of Health and Human Services; 2018.

142. Gertz M, Harrison A, Houston JB, Galetin A. Prediction of human intestinal first-pass metabolism of 25 CYP3A substrates from *in vitro* clearance and permeability data. Drug Metab Dispos. 2010;38(7):1147-58.

143. Peters SA. Evaluation of a generic physiologically based pharmacokinetic model for lineshape analysis. Clin Pharmacokinet. 2008;47(4):261-75.

144. Grimstein M, Yang Y, Zhang X, Grillo J, Huang SM, Zineh I, et al. Physiologically Based Pharmacokinetic Modeling in Regulatory Science: An Update From the U.S. Food and Drug Administration's Office of Clinical Pharmacology. J Pharm Sci. 2019;108(1):21-5.

145. Wang Y. PBPK current status and challenges: a regulatory perspective. Development of Best Practices in Physiologically Based Pharmacokinetic Modeling to Support Clinical Pharmacology Regulatory Decision-Making. Silver Spring, MD: FDA; 2019.

146. El-Khateeb E, Burkhill S, Murby S, Amirat H, Rostami-Hodjegan A, Ahmad A. Physiological-based pharmacokinetic modeling trends in pharmaceutical drug development over the last 20-years; in-depth analysis of applications, organizations, and platforms. Biopharm Drug Dispos. 2020.

147. Watanabe T, Kusuhara H, Maeda K, Shitara Y, Sugiyama Y. Physiologically based pharmacokinetic modeling to predict transporter-mediated clearance and distribution of pravastatin in humans. The Journal of pharmacology and experimental therapeutics. 2009;328(2):652-62.

148. Pan Y, Hsu V, Grimstein M, Zhang L, Arya V, Sinha V, et al. The application of physiologically based pharmacokinetic modeling to predict the role of drug transporters: scientific and regulatory perspectives. J Clin Pharmacol. 2016;56 Suppl 7:S122-31.

149. Barton HA, Lai Y, Goosen TC, Jones HM, El-Kattan AF, Gosset JR, et al. Model-based approaches to predict drug-drug interactions associated with hepatic uptake transporters: preclinical, clinical and beyond. Expert Opin Drug Metab Toxicol. 2013;9(4):459-72.

150. Shebley M, Sandhu P, Emami Riedmaier A, Jamei M, Narayanan R, Patel A, et al. Physiologically based pharmacokinetic model qualification and reporting procedures for regulatory submissions: a consortium perspective. Clin Pharmacol Ther. 2018;104(1):88-110.

151. Stader F, Penny MA, Siccardi M, Marzolini C. A comprehensive framework for physiologically based pharmacokinetic modelling in Matlab((R)). CPT Pharmacometrics Syst Pharmacol. 2019.

152. GitHub. Git handbook 2020 [Available from: https://guides.github.com/introduction/git-handbook/].

153. Benet LZ, Sodhi JK. Investigating the theoretical basis for *in vitro-in vivo* extrapolation (IVIVE) in predicting drug metabolic clearance and proposing future experimental pathways. AAPS J. 2020;22(5):120.

154. Tsamandouras N, Rostami-Hodjegan A, Aarons L. Combining the 'bottom up' and 'top down' approaches in pharmacokinetic modelling: fitting PBPK models to observed clinical data. Br J Clin Pharmacol. 2015;79(1):48-55.

155. Siccardi M. Prediction of dosing, schedule and drug-drug interactions of long acting agents. 16th Residential Course on Clinical Pharmacology of Antiretrovirals; 15/01/2021; Virtual2021.

156. Foy M, Sperati CJ, Lucas GM, Estrella MM. Drug interactions and antiretroviral drug monitoring. Curr HIV/AIDS Rep. 2014;11(3):212-22.

157. Schlaeppi C, Vanobberghen F, Sikalengo G, Glass TR, Ndege RC, Foe G, et al. Prevalence and management of drug-drug interactions with antiretroviral treatment in 2069 people living with HIV in rural Tanzania: a prospective cohort study. HIV Med. 2020;21(1):53-63.

158. Deutschmann E, Bucher HC, Jaeckel S, Gibbons S, McAllister K, Scherrer AU, et al. Prevalence of potential drug-drug interactions in patients of the Swiss HIV Cohort Study in the era of HIV integrase inhibitors. Clin Infect Dis. 2020.

159. Chen R, Chen J, Tang Q, Meng Z, Luo L, Zhang W, et al. Use of comedications and potential drug-drug interactions in people living with HIV in China. Journal of Infection and Chemotherapy. 2020;26(7):722-8.

160. Shitara Y. Clinical importance of OATP1B1 and OATP1B3 in drug-drug interactions. Drug Metab Pharmacokinet. 2011;26(3):220-7.

161. Marzolini C, Battegay M, Back D. Mechanisms of drug interactions II: transport proteins. In: Piscitelli SC, Rodvold KA, Pai MP, editors. Drug Interactions in Infectious Diseases. Totowa, NJ: Humana Press; 2011. p. 43-72.

162. FDA. *In vitro* metabolism- and transporter- mediated drug-drug interaction studies guidance for industry: U.S. Department of Health and Human Services; 2017.

163. Thermo Fisher Scientific. Thawing and plating cryopreserved hepatocytes 2011 [Available from: https://www.thermofisher.com/uk/en/home/references/protocols/drug-discovery/adme-tox-protocols/thawing-and-plating-hepatocytes-protocol.html].

164. Thermo Fisher Scientific. *In vitro* sssessment of transporter-mediated uptake in suspension cryopreserved hepatocytes 2011 [Available from: https://www.thermofisher.com/uk/en/home/references/protocols/drug-discovery/adme-tox-protocols/transporter-uptake-protocol.html].

165. Soars MG, Grime K, Sproston JL, Webborn PJ, Riley RJ. Use of hepatocytes to assess the contribution of hepatic uptake to clearance *in vivo*. Drug Metab Dispos. 2007;35(6):859-65.

166. Prueksaritanont T, Chu X, Evers R, Klopfer SO, Caro L, Kothare PA, et al. Pitavastatin is a more sensitive and selective organic anion-transporting polypeptide 1B clinical probe than rosuvastatin. Br J Clin Pharmacol. 2014;78(3):587-98.

167. Kunze A, Huwyler J, Camenisch G, Gutmann H. Interaction of the antiviral drug telaprevir with renal and hepatic drug transporters. Biochemical pharmacology. 2012;84(8):1096-102.

168. Badolo L, Rasmussen LM, Hansen HR, Sveigaard C. Screening of OATP1B1/3 and OCT1 inhibitors in cryopreserved hepatocytes in suspension. European journal of pharmaceutical sciences : official journal of the European Federation for Pharmaceutical Sciences. 2010;40(4):282-8.

169. Thermo Fisher Scientific. Aseptic technique n.d. [Available from: https://www.thermofisher.com/uk/en/home/references/gibco-cell-culture-basics/aseptic-technique.html].

170. Chemometec. The NucleoCounter® NC-100™ n.d. [Available from: https://chemometec.com/Downloads/Brochures/NC100/990-0002_NC-100%20Brochure_US_web.pdf].

171. Yin T, Liu Q, Zhao H, Zhao L, Liu H, Li M, et al. LC–MS/MS assay for pitavastatin in human plasma and subsequent application to a clinical study in healthy Chinese volunteers. Asian Journal of Pharmaceutical Sciences. 2014;9(6):348-55.

172. Mulvana D, Jemal M, Coates Pulver S. Quantitative determination of pravastatin and its biotransformation products in human serum by turbo ion spray LC/MS/MS. Journal of Pharmaceutical and Biomedical Analysis. 2000;23(5):851-66.

173. Tan A, Awaiye K. Use of internal standards in LC-MS bioanalysis. Handbook of LC-MS Bioanalysis2013. p. 217-27.

174. Hawkins C, Dolan JW. Understanding split peaks2004; 17(1):[10-4 pp.]. Available from: https://www.chromatographyonline.com/view/understanding-split-peaks.

175. Izumi S, Nozaki Y, Komori T, Takenaka O, Maeda K, Kusuhara H, et al. Comparison of the Predictability of Human Hepatic Clearance for Organic Anion Transporting Polypeptide Substrate Drugs Between Different In Vitro-In Vivo Extrapolation Approaches. J Pharm Sci. 2017;106(9):2678-87.

176. Bi YA, Scialis RJ, Lazzaro S, Mathialagan S, Kimoto E, Keefer J, et al. Reliable rate measurements for active and passive hepatic uptake using plated human hepatocytes. AAPS J. 2017;19(3):787-96.

177. Chothe PP, Wu SP, Ye Z, Hariparsad N. Assessment of transporter-mediated and passive hepatic uptake clearance using rifamycin-sv as a pan-inhibitor of active uptake. Molecular pharmaceutics. 2018;15(10):4677-88.

178. Maslow MJ, Portal-Celhay C. 27 - Rifamycins. In: Bennett JE, Dolin R, Blaser MJ, editors. Mandell, Douglas, and Bennett's Principles and Practice of Infectious Diseases (Eighth Edition). Philadelphia: Content Repository Only!; 2015. p. 339-49.e3.

179. Mitra P, Weinheimer S, Michalewicz M, Taub ME. Prediction and quantification of hepatic transporter-mediated uptake of pitavastatin utilizing a combination of the relative activity factor approach and mechanistic modeling. Drug Metab Dispos. 2018;46(7):953-63.

180. Sohlenius-Sternbeck AK. Determination of the hepatocellularity number for human, dog, rabbit, rat and mouse livers from protein concentration measurements. Toxicol In Vitro. 2006;20(8):1582-6.

181. Watanabe T, Kusuhara H, Maeda K, Kanamaru H, Saito Y, Hu Z, et al. Investigation of the rate-determining process in the hepatic elimination of HMG-CoA reductase inhibitors in rats and humans. Drug Metab Dispos. 2010;38(2):215-22.

182. McFeely SJ, Ritchie TK, Ragueneau-Majlessi I. Variability in *in vitro* OATP1B1/1B3 inhibition data: impact of incubation conditions on variability and subsequent drug interaction predictions. Clin Transl Sci. 2020;13(1):47-52.

183. Fujino H, Nakai D, Nakagomi R, Saito M, Tokui T, Kojima J. Metabolic stability and uptake by human hepatocytes of pitavastatin, a new inhibitor of HMG-CoA reductase. Arzneimittelforschung. 2004;54(7):382-8.

184. Bi YA, Qiu X, Rotter CJ, Kimoto E, Piotrowski M, Varma MV, et al. Quantitative assessment of the contribution of sodium-dependent taurocholate co-transporting polypeptide (NTCP) to the hepatic uptake of rosuvastatin, pitavastatin and fluvastatin. Biopharm Drug Dispos. 2013;34(8):452-61.

185. Menochet K, Kenworthy KE, Houston JB, Galetin A. Use of mechanistic modeling to assess interindividual variability and interspecies differences in active uptake in human and rat hepatocytes. Drug Metab Dispos. 2012;40(9):1744-56.

186. Rajoli RKR, Flexner C, Chiong J, Owen A, Donnelly RF, Larraneta E, et al. Modelling the intradermal delivery of microneedle array patches for long-acting antiretrovirals using PBPK. European journal of pharmaceutics and biopharmaceutics : official journal of Arbeitsgemeinschaft fur Pharmazeutische Verfahrenstechnik eV. 2019;144:101-9.

187. Stader F, Siccardi M, Battegay M, Kinvig H, Penny MA, Marzolini C. Repository Describing an Aging Population to Inform Physiologically Based Pharmacokinetic Models Considering Anatomical, Physiological, and Biological Age-Dependent Changes. Clin Pharmacokinet. 2019;58(4):483-501.

188. FDA. Physiologically based pharmacokinetic analyses — format and content guidance for industry: U.S. Department of Health and Human Services; 2018.

189. European Medicines Agency. CPMP/EWP/560/95/Rev. 1 Corr. 2** - Guidelines on the Investigation of Drug Interactions2012. Available from: https://www.ema.europa.eu/en/documents/scientific-guideline/guideline-investigation-drug-interactions-revision-1_en.pdf.

190. Taskar KS, Pilla Reddy V, Burt H, Posada MM, Varma M, Zheng M, et al. Physiologically-based pharmacokinetic models for evaluating membrane transporter

mediated drug-drug interactions: current capabilities, case studies, future opportunities, and recommendations. Clin Pharmacol Ther. 2020;107(5):1082-115.

191. Duan P, Zhao P, Zhang L. Physiologically based pharmacokinetic (PBPK) modeling of pitavastatin and atorvastatin to predict drug-drug interactions (DDIs). Eur J Drug Metab Pharmacokinet. 2017;42(4):689-705.

192. Jones HM, Barton HA, Lai Y, Bi YA, Kimoto E, Kempshall S, et al. Mechanistic pharmacokinetic modeling for the prediction of transporter-mediated disposition in humans from sandwich culture human hepatocyte data. Drug Metab Dispos. 2012;40(5):1007-17.

193. Varma MV, Lin J, Bi YA, Rotter CJ, Fahmi OA, Lam JL, et al. Quantitative prediction of repaglinide-rifampicin complex drug interactions using dynamic and static mechanistic models: delineating differential CYP3A4 induction and OATP1B1 inhibition potential of rifampicin. Drug Metab Dispos. 2013;41(5):966-74.

194. DrugBank. Pitavastatin 2013 [Available from: https://go.drugbank.com/drugs/DB08860].

195. FDA. Clinical pharmacology and biopharmaceutics review(s) application number: 22-363: U.S. Department of Health and Human Services; 2009.

196. Riccardi K, Ryu S, Lin J, Yates P, Tess D, Li R, et al. Comparison of species and cell-type differences in fraction unbound of liver tissues, hepatocytes, and cell lines. Drug Metab Dispos. 2018;46(4):415-21.

197. Abe K, Bridges AS, Brouwer KL. Use of sandwich-cultured human hepatocytes to predict biliary clearance of angiotensin II receptor blockers and HMG-CoA reductase inhibitors. Drug Metab Dispos. 2009;37(3):447-52.

198. Fujino H, Saito T, Tsunenari Y, Kojima J, Sakaeda T. Metabolic properties of the acid and lactone forms of HMG-CoA reductase inhibitors. Xenobiotica. 2004;34(11-12):961-71.

199. Statistics NCfH. Anthropometric reference data for children and adults: United States, 2011–2014. In: Services HaH, editor. 3 ed. Washington2016.

200. Shuter B, Aslani A. Body surface area: du bois and du bois revisited. Eur J Appl Physiol. 2000;82(3):250-4.

201. Bosgra S, van Eijkeren J, Bos P, Zeilmaker M, Slob W. An improved model to predict physiologically based model parameters and their inter-individual variability from anthropometry. Crit Rev Toxicol. 2012;42(9):751-67.

202. Brown RP, Delp MD, Lindstedt SL, Rhomberg LR, Beliles RP. Physiological parameter values for physiologically based pharmacokinetic models. Toxicol Ind Health. 1997;13(4):407-84.

203. Rajoli RKR. Investigation of long-acting antiretroviral nanoformulation pharmacokinetics using experimental and computational methods [PhD]: University of Liverpool; 2017.

204. Yu LX, Amidon GL. A compartmental absorption and transit model for estimating oral drug absorption. Int J Pharm. 1999;186(2):119-25.

205. Fujino H, Yamada I, Shimada S, Yoneda M, Kojima J. Metabolic fate of pitavastatin, a new inhibitor of HMG-CoA reductase: human UDP-glucuronosyltransferase enzymes involved in lactonization. Xenobiotica. 2003;33(1):27-41.

206. Ose L. Pitavastatin: finding its place in therapy. Ther Adv Chronic Dis. 2011;2(2):101-17.

207. Barter ZE, Chowdry JE, Harlow JR, Snawder JE, Lipscomb JC, Rostami-Hodjegan A. Covariation of human microsomal protein per gram of liver with age: absence of influence of operator and sample storage may justify interlaboratory data pooling. Drug Metab Dispos. 2008;36(12):2405-9.

208. Proctor NJ, Tucker GT, Rostami-Hodjegan A. Predicting drug clearance from recombinantly expressed CYPs: intersystem extrapolation factors. Xenobiotica. 2004;34(2):151-78.

209. Riley RJ, McGinnity DF, Austin RP. A unified model for predicting human hepatic, metabolic clearance from *in vitro* intrinsic clearance data in hepatocytes and microsomes. Drug Metab Dispos. 2005;33(9):1304-11.

210. Salem F. Applications of physiologically based pharmacokinetic modelling to prediction of the likelihood of metabolic drug interactions in paediatric population and studying disparities in pharmacokinetics between children and adults [PhD]. Manchester: University of Manchester; 2014.

211. Varma MV, Lai Y, Feng B, Litchfield J, Goosen TC, Bergman A. Physiologically based modeling of pravastatin transporter-mediated hepatobiliary disposition and drug-drug interactions. Pharm Res. 2012;29(10):2860-73.

212. Brandt RB, Laux JE, Yates SW. Calculation of inhibitor Ki and inhibitor type from the concentration of inhibitor for 50% inhibition for Michaelis-Menten enzymes. Biochem Med Metab Biol. 1987;37(3):344-9.

213. Poulin P, Theil FP. Prediction of pharmacokinetics prior to *in vivo* studies. 1. mechanism-based prediction of volume of distribution. J Pharm Sci. 2002;91(1):129-56.

214. Wilkins JJ, Savic RM, Karlsson MO, Langdon G, McIlleron H, Pillai G, et al. Population pharmacokinetics of rifampin in pulmonary tuberculosis patients, including a semimechanistic model to describe variable absorption. Antimicrobial agents and chemotherapy. 2008;52(6):2138-48.

215. Almond LM, Mukadam S, Gardner I, Okialda K, Wong S, Hatley O, et al. Prediction of drug-drug interactions arising from CYP3A induction using a physiologically based dynamic model. Drug Metab Dispos. 2016;44(6):821-32.

216. Svensson RJ, Aarnoutse RE, Diacon AH, Dawson R, Gillespie SH, Boeree MJ, et al. A population pharmacokinetic model incorporating saturable pharmacokinetics and autoinduction for high rifampicin doses. Clin Pharmacol Ther. 2018;103(4):674-83.

217. DrugBank. Rifampicin 2005 [Available from: https://go.drugbank.com/drugs/DB01045].

218. Alghamdi WA, Al-Shaer MH, Peloquin CA. Protein binding of first-line antituberculosis drugs. Antimicrobial agents and chemotherapy. 2018;62(7).

219. Ruslami R, Nijland HM, Alisjahbana B, Parwati I, van Crevel R, Aarnoutse RE. Pharmacokinetics and tolerability of a higher rifampin dose versus the standard dose in pulmonary tuberculosis patients. Antimicrobial agents and chemotherapy. 2007;51(7):2546-51.

220. Rajoli RK, Back DJ, Rannard S, Freel Meyers CL, Flexner C, Owen A, et al. Physiologically based pharmacokinetic modelling to inform development of intramuscular long-acting nanoformulations for HIV. Clin Pharmacokinet. 2015;54(6):639-50.

221. Medellin-Garibay SE, Cortez-Espinosa N, Milan-Segovia RC, Magana-Aquino M, Vargas-Morales JM, Gonzalez-Amaro R, et al. Clinical pharmacokinetics of rifampin in patients with tuberculosis and type 2 diabetes mellitus: association with biochemical and immunological parameters. Antimicrobial agents and chemotherapy. 2015;59(12):7707-14.

222. Roberts MS, Rowland M. Correlation between *in-vitro* microsomal enzyme activity and whole organ hepatic elimination kinetics: analysis with a dispersion model. J Pharm Pharmacol. 1986;38(3):177-81.

223. Roberts MS, Rowland M. A dispersion model of hepatic elimination: 1. formulation of the model and bolus considerations. J Pharmacokinet Biopharm. 1986;14(3):227-60.

224. Chen Y, Zhang W, Huang WH, Tan ZR, Wang YC, Huang X, et al. Effect of a single-dose rifampin on the pharmacokinetics of pitavastatin in healthy volunteers. Eur J Clin Pharmacol. 2013;69(11):1933-8.

225. Peng KW, Bacon J, Zheng M, Guo Y, Wang MZ. Ethnic variability in the expression of hepatic drug transporters: absolute quantification by an optimized targeted quantitative proteomic approach. Drug Metab Dispos. 2015;43(7):1045-55.

226. Platt L, Easterbrook P, Gower E, McDonald B, Sabin K, McGowan C, et al. Prevalence and burden of HCV co-infection in people living with HIV: a global systematic review and meta-analysis. Lancet Infect Dis. 2016;16(7):797-808.

227. WHO. HIV and hepatitis coinfections [Available from: https://www.who.int/hiv/topics/hepatitis/hepatitisinfo/en/].

228. Doyle JS, Aspinall E, Liew D, Thompson AJ, Hellard ME. Current and emerging antiviral treatments for hepatitis C infection. Br J Clin Pharmacol. 2013;75(4):931-43.

229. WHO. Guidelines for the care and treatment of persons diagnosed with chronic hepatitis C virus infection. Geneva: World Health Organisation; 2018.

230. Alric L, Bonnet D. Grazoprevir + elbasvir for the treatment of hepatitis C virus infection. Expert Opin Pharmacother. 2016;17(5):735-42.

231. FDA. Clinical pharmacology and biopharmaceutics review application number: 208261Orig1s000. U.S. Department of Health and Human Services; 2015.

232. Drugbank. Grazoprevir 2016 [Available from: https://go.drugbank.com/drugs/DB11575].

233. PubChem. Grazoprevir: NIH; 2010 [Available from: https://pubchem.ncbi.nlm.nih.gov/compound/44603531].

234. Agency EM. EMA/419807/2016 - assessment report zepatier 2016 [Available from: https://www.ema.europa.eu/en/documents/assessment-report/zepatier-epar-public-assessment-report_en.pdf].

235. Tornio A, Filppula AM, Niemi M, Backman JT. Clinical studies on drug-drug interactions involving metabolism and transport: methodology, pitfalls, and interpretation. Clin Pharmacol Ther. 2019;105(6):1345-61.

236. Shyam T, K.N.Rajinikanth, Kumar VK, Raju VA, Ramana MV, Raju NA. LC-MS/MS method development and validation for simulataneous quantification of elbasvir and grazoprevir in human plasma. European Journal of Biomedical and Pharmaceutical Sciences. 2018;5(12):272-81.

237. Potluri H, Battula SR, Yeturu S. Picogram level quantification of grazoprevir and elbasvir with deuterated internal standards in human plasma samples by LC–ESI-MS/MS. Indian Journal of Pharmaceutical Education and Research. 2016;50(4):612-9.

238. Gameiro M, Silva R, Rocha-Pereira C, Carmo H, Carvalho F, Bastos ML, et al. Cellular models and *in vitro* assays for the screening of modulators of P-gp, MRP1 and BCRP. Molecules. 2017;22(4).

239. Singh G, Pai RS. Optimized self-nanoemulsifying drug delivery system of atazanavir with enhanced oral bioavailability: *in vitro/in vivo* characterization. Expert Opin Drug Deliv. 2014;11(7):1023-32.

240. Desai J, Thakkar H. Darunavir-loaded lipid nanoparticles for targeting to HIV reservoirs. AAPS PharmSciTech. 2018;19(2):648-60.

241. Bode C. Perils and pitfalls of *in vitro* drug transporter assays. Genetic Engineering & Biotechnology News. 2013.

242. Javan F, Vatanara A, Azadmanesh K, Nabi-Meibodi M, Shakouri M. Encapsulation of ritonavir in solid lipid nanoparticles: *in-vitro* anti-HIV-1 activity using lentiviral particles. J Pharm Pharmacol. 2017;69(8):1002-9.

243. Interactions H-D. Atazanavir PK fact sheet Liverpool: HIV-Drug Interactions; 2016 [Available from: https://liverpool-hiv-hep.s3.amazonaws.com/fact_sheets/pdfs/000/000/087/original/HIV_FactSheet_ATV_2016_Mar.pdf].

244. Interactions H-D. Darunavir PK fact sheet Liverpool: HIV-Drug Interactions; 2018 [Available from: https://liverpool-hiv-hep.s3.amazonaws.com/prescribing_resources/pdfs/000/000/070/original/HIV_FactSheet_DRV_2018_Oct.pdf?1539783223].

245. Interactions H-D. Ritonavir PK fact sheet Liverpool: HIV-Drug Interactions; 2016 [Available from: https://liverpool-hiv-hep.s3.amazonaws.com/prescribing_resources/pdfs/000/000/074/original/HIV_FactSheet_RTV_2016_Mar.pdf?1520612705].

246. Interactions H-D. Lopinavir PK fact sheet Liverpool: HIV-Drug Interactions; 2016 [Available from: https://liverpool-hiv-hep.s3.amazonaws.com/prescribing_resources/pdfs/000/000/073/original/HIV_FactSheet_LPV_2016_Mar.pdf?1520612690].

247. Annaert P, Ye ZW, Stieger B, Augustijns P. Interaction of HIV protease inhibitors with OATP1B1, 1B3, and 2B1. Xenobiotica; the fate of foreign compounds in biological systems. 2010;40(3):163-76.

248. Parvez MM, Jung JA, Shin HJ, Kim DH, Shin JG. Characterization of 22 antituberculosis drugs for inhibitory interaction potential on organic anionic transporter polypeptide (OATP)-mediated uptake. Antimicrobial agents and chemotherapy. 2016;60(5):3096-105.

249. UNAIDS. People living with HIV - people aged 50 and over [Available from: http://aidsinfo.unaids.org/].

250. Freedman SF, Johnston C, Faragon JJ, Siegler EL, Del Carmen T. Older HIV-infected adults. Complex patients (III): polypharmacy. Eur Geriatr Med. 2019;10(2):199-211.

251. Stader F, Kinvig H, Penny MA, Battegay M, Siccardi M, Marzolini C. Physiologically based pharmacokinetic modelling to identify pharmacokinetic parameters driving drug exposure changes in the elderly. Clin Pharmacokinet. 2020;59(3):383-401.

252. Burt HJ, Riedmaier AE, Harwood MD, Crewe HK, Gill KL, Neuhoff S. Abundance of hepatic transporters in caucasians: a meta-analysis. Drug Metab Dispos. 2016;44(10):1550-61.

253. Aslam B, Basit M, Nisar MA, Khurshid M, Rasool MH. Proteomics: technologies and their applications. J Chromatogr Sci. 2017;55(2):182-96.

254. MyBioSource. SLCO1B1 ELISA Kit: human solute carrier organic anion transporter family, member 1B1 ELISA Kit [Available from: https://www.mybiosource.com/slco1b1-human-elisa-kits/solute-carrier-organic-anion-transporter-family-member-1b1/9323360].

255. Merck. Nuclear protein extraction without the use of detergent [Available from: https://www.sigmaaldrich.com/technical-documents/protocols/biology/nuclear-protein-extraction.html].

256. Thermo Fisher Scientific. Instructions pierce BCA protein assay kit. 2015.

257. Ho RH, Tirona RG, Leake BF, Glaeser H, Lee W, Lemke CJ, et al. Drug and bile acid transporters in rosuvastatin hepatic uptake: function, expression, and pharmacogenetics. Gastroenterology. 2006;130(6):1793-806.
258. Rattan SI, Derventzi A, Clark BF. Protein synthesis, posttranslational modifications, and aging. Ann N Y Acad Sci. 1992;663:48-62.
259. Prasad B, Evers R, Gupta A, Hop CE, Salphati L, Shukla S, et al. Interindividual variability in hepatic organic anion-transporting polypeptides and P-glycoprotein (ABCB1) protein expression: quantification by liquid chromatography tandem mass spectroscopy and influence of genotype, age, and sex. Drug Metab Dispos. 2014;42(1):78-88.
260. Shammas MA. Telomeres, lifestyle, cancer, and aging. Curr Opin Clin Nutr Metab Care. 2011;14(1):28-34.
261. Vakonaki E, Tzatzarakis M, Tsiminikaki K, Nathena D, Fragkiadaki P, Kalliantasi K, et al. Effect of chronic and heavy drug abuse on biological aging. World Acad Sci J. 2019;1(2):67-73.
262. Dooley KE. High-dose rifampin: shall we be bolder? Am J Respir Crit Care Med. 2018;198(5):558-60.
263. Castellino S, Moss L, Wagner D, Borland J, Song I, Chen S, et al. Metabolism, excretion, and mass balance of the HIV-1 integrase inhibitor dolutegravir in humans. Antimicrobial agents and chemotherapy. 2013;57(8):3536-46.
264. Yamashita F, Sasa Y, Yoshida S, Hisaka A, Asai Y, Kitano H, et al. Modeling of rifampicin-induced CYP3A4 activation dynamics for the prediction of clinical drug-drug interactions from *in vitro* data. PloS one. 2013;8(9):e70330.
265. Acocella G. Pharmacokinetics and metabolism of rifampin in humans. Rev Infect Dis. 1983;5 Suppl 3:S428-32.
266. Smith CM, Faucette SR, Wang H, LeCluyse EL. Modulation of UDP-glucuronosyltransferase 1A1 in primary human hepatocytes by prototypical inducers. J Biochem Mol Toxicol. 2005;19(2):96-108.
267. Bunglawala F, Rajoli RKR, Mirochnick M, Owen A, Siccardi M. Prediction of dolutegravir pharmacokinetics and dose optimization in neonates via physiologically based pharmacokinetic (PBPK) modelling. J Antimicrob Chemother. 2020;75(3):640-7.
268. Reese MJ, Savina PM, Generaux GT, Tracey H, Humphreys JE, Kanaoka E, et al. *In vitro* investigations into the roles of drug transporters and metabolizing

enzymes in the disposition and drug interactions of dolutegravir, a HIV integrase inhibitor. Drug Metab Dispos. 2013;41(2):353-61.

269. Salem F. Applications of physiologically based pharmacokinetic modelling to prediction of the likelihood of metabolic drug interactions in paediatric population and studying disparities in pharmacokinetics between children and adults. Manchester: University of Manchester; 2014.

270. Saeheng T, Na-Bangchang K, Karbwang J. Utility of physiologically based pharmacokinetic (PBPK) modeling in oncology drug development and its accuracy: a systematic review. Eur J Clin Pharmacol. 2018;74(11):1365-76.

271. Schwanhausser B, Busse D, Li N, Dittmar G, Schuchhardt J, Wolf J, et al. Global quantification of mammalian gene expression control. Nature. 2011;473(7347):337-42.

272. Baneyx G, Parrott N, Meille C, Iliadis A, Lave T. Physiologically based pharmacokinetic modeling of CYP3A4 induction by rifampicin in human: influence of time between substrate and inducer administration. Eur J Pharm Sci. 2014;56:1-15.

273. Yang J, Liao M, Shou M, Jamei M, Yeo KR, Tucker GT, et al. Cytochrome p450 turnover: regulation of synthesis and degradation, methods for determining rates, and implications for the prediction of drug interactions. Curr Drug Metab. 2008;9(5):384-94.

274. Sugatani J, Sueyoshi T, Negishi M, Miwa M. Regulation of the human UGT1A1 gene by nuclear receptors constitutive active/androstane receptor, pregnane X receptor, and glucocorticoid receptor. Methods Enzymol. 2005;400:92-104.

275. Apgar JF, Tang JP, Singh P, Balasubramanian N, Burke J, Hodges MR, et al. Quantitative systems pharmacology model of hUGT1A1-modRNA encoding for the UGT1A1 enzyme to treat Crigler-Najjar syndrome type 1. CPT Pharmacometrics Syst Pharmacol. 2018;7(6):404-12.

276. Emi Y, Omura S, Ikushiro S, Iyanagi T. Accelerated degradation of mislocalized UDP-glucuronosyltransferase family 1 (UGT1) proteins in Gunn rat hepatocytes. Arch Biochem Biophys. 2002;405(2):163-9.

277. Elliot ER, Cerrone M, Challenger E, Else L, Amara A, Bisdomini E, et al. Pharmacokinetics of dolutegravir with and without darunavir/cobicistat in healthy volunteers. J Antimicrob Chemother. 2019;74(1):149-56.

278. HIV Drug Interactions. Dolutegravir and rifampicin 2020 [Available from: https://www.hiv-

druginteractions.org/interactions/81704#:~:text=The%20recommended%20adult%20dose%20of,this%20combination%20should%20be%20avoided].

279. DrugBank. Dolutegravir 2013 [Available from: https://go.drugbank.com/drugs/DB08930].

280. DrugBank. Midazolam 2005 [Available from: https://go.drugbank.com/drugs/DB00683].

281. DrugBank. Nifedipine [Available from: https://go.drugbank.com/drugs/DB01115].

282. DrugBank. Raltegravir 2010 [Available from: https://go.drugbank.com/drugs/DB06817].

283. Bunglawala FR, R. Owen, A. Siccardi, M. *In silico* prediction of dolutegravir pharmacokinetics & dose optimisation in neonates [poster presentation]. Conference on Retroviruses and Opportunistic Infections; Seattle2019.

284. Tolle-Sander S, Rautio J, Wring S, Polli JW, Polli JE. Midazolam exhibits characteristics of a highly permeable P-glycoprotein substrate. Pharm Res. 2003;20(5):757-64.

285. Beig A, Miller JM, Dahan A. The interaction of nifedipine with selected cyclodextrins and the subsequent solubility-permeability trade-off. Eur J Pharm Biopharm. 2013;85(3 Pt B):1293-9.

286. Moss DM, Siccardi M, Back DJ, Owen A. Predicting intestinal absorption of raltegravir using a population-based ADME simulation. J Antimicrob Chemother. 2013;68(7):1627-34.

287. Friedrich H, Nada A, Bodmeier R. Solid state and dissolution rate characterization of co-ground mixtures of nifedipine and hydrophilic carriers. Drug Dev Ind Pharm. 2005;31(8):719-28.

288. Heizmann P, Eckert M, Ziegler WH. Pharmacokinetics and bioavailability of midazolam in man. Br J Clin Pharmacol. 1983;16 Suppl 1:43S-9S.

289. Ye M, Nagar S, Korzekwa K. A physiologically based pharmacokinetic model to predict the pharmacokinetics of highly protein-bound drugs and the impact of errors in plasma protein binding. Biopharmaceutics & drug disposition. 2016;37(3):123-41.

290. EMA Europe. Scientific discussion 2008 [Available from: https://www.ema.europa.eu/en/documents/scientific-discussion/isentress-epar-scientific-discussion_en.pdf].

291. PubChem. National center for biotechnology information. PubChem database, dolutegravir, CID=54726191 [Available from: https://pubchem.ncbi.nlm.nih.gov/compound/54726191].
292. PubChem. National center for biotechnology information. PubChem database. nifedipine, CID=4485 [Available from: https://pubchem.ncbi.nlm.nih.gov/compound/4485].
293. PubChem. National center for biotechnology information. PubChem database. raltegravir, CID=54671008 [Available from: https://pubchem.ncbi.nlm.nih.gov/compound/54671008].
294. Zhang J, Hayes S, Sadler BM, Minto I, Brandt J, Piscitelli S, et al. Population pharmacokinetics of dolutegravir in HIV-infected treatment-naive patients. Br J Clin Pharmacol. 2015;80(3):502-14.
295. Gorski JC, Jones DR, Haehner-Daniels BD, Hamman MA, O'Mara EM, Jr., Hall SD. The contribution of intestinal and hepatic CYP3A to the interaction between midazolam and clarithromycin. Clin Pharmacol Ther. 1998;64(2):133-43.
296. Wang L, Soon GH, Seng KY, Li J, Lee E, Yong EL, et al. Pharmacokinetic modeling of plasma and intracellular concentrations of raltegravir in healthy volunteers. Antimicrobial agents and chemotherapy. 2011;55(9):4090-5.
297. Higashikawa F, Murakami T, Kaneda T, Takano M. *In-vivo* and *in-vitro* metabolic clearance of midazolam, a cytochrome P450 3A substrate, by the liver under normal and increased enzyme activity in rats. J Pharm Pharmacol. 1999;51(4):405-10.
298. Chen Y, Liu L, Nguyen K, Fretland AJ. Utility of intersystem extrapolation factors in early reaction phenotyping and the quantitative extrapolation of human liver microsomal intrinsic clearance using recombinant cytochromes P450. Drug Metab Dispos. 2011;39(3):373-82.
299. Ndanusa BU, Mustapha A, Abdu-Aguye I. The effect of single does of rifampicin on the pharmacokinetics of oral nifedipine. J Pharm Biomed Anal. 1997;15(9-10):1571-5.
300. Prueksaritanont T, Vega JM, Rogers JD, Gagliano K, Greenberg HE, Gillen L, et al. Simvastatin does not affect CYP3A activity, quantified by the erythromycin breath test and oral midazolam pharmacokinetics, in healthy male subjects. J Clin Pharmacol. 2000;40(11):1274-9.
301. Reitman ML, Chu X, Cai X, Yabut J, Venkatasubramanian R, Zajic S, et al. Rifampin's acute inhibitory and chronic inductive drug interactions: experimental and

model-based approaches to drug-drug interaction trial design. Clin Pharmacol Ther. 2011;89(2):234-42.

302. Wenning LA, Hanley WD, Brainard DM, Petry AS, Ghosh K, Jin B, et al. Effect of rifampin, a potent inducer of drug-metabolizing enzymes, on the pharmacokinetics of raltegravir. Antimicrobial agents and chemotherapy. 2009;53(7):2852-6.

303. Wang X, Cerrone M, Ferretti F, Castrillo N, Maartens G, McClure M, et al. Pharmacokinetics of dolutegravir 100 mg once daily with rifampicin. Int J Antimicrob Agents. 2019;54(2):202-6.

304. Hargrove JL. Microcomputer-assisted kinetic modeling of mammalian gene expression. FASEB J. 1993;7(12):1163-70.

305. Luke NS, DeVito MJ, Shah I, El-Masri HA. Development of a quantitative model of pregnane X receptor (PXR) mediated xenobiotic metabolizing enzyme induction. Bull Math Biol. 2010;72(7):1799-819.

306. Tebbens JD, Azar M, Friedmann E, Lanzendorfer M, Pavek P. Mathematical models in the description of pregnane x receptor (PXR)-regulated cytochrome P450 enzyme induction. Int J Mol Sci. 2018;19(6).

307. Wang YH. Confidence assessment of the Simcyp time-based approach and a static mathematical model in predicting clinical drug-drug interactions for mechanism-based CYP3A inhibitors. Drug Metab Dispos. 2010;38(7):1094-104.

308. Gurjar R. Investigation of molecular mechanisms regulating drug-drug interactions in antiretroviral therapy. Liverpool: University of Liverpool; 2018.

309. Roberts JA, Pea F, Lipman J. The clinical relevance of plasma protein binding changes. Clin Pharmacokinet. 2013;52(1):1-8.

310. Sangana R, Gu H, Chun DY, Einolf HJ. Evaluation of clinical drug interaction potential of clofazimine using static and dynamic modeling approaches. Drug Metab Dispos. 2018;46(1):26-32.

311. i-Base H. HIV pipeline 2020 new drugs in development2020; 21. Available from: https://i-base.info/htb/wp-content/uploads/2020/03/i-Base-HIV-pipeline-March-2020.pdf.

312. Study SHC. Antiretroviral therapy SHCS key data tables 3.1 - 3.9. Zurich: SWISS HIV Cohort Study; 2019.

313. Cobb DA, Smith NA, Edagwa BJ, McMillan JM. Long-acting approaches for delivery of antiretroviral drugs for prevention and treatment of HIV: a review of recent research. Expert Opin Drug Deliv. 2020;17(9):1227-38.
314. Mochizuki T, Mizuno T, Maeda K, Kusuhara H. Current progress in identifying endogenous biomarker candidates for drug transporter phenotyping and their potential application to drug development. Drug Metab Pharmacokinet. 2020;37:100358.
315. Rodrigues AD, Taskar KS, Kusuhara H, Sugiyama Y. Endogenous probes for drug transporters: balancing vision with reality. Clin Pharmacol Ther. 2018;103(3):434-48.
316. Wood FL, Houston JB, Hallifax D. Clearance prediction methodology needs fundamental improvement: trends common to rat and human hepatocytes/microsomes and implications for experimental methodology. Drug Metab Dispos. 2017;45(11):1178-88.
317. Gonzalo S. Epigenetic alterations in aging. J Appl Physiol (1985). 2010;109(2):586-97.
318. Moskalev A. The challenges of estimating biological age. Elife. 2020;9.
319. Zhavoronkov A, Mamoshina P, Vanhaelen Q, Scheibye-Knudsen M, Moskalev A, Aliper A. Artificial intelligence for aging and longevity research: recent advances and perspectives. Ageing Res Rev. 2019;49:49-66.
320. Kis O, Sankaran-Walters S, Hoque MT, Walmsley SL, Dandekar S, Bendayan R. HIV-1 alters intestinal expression of drug transporters and metabolic enzymes: implications for antiretroviral drug disposition. Antimicrobial agents and chemotherapy. 2016;60(5):2771-81.
321. Dian S, Yunivita V, Ganiem AR, Pramaesya T, Chaidir L, Wahyudi K, et al. Double-blind, randomized, placebo-controlled phase II dose-finding study to evaluate high-dose rifampin for tuberculous meningitis. Antimicrobial agents and chemotherapy. 2018;62(12).
322. Peloquin CA, Velasquez GE, Lecca L, Calderon RI, Coit J, Milstein M, et al. Pharmacokinetic evidence from the HIRIF trial to support increased doses of rifampin for tuberculosis. Antimicrobial agents and chemotherapy. 2017;61(8).
323. Seijger C, Hoefsloot W, Bergsma-de Guchteneire I, Te Brake L, van Ingen J, Kuipers S, et al. High-dose rifampicin in tuberculosis: Experiences from a Dutch tuberculosis centre. PloS one. 2019;14(3):e0213718.

324. Sekaggya-Wiltshire C, Nabisere R, Musaazi J, Aber F, Otaalo B, Lamorde M, et al. PK and safety of high-dose rifampicin in TB/HIV coinfected patients on EFV or DTG. CROI; Virtual: IAS-USA; 2021.